Hybrid continuum robot for middle ear surgery : design, fabrication and demonstration

Dang Viet Anh Nguyen

Thèse de doctorat de l'établissement Université Bourgogne Franche-Comté preparée à l'Institut de Recherche Femto-ST

École doctorale n° 37
Sciences Pour l'Ingénieur et Microtechniques

Doctorat en Automatique

Par

Dang-Viet-Anh Nguyen

Robot continuum hybride pour la chirurgie de l'oreille moyenne : conception, fabrication et démonstration

Thèse présentée et soutenue à Besançon, le 11 juillet, 2023

Composition du Jury :

Yassine HADDAB	Professeur Université de Montpellier, LIRMM, Montpellier	Président
Alexandre KRUSZEWSKI	Professeur École Centrale de Lille, Lille	Rapporteur
Emmanuel VANDER POORTEN	Professeur Associé KU Leuven	Rapporteur
Jérôme SZEWCZYK	Professeur Sorbonne Université, Paris	Co-directeur de thèse
Kanty RABENOROSOA	Professeur Associé (HDR) Département AS2M, Institut FEMTO-ST, UBFC	Directeur de thèse

Ph.D. thesis of the University Bourgogne Franche-Comté prepared at Femto-ST Research Institute

Doctoral school n° 37
Engineering Sciences and Microtechnologies

Ph.D. in Automatic

by

Dang-Viet-Anh Nguyen

Hybrid continuum robot for middle ear surgery: design, fabrication and demonstration

Thesis defended publicly in Besançon, on July 11, 2023

Composition of Jury :

Yassine HADDAB	Professor University of Montpellier, LIRMM, Montpellier	President
Alexandre KRUSZEWSKI	Professor Centrale Lille, Lille	Reviewer
Emmanuel VANDER POORTEN	Associate Professor KU Leuven	Reviewer
Jérôme SZEWCZYK	Professor Sorbonne University, Paris	Co-Supervisor
Kanty RABENOROSOA	Associate Professor (HDR) AS2M Department, FEMTO-ST Institute, UBFC	Supervisor

To my family

Acknowledgment

The completion of this PhD thesis marks the culmination of a transformative rewarding journey that spanned several years. This work would not have been possible without the support, encouragement, and contributions of many people and I am very grateful to them.

First of all, I would like to express my deepest gratitude to my supervisors, Associate Professor Kanty Rabenorosoa and Professor Jérôme SZEWCZYK, for their unwavering support, guidance, and expertise throughout the entire journey of my doctoral research. Your mentorship has been invaluable, and I am truly grateful for the countless hours you dedicated to helping me refine my ideas and navigate the challenges of this project.

Secondly, I extend my heartfelt thanks to the members of my thesis committee, Professor Yassine HADDAB, Professor Alexandre KRUSZEWSKI, and Associate Professor Emmanuel VANDER POORTEN, for their valuable insights, constructive feedback, and scholarly contributions that significantly enriched the quality of this thesis.

Thirdly, I am deeply indebted to the University Bourgogne Franche-Comté and AS2M Department, FEMTO-ST Institute for providing me with the resources, facilities, and a vibrant academic community that fostered an environment conducive to research and learning. The financial support from the ANR μRoCS project has been instrumental in enabling me to carry out this research. I would like to express my gratitude to each member of the project team for your unwavering dedication, expertise, and collaborative spirit throughout the duration of our project.

I extend my appreciation to the numerous research participants who generously volunteered their time and shared their experiences, without whom this research would not have been possible. Your contributions have added depth and relevance to this study. Especially, Mr. Patrick ROUGEOT who helped me a lot for the setup of my experiments, Mr. Pierre ROUX and Mr. Michel GERARD for their technical support on the robot prototype fabrication, Dr. Cédric GIRERD for his sharing on concentric tube robot modeling, and Mr. Quentin BOYER for helping me in the demonstration of cholesteatoma ablation.

Furthermore, my sincere gratitude goes out to Professor Phillipe LUTZ and Professor Yann LE GORREC, the directors of AS2M department during the completion of my doctoral thesis. I also thank every people in the lab, in particular Ms. Isabelle GABET and Ms. Estelle PETITE for their cooperation concerning all the administrative stuff. Thank my colleagues and fellow graduate students who provided invaluable camaraderie, support, and stimulating discussions during this academic journey. Special thanks to all my office colleagues Chifaa, Antoine, and Hugo for theirs cultural exchanges, general discussion, the positive energy they

bring to the workplace. I would like to thank Kejun, Quentin, Chibundo, Nelson Eduardo, Jinlong, Ning, Bhawnath, Jesús, Abbas, Amine, Bassel for being good friends and sharing very nice moments with me.

I would like to acknowledge my family in Vietnam for their unwavering encouragement, understanding, and patience. Your support sustained me during the long hours of research and writing, and I am profoundly grateful for your belief in me. I would like to thank my godfather and mother for supporting me a lot in life, especially during the period of social distancing due to Covid-19. Thank you to all my Vietnamese friends who have been by my side in France. I appreciate the friendship, support, and the wonderful memories we have shared. We are like a distant family, and I am truly grateful for that. I want to express my gratitude to the Vietnamese community in Besançon for consistently providing me with emotional support and encouragement.

In conclusion, this journey has been challenging, transformative, and rewarding in ways I could have never imagined. The acknowledgment of the support and contributions of all those mentioned above is but a small token of my gratitude for their role in making this thesis a reality.

Thank you all for being a part of this journey.

Dang Viet Anh NGUYEN, October 8th, 2023, in Vienne, France

Contents

Acknowledgment iii

Contents v

General Introduction 1

I μRoCS Project 5

I.1 Clinical Context of Cholesteatoma 6
I.1.1 Definition of cholesteatoma 6
I.1.2 Epidemiology and Complications 7
I.1.3 Diagnosis 12
I.1.4 Open surgery as treatment 15
I.1.5 Ablation tools 18

I.2 Proposed Approach for Exhaustive Cholesteatoma Removal 18
I.2.1 Project propositions 19

I.3 Conclusion 21

II Robot-Assisted Middle Ear Surgery 23

II.1 Requirements for Middle Ear Surgical Robots 24
II.1.1 Anatomical constraints 24
II.1.2 Robot tasks 25
II.1.3 Ideal requirements of the microrobotic system 26

II.2 Related Surgical Robots 27
II.2.1 Surgical robotic systems for middle ear 27
II.2.2 Other dexterous surgical robots 35

II.3 Proposed Robot for Exhaustive Cholesteatoma Surgery 50

II.4 Conclusion 51

III Hybrid Concentric Tube Robot Modeling 53

III.1 Model Decomposition and Assumptions 54

III.1.1 Model decomposition 54
III.1.2 Assumptions 55
III.2 Concentric Tube Robot 56
III.2.1 CTR kinematics without tendon load 57
III.2.2 Deformation of the CTR under the free internal tendon load 58
III.3 Notched Tube with Tendon-Actuated 81
III.3.1 Static model of the wrist with optical fiber 82
III.3.2 Model calibration & sensitivity analysis 85
III.4 Graphical User Interface of the Hybrid CTR 88
III.5 Conclusion 88

IV Robot Design Requirements and Fabrication 91

IV.1 Robot design requirements 92
IV.1.1 Anatomical reconstruction and analysis 92
IV.1.2 Robot synthesis based on the anatomy 95
IV.2 Robot fabrication 109
IV.2.1 Precurved tube shape setting 109
IV.2.2 Wrist 111
IV.2.3 End cap 113
IV.2.4 Tendon selection 117
IV.2.5 Benchtop prototype 118
IV.2.6 Laser ablation tool 119
IV.3 Conclusion 119

V Experimental Tests 121

V.1 Prototype performance assessment 122
V.1.1 Robot repeatability 123
V.1.2 Motion path following 125
V.2 Demonstration 130
V.2.1 Deployment in confined space 131
V.2.2 Cholesteatoma ablation 132
V.3 Conclusion 135

Conclusions et perspectives 137

A Notation and definitions 141

A.1 Nomenclature of the quantities used for the robot modeling . . . 142

B Basics of CTR kinematics . . . 145

B.1 Torsional compliant kinematic model of the CTR . . . 146

C Experimental data . . . 149

C.1 Tendon load on a soft tube . . . 150

C.2 Bending of the wrist . . . 153

Bibliography . . . 155

List of Figures . . . 183

List of Tables . . . 193

General Introduction

Context

The ear, situated bilaterally on the human skull, plays a crucial role in the sense of hearing and balance. Among various infections and diseases that may affect this organ, cholesteatoma is a frequent disease that relentlessly invades the middle ear. It is a serious form of chronic otitis presented as an abnormal proliferation of epidermal tissue, with desquamation and destruction of surrounding bones. As a consequence, a hearing loss is the common complication of this disease. Urgent otolaryngology consultation should be obtained as delay in treatment can result in intracranial extension with potentially life-threatening conditions [Player 18].

Each year, around one new case per 10,000 inhabitants in Europe is infected by cholesteatoma [Kemppainen 99, Djurhuus 10, Fiedler 13]. In France, there are a total 6130 new patients (statistics from ATIH [1]) over 67 million inhabitants through the year 2020. The only current treatment of cholesteatoma is to remove the infected tissues through a surgical operation. However, the associated risk of recurrences due to residual cholesteatoma can reach 23-25% of cases depending on the country and age group [Gaillardin 12, Sheehy 77]. Follow-up strategy is systematically applied and induces a painful second examination of the patient, along with additional costs. The complete removal of cholesteatoma is thus a considerable limitation of current practices due to the limited dexterity of the surgical tools working in the tiny and confined space of the middle ear cavity.

Therefore, the μRoCS (MicroRobot-assisted Cholesteatoma Surgery) project proposed a surgical robotic system including flexible microrobots which enable contact with hard-to-reach anatomical targets inside the middle ear and perform the cholesteatoma removal by laser. The aim of this project is to reduce the cholesteatoma recurrence by removing efficiently all infected cells from the first operation with a minimally invasive surgery. This microrobotic system will improve the accuracy and repeatability of the surgeon's gestures. The accurate detection of cholesteatoma cells is supported by using optical biopsies. Thanks to a millimeter size and a high bending curvature of its distal end, the flexible surgical tool would improve the accessibility and minimize the need for large incisions. This thus limits the invasive procedure, as well as reduces the patient recovery time.

This project is funded by ANR (Agence Nationale de la Recherche) with the partners including CHRUB (Centre Hospitalier Régional Universitaire de Besançon), INSERM (Institut National de la Santé et de la Recherche Médicale), FEMTO-ST (Franche-Comté Électronique Mécanique Thermique et Optique -

1. ATIH (Agence Technique de l'Informatique sur l'Hospitalisation). [online] https://www.scansante.fr/applications/statistiques-activite-MCO-par-diagnostique-et-actes

Sciences et Technologies), and ISIR (Institut des Systèmes Intelligents et de Robotique). The project coordinator is Professor Laurent Tavernier, head of ENT Service at CHRUB.

Scientific and Technical Contributions

Started on October 1st, 2018, this PhD thesis was conducted at the AS2M (Automatique et Systèmes Micro Mécatroniques) department of FEMTO-ST Institute (France) with the cooperation of AGATHE (Assistance aux Gestes et Applications THErapeutiques) team of ISIR (France). FEMTO-ST Institute is a leading laboratory specializing in the fundamental and applied engineering with a focus on the micro-/nano-robotics. The AGATHE team works on the design of medical robotic devices with the targets on surgical gesture and on people suffering from a motor deficit.

As part of the μRoCS project, this thesis focuses on the mechatronics discipline of the proposed hybrid continuum robot for middle ear surgery. The cholesteatoma surgery was chosen by surgeons from our clinical partners (CHRUB and INSERM), as it is one of the most frequent otological pathologies that urge to enhance its treatment. The main contributions of this thesis including the specifications, design, modelling, prototype fabrication and low-level control of the proposed microrobot based on anatomic constraints; and are organized hereafter.

Chapter I describes the definition, classification, epidemiology, complications, diagnosis, and current treatment of cholesteatoma; thereby, highlights the challenges of cholesteatoma removal from the first surgery due to the limitation of the surgical tools. Then, the propositions of the μRoCS project and the thesis objectives for an exhaustive cholesteatoma surgery will be presented.

Chapter II will propose a comprehensive description of the robot-assisted cholesteatoma surgery in the literature. To do this, it starts by introducing the ideal requirements to reach such an efficient robotic system. Then, a review of the current surgical robotic systems, especially for middle ear surgeries, is highlighted with a brief on the advantages, the disadvantages and the required improvements to be suitable for cholesteatoma surgery. Finally, the robot design will be proposed by taking the compactness of its structure while improving the dexterity at its distal end.

Chapter III models the proposed robot. As the robot kinematics is designed along the continuum robot concept with variable curvature at its distal section, a hybrid actuation approach will be proposed in this thesis. Then, the kineto-static model of the robot will be derived to describe the robot configuration. This chapter also aims to present the inverse design problem of its dexterous distal end as well as the analysis of the coupled actuation problem.

After obtaining the model, Chapter IV starts with the proposition of the robot design parameters according to the anatomic constraints, as well as to the surgical protocol and regulatory specifications. It provides a set of representative configu-

rations to be satisfied by the microrobot in terms of length, diameter, curvature, workspace, and positioning accuracy. For that, CHRUB and INSERM provided CT scans of the target anatomy which will be converted to 3D STL file. As part of the middle ear where the cholesteama cells are found in most of the cases, the tympanic cavity is considered in this thesis as the main surgical site of the robot. The robot specifications are then derived through a proposed method in order to maximize the coverage volume inside the tympanic cavity. This chapter also discusses on different fabrication methods of the robot components.

In Chapter V, the preliminary prototype will be presented on a benchtop and the low-level model-based control will be developed. The robot performances will also be assessed including the model validation and calibration, the robot repeatability, the deployment of the robot inside a middle ear phantom, and the laser ablation of real cholesteatoma collected after surgical procedures from Besançon Hospital.

The last Chapter gives a general conclusion of our work and the different tracks for the future work.

List of publications: The scientific contributions of this PhD thesis are summarized as:

- **Journals**
  - **D. V. A. Nguyen**, C. Girerd, Q. Boyer, P. Rougeot, O. Lehmann, L. Tavernier, J. Szewczyk, and K. Rabenorosoa, "*A hybrid concentric tube robot for cholesteatoma laser surgery*", IEEE Robotics and Automation Letters, vol. 7, no. 1, pp. 462–469, 2021. DOI: 10.1109/LRA.2021.3128685.
  - **D. V. A. Nguyen**, J. Szewczyk, and K. Rabenorosoa, "*An effective algorithm for finding shortest paths in tubular spaces*", Algorithms, vol. 15, no. 3, p. 79, 2022. DOI: 10.3390/a15030079.
- **Conferences and Proceedings**
  - Q. Boyer, **D. V. A. Nguyen**, P. Rougeot, O. Gaiffe, B. Tamadazte, J. Szewczyk, L. Tavernier, Y. Nguyen, and K. Rabenorosoa, "*OCT as tool for laser ablation monitoring applied to cholesteatoma*", CRAS: Computer/Robot Assisted Surgery, 2022.

Chapter I
µRoCS Project

I.1 Clinical Context of Cholesteatoma 6
I.1.1 Definition of cholesteatoma 6
I.1.2 Epidemiology and Complications 7
I.1.3 Diagnosis 12
I.1.4 Open surgery as treatment 15
I.1.5 Ablation tools 18
I.2 Proposed Approach for Exhaustive Cholesteatoma Removal 18
I.2.1 Project propositions 19
I.3 Conclusion 21

This chapter gives a general overview of cholesteatoma from a medical viewpoint. The disease of interest is an abnormal growth of skin cells that infects the middle ear. These cells gradually expands within the temporal bone and can cause many complications. Its only treatment method is a surgical procedure. However, the complete removal of infected cells is still a considerable limitation of current practices that may result in the recurrence of cholesteatoma. The aim of the µRoCS project is to propose new tools and protocols for an exhaustive cholesteatoma surgery as explained in the following.

I.1 Clinical Context of Cholesteatoma

The clinical context of this disease will be presented in this section. It starts by providing the definition of the disease and describing how it is classified. Other information regarding the number of cases in different countries as well as its complications depending on the infected site will also be provided. Afterwards, the only treatment of the disease (surgery) will be discussed to highlight the challenges of cholesteatoma removal due to the limitation of surgical tools.

I.1.1 Definition of cholesteatoma

Cholesteatoma is a benign, but destructive middle ear tumor, characterized by a growth of keratinizing [1] squamous epithelium that occurs in an abnormal location [Huisman 03]. Although occurring mainly in the middle ear cavity, it has also been reported in other areas of the skull, intracranially, and in the auditory canal (where it could be confused with keratosis obturans) [Persaud 07]. The comparison between normal and infected ears due to cholesteatoma is shown in figure I.1.

This disease has probably been first described by De Verney in France in 1683 as "steatoma" [Duverney 31]. In 1829, the French anatomopathologist Cruveilhier called it as a pearl tumor of the temporal bone ("*tumeur perlée*") [Cruveilhier 42]. The term "*cholesteatoma*", devised by the German physiologist Johannes Müller in 1838, has been well established up to now [Müller 38]. However, this must be considered a misnomer as this benign tumor ("-oma") contains neither cholesterol ("chol-") nor fat ("-stea-").

To date, despite numerous investigations, the origin of this disease has still been controversial [Persaud 07]. There are two different types of cholesteatoma: *congenital* and *acquired*. The congenital cholesteatoma is remnants of epithelial tissue behind an intact tympanic membrane. The acquired cholesteatoma is associated with a defect in the tympanic membrane, which develops from this membrane to the middle ear. The development of acquired cholesteatoma may be caused

1. i.e., producing keratin - a tough, insoluble protein substance that is the chief structural constituent of hair, nails, horns, and hooves.

by various mechanisms: immigration, basal hyperplasia, retraction pocket and/or trauma (iatrogenic or non-iatrogenic). It is often infected and results in chronically draining ears [Persaud 07]. These types of cholesteatoma are shown in figure I.2.

I.1.2 Epidemiology and Complications

I.1.2.a Epidemiology

Several studies describe the frequency and distribution of cholesteatoma in large samples throughout the developed countries. Generally, these statistics consist of hospital-based data, or case series from specialized centres and ear surgeons. They

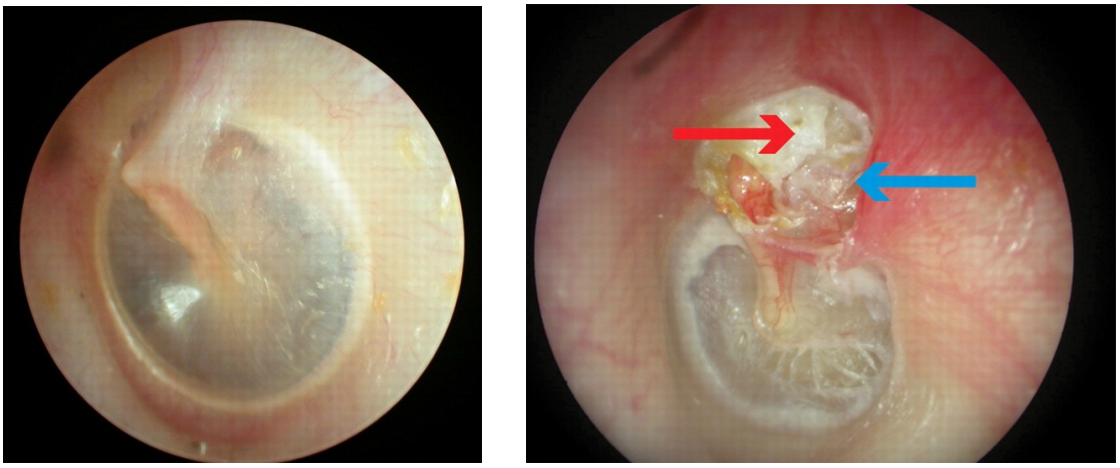

(a) (b)

FIGURE I.1 – Difference between infected and normal ears [Bhutta 11]. (a) Normal tympanic membrane. (b) Red arrow: cholesteatoma arising in the upper part of left tympanic membrane (eardrum). Blue arrow: erosion of surrounding bone.

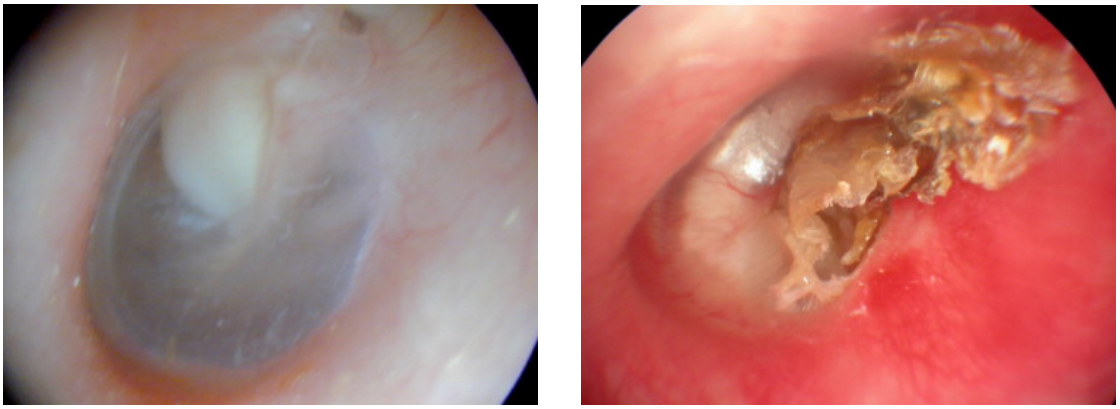

(a) (b)

FIGURE I.2 – (a) Congenital and (b) acquired cholesteatoma [Nevoux 10].

have been reported that the estimation of the annual incidence of cholesteatoma is around 10 per 100,000 inhabitants in Europe [Kemppainen 99, Djurhuus 10, Fiedler 13]. The authors showed in [Koltai 02] that the congenital type is really rare, accounting for 1 to 3% of pediatric cases, and 1 to 5% of cholesteatoma as a whole. Other studies indicate a high prevalence of cholesteatoma among Caucasians followed by people of African descent, and very low in Asians [Olszewska 04, Nevoux 10]. A summary of population-based studies on the incidence rate of cholesteatoma surgery in different countries is shown in Table. I.1. It should further be noted that the incidence of cholesteatoma has declined in recent decades. In addition, the incidence has a male predominance over females and is less in children than in adults [Kemppainen 99, Olszewska 04, Aquino 11] (see figure I.3).

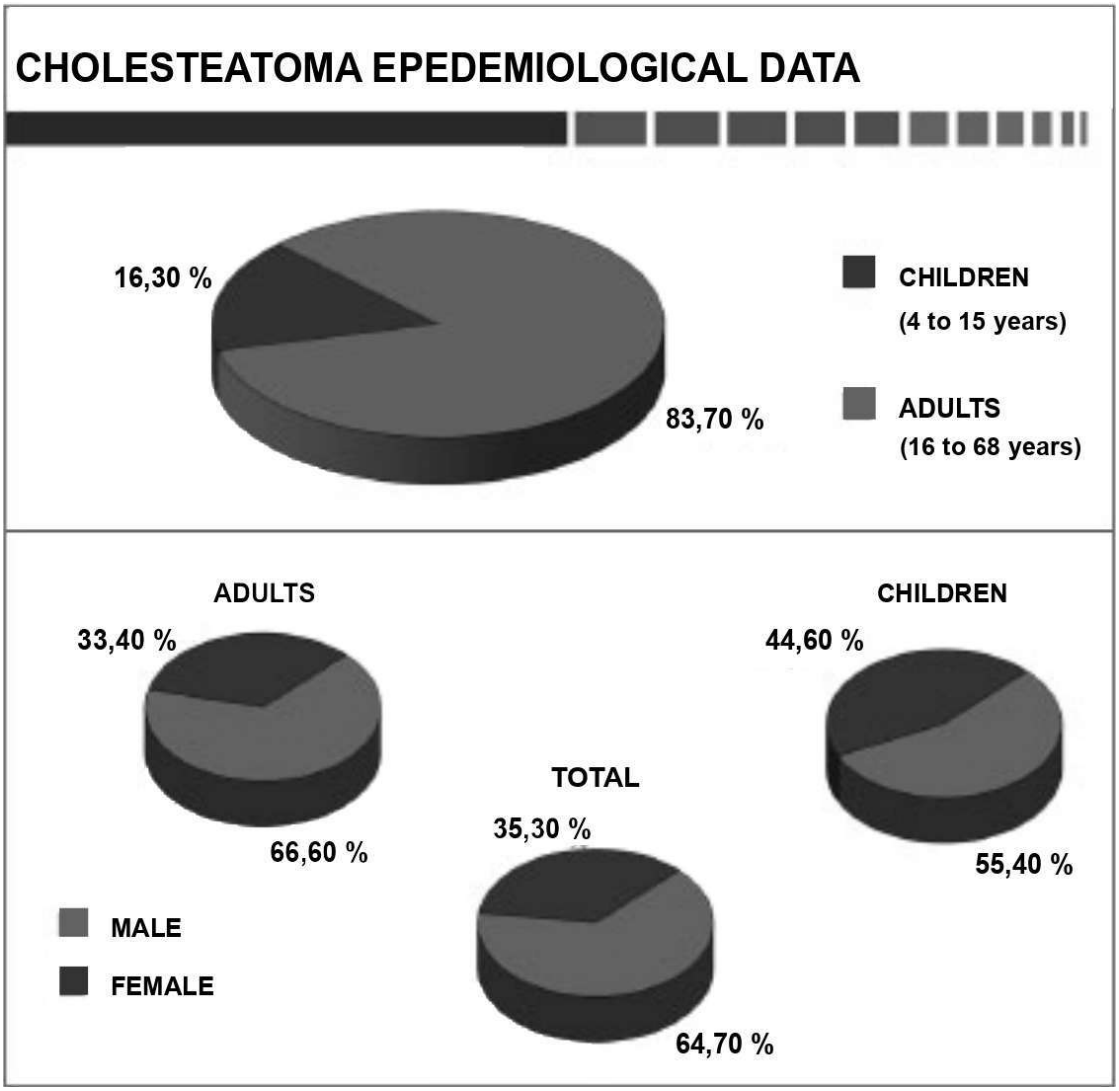

Figure I.3 – A statistical study of 1,146 cholesteatoma surgeries in the period between 1962 and 1988 from all regions of Brazil, of which 960 were adults and 186 were children [Aquino 11].

TABLE I.1 – The incidence rate of cholesteatoma surgery throughout different countries.

Publications	Country	Time	Method of case allocation	Incidence rates (per 100,000 inhabitants)
[Kemppainen 99]	Finland	1982-1991	Individual case record review	Mean incidence of **9.2** (1982–1991)
[Djurhuus 10]	Denmark	1977-2007	International Classification of Diseases (ICD) diagnosis and procedure code analysis	Male: **14.3** (1982), **8.5** (2007); Female: **9.1** (1981), **5.4** (2007)
[Das-Purkayastha 12]	Canada	1987-2007	Mastoidectomy procedure code analysis	**6.93** (1987) and **4.51** (2007)
[Fiedler 13]	Germany	2005	ICD & German Procedure Classification (OPS 301) procedure code analysis	**15** (2005)
[Shibata 15]	Japan	2008	Individual case record review	**6.8** - **10.0** (2008)
[Im 20]	South Korea	2006-2018	Otology procedure code analysis	**7.15** (2006) and **6.17** (2018)
[Li 22]	Australia	2007-2018	ICD principal diagnosis code and procedure code analysis	**8.1** (2007-2008), **8.6** (2017-2018)

Other important statistics data involve the number of cholesteatoma recurrence. Approximately ten to thirty percent of the treatments are reported to be unsuccessful with residual and recurrent cholesteatoma cells [Sheehy 77, Aquino 11, Djurhuus 15], which is even higher in children (up to 45-50%) [Prasad 14]. In France, the recurrence risk in adults has a mean value of 25% from 1998 to 2008

(ranging from 10% to 50% depending on the ENT (ear, nose, and throat) services and the experience of the medical team in cholesteatoma surgery) [Gaillardin 12]. The main reason for this high recurrence rate consists of the difficulties to clearly identify the limits of the cholesteatoma and to reach the hardly accessible area in the middle ear. figure I.4 shows recent French statistics from ATIH that represent the new cases of cholesteatoma interventions (ICD-10 code: H71) as well as the recurrence cases (ICD-10 code: H95.0) every year from 2012 to 2021. There was an unusual drop in data collected in 2020, which is probably explained by the coronavirus lockdowns in France. As shown in the figure, the ratio of H95.0/H71 varies in the range of 9-12% and is on a decreasing trend.

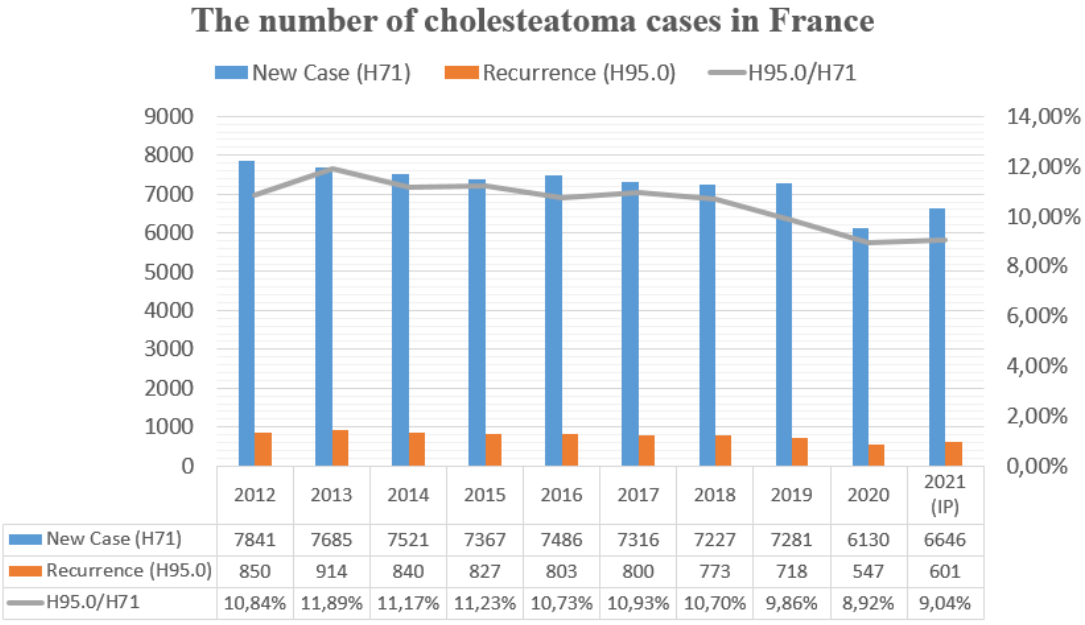

	2012	2013	2014	2015	2016	2017	2018	2019	2020	2021 (IP)
New Case (H71)	7841	7685	7521	7367	7486	7316	7227	7281	6130	6646
Recurrence (H95.0)	850	914	840	827	803	800	773	718	547	601
H95.0/H71	10,84%	11,89%	11,17%	11,23%	10,73%	10,93%	10,70%	9,86%	8,92%	9,04%

FIGURE I.4 – The number of cholesteatoma interventions in France, where H71: the number of patients whose had a first cholesteatoma surgery, H95.0: the number of patients whose had another intervention to remove the residual cholesteatoma. The statistics in 2021 is in progress.

I.1.2.b Complications

Over time, cholesteatoma expands in the middle ear, first filling in the empty cavity around the ossicles, then eroding them (see figure I.6). Draining and hearing loss are usual first symptoms of the cholesteatoma disease. With a delayed treatment, a bone destruction may even spread to the skull base, the inner ear and the facial canal. The risks are then meningitis, vertigo, cophose (total and permanent deafness) or facial palsy (paralysis). In the literature, the complications of cholesteatoma can be classified as intracranial and extracranial complications, the latter being further separated into intra- and extratemporal [Smith 06, Nevoux 10].

- Extratemporal (extracranial):

  - *Subperiosteal abscess* is caused by the infection spread from the mastoid towards the periosteal space.
  - *Bezold's abscess* is a cervical abscess where the bone erosion area at the mastoid apex extends to the neck.
- Intratemporal (extracranial):
  - *Labyrinthine fistula* is a bony erosion of the inner ear.
  - *Mastoiditis* is the internal equivalent of subperiosteal abscess, due to the invasion of the mastoid air cells.
  - *Apicitis* (or petrositis) is the infection of the petrous apex.
  - *Facial paralysis* is due to an fallopian canal erosion which expands to the facial nerve.
- Intracranial:
  - *Meningitis* is an inflammation of meninges that protect the brain and the spinal cord.
  - *Brain abscess* is the most dangerous intracranial complication caused by the infection of brain tissue.
  - *Lateral (sigmoid) sinus thrombosis*[2] is secondary to the infection and inflammation in the middle ear and mastoid air cells as the proximity of them to the dural venous sinuses.
  - *Subdural abscess or empyema* is induced by infection of subdural space.

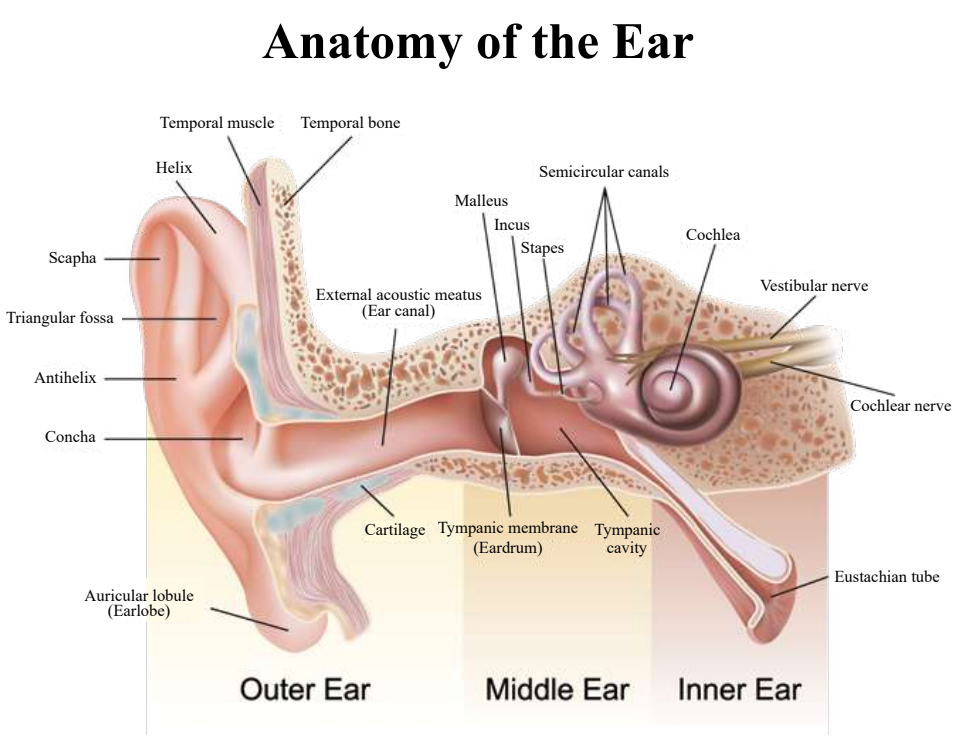

FIGURE I.5 – The three parts of the human ear. [3]

2. Thrombosis occurs when blood clots block veins or arteries.
3. [Online]: https://imgbin.com/png/6wF7XiJp/outer-ear-anatomy-auricle-middle-ear-png.

I.1.3 Diagnosis

Standard diagnosis:

A computerized tomography (CT) scan and a magnetic resonance imaging (MRI) are well known as the standard diagnostic imaging techniques for the pre- and post-operative cholesteatoma procedures [De Foer 14]. Throughout the intra-operative phase, a standard otomicroscopy associated with an otoendoscopy are often used by the surgeon [Khan 16].

- High-Resolution Computer Tomography (HRCT): The HRCT technique provides good information about bony structures such as: the erosion of the ossicular chain and the status of the temporal bone (see figure I.6). However, it is unable to differentiate the soft tissue opacifications [Lemmerling 08].

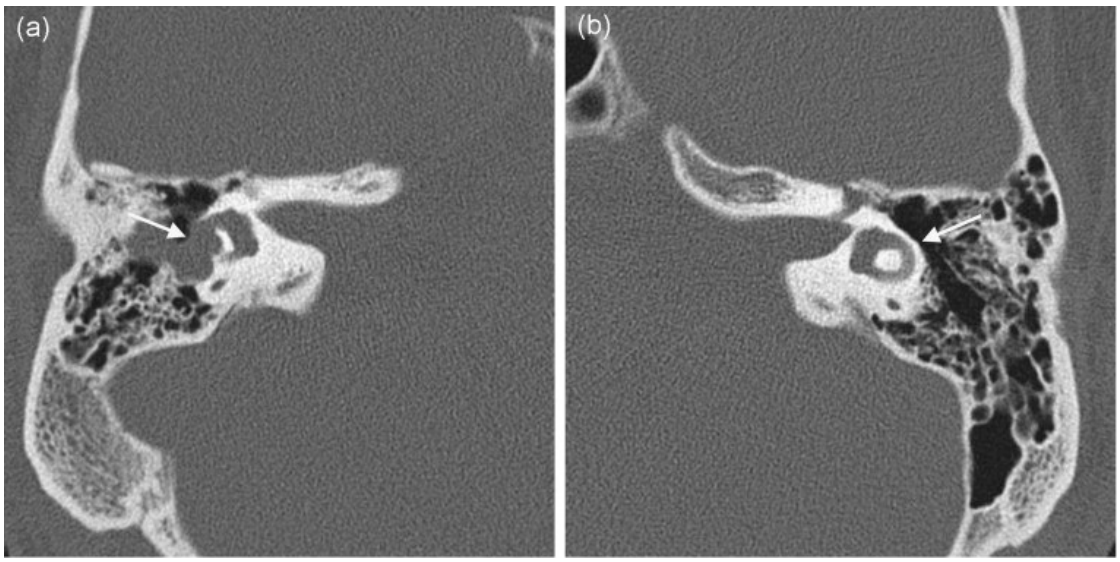

FIGURE I.6 – (a) The HRCT image shows complete erosion of the lateral wall of the lateral semicircular canal (arrow) in a right temporal bone with cholesteatoma. (b) For comparison the corresponding image is shown on the left side, where the intact lateral semicircular canal wall (arrow) is nicely depicted [Lemmerling 08].

- Magnetic resonance imaging: The importance of the MRI compared to the CT scan lies in the exact delineation and description of the cholesteatoma extension in the membranous labyrinth [De Foer 10]. Two different MRI techniques usually used to detect cholestesatoma are the delayed post-Gd T1-weighted imaging and the echo-planar (EP) diffusion-weighted (DWI). A recent work describes a non-EP based DWI sequence that allow the detection of cholesteatoma of 2 mm in size [De Foer 07].

FIGURE I.7 – Surgical setup in middle ear surgery using microscopy [Maier 10].

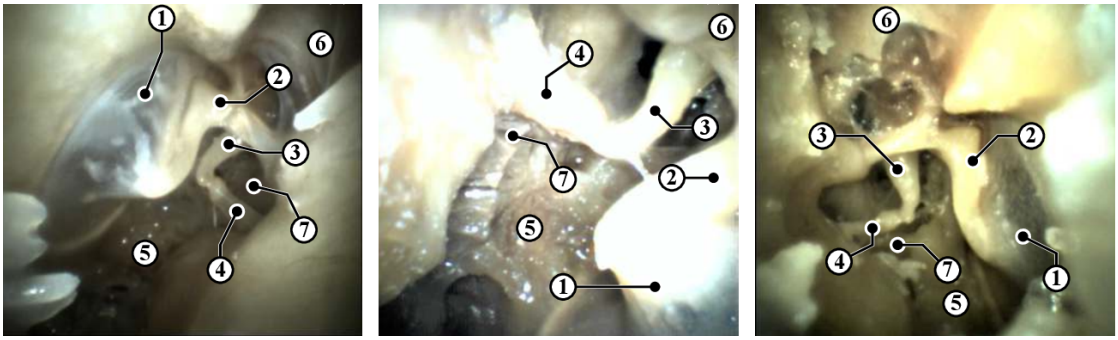

FIGURE I.8 – The middle ear surveillance videos captured of three temporal bone specimens using a miniature steerable digital endoscope. ① Tympanic Membrane, ② Malleus, ③ Incus, ④ Stapes, ⑤ Mesotympanum, ⑥ Epitympanum, ⑦ Sinus Tympani. With the exception of sinus tympani, the picture quality of specimen 1 (left) always outperforms that of specimen 2 (middle). The picture quality of specimen 3 (right) lies between that of specimens 1 and 2. [Gafford 21]

- Otomicroscopy: It is useful for visualizing big cholesteatoma fragments. However, this technique is restricted in field of view, especially to observe the lateral region within the middle ear cavity that may leads to a high risk of leaving cholesteatoma cells behind. figure I.7 shows the middle ear surgery using otomicroscopy.

- Otoendoscopy: Besides the otomicroscopy, the surgeon may also use an otoendoscope to improve the field of view during the surgery [Ayache 08, Hanna 14]. figure I.8 shows the middle ear surveillance using a steerable Trans-Eustachian tube (ET) endoscope. In France, the RobOtol system has been proven that it could be used safely and with accurate control as an endoscope holder for middle ear surgery and cochlear implantation [Vittoria 21].

Cholesteatoma biopsy:

The term "optical biopsy" refers to the use of non-invasive optical methods to perform instant tissue diagnosis by recording optical signatures that are specific to the investigated area [Wang 04]. Promising optical techniques used to detect cholesteatoma include *in situ* Raman spectroscopy [Pandey 15], *in vivo* fluorescence imaging [Valdez 14], and *in vivo* optical coherence tomography (OCT) [Djalilian 10, Guay-Lord 16].

- Raman spectroscopy: It is performed by illuminating tissue with near-infrared (NIR) photons that are absorbed by the unique vibrational modes of molecular bonds that provide a "fingerprint" of the pathophysiological conditions [Pandey 15]. However, this effect is much weaker than that of fluorescence and can be obscured easily by fluorescence from the tissue or optical fiber itself.

- Spectroscopic fluorescence imaging: In order to provide access to the spatial distribution of biochemical markers that indicate changes in the pathophysiological functions, a spectroscopic fluorescence imaging system is used. Based on the analysis of the fluorescence emitted by the tissues, it is considered as a rapid and accurate detection modality which can potentially be used for early detection [Olarte 15]. In case of cholesteatoma, fluorescence properties are influenced by the tissue keratinization [Wu 06]. This method was applied to locate cholesteatoma in real time as reported in [Levy 13, Valdez 14]. This techinique is well suited for the biomolecular composition information of the upper 150 µm of the skin [Lademann 07].

- Optical coherence tomography: It is a high-resolution imaging method that generates cross-sectional images of the tissue and relies on intrinsic differences in its optical properties for image contrast (see figure I.9). The resolution of OCT approaches that of light microscopy [Djalilian 10]. It also performes a better imaging of skin structure (up to a depth of 2 mm) compared to the fluorescence technique [Lademann 07].

In summary, HRCT and MRI techniques are widely used in the current medical practice to diagnose cholesteatoma during pre- and post-operative assessments. The HRCT provides good information about the ossicles and the surrounding bony

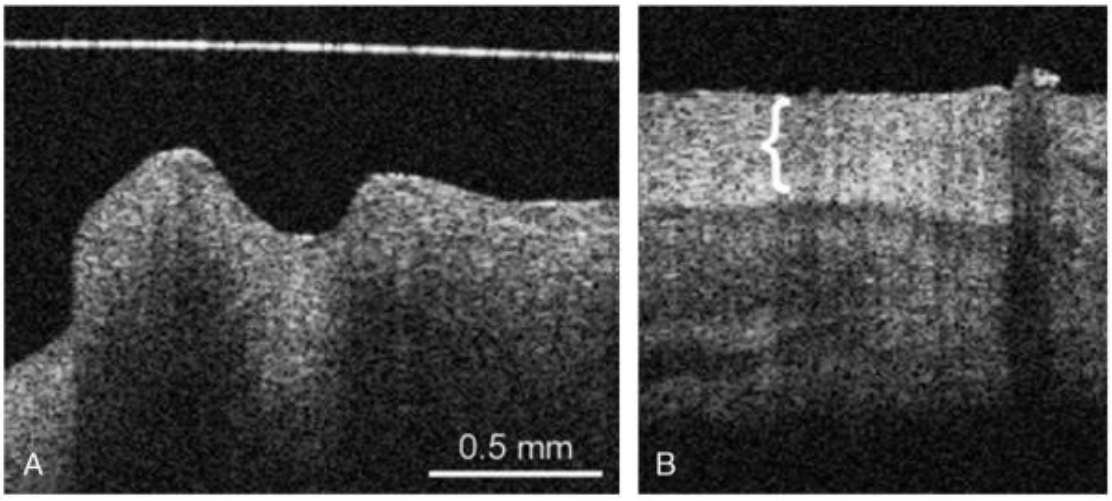

FIGURE I.9 – OCT images of (a) normal middle ear mucosa and (b) cholesteatoma with the keratin layer (bracket) [Djalilian 10].

structures while the MRI gives a closer look on soft tissues, such as cholesteatoma. The MRI method is preferred to used if an infection is suspected to have spread to the inner ear [Sone 12]. The size of the smallest detected cholesteatoma by an MRI is 2 mm [De Foer 07]. Even so, the diagnosis of residual cholesteatoma is often difficult in many cases which explains the need of a second look [McJunkin 14].

A standard otomicroscopy together with an otoendoscopy can be used by the surgeon for visualizing the big fragments of cholesteatoma during the operation. The otoendoscopy technique based on optical fibers is suitable for a minimally invasive procedure and may allow reducing the rate of residual cholesteatoma during the primary surgery [Sajjadi 13] by increasing the field of view in comparison with a conventional otomicroscopy. Nevertheless, as using a visual imaging, this method is not really reliable and does not allow for a clear distinction of small cholesteatoma cells.

Other methods, collectively known as cholesteatoma biopsy, can be considered to deal with the difficulty of detecting residual cholesteatoma, especially for intra-oparative phase. Among these, fluorescence imaging and OCT are the two promising methods with several in vivo experiments. Fluorescence spectroscopy provides information on the biomolecular composition of tissues while OCT allows describing their physical structure. Within μRoCS project, we propose to couple spectroscopic fluorescence imaging with OCT in a bimodal approach [Guay-Lord 16, Pahlevaninezhad 16]. However, the proposed cholesteatoma biopsy will not be presented in this thesis.

I.1.4 Open surgery as treatment

The only treatment of the cholesteatoma disease in the current practice is a surgery. The main goal of the treatment is to eliminate the cholesteatoma and chronic infection to minimize the risk of recurrence [Hildmann 06]. The second ob-

jective is the reconstruction of ear function and the conservation (or improvement) of residual hearing [Blanco 14]. It is important to note that only the first goal will be considered in this thesis. The cholesteatoma cells generally begin in the upper part of the eardrum, expand into the middle ear and fill in the tympanic cavity around the ossicles. Overtime, they can extend from the attic to the antrum of the mastoid portion and cause the invasion of the mastoid air cells (mastoiditis) (see figure I.10).

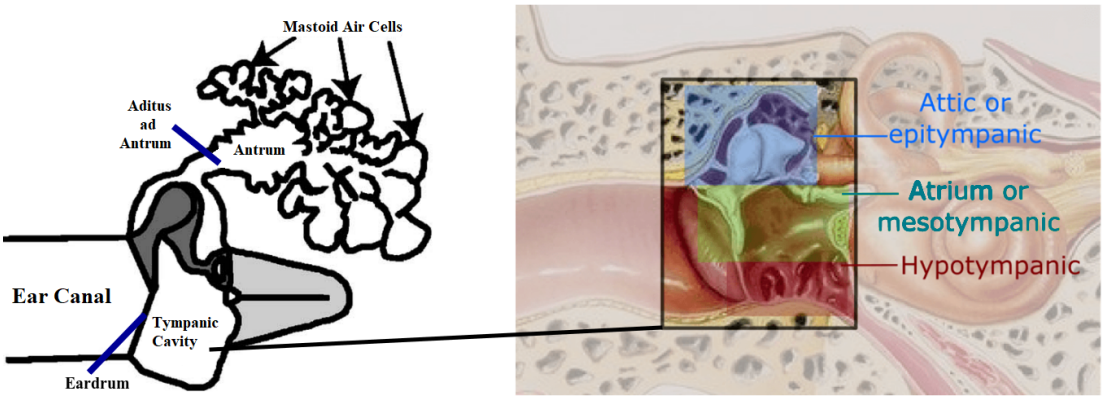

(a) (b)

FIGURE I.10 – (a) Schematic of the human middle ear including tympanic cavity, aditus ad antrum, antrum of mastoid, and mastoid air cells [Stepp 05]. (b) Different regions of the tympanic cavity (epi-, meso-, and hypotympanic) [Dahroug 18a].

Depending on the surgical site, various methods can be used to gain access into the middle ear. Typically, there are three approaches which are often described for this surgical procedure: through the ear canal (transcanal, also called endomeatal or transmeatal approach), through an incision in the ear auricle (endaural approach), or through an incision behind the auricle (postauricular approach or mastoidectomy) [Hildmann 06] (see figure I.11). The last one can be separated into two different types: canal wall down and canal wall up.

Transcanal approach: it is the least traumatic approach which requires a temporary displacement or an opening of the tympanic membrane (see Figure I.12a). This method is used when the mesotympanum and hypotympanum are the surgical sites (see figure I.10b).

Endaural approach: this technique is faster and less traumatic compared to the postauricular approach. It enters the middle ear through the posterior and superior portion of external ear canal and the auricle is pulled up and back to get a good view [Bordure 05] (see Figure I.12b). It is often applied when the cholesteatoma cells are in the attic region of the tympanic cavity. [Nikolopoulos 09].

4. The image is available online on: https://otosurgeryatlas.stanford.edu.

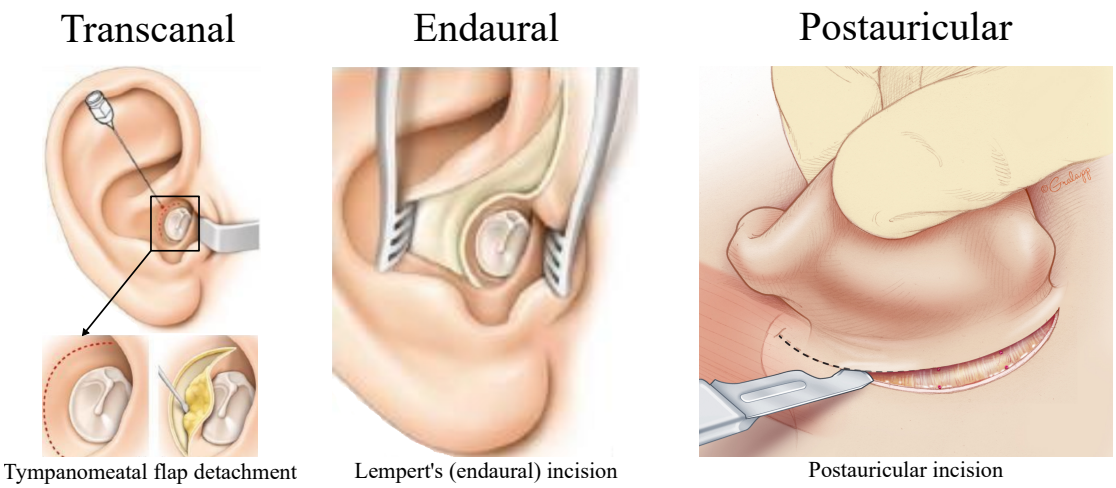

FIGURE I.11 – Different approaches to middle ear [4].

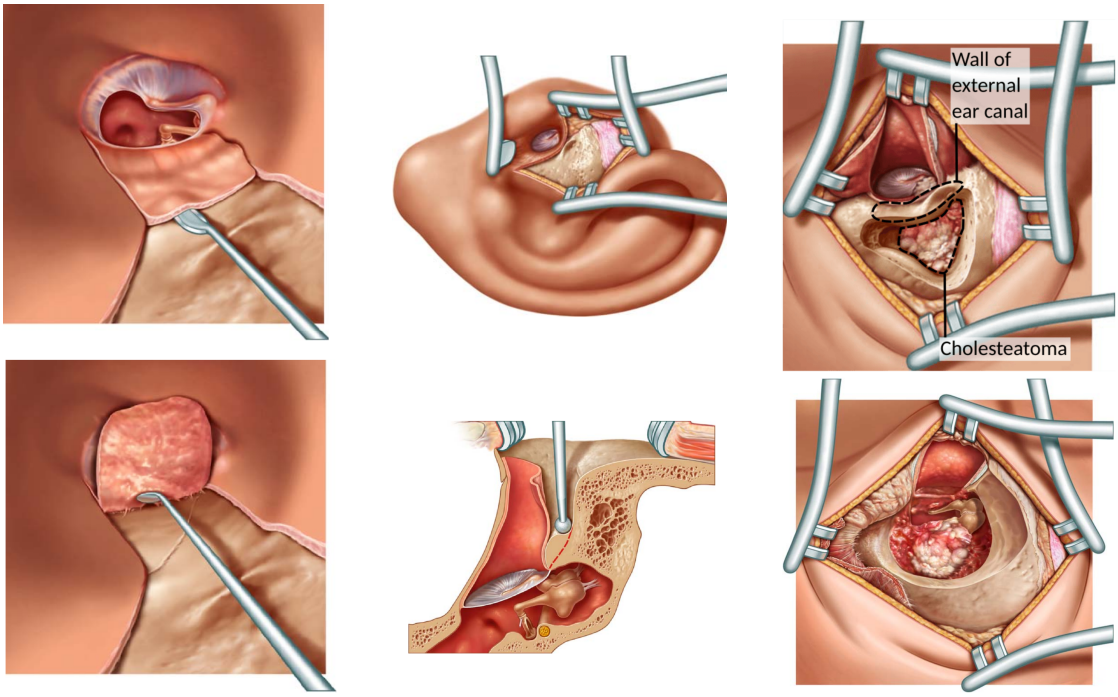

FIGURE I.12 – (a) The transcanal approach with a temporary displacement of the tympanic membrane. (b) The endaural approach: top and side view. (c) The mastoidectomy with canal wall up (top) and down (bottom) processes where the external ear canal is conserved or partitial removed, respectively [Hildmann 06].

Postauricular approach: this method need to be considered when the cholesteatoma extends from the attic to the mastoid portion (see figure I.10). It requires a 3-4 cm incision [Doblan 21] to create a hole (about 3 cm in width [Dahroug 18b]) through the mastoid bone and is divided into two types: canal wall down (CWD)

and canal wall up (or canal wall intact (CWI)). As the name implies, the main difference between these two types is the intactness (for CWI) or not (for CWD) of the external ear canal (see Figure I.12c). The CWD process is an invasive method which creates a bigger orifice (than the CWI) through the mastoid bone to ease the visualization and the elimination of the disease. This technique has the disadvantages of lifelong mastoid care. As less invasive than the previous one, the CWI type is the most used technique which has the potential for a reconstruction (preserving/restoring of hearing) and the better chance to avoid infection after the surgery. As there exist limitations in visualization compared to the previous type, the CWI process probably leaves behind residual cholesteatoma [Alper 04].

I.1.5 Ablation tools

As the excision of cholesteatoma cells requires high dexterity [Bordure 09], the surgeon should be equipped with standard instruments to scatter and suck out the big fragments of cholesteatoma as well as specific ablation tools for burning the residual ones. Such specific tools are usually equipped with laser instrument [Lau 21].

Laser tool: The ablation of the detected residual cholesteatoma using a laser tool has been demonstrated to be efficient in [Hamilton 05]. In this work, solid-state potassium titanyl phosphate (KTP) lasers ($\lambda = 532$ nm) were used for 36 patients and only one patient had residual cholesteatoma after laser ablation compared to (10 out of 33 residual disease cases under treatment without the laser). This result was then extended to 70 patients without any complications associated with KTP laser use [Sharma 20].

Other potential solutions: The idea of using ultrasonic cutting and MEMS (Micro-Electro-Mechanical System) techologies has not been yet applied to the ablation tools of cholesteatoma. However, they could be useful for this surgery. Indeed, the ultrasound technique (Piezosurgery device - Mectron Medical Technology, Genoa, Italy) can perform a mastoidectomy while preserving the facial nerve [Salami 09] and the MEMS tool (Microfabrica Inc, Van Nuys, CA) has a rotor-stator design at a millimeter size (1.8 mm in diameter) to produce a scissoring action on the target tissue in a confined workspace [Gosline 12b].

I.2 Proposed Approach for Exhaustive Cholesteatoma Removal

The µRoCS project aims to propose a novel integrated robotic system that is able to exhaustively and efficiently remove cholesteatoma cells (figure I.13). As part of the project, this thesis focuses on the mechatronic aspects of the foreseen system. The project propositions as well as the thesis objectives will be presented in the remaining of this section.

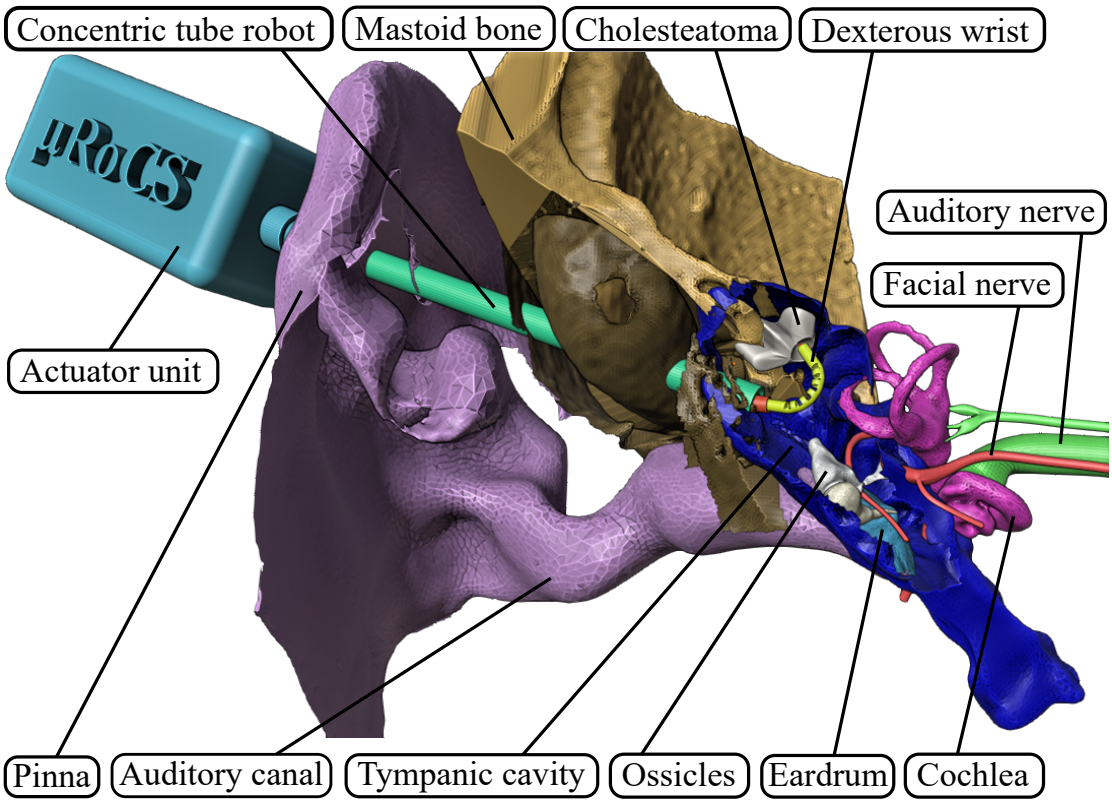

FIGURE I.13 – Conceptual scheme of μRoCS system.

I.2.1 Project propositions

I.2.1.a Global objective

As part of Challenge 4 – *Life, Health and Well-being* of the ANR call, µRoCS aims to drastically reduce the recurrence of cholesteatoma (25% to 10%) by proposing a new surgical protocol associated with an innovative method for residual cholesteatoma detection, high dexterity continuum robots assisted cholesteatoma laser ablation and a surgeon robot interface (SRI) for the complete system control (see figure I.15). The novel integrated robotic system is intended to exhaustively perform residual cholesteatoma ablation through a minimally invasive surgery, especially in the hardly accessible area located behind the mastoid bone (attic) (see figure I.10). The proposed robot is expected to enter the middle ear by a small incision below the eardrum and/or via a small access tunnel drilled through the mastoid bone to the attic. The diagnosis system proposed by µRoCS will allow acquiring at each position of the robot, a 1-D signal that can be employed as an optical biopsy. It is based on a multimodal in-situ tissue characterization technique which couples a fluorescence spectroscopy and an OCT [Guay-Lord 16, Pahlevaninezhad 16] (figure I.15c). Fluorescence spectroscopy will provide information on the biomolecular composition of tissues while OCT will provide information on their physical structure. Data obtained will be analyzed using specifically developed statistical

classification algorithms. With the new surgical protocol, the operating scene will be modeled in order to specifically target regions affected by cholesteatoma in the middle ear cavity. Then, an SRI, a visual servoing, and an automatic local scanning have to be developed for a teleoperated surgical system. The project follows a cross-disciplinary approach including robotics and microrobotics, optical diagnosis, surgeon-robot interface and image-guided interventions. In accordance with the proposed approach, µRoCS project is organized in 6 main work packages:

- Surgical protocol development (CHRUB/INSERM)
- Optical tools for cholesteatoma detection and removal (CHRUB/FEMTO-ST)
- Micromechatronics for middle ear surgery (FEMTO-ST)
- Image-guided surgery (ISIR)
- Integration and evaluation (INSERM)
- Dissemination and exploitation (ISIR)

As part of the project, this thesis focuses on the micromemechatronics work package.

I.2.1.b **Thesis objective**

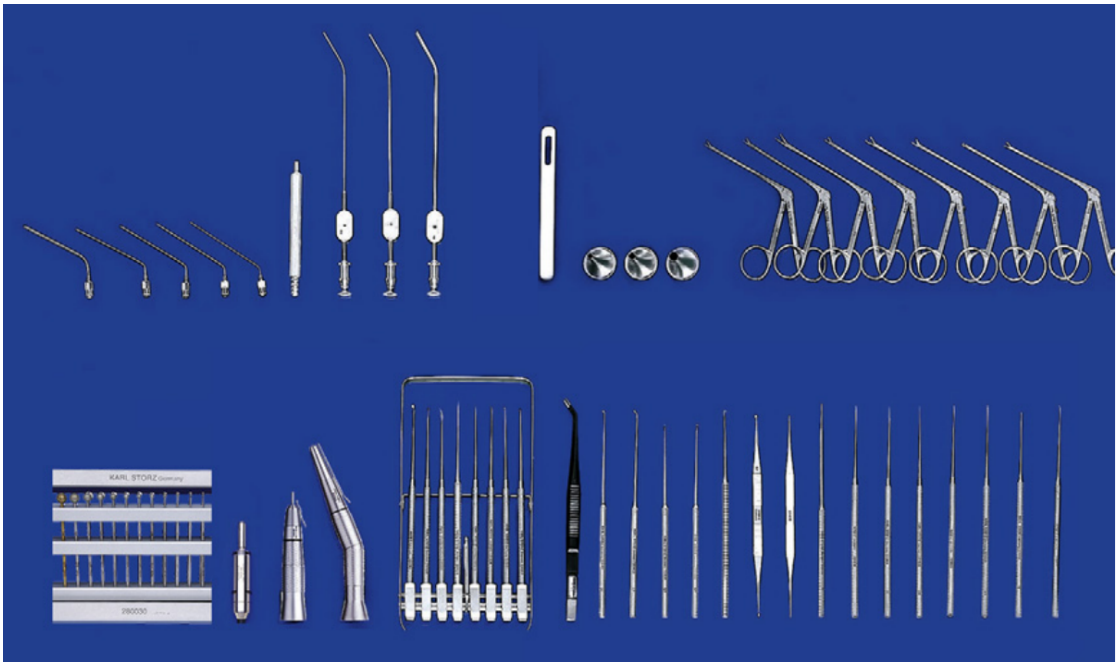

FIGURE I.14 – Standard otologic instruments set used in all regular microscopic ear surgery [Badr-El-Dine 13].

The conventional tools usually used for the microscopic ear surgery need to be thin, in cannula form, and curved at their distal end as reported in [Badr-El-Dine 13] (see figure I.14). However, they are rigid and provide insufficient dexterity to work

in a confined workspace like the middle ear, especially to access hard-to-reach locations. As a consequence, the current treatment of the disease requires an open surgery to improve the effectiveness in surgical manipulation. Even so, the associated risk of recurence due to residual cholesteatoma is still high (Section I.1.2) and the patient may need to have a follow up. For that reason, the proposed surgical instrument (used for cholesteatoma removal) will consist of flexible microrobots (less than 2.5 mm in diameter) that are able to reach any part of the middle ear and perform cholesteatoma detection and removal. To do this, such robots need to have a high dexterity in confined space and has to undertake a maximum volume coverage through a minimally invasive access to the anatomy of interest (see figure I.13). The total middle ear volume, defined as the continuous space occupied by the tympanic cavity and mastoid air cells [Stepp 05, Carpenter 17] is known to be really confined (around 6.5 cm^3 [Molvaer 78]) (see figure I.10). This value can even reduce to 1.1 cm^3 in lesioned ears [Ahn 08]. Considering that, the proposed approach is based on continuum robots with hybrid actuation allowing the navigation of the robots into the middle ear combined with the variable curvature at their distal section. In addition, through the free channel of the instrument, the surgeon can pass either a fiber-based imaging system or a surgical laser. The microrobotic system will be integrated (macro-micro approach) into the otologic robotic system RobOtol (marked CE in 2016) for preclinical experimentations (figure I.15).

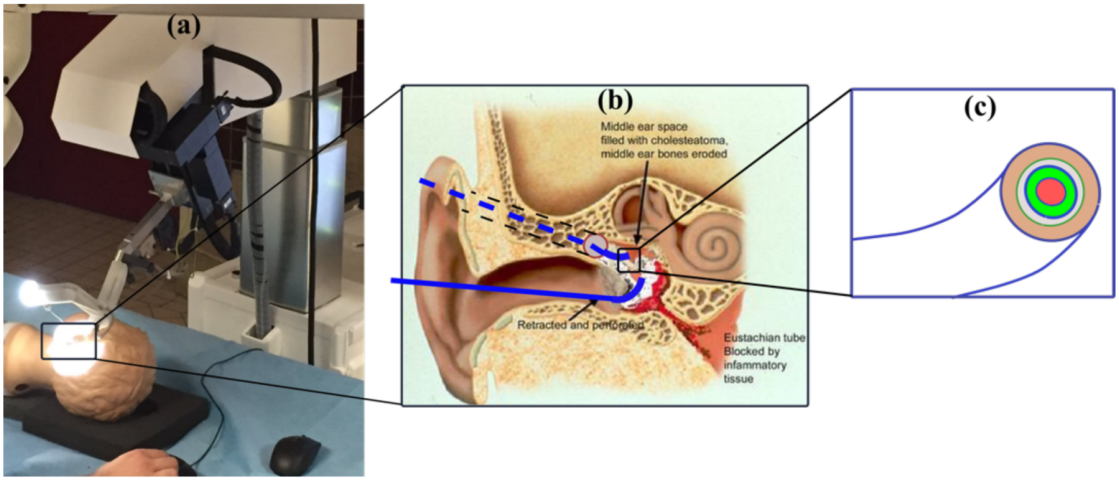

Figure I.15 – (a) µRoCS targeted concept illustrated with RobOtol with (b) two accesses to the middle ear with endoscopic flexible microrobots and (c) multimodal optical system for simultaneous cholesteatoma detection and removal.

I.3 Conclusion

This chapter presented the challenges of the treatment of cholesteatoma disease located inside the middle ear. In fact, the surgeon cannot remove exhaustively the infected cells from the first operation due to the tiny workspace as well as the

limitations in the diagnosis of the imaging tools and in the dexterity of the surgical instruments. Therefore, the µRoCS project aims to propose a flexible and dexterous integrated robotic system to efficiently remove the residual cholesteatoma. The robot will embed an imaging tool (OCT+fluorescence) and a laser (ablation tool) inside its lumen. The following chapter will focus on the state of the art of robot assisted middle ear surgery and will detail the proposed hybrid continuum robot for exhaustive cholesteatoma removal.

Chapter II
Robot-Assisted Middle Ear Surgery

II.1 Requirements for Middle Ear Surgical Robots 24
II.1.1 Anatomical constraints 24
II.1.2 Robot tasks 25
II.1.3 Ideal requirements of the microrobotic system 26
II.2 Related Surgical Robots 27
II.2.1 Surgical robotic systems for middle ear 27
II.2.2 Other dexterous surgical robots 35
II.3 Proposed Robot for Exhaustive Cholesteatoma Surgery . . 50
II.4 Conclusion 51

In this chapter, we first present the specific requirements the microrobot needs to satisfy according to the anatomical constraints imparted to exhaustive cholesteatoma surgery. Then, a comprehensive review of related robotic systems is reported in this chapter to show the current state of the research in this field and what is missing to reach the requirements. To finish, by considering the advantages and limitations of each system, we explain why the hybrid actuation combining concentric tubes and tendon-driven actuators will be a good candidate for this type of surgery.

II.1 Requirements for Middle Ear Surgical Robots

In this section, the anatomical area of interest for our project will be presented. Then, the tasks that must be fulfilled by the robot to cover the complete volume of tympanic cavity (see figure II.1) and perform the removal of residual cholesteatoma will be described. Finally, based on the anatomical constraints and the robot tasks, the ideal requirements of the robotic structure will be discussed.

II.1.1 Anatomical constraints

As previously mentioned, the anatomical area of interest is the middle ear, more specifically the tympanic cavity. Its volume is typically between 0.5 and 1 cm^3 as given in the literature [Stepp 05]. This confined space has a vertical diameter of about 18 mm, an anteroposterior diameter of about 10 mm, and a transverse diameter from 3 to 5 mm [Liem 04]. In the anatomical representation of the ear shown in Figure II.1a, one can observe that the tympanic cavity has a pocket-like shape separated from the auditory canal by the eardrum. To ensure pressure wave transmission for hearing, the latter is linked to the cochlea by ossicles. Among the accesses to the middle ear, the transmastoid access to the attic (upper part of tympanic cavity) (Figure II.1b) is of major importance as the attic is the most frequent site of residual cholesteatoma [Gaillardin 12]. In order to ensure the minimally invasive aspect of procedure, the created tunnel through mastoid bone has a small diameter of 3 mm and its location should be optimized in order to drill the minimal distance (around 3 cm for reaching the cholesteatoma cells. As reported in [Kelly 96], the auditory canal has an average length of 25 mm in the posterosuperior wall and is longer, about 31 mm, in the anteroinferior wall because of the inclination of the eardrum. The total volume of this canal is approximately 850 mm^3 with the average diameter of 7 mm (Figure II.1c).

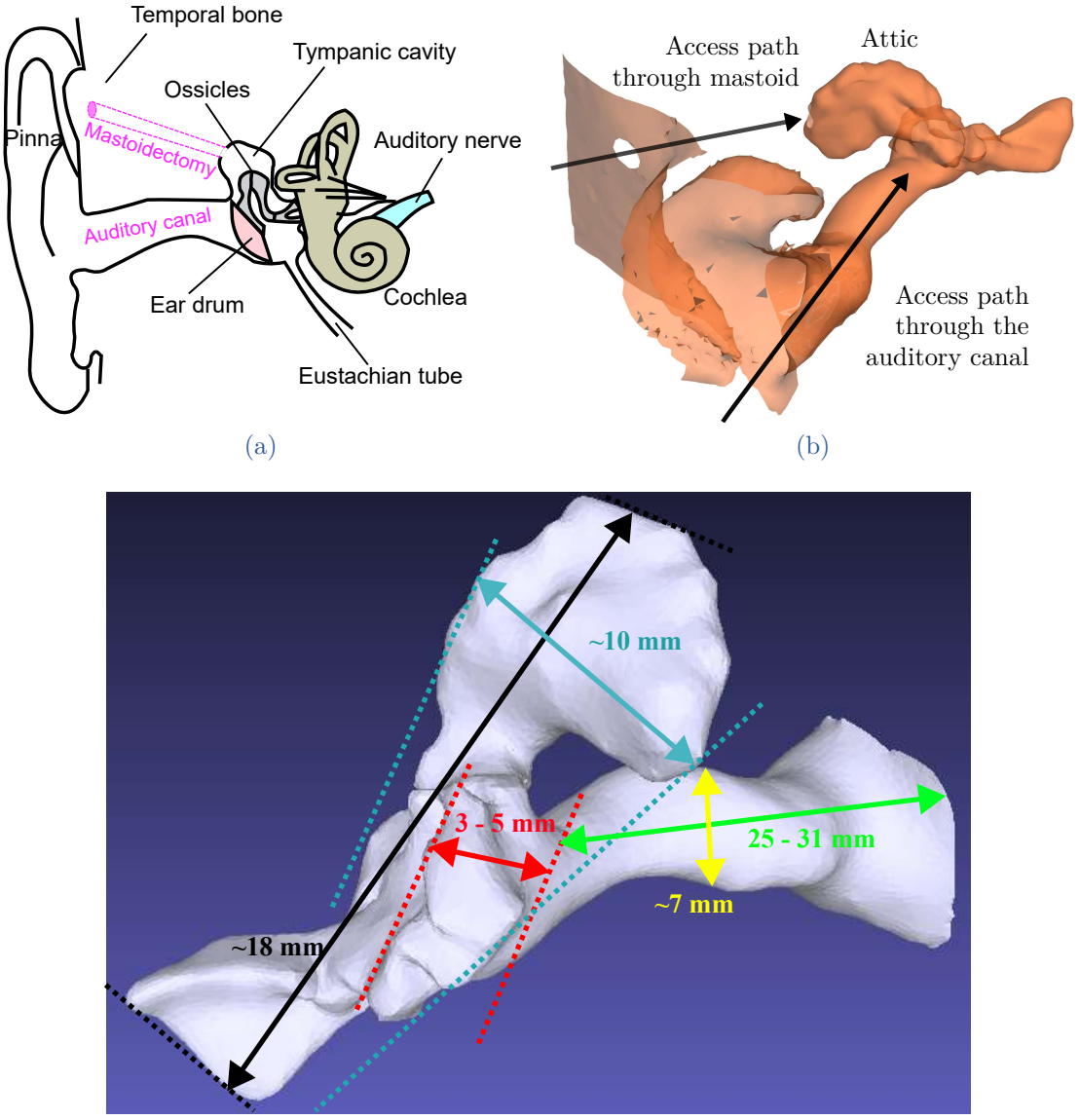

FIGURE II.1 – (a) Anatomical representation of the ear, (b) two accesses used for the proposed surgical protocol, and (c) dimensions of the ear [Nguyen 21a].

II.1.2 Robot tasks

The complete treatment of residual cholesteatoma requires two main tasks. The first one consists in searching residual cholesteatoma by optical biopsy. In the µRoCS project, we envision to use OCT combined with fluorescence spectroscopy to ensure efficiency of the detection. Nevertheless, it is important to note that the cholesteatoma biopsy is not the purpose of this thesis as it is managed by another partner of the project. Afterwards, the biopsy of the sites of interest would be sent to a machine learning classifier previously trained to determine whether or not the observed tissue is composed of residual cholesteatoma. The second task

is to perform the ablation of the detected residual cholesteatoma by a green laser (532 nm). The robot, which has to perform these two operations sequentially, is considered to be inserted through the mastoid (via a created hole) or through the auditory canal by displacing the eardrum. It then sweeps inside the desired volume (tympanic cavity) and enables contact with hard-to-reach anatomical targets. The cholesteatoma surgery can be carried out in one of two scenarios: detection and ablation or detection with mapping followed by ablation (more restrictive because it requires a very good repeatability).

II.1.3 Ideal requirements of the microrobotic system

As preliminary results of the µRoCS project, [Dahroug 18a] presented the general requirements of the cholesteatoma surgical robotic structure in an ideal case for both the surgical tools and the robotic systems without any consideration for the applied technology. In this subsection, the requirements impacting the microrobot based on the anatomical constraints and the robot tasks are analyzed. The following requirements are established reasonably based on the exchanges with experienced surgeons and previous results in [Dahroug 18b].

Form and dimension based on the anatomy: the microrobot need to be inserted via the auditory canal or the created tunnel via the mastoid bone, thus it must be slender in form. As the tunnel through mastoid has 3 mm in diameter, the microrobot is required to have a maximum diameter of 2.5 mm to ensure that it can be inserted easily through the created hole without any unexpected collision caused by the imperfect shape of the borehole and/or an undesirable small curvature of the robot shape that may occur, for example, in case of a concentric tube design.

Kinematic properties: the microrobot has to achieve a large curvature at the distal part, in order to be able to sweep the desired volume and to access the hard-to-reach anatomical targets. Furthermore, the microrobot is required to move the distal section while keeping the rest of the body in the constrained environment (i.e. the navigation section is decoupled with the exploration section). The kinematic requirements for this robot are in the following:

- ideally 6-DoF system (or at least 2 rotations + 1 translation [Fichera 17]),
- bendable distal section [Dahroug 18b],
- 2 curved segments [Dahroug 18b],
- distal bending radius (< 5 mm [Gafford 21]),
- distal bending angle ($\geq 90°$ [Fichera 17]),
- workspace that cover the tympanic cavity ($5 \times 18 \times 18$ mm),
- outer diameter (< 2.5 mm),
- length (> 30 mm),
- resolution (< 0.02 mm [Miroir 10]),
- repeatability equals to the spot size of the optical biopsy.
- linear and angular errors need to be smaller than 0.5 mm [Danilchenko 11, Dillon 14] and 5°, respectively.

The bending radius does not consider the technical limitation of the optical fiber used for the laser ablation tool. This will be detailed in Chapter III. In addition, other specifications includes:

Material: bio-compatible material is required for the microrobot. In addition, its hardness must be sufficient to constrain the embedded optical fibers.

Actuation: any actuation principle (concentric tube, tendon-driven, smart material or magnetic field) which has to comply with the requirements of the constrained workspace.

Ablation tools: green laser (532 nm, 8 W) will be considered to perform cholesteatoma removal [Hamilton 05].

II.2 Related Surgical Robots

The surgical robots presented in this section are classified into two main groups. The first group is devoted to robotic systems that are applied to middle ear surgeries. The second group reviews different approaches used in other surgical applications which could be helpful in the middle ear surgery. According to the fact that rigidity is a major limitation of minimally invasive surgery, the second group focuses on flexible robots (or continuum robots) which are developed to increase the dexterity. As a definition, a continuum robot consists of a flexible structure, which deforms under the action of forces/torques created by actuators and forming a curve along which its tangent vector evolves continuously [Burgner-Kahrs 15]. The strengths and weaknesses of each robot under consideration will be presented to show whether or not it satisfies the requirements for an exhaustive cholesteatoma ablation.

II.2.1 Surgical robotic systems for middle ear

II.2.1.a Robots using rigid tools

At Hanyang University, South Korea, an image-guided robotic system was proposed to carry out mastoidectomy [Lim 11]. The robot mechanism consists of a 5-DOF serial robot and was proposed for imposing the physical constraints on the surgical tool (i.e., the fulcrum effect). An optical tracker is utilized and a navigation software which can provide a warning mode when the driller approaches ($< 3\ mm$ in distance) critical structures (e.g., the facial nerve) is also implemented. The system also provides a human-robot collaboration control to compensate the hand tremor. The workspace of the robot is enough to perform a mastoidectomy ($40{\times}40{\times}40\ mm$). The experimental results were conducted on a human temporal bone phantom model. Table II.1 gives a description of this robotic system by considering the requirements for the desired microbot.

TABLE II.1 – Summary of the mastoidectomy robotic system [Lim 11]

DOF of macro-system	5
Added-DOF of surgical tools	0
Surgical instrument types	Drill tool
Workspace	$260 \times 260 \times 254\ mm$
Curved segments	0
Rigid/bendable	Rigid
Outer diameter	-
Hollow channel diameter	-
Distal bending radius	-
Distal bending angle	-
Material of the instrument	-
Ablation tool	No ablation tool
Accuracy	$< 1\ mm$
Actuation type	Serial rigid links connected by active joints
Control	Admittance cooperative controller
Validation status	On a human temporal bone phantom model
Comment: The image-guided robotic approach is effective for safe and precise mastoidectomy. In addition, the cooperative control can eliminate the hand tremor. However, this robot has neither soft tissue cutting tool nor cholesteatoma imaging tool.	

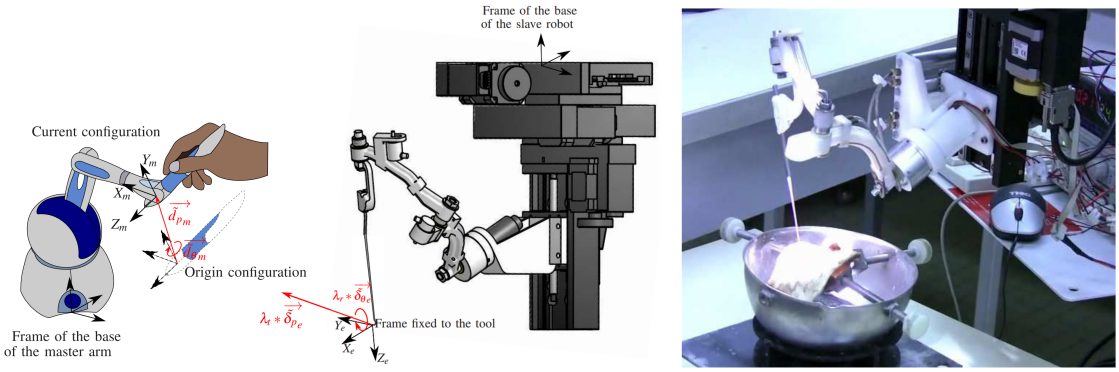

(a) (b)

FIGURE II.2 – RobOtol. (a) Master-slave surgical robotic system, and (b) experimental setup to demonstrate access to the middle ear. [Miroir 10].

At ISIR, France, a tele-operated robotic system named *RobOtol* was proposed to perform stapedectomy surgery through the auditory canal [Miroir 08, Miroir 10, Nguyen 12]. The system design consists of a robotic arm that is controlled via a master joystick (figure II.2). The arm has 6-DOF with a special kinematic struc-

ture that allows enhancing the field of vision provided to the surgeon for performing more complex gestures. Besides, the distal tip shows movements with a 5 μm resolution and can reach distant target points. The robotic system has been commercialized through a cooperation between scientists at the Inserm/UPMC UMR-S 1159 unit and engineers at Collin, a French SME specialized in the ENT field. The summary of the robotic system is detailed in Table II.2.

Table II.2 – Summary of RobOtol robotic system [Miroir 10]

DOF of macro-system	6
Added-DOF of surgical tools	0
Surgical instrument types	Standard otologic instruments
Workspace	-
Curved segments	-
Rigid/bendable	Rigid
Outer diameter	$< 3.3\ mm$ [Vittoria 21]
Hollow channel diameter	-
Distal bending radius	-
Distal bending angle	-
Material of the instrument	Titanium or Nitinol
Ablation tool	Micro-scissors or laser
Accuracy	Expected for a linear error of 5 µm and an angular error of 0.3° but not yet verified [Nguyen 12]
Actuation type	Serial rigid links connected by active joints
Control	Teleoperated System
Validation status	Commercial product
Comment: The proposed robotic system is equipped with micro-ablation tools, driller, and endoscope. The specific kinematic structure makes it possible to manipulate the tool inside the middle ear via the auditory canal. Tele-operated mode allows eliminating the surgeon's hand tremor. However, the rigid tools constitute the main limitation of the robotic system. They cannot access to the attic or the hypotympanic of the tympanic cavity where residual cholesteatoma is frequently found.	

Another tele-operated system named MicroManipulator System (MMS) was developed at München University, Germany, to perform stapedectomy surgeries [Maier 10]. By employing this system, the surgeon can manipulate standard surgical instruments inside the middle ear. MMS consists of a small 4-DOF manipulator and a control console using two joysticks (Figure II.3a). It also allows measuring the distance between the stapes and the incus to determine the prosthesis length [Maier 11]. The position accuracy of the tool tip is around 0.02 mm for a small workspace, range $20 \times 20 \times 20\ mm$ To improve the workspace and the features of

the MMS system, another system named Micro-Macro Telemanipulation System (MMTS) was proposed in [Entsfellner 13] as shown in Figure II.3b. The experimental validation was conducted on a patient phantom. This version consists of a joystick console fixed on the operation table, a 6-DOF macro-manipulator arm with 1.6 *mm* positioning accuracy for large displacement, and the robotic fingers which hold the adaptor used for gripping different tools (e.g., micro-manipulator MMS for fine movement, endoscope or driller). Eventually, the system allows measuring the applied force at the instrument tip using four force sensors. Table II.3 summarizes the characteristics of the robotic system.

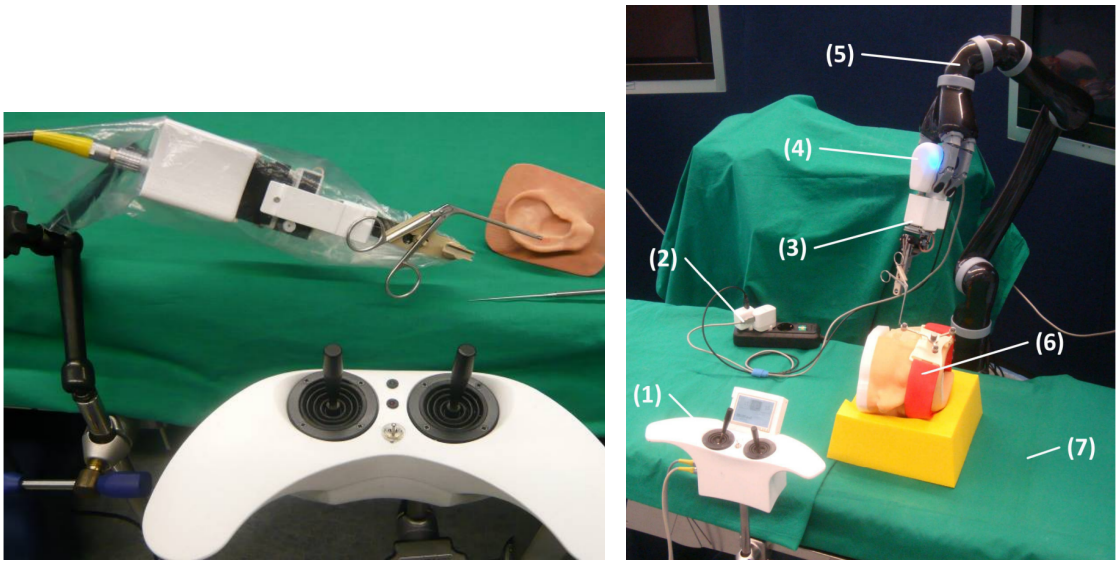

(a) (b)

FIGURE II.3 – (a) Master-slave MMS surgical robotic system with forceps tool [Maier 10], and (b) experimental setup of master-slave MMTS surgical robotic system: (1) joystick console, (2) energy supply, (3) MMS, (4) active gripping adapter, (5) carrier robot, (6) patient phantom, (7) OR-table [Entsfellner 13].

TABLE II.3 – Summary of MMTS robotic system [Entsfellner 13]

DOF of macro-system	6-DOFs + 4-DOFs of the MMS
Added-DOF of surgical tools	0
Surgical instrument types	Standard surgical instruments
Workspace	$20 \times 20 \times 20$ *mm* for MMS
Curved segments	-
Rigid/bendable	Rigid
Outer diameter	-
Hollow channel diameter	-

Continued on next page

Table II.3 – continued from previous page

Distal bending radius	-
Distal bending angle	-
Material of the instrument	Titanium or Nitinol
Ablation tool	-
Accuracy	Macro system: 1.6 mm, MMS: 0.02 mm
Actuation type	Serial rigid links connected by active joints
Control	Teleoperated System
Validation status	On a patient phantom
Comment: MMS is available for different surgical tools, while MMTS could switch between endoscope, driller or MMS. A wide workspace with precise displacements can be obtained using the coupled coarse and fine motions. However, MMTS is not precise without MMS which employs rigid tools.	

II.2.1.b Robots using flexible tools

At Vanderbilt University, USA, a hybrid parallel-serial robot with a dexterously orientable gripper was proposed to expand the ability of middle ear surgeons including: i) touching the round window niche, Eustachian tube orifice, and sinus tympani; ii) placing a stapes prosthesis; and iii) removing of mockup diseased tissue in the sinus tympani [Yasin 17]. The robotic manipulator consists of two modules: a 6-DOF parallel robot and a 2-DOF distal dexterity robot (DDR). These two modules are then connected in series by a 1-DOF rotary axis in order to obtain a 9-DOF robot as shown in figure II.4. The gripper was inspired by an ophthalmic gripper and is attached to a long cable encased by a slightly larger cannula. To close the gripper, the cable needs to be pulled back into the cannula. The cannula is a 0.65 mm superelastic Nitinol tube with a bending radius of 7.5 mm which allows the robot to reach challenging anatomic regions inside the middle ear. A stainless-steel stem is used to constrain the cannula into a straight form. Ex vivo experiments were conducted using a temporal bone specimen with optical tracking marker affixed to the experimental bowl. Thank to the extendable cannula, the workspace of the robot increases of 355% compared to the manual tool. The teleoperated mode allows considerably reducing the tracking errors (0.09 ± 0.08 mm). In addition, the robot has a steadier movement, but longer time is required to complete the tasks in comparison with the manual tool. The summary of the hybrid parallel-serial robot is given in Table II.4.

Table II.4 – Summary of the hybrid parallel-serial robot [Yasin 17]

DOF of macro-system	6
Added-DOF of surgical tools	3
Surgical instrument types	Gripper
Continued on next page	

Table II.4 – continued from previous page

Workspace	1960 mm^3
Curved segments	1
Rigid/bendable	Steerable and prefixed-curvature
Outer diameter	0.65 mm for the cannula
Hollow channel diameter	-
Distal bending radius	7.5 mm
Distal bending angle	-
Material of the instrument	Nitinol and stainless steel
Ablation tool	-
Accuracy	Tracking errors of $(0.09 \pm 0.08\ mm)$
Actuation type	Hybrid parallel-serial robot.
Control	Collaborative control and Telemanipulation
Validation status	Ex vivo experiments
Comment: The combination of the bending superelastic Nitinol cannula and the straight stainless steel stem (as a concentric tube design) allows improving the workspace of the robot. However, the bending radius of the cannula is fixed. The inner diameter of the Nitinol tube is quite small for embedding optical fibers to perform cholesteatoma surgery.	

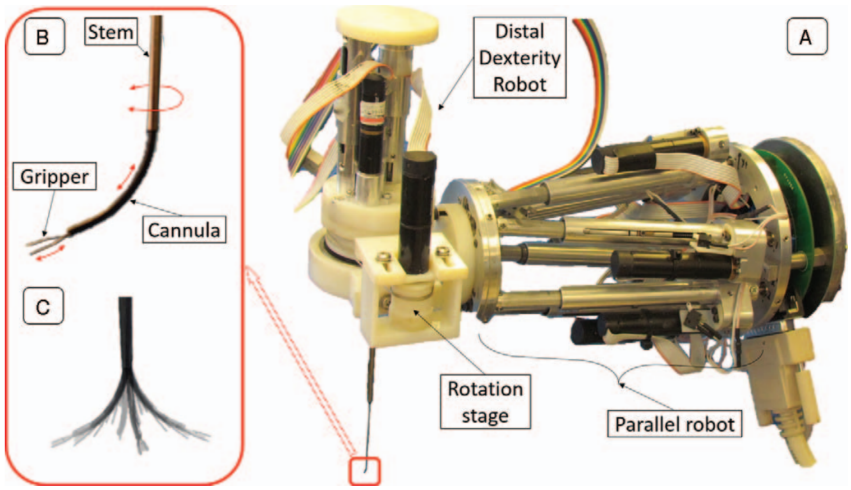

FIGURE II.4 – The hybrid parallel-serial robot. (A) Parallel robot, distal dexterity robot, and rotation stage. (B) The stem, cannula, and gripper. (C) Different configurations of the gripper when it is extended and rotated [Yasin 17].

Also at Vanderbilt University, USA, a bendable endoscope was proposed in [Fichera 17, Gafford 21] to visualize cholesteatoma tissue within the middle ear cavity through the Eustachian tube. The bendable distal end, called the wrist, is fabricated by notching several asymetric cutouts on a superelastic Nitinol tube. The tube bends with a single internal tendon drive (figure II.5). The tube can

translate along and rotate around its central axis. The outer diameter of the tube can be smaller than 2 mm. Experimental results were conducted on a 3D printed middle ear phantom that shows the increase in the visibility of sinus tympani region by 74.16%, compared to a conventional straight endoscope (6.9%) [Fichera 17]. The steerability afforded by the endoscope was then showed with a series of visualization experiments in cadaveric temporal bone specimens [Gafford 21]. The characteristics of this robot is detailed in Table II.5.

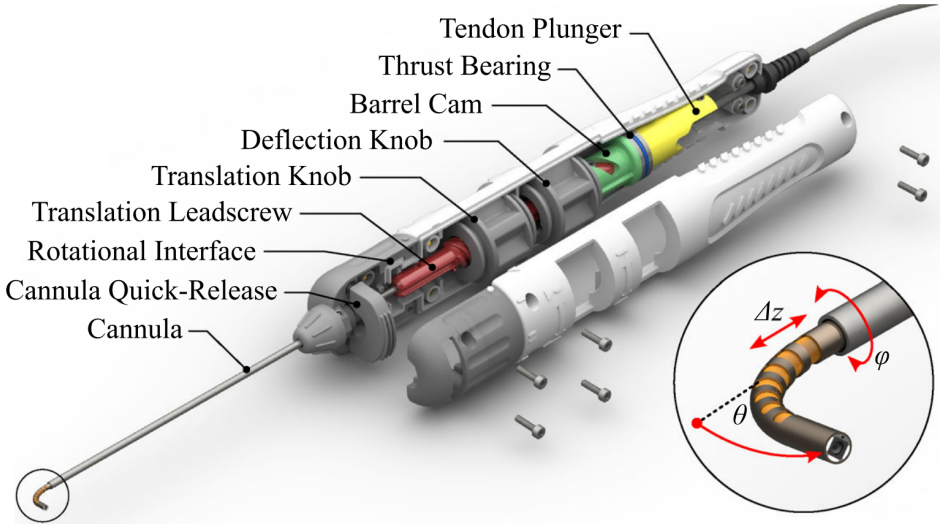

FIGURE II.5 – The handle design of the miniature steerable digital endoscope with 3-DOF actuation which include Δz (insertion/retraction), Φ (axial rotation), and θ (tip deflection)) [Gafford 21].

TABLE II.5 – Summary of the bendable endoscope [Gafford 21]

DOF of macro-system	0 (hand-held system)
DOF of surgical tools	3
Surgical instrument types	Endoscope
Visual coverage	74.16% [Fichera 17]
Curved segments	1
Rigid/bendable	Bendable tool
Outer diameter	1.62 mm
Hollow channel diameter	1.40 mm
Distal bending radius	5 mm
Distal bending angle	90°
Material of the instrument	Nitinol tube
Ablation tool	-
Accuracy	Root mean square error of 3.71° [Fichera 17]
Actuation type	Cable-driven robot

Continued on next page

Table II.5 – continued from previous page

Control	Ergonomic handle
Validation status	On temporal bone specimens
Comment: The bendable endoscope improve the visibility. The dimension of the tube is relatively small and suitable for a minimally invasive approach. However, to perform cholesteatoma surgery, ablation tool need to be integrated within the instrument.	

In the literature, there are a large number of otological robotic systems dedicated to cochlear implantation for treating a sensorineural hearing loss. These robots could offer compelling inspirations for the required microrobot as they also employ the accesses to the middle ear. At Hannover University, Germany, [Leinung 07, Majdani 09, Baron 10] developed a robotic system based on the 6-DOF industrial robot (KUKA KR3) for cochlear implantation. The validation was conducted on ten human cadaveric temporal bones. Nine out of ten procedures were completed without complications and the targeting mean deviation error was about 0.5 mm, essentially due to the calibration errors. Some researchers of this university also proposed a mechatronic device to insert automatically the electrode array inside the inner ear [Hussong 08]. At ARTORG centre, Switzerland, a pro-

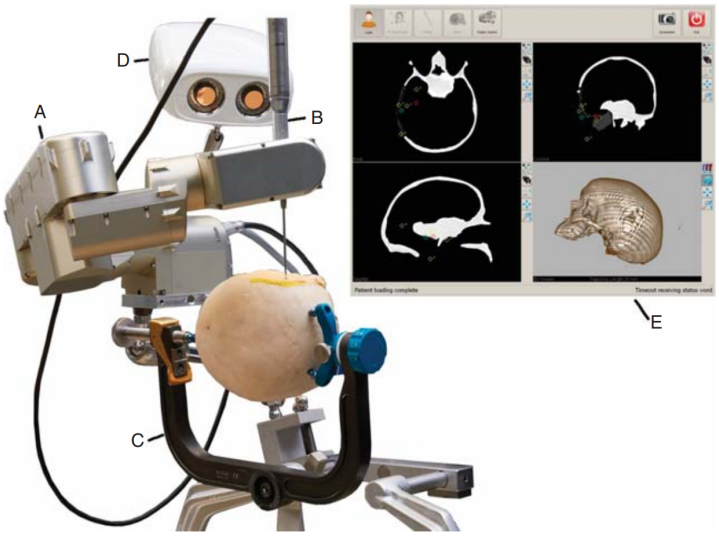

Figure II.6 – Different components of ARTORG robotic system: (A) robot arm, (B) surgical driller, (C) head clamp, (D) optical tracking, (E) touch screen as the interface to the planning software [Bell 12].

totype robotic system [Bell 12, Gerber 14] was developed for stereotactic cochlear electrode implantation. A mechanical driller was employed to create a 2 mm tunnel from the mastoid's outer surface, passing through the facial recess, to reach the cochlear. The components of the system are shown in figure II.6. A custom-built 5-DOF serial robot was attached to the Operation Room (OR) table due to its light weight (5.5 kg). To register the pre-operative plan to the patient and control

the tool position, an optical tracking system with high accuracy ($< 0.05\ mm$) was used. The system continuously estimates the tool position [Williamson 12] and monitors the facial nerve [Ansó 14] to ensure its safety during the drilling stage. This robotic system was tested on eight human heads and the results showed 0.18 mm mean accuracy [Bell 13]. In 2016, a patient with bilateral deafness underwent a clinical feasibility trial involving the robotic system for a right-side cochlear implantation, which was approved by the Cantonal Ethics Commission of Bern and Swissmedic. Generally, these robots are suitable for realistic clinical applications, especially for creating a tunnel to the tympanic cavity. However, as they are not designed for cholesteatoma surgery, they are not equipped with soft tissue cutting tool, bendable end-effector, imaging tool for detecting cholesteatoma and laser ablation tool for residual cholesteatoma removal.

As a conclusion, most of the robotic systems used for middle ear surgery so far are equipped with rigid or non-bendable surgical tools that may lead to difficulties in the complete removal of cholesteatoma. The only bendable tool proposed in the literature is simply employed for the endoscopy and not for the surgery procedure. Thus, the research on a novel bendable surgical robot with embedded ablation tool to perform exhaustive cholesteatoma surgery is required.

II.2.2 Other dexterous surgical robots

The purpose of this section is to focus on the surgical robots that perform minimally invasive surgeries by using bendable distal tool and continuum robots. During the last two decades, continuum robots have been active topics in the research community through various applications, especially in the medical field [Webster III 10, Burgner-Kahrs 15, Li 21]. They must be hollow to allow passing through the different instruments (e.g., suction, irrigation, laser or OCT). In the literature, there are many actuation sources for the distal tool tip classified as either intrinsic and extrinsic types [Burgner-Kahrs 15] (see figure II.7). Intrinsic actuators are integrated within the microrobot structure such as pneumatic [Sénac 19], hydraulic [De Volder 10], smart material [Gu 14] or magnetic fields [Carpi 09]. On the other hand, extrinsic actuators are outside the robotic structure and the actuation force should be transmitted through mechanical components, for instance cable-driven (also called tendon-driven) [Legrand 18], concentric tubes [Webster III 10], or multibackbone structures [Simaan 09].

In particular, hydraulic and pneumatic actuators present the advantage to be safe as they do not require rigid parts nor electrical voltage [Decroly 21]. However, most of the designs of pneumatic and hydraulic actuators are characterized by a large dimension (over 10 mm in diameter) compared to the requirements for the middle ear [Abidi 18, Garbin 18, Brancadoro 19]. Smaller diameter designs have also been reported in the literature for both hydraulic [Ikuta 06] and pneumatic [Gorissen 18] actuators. Even so, they comprise only one chamber within their cross-section and do not include any working channel to embed the optical fibers. Thus, more research efforts need to be performed in order to apply these actuation methods for middle ear surgery.

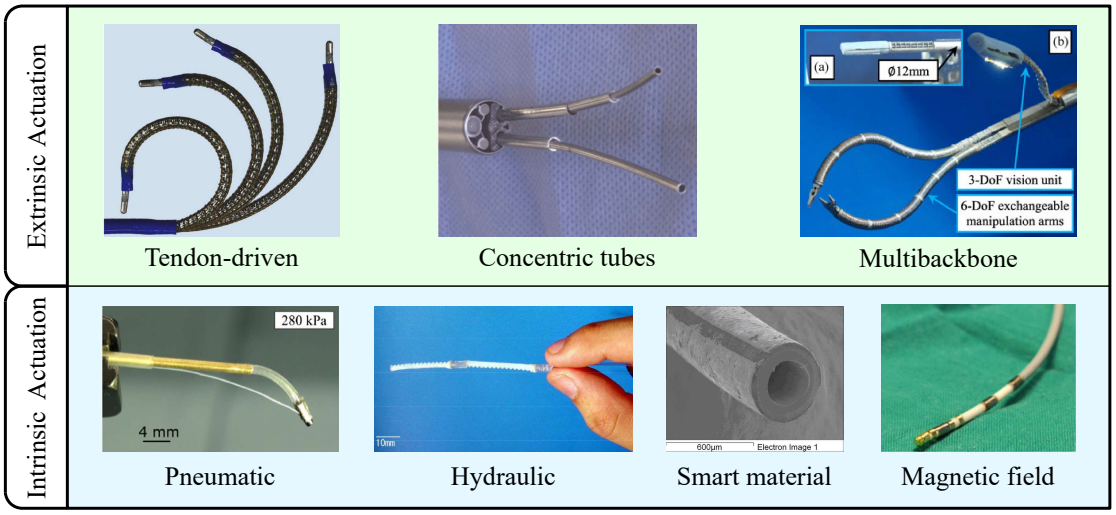

FIGURE II.7 – Different types of continuum robot in the literature according to their actuation method: tendon-driven [Camarillo 08], concentric tubes [Hendrick 15b], multibackbone [Xu 14], pneumatic [Gorissen 18], hydraulic [Ikuta 06], smart material [Shoa 08], magnetic field [Filgueiras-Rama 13].

There exist various subtypes in the family of smart materials including piezoelectric [Gu 14], Shape Memory Alloy (SMA) [Jani 14], and Electro-Active Polymers (EAP) [Shoa 08]. Piezoelectric actuators require a very high voltage to obtain very small deformations. They have a fast response time but they are highly demanding during the control to eliminate both vibration and hysteresis effects. SMA actuators allow a heavy payload and can be miniaturized. Nevertheless, the generated heat during the operation is the main limitation of this actuation method [El Naggar 20]. The EAP used in [Shoa 08] (Polypyrrole conjugated ionic polymer) is lightweight and requires very low activation voltages ($< 2\ V$) without any additional heating, in contrast with piezoelectric and SMA materials. However, the required time to achieve the minimum bending radius ($10\ mm$) is quite long ($\sim 30\ s$).

Magnetic continuum robots (m-CRs) have been proposed to use in cardiac surgery [Carpi 09, Liu 14, Edelmann 17, Chautems 18], eye surgery [Ullrich 14, Charreyron 18], and cochlear implants [Clark 12]. This actuator has the advantage to manipulate the robot without contact. Indeed, the robot backbone can be deformed and its distal tip can be steered under the external torques and forces generated by a magnetic resonance imaging (MRI) machine [Liu 14]. To do that, the distal tip as well as several sections of the robot should consist of ferromagnetic materials or permanent magnets [Clark 12]. Thus, the obtained kinematic performance depends on the mechanical properties of the backbone; on the number, location and properties of the employed magnetic elements; and on the magnetic field generator machine. Controlling the robot shape in space requires generating different magnetic fields for each magnets along the robot length. In the current practice, it is quite difficult to generate very different magnetic fields for each ma-

gnet due to their proximity compared to the large working zone of the magnetic field. This problem is the subject of the recent work in magnetic manipulation of independent microrobots [Ongaro 18] but it has not yet been applied to the m-CR.

The idea of concentric tubes is to arrange precurved and superelastic tubes in a telescopic manner. Most tubes are made of Nitinol, and some of them are made of polymers including polyether block amide and polypropylene-like material [Morimoto 16]. The concentric tubes are translated along and rotated axially around their concentric axis by actuating the tubes at proximal ends on the actuation unit. In this way, the tip can reach different positions in 3D space. CTRs are known as one of the smallest actuation methods in the family of continuum robots [Gilbert 16a]. Nevertheless, these robots have two main drawbacks. First, the tube curvatures are prefixed during the fabrication process and their limit is inversely proportional to their external diameter [Webster 06]. Indeed, increasing the bending of each precurved tube requires its more slender form that can shrink the hollow channel of the innermost tube. The other drawback of concentric tubes actuation is the snapping effect [Kim 14, Gilbert 16a] which is an incompatible phenomenon within a tiny space like middle ear cavity. The snapping problem occurs when the torsion energy of the actuated tubes is suddenly released that makes the robot snap to a remote position.

A tendon-driven continuum robot consists of an elastic beam, which constitutes the backbone of the robot, along which tendons are attached. Pulling these tendons generates forces on the backbone and deforms it. This actuator could achieve high bending angles (e.g., [Camarillo 08, York 15, Legrand 18]). Even so, the tendons occupy space within the hollow channel and reduce the space for inserting optical tools. Furthermore, the tendon slack is also a problem and need to be considered during the control.

A multibackbone continuum robot is a mechanism made up of several parallel, elastic rods or tubes that are somehow restrained relative to one another. This design increases the robot's bending direction, but since it necessitates the integration of several rods or tubes, the robot's external diameter is rather big (over 10 mm) in comparison to the anatomical constraint [Xu 14].

As there is a trade-off between the actuation choice and the design requirements, a possible solution combining two actuation types could be considered. Among many actuation techniques used for continuum robots, concentric tubes and tendon-driven are considered as good candidates for developing a flexible microrobotic system for minimally invasive surgery within a confined workspace thank to the compact size of the robotic structure and of the actuation unit. In the following, these two actuators as well as the hybrid actuation based on them will be discussed in details.

II.2.2.a Concentric tube robots

The conception of CTR was originaly and independantly introduced by Webster et al. in [Webster 06] and by Sears and Dupont in [Sears 06]. In the medical aspect, CTRs have been widely used for the design of robots working in confined workspaces such as in cardiac surgery [Gosline 12a, Gosline 12b, Vasilyev 12], endonasal surgery [Burgner 11, Swaney 12], neurosurgery [Butler 12], transoral throat surgery [Webster III 08], eye and deep orbital interventions [Wei 07, Wei 08, Lin 15, Gilbert 16b, Mitros 20], cancer ablation [Burdette 10, Burgner 12, Yu 16], transoral lung biopsy and therapy delivery [Lyons 10], hemodialysis graft procedures [Berns 11], prostate brachytherapy [Walsh 11], or olfactory epithelium inspection [Girerd 18]. Such robots can be used for various tools including forceps, flexible endoscope, or irrigation tool (see Figure II.8a). Recently, a hand-held concentric tube robot for minimally invasive surgery was proposed in [Girerd 20] with an associated position control method (see Figure II.8b). Among all these applications, the three that have been studied most extensively and could provide a good inspiration for designing the required microrobotic system are the cardiac, the endonasal, and the eye surgeries.

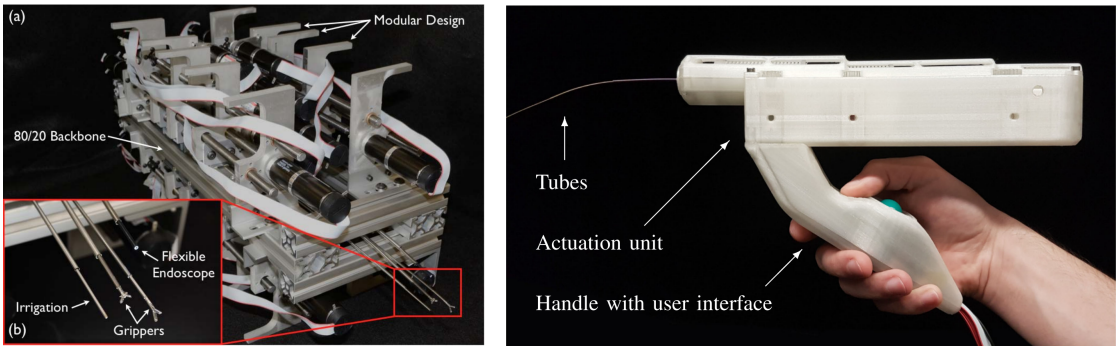

(a) (b)

FIGURE II.8 – (a) Global view on the Quadromanual robot with the four arms used for different tools [Swaney 12], and (b) the hand-held concentric tube robot with deployed tubes, actuation unit, and handle using a user interface [Girerd 20].

Cardiac surgery: Heart surgery is an acute procedure that usually requires opening the chest wall to expose the heart by cutting through the sternum (breastbone) and spreading the ribs. Then, the final intervention in a non-beating heart is performed using a cardiopulmonary bypass (CPB) pumb. As providing better results than the procedures using cardioplegic (non-beating heart) solutions, there is growing interest in beating heart surgeries that could obviate the use of the CPB pumb [Morfa 09]. Even so, a safety deployment method is compulsory to avoid the risk of adverse effects and co-morbidity. In recent years, CTRs have been reported as a good choice to improve the effectiveness of heart surgery.

Gosline *et al.* proposed in [Gosline 12a, Gosline 12b] a CTR prototype to deliver the metal MEMS tool to intracardiac locations inside the right atrium of the

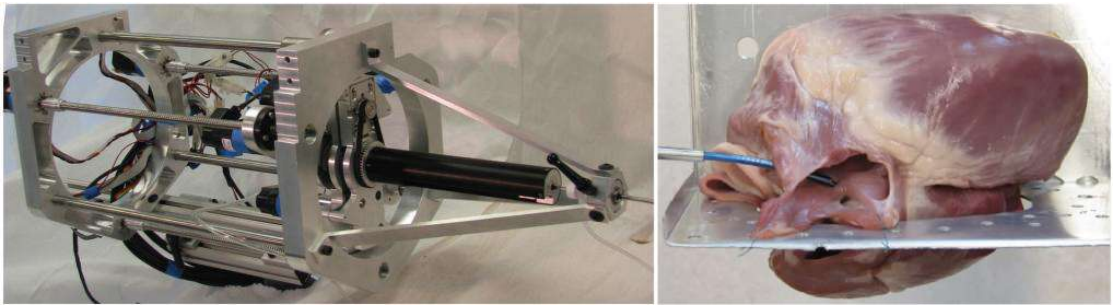

FIGURE II.9 – (Left) Drive system of the intracardiac surgical robot. (Right) Ex vivo testing with a porcine heart in which the robot enters the right atrium from the superior vena cava [Gosline 12a].

heart (see figure II.9). This work was the first ever use of CTRs as tools to deliver micro-manufactured instruments rather than only as active cannulas. The effectiveness of the approach is demonstrated through ex vivo and in vivo trials. This was also the first time a CTR was used in a live animal [Dupont 12, Gosline 12a]. Lately, Fagogenis *et al.* [Fagogenis 19] demonstrated an autonomous navigation of CTR inside porcine heart by following tissue walls to reach the targets while ensuring low-force contact with the heart tissue. The robotic catheter has a small diameter (< 2 mm) and a hollow channel of 1.6 mm. The obtained radius of curvature is 40 mm and pretty large for the required robotic system.

Endonasal surgery: It is a minimally invasive technique used mainly in neurosurgery and otolaryngology. The surgeons use an endoscope that is entered through the nose to fix or remove brain defects or tumors in the anterior skull base. Conventional approaches using rigid instruments limit the effectiveness of procedures as they must follow straight trajectories resulting in increased danger to harm critical tissues and structures. CTRs, promising to dexterously access regions within the skull base, have reported potentially game-changing benefits in endonasal surgery.

Burgner *et al.* proposed in [Burgner 11, Burgner 13] a teleoperated system for endonasal skull base surgery. A straight manually operated endoscope was used for visualization. The robotic system comprised two Nitinol concentric tube arms holding a ring curette and a gripper as shown in figure II.10. Each arm consisted of three concentric tubes including a straight outer tube and precurved middle and inner tubes. The validation was conducted with a mock-up surgery on a human cadaver head. The two surgical instruments entered the nasal passage of the cadaver through a single nostril and successfully reached the pituitary gland. Each arm has an outer diameter (2.32 mm) and a hollow channel of 0.76 mm. The maximum bending curvatures of the gripper and the curette are 0.0128 mm^{-1} (or bending radius of 78.125 mm) and 0.0174 mm^{-1} (or bending radius of 57.571 mm). These values still do not meet the requirements of the desired microrobot.

Eye surgery: Intraocular and orbital procedures are challenging as the forces that relevant tissues can withstand without damage are minuscule, while the constrained workspace requires dexterous maneuvers of sub-millimeter surgical tools. CTRs were developed to offer compelling new solutions for this challenge

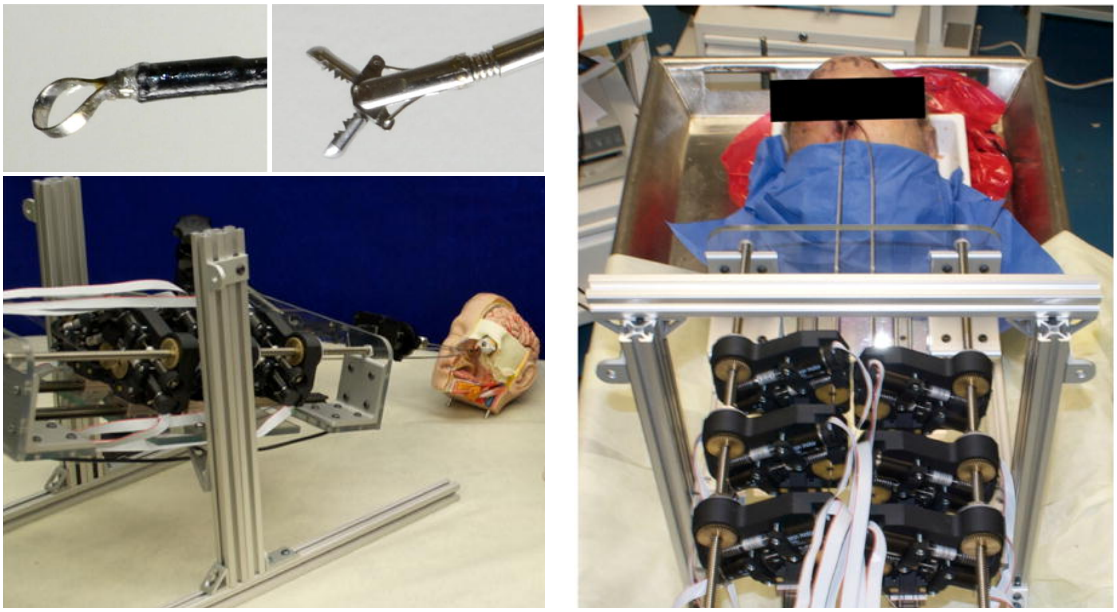

FIGURE II.10 – (Left) Prototype robot system actuates two cannulas for transnasal skull base surgery. (Right) Experimental setup of the transnasal skull base surgery using the bimanual robot in a human cadaver head [Burgner 13].

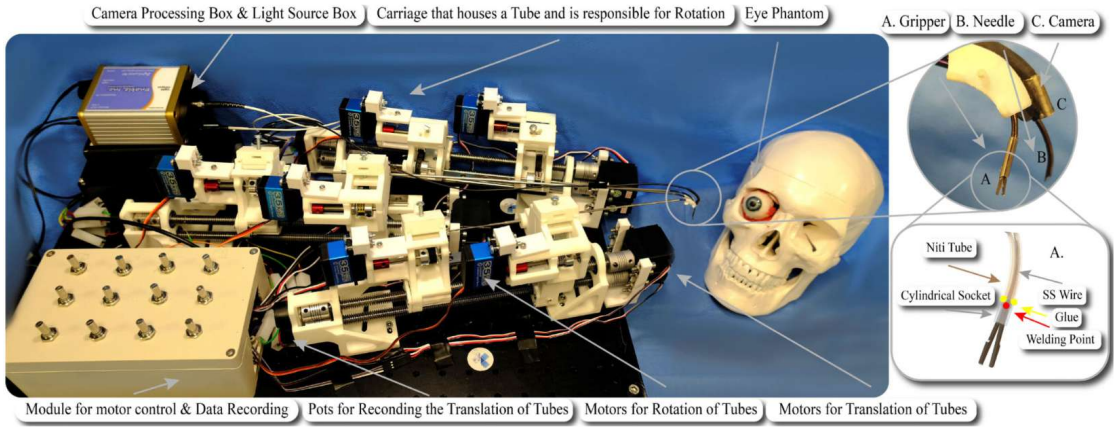

FIGURE II.11 – Multi-arm CTR system for deep orbital interventions [Mitros 20].

[Lin 15]. Wei *et al.* proposed the first use of CTRs for vitreoretinal surgery in [Wei 07, Wei 08]. The proposed 16-DOF hybrid robotic system dexterous manipulation is involved in Internal Limiting Membrane pealing and treatment of severe retinal detachments. The intraocular part of the robot that provides an additional bending motion inside the eye is a 2-DoF CTR consisting of a precurved NiTi inner tube and a straight outer cannula. The parallel part of the robot allowed global precise positioning of the eye and the surgical instrument.

The authors of [Lin 15, Wu 15] developed two one-arm CTRs with 4, and 3 DoFs, respectively. These were the first attempts to miniaturize the CTR actuators. Validation tests were conducted on custom-made phantoms [Lin 15] and on porcine

eyes [Wu 15]. The modular unit of [Lin 15] measured just $66 \times 52.2 \times 29.65$ mm, with a linear travel range of 30 mm, corresponding to the diameter of the eye. The diameter of the outer tube is 0.635 mm. The inner tube, with a bending radius of 27 mm, housed a gripper, which comprised steel forceps. The compact prototype presented in [Wu 15] has a total size of $40 \times 40 \times 210$ mm. The outer tube complied to the 20-gauge (0.91 mm [1]) surgery, while the inner tube, with a radius of curvature 30 mm, was less than 23-gauge (0.64 mm) with a hollow channel sufficient to house a 25-gauge (0.52 mm) light pipe. Hollow shaft motors eliminated the need for gears or lead screws and avoided backlash. They were controlled by a custom made joystick and buttons on the top side of the robot. The robot was very light (total weight of 0.496 kg) to enable handheld operation.

The first multi-arm CTR system proposed for deep orbital interventions with a focus on Optic Nerve Sheath Fenestration (ONSF) is shown in figure II.11 [Mitros 20]. The robot with 3 arms provided 12 DoFs in total. The CTR arms collaboratively performed the intervention of the eye orbit and the optic nerve by navigating periocularly and following the eye surface. One arm held a 1.2 mm chip-on-tip camera (Enable Inc., United States), while the others held a gripper and a cannula. Optical fibers stored inside the camera body are utilized to create illumination. A prototype of the robot was fabricated and ex vivo researched on porcine optic nerves comparing to their stiffness of human ones to evaluate its capacity to enter the optic nerves. The CTRs holding the gripper and the cannula consisted of the same tubes with the external diameter of 1.80 mm and the internal diameter (the channel) of 0.80 mm. The radius of curvature of the inner tube was 9 mm. Table II.6 provides the characteristics of this robotic system as a representative of CTR family operating in a confined workspace.

Table II.6 – The multi-arm CTR system for deep orbital interventions [Mitros 20]

DOF	3 arms with 12 DoFs in total
Surgical instrument types	Endoscope, gripper, cannula
Volume coverage	275 mm^3
Curved segments	2
Rigid/bendable	Steerable and prefixed-curvatures
Outer diameter	1.80 mm
Hollow channel diameter	0.80 mm
Distal bending radius	9 mm
Distal bending angle	-
Material of the instrument	Nitinol tube
Ablation tool	-
Accuracy	-

Continued on next page

1. Needle Gauge [online]: https://www.hamiltoncompany.com/laboratory-products/needles-knowledge/needle-gauge-chart.

Table II.6 – continued from previous page

Actuation type	Concentric tube robot
Control	Intuitive control
Validation status	On an eye phantom
Comment: In general, the diameter of Nitinol tubes are compatible to surgical needles ($1-2$ mm) which is suitable for working within very confined workspaces. The hollow of the inner tube allows the integration of optical fibers. However, the precurvature of the tubes imposes limitations regarding the volume that can be swept by the tip, while keeping the rest of the CTR body in the constrained environment. To increase the bending curvature, the diameter of the tube must reduce resulting in the narrowing of the channel of the innermost tube. In addition, snapping problem may occur during operation. In this case, the robot moves quickly from one configuration to another with the suddenly released energy [Hendrick 15a] that may harm the patient.	

II.2.2.b **Tendon-driven robots**

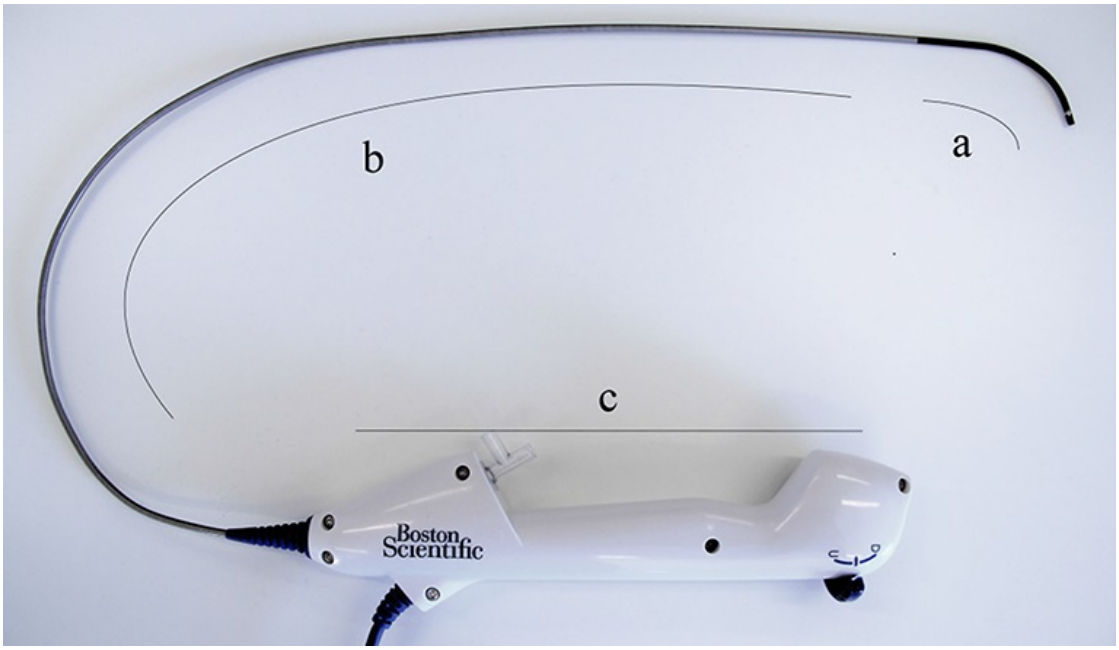

FIGURE II.12 – LithoVue (Boston Scientific, Natick, USA): (a) distal flexible tip, (b) proximal non-rigid part, (c) handle [Legrand 18].

Such robots have been considered in many medical applications including cardiac surgery [Ataollahi 13], gastroscopic surgery [De Donno 13], sinus surgery [Yoon 18], osteology [Dario 00, Kutzer 11], neurosurgery [Kato 15, Kato 16, Gao 19], etc. They can also be found in commercial market, Hansen Medical, USA, produced the Sensei robotic system [Kanagaratnam 08, Riga 11], Medtronics, an American-Irish registered medical device company, produced the Medrobotics Flex system

[Remacle 15], or Boston Scientific, USA, produced the LithoVue digital flexible ureteroscope [Butticè 16] (see figure II.12) which was then modified as a lightweight fetoscope [Legrand 18]. An obviously common feature of most of these designs is that an elastic structure is utilized as a "backbone" which can bend under the tendon load(s). The backbone can be an elastic tube [Li 16], an elastic notched tube [Moses 15, York 15], a helical spring [Yoon 18], or a compliant-joint [Zhang 21]

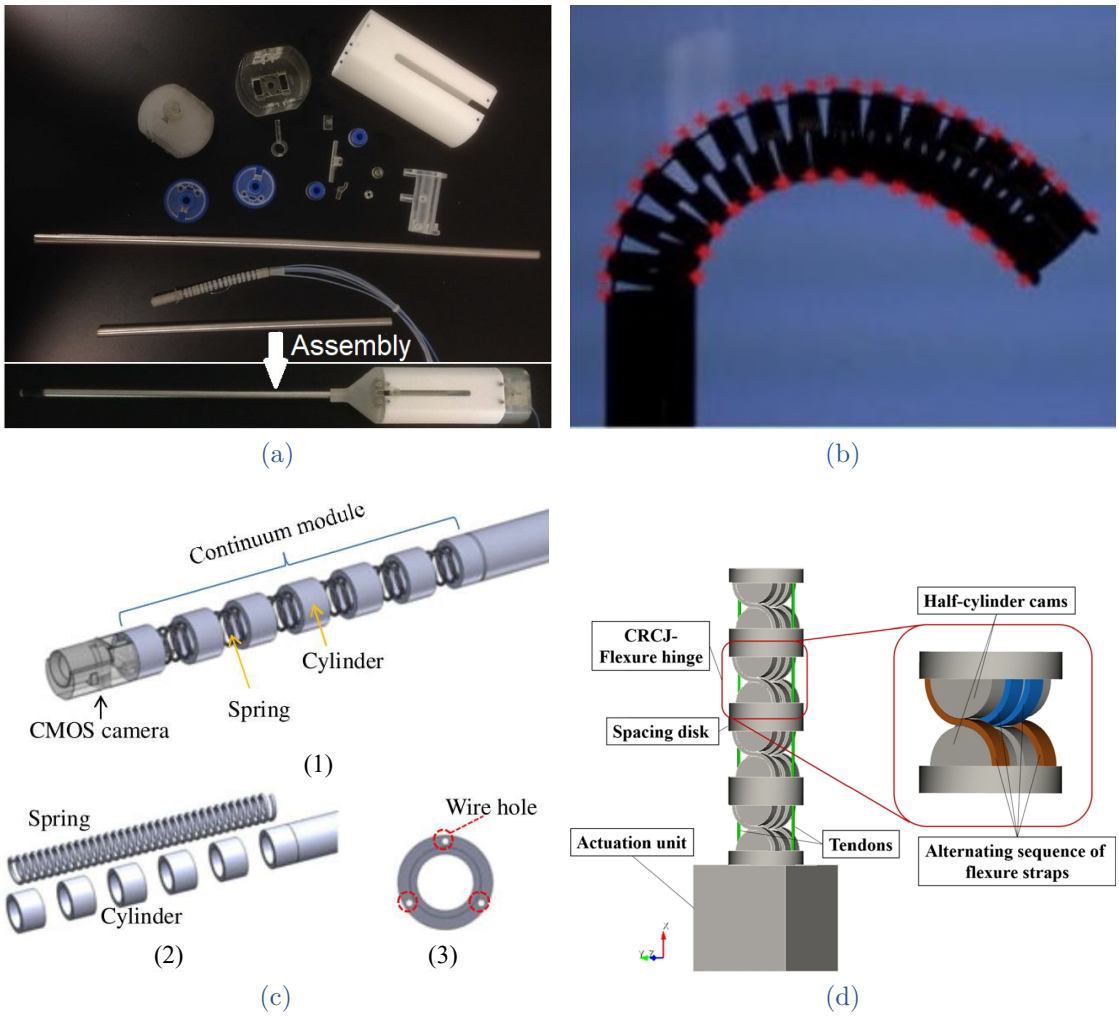

FIGURE II.13 – (a) A flexible endoscope designed for mini-mally invasive cardiac surgery - cardioscope [Li 16]. Its flexible section is composed of an elastic tube, a number of spacing discs, a constraint tube and four tendons. (b) A high-strength cable-driven dexterous manipulator [Moses 15]. Its backbone is fabricated by notching on a Nitinol tube. (c) Structure of the endoscope end-effector with spring backbone for maxillary sinus surgery. (1) Assembled state. (2) Disassembled state. (3) Cross-sectional view of a cylinder [Yoon 18]. (d) A novel tendon-driven manipulator structure based on monolithic compliant rolling-contact joint for minimally invasive surgery [Zhang 21].

(see figure II.13). In these mechanisms, the tendon(s) pass through guide eyelets on support disks whereby they are routed outside the backbone [Yoon 18] or they can be embedded freely inside the elastic tube [York 15].

Considering the anatomical constraints of middle ear surgery, the notched tube design with a small diameter of $1-2$ *mm* that allows obtaining a high curvature in confined workspaces will be the best choice compared to other tendon-driven robots [Swarup 21]. There are many types of notched tube design in the literature including uni-directional [York 15, Fichera 17, Eastwood 18], bi-directional symmetric [Liu 13, Dewaele 14], bi-directional asymmetric [Kutzer 11, Du 15, Gao 16b], and multi-directional [Francis 18] (see figure II.14). The tendon-driven robots with a distal notched tube design working in middle ear cavity was described in [Fichera 17, Gafford 21] with kinematics analysis have been analyzed before (see Table II.5). The fabrication of the notched patterns can be performed using computer numerical control (CNC) machining, electrical discharge machining (EDM), or femtosecond laser. The detailed discussion on each fabrication method will be presented in Chapter IV.

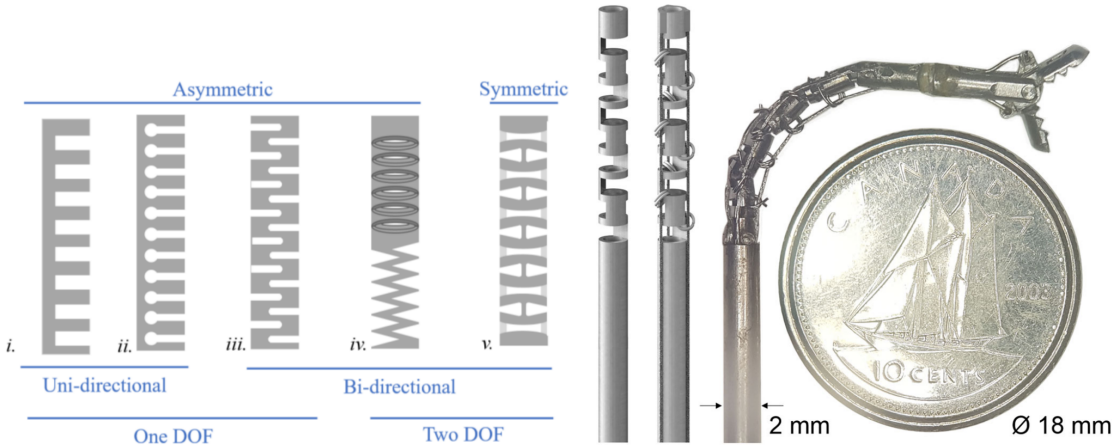

FIGURE II.14 – (a) Uni- and bi-directional notched tubes [Eastwood 18], and (b) multi-directional notched tube design with 120 notch spacing, three cables and cable guides [Francis 18].

Moreover, the notched tube segments can be connected in series as a multi-DOF tendon-driven robot. Chitalia *et al.* proposed such a robot for pediatric neuroendoscope [Chitalia 20a] (see figure II.15). The authors considered different asymmetric notch joints for the 2-DOF robot while varying tendon routing techniques. The robot was fabricated using laser micromachining on a Nitinol tube of 1.93 *mm* in outer diameter. The tube wall thickness was 0.22 *mm* leading to a hollow channel diameter of 1.49 *mm*. The possible bending angle of each curved segment can reach 40.8°. As the lengths of the proximal and distal joints are 6 *mm* and 4.9 *mm*, respectively, one can infer the the radii of proximal and distal bending curvature are 8.43 *mm* and 6.88 *mm* [Chitalia 20a]. To obtain precise and robust

position control, a PID controller and a disturbance observer was implemented in the system. Finally, the authors proposed a hand-held controller that was able to dock itself into a connector module interfacing with the MINOP neuroendoscope (Aesculap Inc., PA, USA). Table II.7 summarizes the characteristics of the robotic system.

TABLE II.7 – The multi-segment notched-tube tendon-driven robot [Chitalia 20a]

DOF	2
Surgical instrument types	Endoscope
Visible coverage	-
Curved segments	2
Rigid/bendable	Bendable
Outer diameter	1.93 mm
Hollow channel diameter	1.49 mm
Distal bending radius	6.88 mm
Distal bending angle	40.8°
Material of the instrument	Nitinol tube
Ablation tool	-
Accuracy	-
Actuation type	Tendon-driven
Control	Hand-held controller and PID controller
Validation status	Hand-held prototype
Comment: In general, the dimension of the robot is suitable for middle ear surgery. The robot tip can sweep inside a confined workspace with a small bending radius. However, the most important drawback of tendon-driven designs is the difficulty to combine more than 2 DOFs due to cable obstructing the internal lumen especially, in the presence of the optical fibers. Besides there is the coupling issue between active sections actuated by tendons. Furthermore, the relative angle (about the centerline axis) between the bending directions of different active segments is prefixed that still limits the accessible zone of the robot tip. Finally, the ablation tool has not been embedded yet within the robot lumen.	

II.2.2.c **Hybrid actuation**

Several hybrid actuation designs that combine a CTR and a tendon-driven robot can be found in the literature. By replacing the central elastic tube of a tendon-driven robot by a CTR, the authors in [Nguyen 15] propose a tendon-driven continuum robot consisting of tube sections that can be extendable (see figure II.16). To ensure the equidistant spacing of the disks at any lengths of each robot section, the magnetic repulsion forces were employed by embedding permanent magnets with alternating pole orientation into the spacer disks. This design

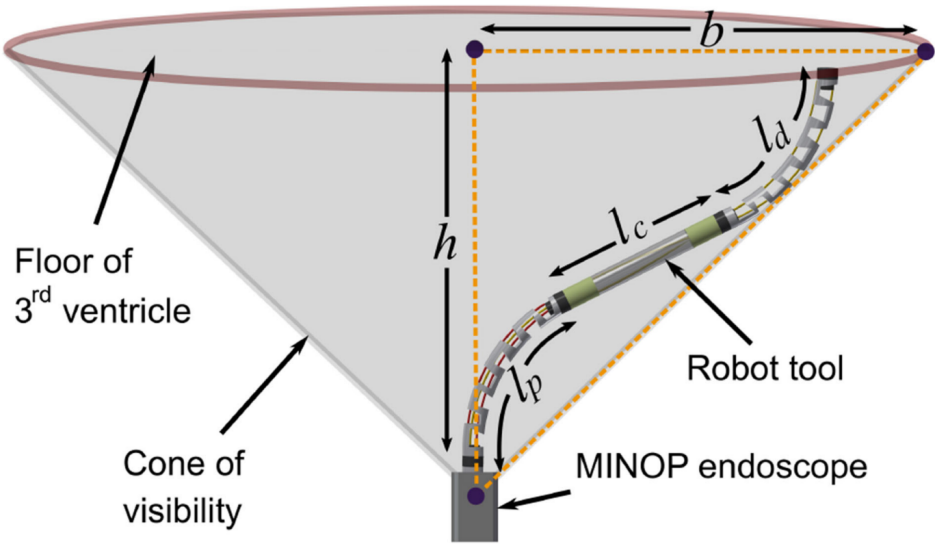

FIGURE II.15 – Design of a robotic tool with two notched-tube segments that is always within the cone of visibility of the endoscope [Chitalia 20a].

improves the dexterity of conventional tendon-driven robots by changing its active length. In addition, it inherently allows for deployment in a follow-the-leader manner. However, as the tendons are externally routed with rigid disks, the dimension of the robot is quite large and not suitable for middle ear surgery. Another approach based on a CTR design with several bendable segments driven by the tendon load are described in [Wu 16] for the purpose of improving the workspace of the CTR (figure II.17). Simulation results were carried out in MATLAB to analyse the workspace of the three robots.

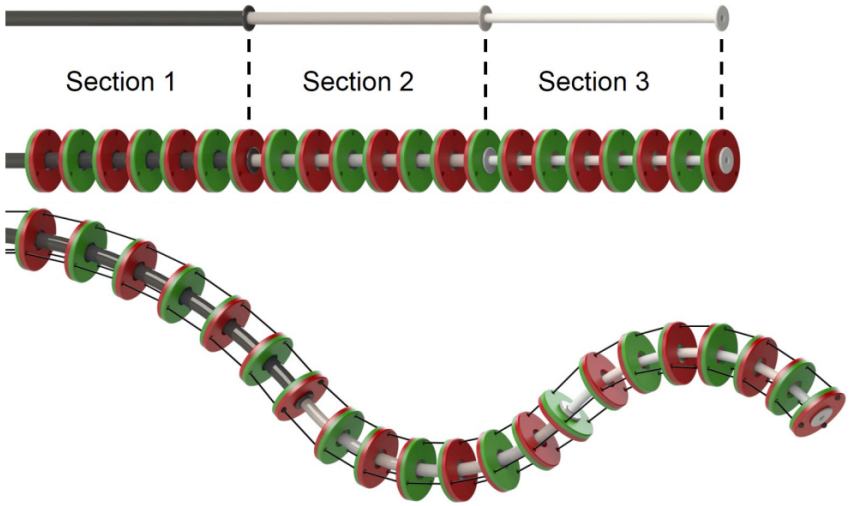

FIGURE II.16 – The tendon-driven continuum robot with 3 extensible sections based on CTR [Nguyen 15]. The magnetic spacer disks distribute with equidistant spacing due to magnetic repulsion forces at any section length.

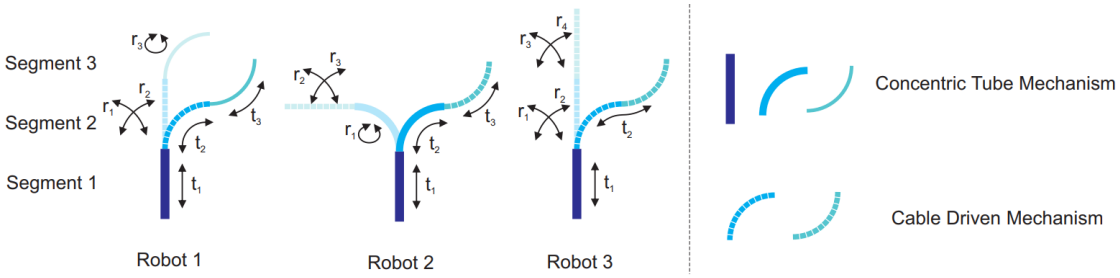

FIGURE II.17 – The 6-DOF hybrid continuum robots where t stands for translational DOF and r stands for rotational DOF [Wu 16].

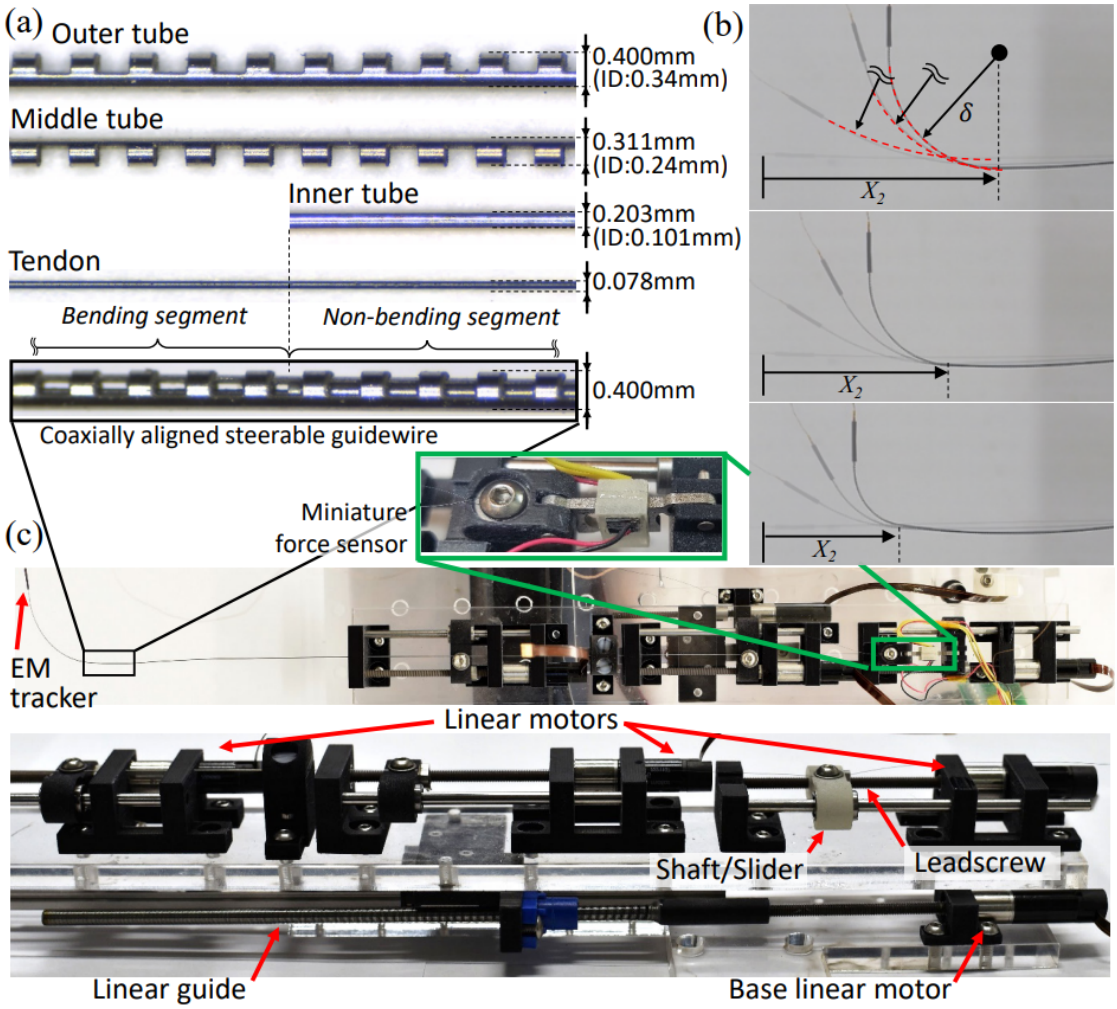

FIGURE II.18 – (a) Coaxial tubes and dimensions, (b) demonstration of COAST achieving different curvatures and arc lengths, and (c) actuation stage using individual linear motors to control the COAST guidewire [Jeong 20].

Recently, to reduce the robot size, notched tube can be utilized. Such a robot as proposed in [Jeong 20] consists of an outer and a middle straight notched tubes together with an inner stainless steel straight tube that allows achieving various

joint lengths and curvatures by varying relative positions of the tubes and the tendon (figure II.18). The robotic system was very slender (0.4 mm in outer diameter) and was proposed to use as a guidewire robot. The characteristic summary of the robotic system will be given in Table II.8.

Table II.8 – The COAST guidewire robot [Jeong 20]

DOF	4
Surgical instrument types	Guidewire robot
Workspace	-
Curved segments	1
Rigid/bendable	Bendable
Outer diameter	0.4 mm
Hollow channel diameter	0.102 mm
Bending radius	can achieve 11.9 mm
Distal bending angle	can achieve 180°
Material of the instrument	Nitinol and stainless steel tubes
Ablation tool	-
Accuracy	Distance error of 4.53 mm in low curvature paths and of 14.66 mm in high curvature paths.
Actuation type	Hybrid concentric tube and tendon-driven continum robot
Control	Model based controller
Validation status	On a vascular phantom with a benchtop prototype
Comment: The bending angle is high enough for working in a confined workspace. The robot integrates the deployment in a follow-the-leader manner of a CTR and the bendable structure of a tendon-driven actuator. However, as a guidewire robot, the diameters of the tubes are very small in order to embed the ablation tool within the robot lumen.	

Researchers at FEMTO-ST Institute also developed continuum robots with hybrid actuation that can be employed for working in confined spaces. Chikaoui *et al.* proposed in [Chikhaoui 14b] a micro-endoscope based on EAP and concentric tube actuators. This design was then considered for intracorporeal laser steering [Chikhaoui 17]. However, as the bending section of the robot consists of the soft material (PolyPyrrole), it is quite challenging to obtain high bending angle for cholesteatoma ablation within the middle ear cavity. Peyron *et al.* proposed a magnetic concentric tube robot (m-CTR) that can operate inside a confined workspace like middle ear cavity [Peyron 19, Peyron 22]. Nevertheless, this robotic system requires a big electromagnetic navigation system which is not suitable for the purpose of the µRoCS project. In addition, to generate enough magnetic

forces/torques and provide sufficient clearance between the patient and the manipulator, the magnet dimensions should be increased [Clark 12]. This may not meet the requirement of a miniature robotic design.

II.2.2.d **Summary**

The miniaturization issue is a big scientific and technical challenge, especially for a tiny workspace as the middle ear cavity. Different robotic systems have been derived for middle ear surgery. Nevertheless, they used rigid tools to perform this task that caused the difficulty to access hard-to-reach positions inside the tympanic cavity. Thus, several medical robotic systems from other surgical applications which could be used, with some adaptations, for the middle ear surgery have also been considered. These designs improve the dexterity of the surgical tool using different types of actuation. Even so, each actuation method imposes limitations in comparison with the requirements of the proposed robot.

Hydraulic and pneumatic actuators can be deployed safely, but require a large dimension or do not have hollow channel for optical fiber integration. Piezoelectric actuators obtain a fast response time but require a very high voltage for a small deformation and a highly demanded control to eliminate vibration and hysteresis effects. SMA actuators allow a heavy payload as well as being miniaturized. However, they generate heat during the operation. EAP materials, without the limitations of piezoelectric and SMA materials, but they required long time for the deformation and do not allow a high bending angle at the distal end of the robot in the presence of optical fibers. m-CRs can be manipulated without contact, however, controlling the robot shape in confined spaces using a large magnetic field is quite challenging. Moreover, the required size of the magnets can be much larger than that of the proposed microrobot. Multibackbone robots improve the dexterity of the surgical tools but their dimensions are still large in comparison with the anatomical constraint. CTRs and tendon-driven robots are suitable for a minimally invasive surgery as they are slender and allow integrating optical fibers for cholesteatoma detection and removal through their lumen. Furthermore, the material is bio-compatible with a proper hardness to constrain the embedded optical fiber. Even so, they also have several limitations. The CTR has a prefixed curvature depending on the outer diameter of the tube that imposes limitations of the volume scanned by the robot tip. Not only that, but the snapping could occur during the operation, that may harm the patient. The main drawback of tendon-driven actuators is the difficulty to obtain more than 2 DOFs due to cable obstructing the internal lumen. Besides, the coupling issue between active sections and the tendon slack effect also need to be considered. It was demonstrated that hybrid actuation enables to improve kinematic performances [Wu 16, Chikhaoui 17, Peyron 22]. Even so, more studies are required to apply them to the middle ear surgery. To the best of the author's knowledge, there is not any microrobot that is capable to perform exhaustive cholesteatoma surgery using an embedded laser optical fiber.

The hybrid actuation that combines concentric tubes and tendon-driven actuators can be a good candidate for the proposed robot. For that, the robot need to be designed so that it inherits the advantages and eliminates the limitations of each method. Besides, the new robotic system should be ergonomic and overcome the kinematic requirements dedicated for exhaustive cholesteatoma including: inserting the microrobot via a small entrance tunnel (the 3 mm created hole through mastoid or the auditory canal), bending and sweeping its distal tip inside the tiny workspace (about 1 cm^3) without changing the shape of the rest part, and adding diagnostic and ablation tools to perform the robot tasks. In the following, a new microrobot using hybrid actuation combining CTR and tendon-driven robot for exhaustive cholesteatoma laser surgery will be proposed.

II.3 Proposed Robot for Exhaustive Cholesteatoma Surgery

A hybrid CTR-tendon driven miniature robot will be considered for the design of our microrobot in order to achieve the targeted minimally invasive surgery as well as the integration of optical fibers. The proposed robot has to achieve a large curvature at the tip to sweep the desired volume. Considering different mechanisms in the literature, uni-directional asymmetric notched tube is the best design for such a distal end to maximize its bending curvature. In addition, to ensure a collision-free deployment as well as an access to challenging anatomic regions for cholesteatoma removal, the robot needs to have at least two curved segments. Several robots in the literature can provide such a design [Chitalia 20a, Jeong 20]. However, the proposed robot dedicated for cholesteatoma surgery need to obtain a perfectly decoupled actuation between the bendable distal end and the proximal part. Thus, the thesis proposes to use concentric tube robot, without notch, for the rest part in order to ensure a much higher stiffness than the wrist and keep the robot body stationary when the distal end is bent. Furthermore, this design provides multiple bending directions in space thanks to the independent rotations of the tubes. It also allows deploying the robot with a follow-the-leader manner even if it is not the focus of this thesis. The concept combining a needle-size wrist with tendon driven actuation on the innermost tube of a CTR at its distal end is originally presented in [Swaney 17]. Even so, in this work the authors only focused on the tendon-driven notched wrist mechanism. They only suggested a potential use of the wrist by integrating it at the distal end of a CTR without any quantitative test for the hybrid actuation to compare with the needs of cholesteatoma surgical process. To adapt for this surgery, materials and dimensions of the tubes need to be selected to guarantee an outer diameter smaller than 3 mm to ensure minimally invasive surgery and the lumen need to be large enough (> 0.8 mm in diameter) to embed the optical fibers,

Furthermore, the design parameters (i.e., the precurvature of the tubes, the length of the distal notched end, the number of cutouts, the height and the depth of cut,...) must be examined to optimize the volume within the anatomy scanned by the robot tip. Finally, a laser optical fiber is embedded in the lumen of the innermost tube to perform the exhaustive cholesteatoma ablation. The structure of the proposed hybrid CTR for exhaustive cholesteatoma surgery is shown in figure II.19 and will be then discussed in Chapter IV of the thesis.

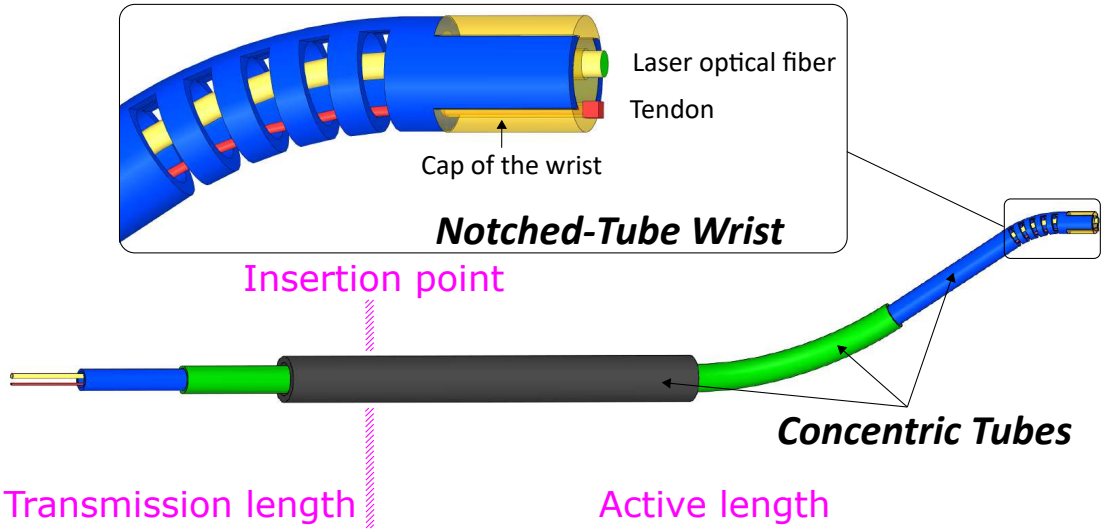

Figure II.19 – The proposed hybrid CTR scheme.

II.4 Conclusion

In this chapter, the ideal requirements for implementing a flexible microrobot to perform a minimally invasive cholesteatoma surgery is presented. Through a comprehensive review on the robotic systems that are related to the middle ear surgery and others dexterous surgical robots, we show that there is not any micro-robotic system fulfilling all the requirements of exhaustive cholesteatoma surgery. The main challenges are the miniaturization and dexterity of the surgical tool that has to work in a tiny workspace as the middle ear cavity. Some medical robotic systems from other surgical applications are also discussed. CTRs and tendon-driven robots are the most suitable designs that could be adapted for cholesteatoma surgery. The design of these robots based on elastic tubes will allow the integration of optical fibers for the cholesteatoma detection and ablation. However, the volumes covered by the tip of these robots are still limited especially for hard-to-reach locations. Thus, by taking advantage of the strengths of each design, the hybrid actuation combining a CTR and a tendon-driven wirst is proposed in this chapter for exhaustive cholesteatoma ablation. The following chapter will present the modeling of the proposed robot.

Chapter III
Hybrid Concentric Tube Robot Modeling

III.1 Model Decomposition and Assumptions 54
III.1.1 Model decomposition. 54
III.1.2 Assumptions. 55
III.2 Concentric Tube Robot 56
III.2.1 CTR kinematics without tendon load 57
III.2.2 Deformation of the CTR under the free internal tendon load 58
III.3 Notched Tube with Tendon-Actuated. 81
III.3.1 Static model of the wrist with optical fiber 82
III.3.2 Model calibration & sensitivity analysis 85
III.4 Graphical User Interface of the Hybrid CTR 88
III.5 Conclusion 88

In the previous chapter, the hybrid CTR was selected to perform the exhaustive cholesteatoma surgery. In order to obtain the robot design and control, the modeling of the robot need to be established. The proposed robot consists of two main parts: the CTR and the wrist actuated by a tendon. Both of these components are modeled in this chapter. Besides, the deformation of the concentric tubes under the tendon load and the sensitivity analysis of the wrist are also discussed. Last but not least, a graphical user interface will be used to visualize the simulation outcome of the modeling.

III.1 Model Decomposition and Assumptions

This section starts by describing the model decomposition of the proposed robot. As the proposed robot combines different actuator techniques, decomposing the robot model into two smaller sections (i.e. CTR and wrist) that correspond to each actuation method should be a preferable option. Also, the modeling's underlying assumptions are highlighted in this section.

III.1.1 Model decomposition

The modeling problem which involves determining the robot shape for a given set of actuation variables can be divided into three phases:

i. Deployment of the CTR in order to access to the site of interest by translating and rotating the tubes.

ii. Deformation of the CTR under the tendon load (coupled actuation).

iii. Bending of the wrist driven by pulling the tendon.

We first use a kinematic model to obtain the form of the CTR by neglecting all external forces and moments on the tubes caused by the tendon and other sources (e.g. gravitational effects) (Problem [i.]). Then, the tendon and other external loads are considered in a static model to calculate the final deformation of the CTR (Problem [ii.]). Finally, a static model is developed to predict the bending of the wrist considering the stiffness of the optical fiber (Problem [iii.]). In this study, the applied tendon force rather than the tendon displacement is taken into account as the actuation mechanism of the wrist to avoid the extension effect.

The main variables used for the modeling are shown in figure III.1 where different colors denote different tubes. By s, we designate the arc length along the robot from the point where it extends out of the actuation unit. Let $\boldsymbol{B}$ be the constrained entry point, also named the insertion point ($s_B = 0$). On it, a fixed global base frame $g_B = I$ is located to describe the shape of the robot. The part of each tube in front of the constrained entry point ($s > 0$) is called active length.

Inversely, we use transmission length to call the negative arc length part ($s < 0$) of each tube. ***O*** is the point on the centerline of the robot that joins the wrist and the CTR. Let ***T*** be the distal end of the robot centerline, the homogeneous transformation matrix of the entire robot from the base to the tip is given by equation III.1.

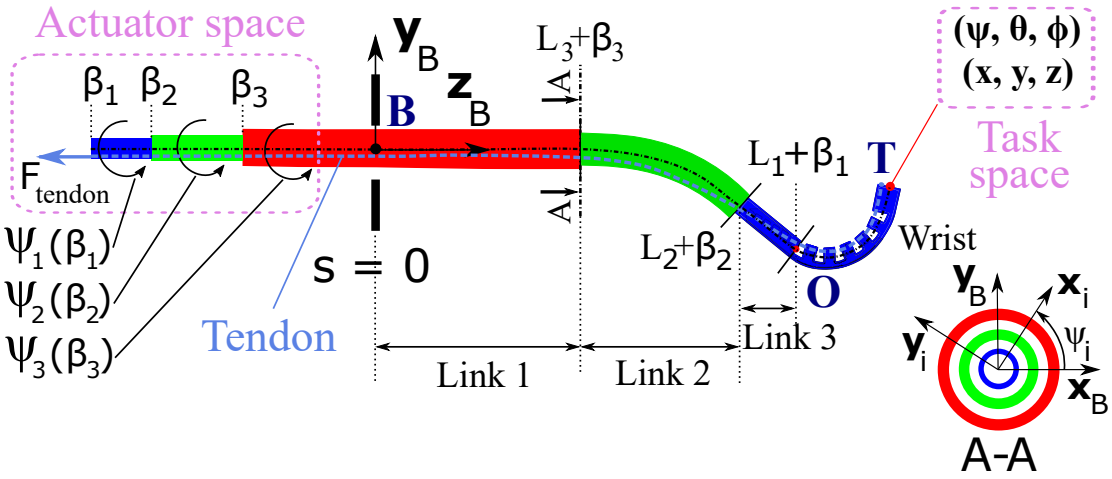

FIGURE III.1 – Representation of the hybrid concentric tube robot composed of a CTR and a dexterous wrist integrated to the inner tube, with associated parameterization.

$$g_B^T = g_B^O g_O^T \tag{III.1}$$

where g_B^O is the homogeneous transformation matrix of the CTR and g_O^T is the transformation matrix for describing the bending of the wrist. Calculating g_B^O consists of resolving problem [i.] and [ii.] while determining g_O^T required addressing problem [iii.].

III.1.2 Assumptions

The following assumptions will be taken into consideration throughout this chapter in order to simplify the investigated model:

CTR

- The coaxiality of the tubes is always preserved during operation. This holds when the spaces between the tubes are small.
- Ignoring the friction among the tubes as well as between the innermost tube and the tendon. The authors of [Ha 18] provide an approach to examine the effect of the friction in the CTR model. However, it greatly increases the complexity of the studied problem as well as does not take into account the friction caused by the tendon. Thus, this will be left to future work.

- The CTR model assumes that the extension and transverse shear strain of the tubes can be neglected. This assumption is considered reasonable for long, slender rods such as the tubes employed in building the proposed robot. [Rucker 10b].

Wrist

- The bending of the wrist is uniform and uni-direction.
- Only the corners of the wrist experience friction with the tendon.
- Only the notched portions bends during operation.

In addition, the cross-sectional area of the robot at any arc length position is considered remaining constant during operation for both the CTR and the wrist.

III.2 Concentric Tube Robot

This section focuses on the model describing the shape of the CTR according to the actuation variables. As a well known topic, many investigated models have been proposed in the literature including: (i) weighted superposition of the curvatures combined with torsional rigidity [Sears 07, Dupont 09, Webster III 10], (ii) differential equations for kinematic variables using the minimization of bending and torsion stored energy [Webster 08, Rucker 09, Rucker 10b], (iii) approximation of the robot forward using Fourier series [Dupont 10], (iv) reduced-order techniques using piecewise constant strain assumption [Baek 16, Pourafzal 21, Renda 21], (v) polynomial shaped approximation [Sadati 20], and (vi) learning-based approaches [Fagogenis 16, Grassmann 18, Kuntz 20]. Among these methods, the models (i) and (ii) are two of the most widely considered and referenced.

In the curvature weighted superposition approach, the kinematics of the tubes are determined using weighted curvature superposition without the torsional effect where the curvature weights are the bending and torsional stiffness values of the tubes. The model results in a Initial Value Problem (IVP) that is simple to integrate into a real-time numerical system.

In the energy based approach, the curvatures and torsion of each tube is known as kinematic variables in a system of differential equations which form a two points Boundary Value Problem (BVP) (boundary conditions at the base and tip of the robot backbone). The system can be solved using numerical optimisation, e.g. shooting method. This model provides a good prediction of the CTR shape as it consider the torsional effect.

Besides depending on the actuation input values, the shape of the CTR is affected by their time history due to the friction among the concentric tubes. Early mechanical investigation has been proposed in the literature to modeling this phenomena [Lock 11]. The authors suggested that the dominant effect of the frictional force is associated with concentrated bending moment at the tube ends

as the passive actuation of the RTC. The friction induces twisting of the tubes during their rotation, making the shape of the RTC dependent on the previous rotational direction of the tubes. However, this modeling remains insufficient and leads to significant errors. The important source of errors includes the clearance between the tubes that influence the location of the contact zones between them which is not taken into account. More recently, [Ha 18] presented the distributed torsional friction as the main source of CTR modeling inaccuracy compared to the tube clearances. Even so, it seems that frictional effects will be complex functions of a number of parameters including hard to estimate parameters such as surface smoothness or lubrication, etc. Thus, it will be neglected in this work as has been done in almost CTR models in the literature. Furthermore, the mass of the tubes will not be considered in the kinematic models.

As a common method used to describe the CTR mechanisms, the torsional compliant [Webster 08, Rucker 09, Rucker 10b] kinematic models will be briefly summarized in the following. Even so, this model does not considered the tendon load on the tubes. Hence, the later of this section presents a novel approach to investigate the deformation of the CTR under the loads caused by the internal tendon. This model focuses on solving the coupling between the BVP for the CTR's shape and the shortest path problem for the tendon location.

III.2.1 CTR kinematics without tendon load

Considering a collection of n concentric tubes with general precurved shapes. The index $i = \{1, \ldots, n\}$ indicates the order of the tube (from inner to outer tubes). The proximal end of the i^{th} tube is located at $s = \beta_i < 0$, and is rotated about the z-axis by an angle ψ_i with respect to the fixed base frame. Therefore, the robot's actuator variables is the set $\boldsymbol{q} = \{\psi_1, \ldots, \psi_n, \beta_1, \ldots, \beta_n\}$. We then determine the resulting shape of the robot for a given set of tubes and actuation variables (see figure III.1). Let L_i be the total length of the i^{th} tube. We note that the inequality $L_n \leq \ldots \leq L_i \leq \ldots \leq L_1$ must be respected in the model, so that the tubes can be deployed in a telescopic manner and can be grasped at their bases by a manipulation system.

The energy approach based on minimizing the elastic bending and torsion energy stored in the tubes to determine the shape of the CTR in free space with out any external load. The model proposed in [Webster 08, Rucker 09, Rucker 10b] is described in the Appendix B.1. It is briefly summarized here for the purpose of completeness. The governing differential equations of the torsional compliant kinematic model is given by equation III.2. The main variables for the modeling are reported in Appendix A.

$$\begin{aligned} \dot{\psi}_i &= u_{iz} \\ \dot{u}_{iz} &= \frac{E_i I_i}{EIG_i J_i} \sum_{j=1}^{n} E_j I_j \kappa_i \kappa_j sin(\psi_i - \psi_j) \end{aligned} \tag{III.2}$$

with $EI = \sum_{j=1}^{n} E_j I_j$. Continuity of the tube angles and their torsion must be ensured between each link, and the boundary conditions given by equation (III.3) apply at the insertion point $s = 0$ of the tubes as well as at their tips, at $s = L_i + \beta_i$.

$$\begin{cases} \psi_i(0) = \psi_i(\beta_i) - \beta_i \dot{\psi}_i(0) \\ \dot{\psi}_i(L_i + \beta_i) = 0 \end{cases} \tag{III.3}$$

Solving the system of equations (III.2) associated with the boundary conditions (III.3) can be done for example in Matlab, which offers a function named bvp5c (for multi-region boundary value problem). After solving for the torsion of the tubes along their lengths, their curvature components along the x and y axes are computed using equation (III.4).

$$u_{ixy} = \frac{1}{EI} \sum_{j=1}^{n} R_{\psi_j - \psi_i} E_j I_j u^*_{ixy} \tag{III.4}$$

Having the full curvature vector $\boldsymbol{u}_i(s) = [u_{ix}, u_{iy}, u_{iz}]^T$ of the tubes makes it possible to obtain the position of each tube in 3D space by integrating (III.5).

$$\dot{\boldsymbol{p}}_i = R_i \boldsymbol{e}_3, \qquad \dot{R}_i = R_i \hat{\boldsymbol{u}}_i, \tag{III.5}$$

where $\hat{\boldsymbol{u}}_i$ is the skew-symmetric matrix computed from $\boldsymbol{u}_i(s)$, with initial conditions $\boldsymbol{p}(0) = \boldsymbol{0}$ and $R(0) = R_z(\psi_i(0))$. The forward transformation matrix from the base to the connection point g_B^O as given in the equation (III.1) can be obtained using the knowledge of the inner tube pose at O. Even so, the model does not take into account the tendon load. Thus, a static model that try to determine the final deformation of the CTR under the tendon load will be provided in the following. For convenience, superscript $(^e)$ will be used for the obtained result of the torsional compliant model to specify the case that the CTR is in equilibrium state without any external load.

III.2.2 Deformation of the CTR under the free internal tendon load

During operation, the distal curvature of the robot can be varied under the tendon load to improve the robot dexterity at the tip. However, the tight tendon also applies distributed force and moment on the rest part of the robot (the CTR) and make it deformed. This section will provide a modeling approach to investigate the deformation which will be useful to quantify the coupling effect.

III.2.2.a Problem formulation

It is necessary to clarify the three states of the concentric tubes: the *pre-curvature tube state* when each tube is not constrained by other ones, the *unloaded state* of the CTR when the tendon tension is zero, and the *loaded state* when the

tendon is tight. This subsection focuses on the deformation of the CTR from the unloaded state to loaded state. This deformation depends on the location of the tendon. As cable-routing along the tubes requires an innovative fabrication, we choose to let the tendon free inside the inner tube so that it can naturally conform to the inner tube wall when pulled [York 15]. Under the assumption of non-friction interaction between the tendon and the lateral wall of the tube, the shape of the tight tendon describes the shortest path inside the tube connecting the two endpoints at the base and at the tip. In addition, it should be pointed out that the solution of the shortest path problem also depends on the shape of the innermost tube and consequently leads to a hard question about the coupling between the tendon location and the deformation of the tubes. To simplify the problem, the following assumptions will be considered in this study:

i. As the problem to deal with in this sub-section focuses on the deformation of the CTR under the tendon load, the bending of the wrist is temporarily not studied here. Thus, in a static approach, the wrist part of the proposed robot can be considered as an equivalent endcap of the CTR with the length of approximately 0 as illustrated in figure III.2 and the segment QR of the tendon degenerates to the attached point Q on the endcap. Indeed, the location and the tension of the tendon within the segment between P and Q are the same in both model A and B (see figure III.2). As the tendon path connecting P and R in model A is the shortest path, hence the tendon segment between P and Q must be also the shortest path joining them. It coincides with the location of the tight tendon in the equivalent model (model B). Furthermore, as there is no friction, the tendon tension is constant throughout this segment and equals to the force applied on the tendon at the robot base. Consequently, the tendon loads impact on the CTR are the same in both models.

ii. The individual torsion of each tube will be neglected in this problem so that the CTR can be treated as an elastic tube of multi-stiffness sections (the stiffness of each section equals the total stiffness of the tubes in it). Relying on the equation (B.14), this consideration holds for a CTR body that has at most one curved tube for any of its sections, which is the case in this work (see Chapter IV).

iii. The tendon is located inside the tube, the level arm of the moment caused by the tendon is small, this leads to a small deformation of the CTR comparing to the tube lengths. Furthermore, under the assumption of zero friction between the tendon and the innermost tube, the distributed force caused by the tendon is perpendicular to the tube surface and does not produce twisting torque acting on the tubes.

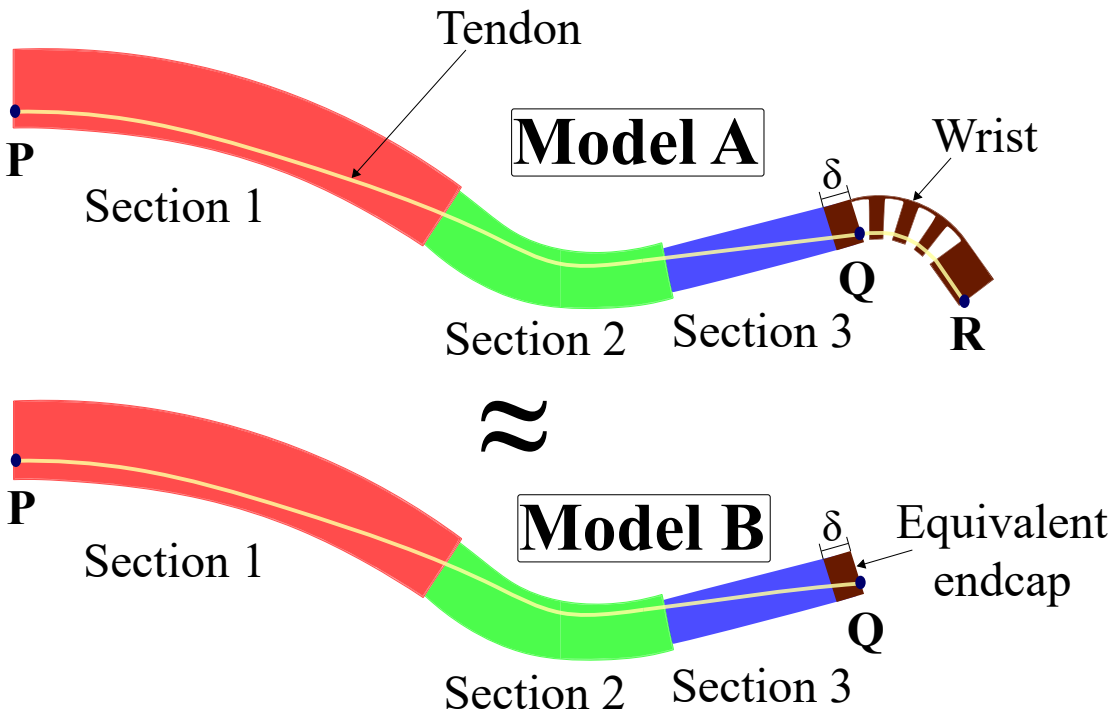

FIGURE III.2 – The wrist of the robot can be considered as an equivalent endcap of the CTR in the static model. The length of the endcap δ is approximately 0.

Concerning the elastic rod/tube-like structures under tendon load, several models were derived under the assumption that the backbone is piecewise constant-curvature when the tendons are tight [Camarillo 08, Dalvand 18]. For physical based approaches, [Gravagne 02] utilized an energy-base model to describe the statics and dynamics of a planar continuum robot under in-plane load. [Yekutieli 05] proposed a spring-mass-based study that was successfully applied to the simulation of octopus arms. Davis and Hirschorn early showed in their theoretical research the dynamics of the elastica with embedded tendons [Davis 94]. The theory of rod using no approximation related to kinematic variables (also called "geometrically exact") was proved as an effective method to describe the deformation of rod/tube-like structure under general external distributed force and moment [Antman 05]. Some of the most popular examples are Cosserat rod [Pai 02, Van der Heijden 02, Cao 08, Fang 13] and Kirchhoff rod [Bertails 06, Casati 13, Wang 17], which is a particular case of Cosserat rod under the constraints of 1) neither shearing nor extension, and 2) bending and torsion are expressed by linear constitutive equations. Applications of the rod theory in tendon-driven mechanisms can be found for both Cosserat rod [Rucker 11a, Neumann 16] and Kirchhoff rod [Rucker 10a, Rucker 10b]. Among these, the approach coupling the classical Cosserat rod and string presented in [Rucker 11a] is closest to the mechanics of the studied problem and has potential applications for soft materials. This method can be applied with modifications to formulate the studied problem as a two-point boundary value problem (BVP).

As the tendon is free within the lumen of the innermost tube, its location need to be figured out to solve the problem. Finding the shortest path in the presence of obstacles, referred to as the Euclidean shortest path (ESP) problem [Li 11], is one of the fundamental problems in path planning with numerous algorithms [Dijkstra 59, Hart 68, LaValle 98]. As conventional graph-based methods, these algorithms do not take into consideration the geometrical properties of tubular spaces to improve the accuracy and smoothness of the shortest path as well as enhance the calculation speed. In this work, we propose a new approach for solving the shortest path relying on the discretization of the storage space inside the tube into meshed circular disks perpendicular to the central axis [Nguyen 22]. The numerical validation and comparison results with Dijkstra's algorithm were given by considering various types of tubular spaces. As a result, the solution obtained by using the proposed algorithm is shorter, smoother and faster than that provided by Dijkstra's method.

The problem to be solved is a coupled one that simultaneously necessitates: 1) formulating the static model for the deformation of the multi-stiffness tube (the BVP) and 2) simultaneously indicating the tendon path inside the tube (the ESP) as shown in figure III.3. The difficulty of solving this coupled problem stems from the fact that, it cannot be expressed explicitly. Although the BVP can be written as a system of differential equations, we do not have any explicit formula to describe the ESP problem, which can only be solved through a searching algorithm. The following subsection will address this coupled problem.

III.2.2.b Elastic rod and internal string coupled model

In this work, the classical Cosserat rod model is employed to describe the elastic multi-stiffness tube while the tendon is defined as an extensible string. The distributed load applied by the tendon on the tube will be expressed by coupling the string and rod model. We first derive the governing equations of the coupled rod and string model where the tendon location will be considered as an unknown parameter depending on the arc length s.

Basics of rod theory

A Cosserat rod can be characterized by a parameterized, homogeneous transformation, $g(s) \in SE(3)$ as follows:

$$g(s) = \begin{bmatrix} R(s) & \boldsymbol{p}(s) \\ 0 & 1 \end{bmatrix} \tag{III.6}$$

where $R(s) \in SO(3)$ and $\boldsymbol{p}(s) \in \mathbb{R}^3$ describe the orientation matrix and the position in space of a local frame sliding along the central line and localised on it by its curvilinear abscissa. In coordinates of $g(s)$ (body frame), by $\boldsymbol{v}(s)$ and $\boldsymbol{u}(s)$, we denote the linear and angular rates of change of $g(s)$ with respect to s. We also denote the internal force and moment vectors in global frame coordinates by $\boldsymbol{n}(s)$ and $\boldsymbol{m}(s)$, and the applied force and moment distribution per unit of s by $\boldsymbol{f}(s)$

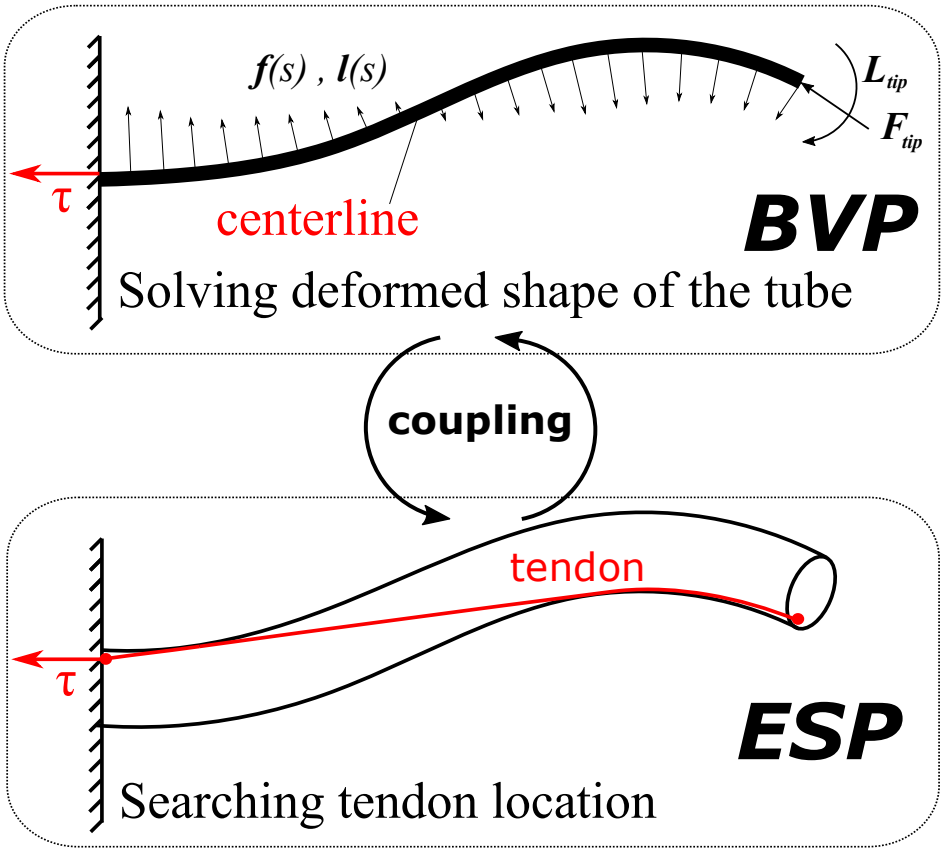

FIGURE III.3 – The main problem to be studied: the static model (coupled Cosserat rod and string model) for the deformation of the tube coupling with the shortest path problem inside the tubular space for the tendon location.

and $\boldsymbol{l}(s)$ respectively. The equilibrium differential equations for the Cosserat rod are (see, e.g., [Antman 05]):

$$\dot{\boldsymbol{p}}(s) = R(s)\boldsymbol{v}(s) \tag{III.7}$$
$$\dot{R}(s) = R(s)\hat{\boldsymbol{u}}(s) \tag{III.8}$$
$$\dot{\boldsymbol{n}}(s) = -\boldsymbol{f}(s) \tag{III.9}$$
$$\dot{\boldsymbol{m}}(s) = -\dot{\boldsymbol{p}}(s) \times \boldsymbol{n}(s) - \boldsymbol{l}(s) \tag{III.10}$$

In the following, superscript * is utilized for variables g, R, $\boldsymbol{p}$, $\boldsymbol{u}$, $\boldsymbol{v}$ in the sense that the tube is in its undeformed reference configuration. Among them, R^* and $\boldsymbol{p}^*$, hence g^* are given as design parameters and the reference kinematic variables $\boldsymbol{u}^*$ and $\boldsymbol{v}^*$ can be then calculated as follows.

$$\begin{bmatrix}\boldsymbol{v}^{*T}(s) & \boldsymbol{u}^{*T}(s)\end{bmatrix}^T = \left(g^{*-1}(s)\dot{g}^*(s)\right)^\vee \tag{III.11}$$

Under the assumption that the $\boldsymbol{x}$ and $\boldsymbol{y}$ axes of $g^*(s)$ are aligned with the main axis of the cross-section, we obtain the linear constitutive law:

$$\begin{aligned} \boldsymbol{n}(s) &= R(s)K_{SE}(s)\left(\boldsymbol{v}(s) - \boldsymbol{v}^*(s)\right) \\ \boldsymbol{m}(s) &= R(s)K_{BT}(s)\left(\boldsymbol{u}(s) - \boldsymbol{u}^*(s)\right) \end{aligned} \tag{III.12}$$

where $K_{SE}(s)$ and $K_{BT}(s)$ are the stiffness matrix for *shear and extension* and for *bending and torsion* respectively.

Approximate the CTR as a multi-stiffness tube

Considering an arbitrary section of the CTR. Assuming that this section has n tubes of the same length. The index $i = \{1, \ldots, n\}$ indicates the order of the tube (from inner to outer tubes). As the tubes are concentric, their final deformed centerlines must be the same, i.e.,

$$\boldsymbol{p}_1(s) = \boldsymbol{p}_2(s) = \ldots = \boldsymbol{p}_n(s) \tag{III.13}$$

Each rotation matrix $R_i(s)$ differs from the others by a rotation about the local tangent z-axis. Then, $R_i(s)$ can be determined by rotating $R_1(s)$ an angle $\theta_i(s)$ about the local z-axis, i.e.,

$$R_i(s) = R_1(s)R_{\theta_i}(s) \tag{III.14}$$

Assuming that there is no external load acting on the CTR, the linear constitutive equations of tube i^{th} are as follows:

$$\begin{aligned} \boldsymbol{n}_i^e(s) &= R_i^e(s)K_{SE_i}(s)\left(\boldsymbol{v}_i^e(s) - \boldsymbol{v}_i^*(s)\right) \\ \boldsymbol{m}_i^e(s) &= R_i^e(s)K_{BT_i}(s)\left(\boldsymbol{u}_i^e(s) - \boldsymbol{u}_i^*(s)\right) \end{aligned} \tag{III.15}$$

Note that the internal force and moment of each tube are generally not zero under the interaction with other tubes. However, the total of them must be equal to zero without any external load acting on the CTR, therefore

$$\begin{aligned} \sum_{i=1}^{n} \boldsymbol{n}_i^e(s) &= 0 \\ \sum_{i=1}^{n} \boldsymbol{m}_i^e(s) &= 0 \end{aligned} \tag{III.16}$$

From (III.14), (III.15), and (III.16), we obtain:

$$\begin{aligned} R_1^e(s) \sum_{i=1}^{n} R_{\theta_i}^e(s)K_{SE_i}(s)\left(\boldsymbol{v}_i^e(s) - \boldsymbol{v}_i^*(s)\right) &= 0 \\ R_1^e(s) \sum_{i=1}^{n} R_{\theta_i}^e(s)K_{BT_i}(s)\left(\boldsymbol{u}_i^e(s) - \boldsymbol{u}_i^*(s)\right) &= 0 \end{aligned} \tag{III.17}$$

Generally, $R_1^e(s) \neq 0$, hence

$$\begin{aligned} \sum_{i=1}^{n} R_{\theta_i}^e(s) K_{SE_i}(s) \left(\boldsymbol{v}_i^e(s) - \boldsymbol{v}_i^*(s)\right) = 0 \\ \sum_{i=1}^{n} R_{\theta_i}^e(s) K_{BT_i}(s) \left(\boldsymbol{u}_i^e(s) - \boldsymbol{u}_i^*(s)\right) = 0 \end{aligned} \tag{III.18}$$

Then, we apply the linear constitutive law for tube i^{th} under loaded

$$\begin{aligned} \boldsymbol{n}_i(s) = R_i(s) K_{SE_i}(s) \left(\boldsymbol{v}_i(s) - \boldsymbol{v}_i^*(s)\right) \\ \boldsymbol{m}_i(s) = R_i(s) K_{BT_i}(s) \left(\boldsymbol{u}_i(s) - \boldsymbol{u}_i^*(s)\right) \end{aligned} \tag{III.19}$$

By noting (III.14), the sum of internal force and moment are given as

$$\begin{aligned} \sum_{i=1}^{n} \boldsymbol{n}_i(s) = R_1(s) \sum_{i=1}^{n} R_{\theta_i}(s) K_{SE_i}(s) \left(\boldsymbol{v}_i(s) - \boldsymbol{v}_i^*(s)\right) \\ \sum_{i=1}^{n} \boldsymbol{m}_i(s) = R_1(s) \sum_{i=1}^{n} R_{\theta_i}(s) K_{BT_i}(s) \left(\boldsymbol{u}_i(s) - \boldsymbol{u}_i^*(s)\right) \end{aligned} \tag{III.20}$$

For purpose of simplicity, character s is removed from (III.21). Noting that $\boldsymbol{v}_i - \boldsymbol{v}_i^* = (\boldsymbol{v}_i - \boldsymbol{v}_i^e) + (\boldsymbol{v}_i^e - \boldsymbol{v}_i^*)$, (III.20) can be rewritten as:

$$\begin{aligned} \sum_{i=1}^{n} \boldsymbol{n}_i = R_1 \sum_{i=1}^{n} R_{\theta_i} K_{SE_i} \left(\boldsymbol{v}_i - \boldsymbol{v}_i^e\right) + R_1 \sum_{i=1}^{n} R_{\theta_i} K_{SE_i} \left(\boldsymbol{v}_i^e - \boldsymbol{v}_i^*\right) \\ \sum_{i=1}^{n} \boldsymbol{m}_i = R_1 \sum_{i=1}^{n} R_{\theta_i} K_{BT_i} \left(\boldsymbol{u}_i - \boldsymbol{u}_i^e\right) + R_1 \sum_{i=1}^{n} R_{\theta_i} K_{BT_i} \left(\boldsymbol{u}_i^e - \boldsymbol{u}_i^*\right) \end{aligned} \tag{III.21}$$

Considering the assumptions ii. and iii., we obtain the following relation for all tubes

$$R_{\theta_i} = R_{\theta_i}^e \tag{III.22}$$

Substituting (III.18) and (III.22) into (III.21) yields

$$\begin{aligned} \sum_{i=1}^{n} \boldsymbol{n}_i = R_1 \sum_{i=1}^{n} R_{\theta_i}^e K_{SE_i} \left(\boldsymbol{v}_i - \boldsymbol{v}_i^e\right) = R_1 \sum_{i=1}^{n} R_{\theta_i}^e K_{SE_i} \Delta \boldsymbol{v}_i \\ \sum_{i=1}^{n} \boldsymbol{m}_i = R_1 \sum_{i=1}^{n} R_{\theta_i}^e K_{BT_i} \left(\boldsymbol{u}_i - \boldsymbol{u}_i^e\right) = R_1 \sum_{i=1}^{n} R_{\theta_i}^e K_{BT_i} \Delta \boldsymbol{u}_i \end{aligned} \tag{III.23}$$

where $\Delta \boldsymbol{v}_i$ and $\Delta \boldsymbol{u}_i$ respectively represent the variations of $\boldsymbol{v}_i$ and $\boldsymbol{u}_i$ without and with external loads. As there is no torsion of each tube in the considered CTR (assumption ii.) and as the cross-sections of the tubes are circular, it is easy to see that rotating any tube except the innermost one, at the end of which the tendon is attached, will not change the method of resolution of the studied problem (the deformation of the CTR under the tendon load). Without loss of generality, we

assume that each tube $i = \{2, \ldots, N\}$ is rotated so that θ_i is a multiple of 2π (note that $\theta_1 = 0$). We then have

$$\begin{aligned} \sum_{i=1}^{n} \boldsymbol{n}_i &= R_1 \sum_{i=1}^{n} K_{SE_i} \Delta \boldsymbol{v}_i \\ \sum_{i=1}^{n} \boldsymbol{m}_i &= R_1 \sum_{i=1}^{n} K_{BT_i} \Delta \boldsymbol{u}_i \end{aligned} \tag{III.24}$$

As the tubes are concentric, their bending curvatures must be the same, thus

$$\Delta \boldsymbol{u}_1 = \ldots = \Delta \boldsymbol{u}_i = \ldots = \Delta \boldsymbol{u}_n \tag{III.25}$$

The constitutive law for bending and torsion of the tubes can be rewritten as

$$\sum_{i=1}^{n} \boldsymbol{m}_i = R_1 K_{BT} \Delta \boldsymbol{u}_1 \tag{III.26}$$

where $K_{BT} = \sum_{i=1}^{n} K_{BT_i}$. We expect to obtain a similar form for the constitutive equation of shearing and extension. However, this is not a straightforward task because the term $\Delta \boldsymbol{v}_i$ varies among the tubes. But, the shearing and extension effect of the CTR can be considered as extremely small ($\boldsymbol{v}_i \approx \boldsymbol{v}_i^* = [0, 0, 1]^T$) and are usually neglected in some models in the literature [Rucker 10a, Rucker 10b]. This allows us to consider that the $\Delta \boldsymbol{v}_i$ (i.e., $\boldsymbol{v}_i - \boldsymbol{v}_i^e$) are the same among the tubes for the purpose of simplifying the model. Then, we can write:

$$\sum_{i=1}^{n} \boldsymbol{n}_i = R_1 K_{SE} \Delta \boldsymbol{v}_1 \tag{III.27}$$

where $K_{SE} = \sum_{i=1}^{n} K_{SE_i}$. It is necessary to note that we employ the Cosserat rod model ($\Delta \boldsymbol{v}_i \neq 0$) and neglect the error caused by considering equation (III.27) instead of using the Kirchhoff rod model ($\Delta \boldsymbol{v}_i = 0$) as we expect to apply the proposed model to elastic tubes of soft material and for large deformations that will be discussed later in this section. These tubes are obtained by 3D printing method.

On another aspect, by taking derivative of the internal efforts for a finite section, similarly to (III.9) and (III.10), we can infer the following differential equations

$$\sum_{i=1}^{n} \dot{\boldsymbol{n}}_i + \boldsymbol{f} = 0 \tag{III.28}$$

$$\sum_{i=1}^{n} \dot{\boldsymbol{m}}_i + \sum_{i=1}^{n} (\dot{\boldsymbol{p}}_i \times \boldsymbol{n}_i) + \boldsymbol{l} = 0 \tag{III.29}$$

where $\boldsymbol{f}$ and $\boldsymbol{l}$ are the total distributed force and moment acting on the CTR. Note that $\dot{\boldsymbol{p}}_i$ are the same for all tubes, we can rewrite these equations as follows

$$\sum_{i=1}^{n} \dot{\boldsymbol{n}}_i = -\boldsymbol{f} \tag{III.30}$$

$$\sum_{i=1}^{n} \dot{\boldsymbol{m}}_i = -\dot{\boldsymbol{p}}_1 \times \sum_{i=1}^{n} \boldsymbol{n}_i - \boldsymbol{l} \tag{III.31}$$

Considering the innermost tube, we have the following equations

$$\dot{\boldsymbol{p}_1} = R_1 \boldsymbol{v}_1 \tag{III.32}$$

$$\dot{R}_1 = R_1 \hat{\boldsymbol{u}}_1 \tag{III.33}$$

By unifying:

- the differential equations (III.32), (III.33), (III.30) and (III.11) with (III.7), (III.8), (III.9) and (III.10) respectively,
- the system of equations (III.27) and (III.26) with the constitutive equations (III.12),

we can see the CTR as equivalent to an elastic tube of multi-stiffness segments. Indeed, this equivalent elastic tube has the kinematic variables $(\boldsymbol{p}, R, \boldsymbol{v}, \boldsymbol{u})$ that are the same with the corresponding variables of the innermost tube

$$\boldsymbol{p} = \boldsymbol{p}_1,\ R = R_1,\ \boldsymbol{u} = \boldsymbol{u}_1,\ \boldsymbol{v} = \boldsymbol{v}_1 \tag{III.34}$$

Besides, the undeformed reference configuration of the equivalent tube is equal to the equilibrium concentric configuration of the innermost tube of the CTR without any external loads.

$$\boldsymbol{p}^* = \boldsymbol{p}_1^e,\ R^* = R_1^e,\ \boldsymbol{u}^* = \boldsymbol{u}_1^e,\ \boldsymbol{v}^* = \boldsymbol{v}_1^e \tag{III.35}$$

Furthermore, its internal force $\boldsymbol{n}$, internal moment $\boldsymbol{m}$, shearing/extension stiffness matrix K_{SE}, and bending/torsion stiffness matrix K_{BT} are the sums of the corresponding quantities of the tubes appearing in the considered cross-section (at the arclength s).

$$\boldsymbol{n} = \sum_{i=1}^{n} \boldsymbol{n}_i \tag{III.36}$$

$$\boldsymbol{m} = \sum_{i=1}^{n} \boldsymbol{m}_i \tag{III.37}$$

$$K_{SE} = \sum_{i=1}^{n} K_{SE_i} \tag{III.38}$$

$$K_{BT} = \sum_{i=1}^{n} K_{BT_i} \tag{III.39}$$

After unifying, the equilibrium differential equations and the constitutive law of the equivalent tube are given as in (III.7)-(III.10) and in (III.12), respectively. Under the assumption of constant stiffness matrices (with respect to s) for the considered tube section, one can derive the following differential equations:

$$\begin{aligned}
\dot{\boldsymbol{p}} &= R\boldsymbol{v} \\
\dot{R} &= R\hat{\boldsymbol{u}} \\
\dot{\boldsymbol{v}} &= \dot{\boldsymbol{v}}^* - K_{SE}^{-1}\left(\hat{\boldsymbol{u}}K_{SE}\left(\boldsymbol{v}-\boldsymbol{v}^*\right) + R^T\boldsymbol{f}\right) \\
\dot{\boldsymbol{u}} &= \dot{\boldsymbol{u}}^* - K_{BT}^{-1}\left(\hat{\boldsymbol{u}}K_{BT}\left(\boldsymbol{u}-\boldsymbol{u}^*\right) + \hat{\boldsymbol{v}}K_{SE}\left(\boldsymbol{v}-\boldsymbol{v}^*\right) + R^T\boldsymbol{l}\right)
\end{aligned} \tag{III.40}$$

The above equation system illustrates how the robot shape depends on the distributed force $\boldsymbol{f}$ and moment $\boldsymbol{l}$. The following part of this subsection will present a method to formulate these loads using the kinematics variables of the tube. Thus, we can establish the governing equations for solving the tube's kinematics.

Tendon as a string model

To investigate the tendon distributed loads, we use the approach proposed in [Rucker 11a] that considers the tendon as an ideal string model. In coordinates of the body frame $g(s)$, the tendon location within the robot cross-section can be considered as follows:

$$\boldsymbol{r}_s(s) = \begin{bmatrix} x_s(s) & y_s(s) & 0 \end{bmatrix}^T \tag{III.41}$$

In the global frame, the tendon can be described by a parametric space curve:

$$\boldsymbol{p}_s = R\boldsymbol{r}_s + \boldsymbol{p} \tag{III.42}$$

If the distributed force $\boldsymbol{f}_s$ applied to the tendon per unit of s is Lebesgue-integrable, by taking derivative of the static equilibrium conditions for a finite section, we obtain the differential equation for the statics of the extensible string:

$$\dot{\boldsymbol{n}}_s + \boldsymbol{f}_s = 0 \tag{III.43}$$

where $\boldsymbol{n}_s$ is the internal force in the tendon. Under the frictionless assumption, the tension is considered to be constant along the tendon length and denoted by τ. Hence, the internal force is consistently tangent to the tendon path, we then have

$$\boldsymbol{n}_s = \tau \frac{\dot{\boldsymbol{p}}_s}{\|\dot{\boldsymbol{p}}_s\|} \tag{III.44}$$

We rewrite (III.43) by taking the derivative of (III.44), the calculation is detailed in [Rucker 11a]

$$\boldsymbol{f}_s = -\dot{\boldsymbol{n}}_s = \tau \frac{\left(\hat{\dot{\boldsymbol{p}}}_s\right)^2}{\|\dot{\boldsymbol{p}}_s\|^3}\ddot{\boldsymbol{p}}_s \tag{III.45}$$

Distributed load on the tube

The distributed loads on the tube $\boldsymbol{f}$ and $\boldsymbol{l}$ can be separated into the distributed loads by the tendon $\boldsymbol{f}_t$ and $\boldsymbol{l}_t$ and the other external interactions $\boldsymbol{f}_g$ and $\boldsymbol{l}_g$ (e.g., the tube weight) on the active length from the base to the tip:

$$\begin{aligned} \boldsymbol{f} &= \boldsymbol{f}_t + \boldsymbol{f}_g \\ \boldsymbol{l} &= \boldsymbol{l}_t + \boldsymbol{l}_g \end{aligned} \tag{III.46}$$

The distributed force that the tendon applies on the tube is equal and opposite to the distributed force on the tendon as given in (III.45), then

$$\boldsymbol{f}_t = -\boldsymbol{f}_s = -\tau \frac{\left(\hat{\dot{\boldsymbol{p}}}_s(s)\right)^2}{\|\dot{\boldsymbol{p}}_s\|^3} \ddot{\boldsymbol{p}}_s \tag{III.47}$$

The distributed moment at the tube centroid can be determined by the cross products of the moment arm and the tendon distributed force. We have

$$\boldsymbol{l}_t = -\left(\boldsymbol{p}_s - \boldsymbol{p}\right) \times \boldsymbol{f}_s = -\tau \left(R\boldsymbol{r}_s\right)^{\wedge} \frac{\hat{\dot{\boldsymbol{p}}}_s^2}{\|\dot{\boldsymbol{p}}_s\|^3} \ddot{\boldsymbol{p}}_s \tag{III.48}$$

To obtain $\dot{\boldsymbol{p}}_s$ and $\ddot{\boldsymbol{p}}_s$, we derive twice the expression (III.42) and consider the anticommutative of cross product:

$$\begin{aligned} \dot{\boldsymbol{p}}_s &= R\left(\hat{\boldsymbol{u}}\boldsymbol{r}_s + \dot{\boldsymbol{r}}_s + \boldsymbol{v}\right) \\ \ddot{\boldsymbol{p}}_s &= R\left(\hat{\boldsymbol{u}}\left(\hat{\boldsymbol{u}}\boldsymbol{r}_s + 2\dot{\boldsymbol{r}}_s + \boldsymbol{v}\right) + \ddot{\boldsymbol{r}}_s + \dot{\boldsymbol{v}} - \hat{\boldsymbol{r}}_s\dot{\boldsymbol{u}}\right) \end{aligned} \tag{III.49}$$

We can write (III.49) in body-frame coordinates, i.e.,

$$\begin{aligned} \dot{\boldsymbol{p}}_s^b &= \hat{\boldsymbol{u}}\boldsymbol{r}_s + \dot{\boldsymbol{r}}_s + \boldsymbol{v} \\ \ddot{\boldsymbol{p}}_s^b &= \hat{\boldsymbol{u}}\left(\hat{\boldsymbol{u}}\boldsymbol{r}_s + 2\dot{\boldsymbol{r}}_s + \boldsymbol{v}\right) + \ddot{\boldsymbol{r}}_s + \dot{\boldsymbol{v}} - \hat{\boldsymbol{r}}_s\dot{\boldsymbol{u}} \end{aligned} \tag{III.50}$$

By substituting (III.50) to (III.47)-(III.48) via (III.49) and utilizing Lemma 2.1. in [Murray 94], we find

$$\begin{aligned} \boldsymbol{f}_t &= -R\tau \left(\hat{\dot{\boldsymbol{p}}}_s^b\right)^2 \left\|\dot{\boldsymbol{p}}_s^b\right\|^{-3} \ddot{\boldsymbol{p}}_s^b \\ \boldsymbol{l}_t &= -R\hat{\boldsymbol{r}}_s\tau \left(\hat{\dot{\boldsymbol{p}}}_s^b\right)^2 \left\|\dot{\boldsymbol{p}}_s^b\right\|^{-3} \ddot{\boldsymbol{p}}_s^b \end{aligned} \tag{III.51}$$

To simplify the preceding expressions, we now define matrix A and vector $\boldsymbol{b}$ as follows:

$$A = -\tau \left(\hat{\dot{\boldsymbol{p}}}_s^b\right)^2 \left\|\dot{\boldsymbol{p}}_s^b\right\|^{-3}, \quad \boldsymbol{b} = \hat{\boldsymbol{u}}\left(\hat{\boldsymbol{u}}\boldsymbol{r}_s + 2\dot{\boldsymbol{r}}_s + \boldsymbol{v}\right) + \ddot{\boldsymbol{r}}_s \tag{III.52}$$

The equations (III.51) can be rewritten as

$$\begin{aligned} \boldsymbol{f}_t &= RA\left(\boldsymbol{b} + \dot{\boldsymbol{v}} - \hat{\boldsymbol{r}}_s\dot{\boldsymbol{u}}\right) \\ \boldsymbol{l}_t &= R\hat{\boldsymbol{r}}_s A\left(\boldsymbol{b} + \dot{\boldsymbol{v}} - \hat{\boldsymbol{r}}_s\dot{\boldsymbol{u}}\right) \end{aligned} \tag{III.53}$$

The governing differential equations for the coupled rod and string model obtained by substituting (III.53) to (III.40) via (III.46) seem to be in an implicit form as $\boldsymbol{f}_t$ and $\boldsymbol{l}_t$ depend on $\dot{\boldsymbol{u}}$ and $\dot{\boldsymbol{v}}$. Fortunately, the linear relation in (III.53) let us write them explicitly. We then derive the the model equations:

$$\dot{\boldsymbol{p}} = R\boldsymbol{v} \tag{III.54a}$$

$$\dot{R} = R\hat{\boldsymbol{u}} \tag{III.54b}$$

$$\begin{bmatrix} \dot{\boldsymbol{v}} \\ \dot{\boldsymbol{u}} \end{bmatrix} = \begin{bmatrix} (K_{SE} + A) & -A\hat{\boldsymbol{r}}_s \\ \hat{\boldsymbol{r}}_s A & (K_{BT} - \hat{\boldsymbol{r}}_s A \hat{\boldsymbol{r}}_s) \end{bmatrix}^{-1} \begin{bmatrix} \boldsymbol{c} \\ \boldsymbol{d} \end{bmatrix} \tag{III.54c}$$

where

$$\begin{aligned} \boldsymbol{c} &= K_{SE}\dot{\boldsymbol{v}}^* - \hat{\boldsymbol{u}}K_{SE}\left(\boldsymbol{v} - \boldsymbol{v}^*\right) - A\boldsymbol{b} - R^T\boldsymbol{f}_g \\ \boldsymbol{d} &= K_{BT}\dot{\boldsymbol{u}}^* - \hat{\boldsymbol{u}}K_{BT}\left(\boldsymbol{u} - \boldsymbol{u}^*\right) \\ &\quad -\hat{\boldsymbol{v}}K_{SE}\left(\boldsymbol{v} - \boldsymbol{v}^*\right) - \hat{\boldsymbol{r}}_s A\boldsymbol{b} - R^T\boldsymbol{l}_g \end{aligned}$$

Boundary Conditions

By choosing the global coordinate frame at the base, then:

$$\boldsymbol{p}(s=0) = \begin{bmatrix} 0 & 0 & 0 \end{bmatrix}^T, \quad R(s=0) = I_{3\times 3} \tag{III.55}$$

The tendon terminates at the tip and applies on it a point force and a point moment vectors, we then obtain the following conditions:

$$\boldsymbol{n}(\mathrm{l}) = \boldsymbol{F}_{tip}, \quad \boldsymbol{m}(\mathrm{l}) = \boldsymbol{L}_{tip} \tag{III.56}$$

The point force is equal and opposite to the internal force in the tendon $\boldsymbol{n}_s(s)$ given by (III.44) and creates the point moment with a moment arm of $(\boldsymbol{p}_s(\mathrm{l}) - \boldsymbol{p}(\mathrm{l}))$. By noting (III.42) and (III.49), we obtain

$$\begin{aligned} \boldsymbol{F}_{tip} &= -\tau \frac{R(\mathrm{l})\left(\hat{\boldsymbol{u}}(\mathrm{l})\boldsymbol{r}_s(\mathrm{l}) + \dot{\boldsymbol{r}}_s(\mathrm{l}) + \boldsymbol{v}(\mathrm{l})\right)}{\left\|R(\mathrm{l})\left(\hat{\boldsymbol{u}}(\mathrm{l})\boldsymbol{r}_s(\mathrm{l}) + \dot{\boldsymbol{r}}_s(\mathrm{l}) + \boldsymbol{v}(\mathrm{l})\right)\right\|} \\ \boldsymbol{L}_{tip} &= -\tau \left(R(\mathrm{l})\boldsymbol{r}_s(\mathrm{l})\right)^{\wedge} \frac{R(\mathrm{l})\left(\hat{\boldsymbol{u}}(\mathrm{l})\boldsymbol{r}_s(\mathrm{l}) + \dot{\boldsymbol{r}}_s(\mathrm{l}) + \boldsymbol{v}(\mathrm{l})\right)}{\left\|R(\mathrm{l})\left(\hat{\boldsymbol{u}}(\mathrm{l})\boldsymbol{r}_s(\mathrm{l}) + \dot{\boldsymbol{r}}_s(\mathrm{l}) + \boldsymbol{v}(\mathrm{l})\right)\right\|} \end{aligned} \tag{III.57}$$

Substituting (III.56) to (III.12) via (III.57), and then simplifying $R(l)$ on both sides of the results by using the property of rotation transformation that preserves the length of vector and Lemma 2.1. in [Murray 94], we then have :

$$\begin{aligned} K_{SE}\left(\boldsymbol{v}(\mathrm{l}) - \boldsymbol{v}^*(\mathrm{l})\right) &= -\tau \frac{\hat{\boldsymbol{u}}(\mathrm{l})\boldsymbol{r}_s(\mathrm{l}) + \dot{\boldsymbol{r}}_s(\mathrm{l}) + \boldsymbol{v}(\mathrm{l})}{\left\|\hat{\boldsymbol{u}}(\mathrm{l})\boldsymbol{r}_s(\mathrm{l}) + \dot{\boldsymbol{r}}_s(\mathrm{l}) + \boldsymbol{v}(\mathrm{l})\right\|} \\ K_{BT}\left(\boldsymbol{u}(\mathrm{l}) - \boldsymbol{u}^*(\mathrm{l})\right) &= -\tau\hat{\boldsymbol{r}}_s(\mathrm{l}) \frac{\hat{\boldsymbol{u}}(\mathrm{l})\boldsymbol{r}_s(\mathrm{l}) + \dot{\boldsymbol{r}}_s(\mathrm{l}) + \boldsymbol{v}(\mathrm{l})}{\left\|\hat{\boldsymbol{u}}(\mathrm{l})\boldsymbol{r}_s(\mathrm{l}) + \dot{\boldsymbol{r}}_s(\mathrm{l}) + \boldsymbol{v}(\mathrm{l})\right\|} \end{aligned} \tag{III.58}$$

The second equation can be simplified as follows

$$K_{BT}\left(\boldsymbol{u}(\mathrm{l})-\boldsymbol{u}^{*}(\mathrm{l})\right)=\hat{\boldsymbol{r}}_{s}(\mathrm{l})K_{SE}\left(\boldsymbol{v}(\mathrm{l})-\boldsymbol{v}^{*}(\mathrm{l})\right) \tag{III.59}$$

As a remark, for a given tendon location $\boldsymbol{r}_s(s)$, the system of equations (III.58) has the basic form $F\left(\boldsymbol{u}(\mathrm{l}),\boldsymbol{v}(\mathrm{l})\right)=0$ and can be numerically solved using the Newton-Raphson method [Ben-Israel 66]. Furthermore, at each section transition, we consider the continuous condition for $\boldsymbol{p}$ and R

$$\begin{aligned}\boldsymbol{p}(\sigma^{+})&=\boldsymbol{p}(\sigma^{-})\\ R(\sigma^{+})&=R(\sigma^{-})\end{aligned} \tag{III.60}$$

where σ^+ and σ^- denote locations just before and just after the section transitions. Except for the point load at the tube tip, if there is no point force $\boldsymbol{F}(\sigma)$ as well as point moment $\boldsymbol{L}(\sigma)$ applied to the tube along its length, we have the continuous conditions of the internal force and moment.

$$\begin{aligned}\boldsymbol{n}(\sigma^{+})&=\boldsymbol{n}(\sigma^{-})\\ \boldsymbol{m}(\sigma^{+})&=\boldsymbol{m}(\sigma^{-})\end{aligned} \tag{III.61}$$

Then, the studied model as given in (III.54) becomes a two point boundary value problem with the boundary conditions at the base for $\boldsymbol{p}(0)$, $R(0)$ as shown in (III.55) and at the tip for $\boldsymbol{v}(\mathrm{l})$, $\boldsymbol{u}(\mathrm{l})$ as detailed in (III.58). The solution is only found with the knowledge of the tendon location $\boldsymbol{r}_s(s)$ and its derivatives. As mentioned, the tight tendon inside the tube describes the shortest path connecting the two location points (at the base and at the tip). The following subsection will present the searching algorithm for the shortest path inside a general tubular space.

III.2.2.c Tendon location - the ESP in a tubular space

In this part, the internal space of the tube is considered as a given tubular space and a novel algorithm is proposed for searching the shortest path between two points within this space. To numerically solve the problem, the tubular space is converted into a series of meshed circular disks from S_0 (at the base) to S_{N+1} (at the tip) as shown in figure III.4. The source $\mathfrak{P}$ and the destination $\mathfrak{Q}$ are the two location points of the tendon at the base and at the tip. As the shortest path from the source to the destination must obviously pass through each cross-section at only one point, we have the weighted directed graph $G(V,A)$ as shown in Fig. III.4. This directed graph is defined by a finite set V of *vertices* and a set A of *arcs* between those vertices. All vertices of the graph (except $\mathfrak{P}$ and $\mathfrak{Q}$) are located at the nodes of the meshed disks $S_1,...,S_N$. Every two adjacent nodes (connected by one arc) in the graph are belong to two consecutive disks. The source $\mathfrak{P}$ is connected with all nodes of disk S_1. Each node of disk S_i is connected by one arc to every node of disk S_{i+1} for all $i\in\{1,...,N-1\}$. Eventually, every node of disk S_N is connected directly to the destination $\mathfrak{Q}$.

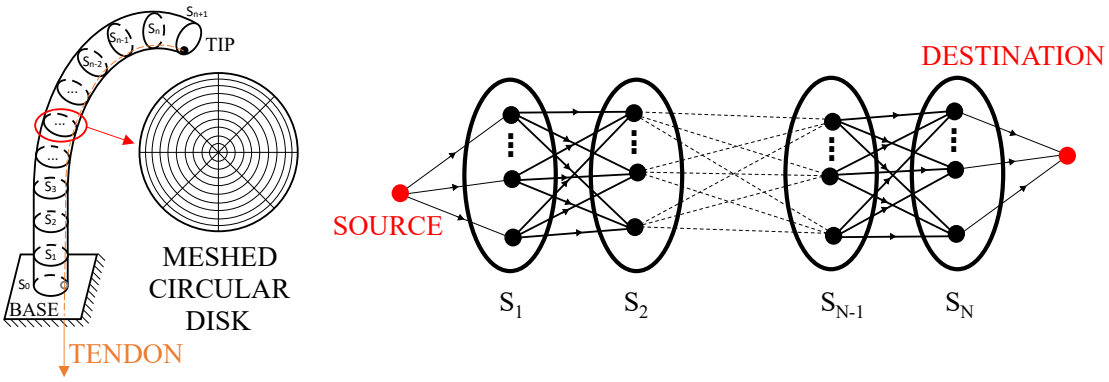

FIGURE III.4 – Discrete approach for the ESP problem. (Left): Inner space of the tube transformed into a series of meshed circular disks and (Right): the directed graph [Nguyen 22].

Many methods can be applied to determine the shortest path between two points in the weighted graph. Some of the most common algorithms can be found in the literature are Dijkstra's algorithm [Dijkstra 59] and A^* algorithm [Hart 68]. However, these methods do not consider the distinctive geometric properties of the tubular space which can be utilized to reduce the computation time. Hence, we proposed in [Nguyen 22] a novel algorithm for solving this problem by taking into account the geometry of a tube portion that can be seen by a virtual particle (VP) moving along the tendon path that allows a fast computation speed in comparison with Dijkstra's algorithm. The proposed method was detailed in [Nguyen 22]. For convenience, we provide hereinafter a brief overview of this method to complete this subsection.

With this method, the ESP will be gradually figure out by determining the correct moving direction of the particle from the source $\mathfrak{P}$ to the destination $\mathfrak{Q}$. Based on the geometric properties of the tubular space, the ESP inside a tubular space a can be divided into three partitions as given in Remark 1.

Remark 1. *For any type of tubular space, the searching shortest path* $\boldsymbol{p}(s)$ *can be segmented into three partitions:*

- Partition 1 (**P1**) : *Includes points that can see the destination* $\mathfrak{Q}$*. The direction* $\dot{\boldsymbol{p}}_s(s)$ *at any point in this partition is always towards* $\mathfrak{Q}$*.*
- Partition 2 (**P2**) : *Includes points that can see the ending cross-section* S_{N+1}*, but cannot see* $\mathfrak{Q}$*. The direction* $\dot{\boldsymbol{p}}_s(s)$ *at any point* $\boldsymbol{X}$ *in this partition is always towards a visible point* $\boldsymbol{Y}$ *in the ending cross-section such that the angle between* $\boldsymbol{XY}$ *and* $\boldsymbol{X\mathfrak{Q}}$ *is the smallest one.*
- Partition 3 (**P3**) : *Includes points that cannot see the ending cross-section* S_{N+1}*. The direction of* $\dot{\boldsymbol{p}}_s(s)$ *at any point in this partition is the positive direction corresponding to the longest-length-of-sight.*

For every point $\boldsymbol{X}$ inside the tubular space, the cross-section containing it divides the tube into 2 sub-spaces, a direction from $\boldsymbol{X}$ is said to be positive (+) if it is towards the sub-space containing the destination. The algorithm for finding the ESP within the tubular space is based on Remark 1 as illustrated in figure III.5 [Nguyen 22].

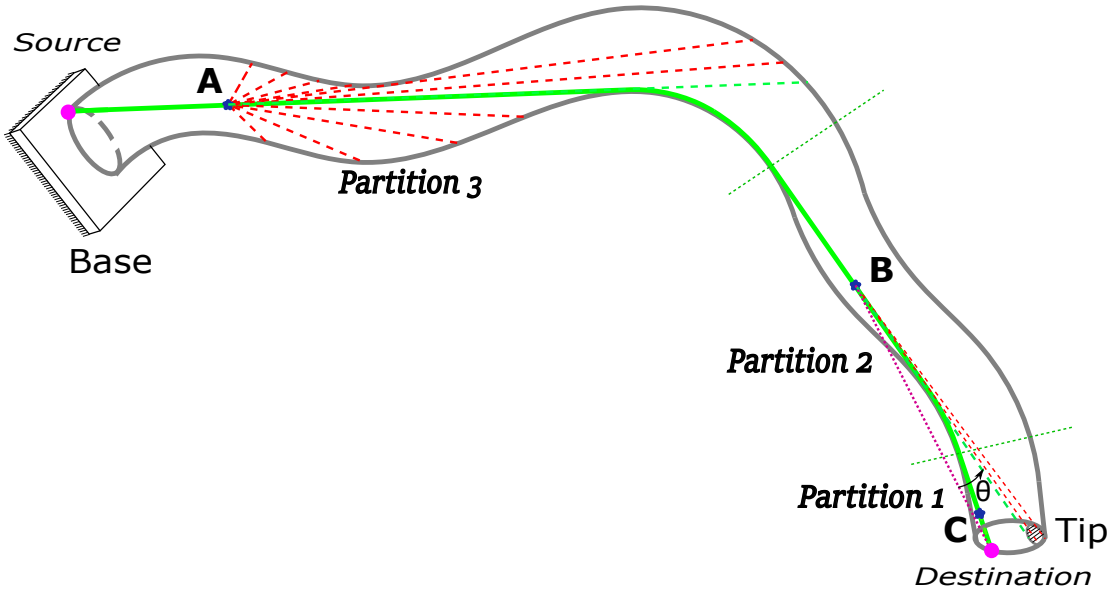

FIGURE III.5 – Three partitions of the shortest path inside the tubular space. At $\boldsymbol{A}$ belonging to **P3**, the VP cannot see the ending cross-section S_{N+1}. The correct direction corresponds to the longest-length-of-sight. At $\boldsymbol{B}$ belonging to **P2**, it can see S_{N+1}, but not $\boldsymbol{\Omega}$. The correct direction is towards the visible point $\boldsymbol{Y}$ in S_{N+1} so that the angle θ between $\boldsymbol{BY}$ and $\boldsymbol{B\Omega}$ is the smallest one. At $\boldsymbol{C}$ in **P1**, the particle can see $\boldsymbol{\Omega}$. The correct direction is towards $\boldsymbol{\Omega}$ [Nguyen 22].

Besides the length, the smoothness of the obtained shortest path is important as the derivatives of this path with respect to the arc length s of the tube is required for the established equations of the model. Unlike conventional graph-based methods (e.g. Dijkstra's searching algorithm) in which the shortest path is made up of the graph nodes, the proposed method allows finding each correct point on the ESP by determining the intersection point between the exact moving direction and the next cross-section. This intersection point is not necessary a node of the mesh and leads to a smoother and shorter solution than one by Dijkstra's algorithm.

So far, we have independently derived two problems: the two points BVP to formulate the deformation of the tube under the tendon loads and the ESP problem to describe the tendon location inside the tube. However, to solve each of these problems, the solution of the other is always required beforehand. This leads to a very hard question about dealing with these two problems at the same time. In the following, a solver will be proposed for the global coupled problem between the tube deformation and the tendon location.

III.2.2.d Global solver

In this part, the differential equations (III.54) of the BVP (*Problem A*) must be solved simultaneously with the ESP problem (*Problem B*). As mentioned, the result of *Problem A* is the input of *Problem B* and vice versa. For the purpose of convenience, we define four following groups of quantities: 1) the tube kinematics $\mathrm{H} = \{\boldsymbol{p},\ R,\ \boldsymbol{u},\ \boldsymbol{v}\}$, 2) the set of constant values and matrices of the tube $\mathrm{K} = \{D_i,\ D_o,\ K_{SE},\ K_{BT}\}$ where $D_i,\ D_o$ are the inner and outer diameters of the tube, 3) the tendon location parameter on the body frame $\Psi = \{\boldsymbol{r}_s,\ \dot{\boldsymbol{r}}_s,\ \ddot{\boldsymbol{r}}_s\}$ for the entire tendon length, and 4) the inputs of the main problem $\mathrm{W} = \{\tau,\ \boldsymbol{f}_g,\ \boldsymbol{l}_g,\ \mathfrak{P},\ \mathfrak{Q}\}$ where $\mathfrak{P} = \boldsymbol{r}_s(0)$ and $\mathfrak{Q} = \boldsymbol{r}_s(l)$. The problem is then reformulated as follows:

- Given H^* and K
- Input W
- Determine H and Ψ satisfying *Problem A* and *B* simultaneously.

As we do not have any formula expression to describe *Problem B*, which is only solved by employing the searching algorithm, forming the explicit system of equations for the unknowns H and Ψ simultaneously is an extremely difficult task. We therefore propose in this work a guessing method for the solution H and Ψ of the two *Problem A* and *B* by iteratively updating the quasi-solutions of each problem until the residual errors are satisfied within specified tolerances.

Quasi-solve *Problem A*

We now find the quasi-solution H of *Problem A* corresponding to a given value of Ψ (e.g., from the result of *Problem B*). Many standard numerical method can be utilized to solve the BVP of the form $\dot{\boldsymbol{y}} = f(s, \boldsymbol{y})$ such as shooting and finite difference methods [Keller 18]. We employ in this subsection a shooting method to iteratively solve for the unknown $\boldsymbol{\chi} = [\boldsymbol{v}^T(0),\ \boldsymbol{u}^T(0)]^T$ and subject to the boundary conditions given in (III.55) and (III.58). This method is favorable because of accuracy, generality, and robustness.

Algorithm 1 Calculate Jacobian Matrix

1: Given the current $\boldsymbol{\chi}$
2: Integrate the IVP along the rod from base to tip
3: Calculate the current distal error vector $\boldsymbol{F}$
   As $\boldsymbol{\chi}$ *is a vector of 6 elements:* $[\chi_1, \chi_2, \chi_3, \chi_4, \chi_5, \chi_6]^T$
4: **for** $i = 1$ to 6 **do**
5: Update χ_i by $\chi_i + \Delta$ to obtain $\boldsymbol{\chi}_{new}$
6: Integrate the IVP along the rod from base to tip
7: Calculate the new distal error vector $\boldsymbol{F}_{new}$
8: Column i of the Jacobian matrix: $\boldsymbol{J}_i \approx \frac{\boldsymbol{F}_{new} - \boldsymbol{F}}{\Delta}$
9: Update χ_i by $\chi_i - \Delta$ for the next iteration
10: **end for**

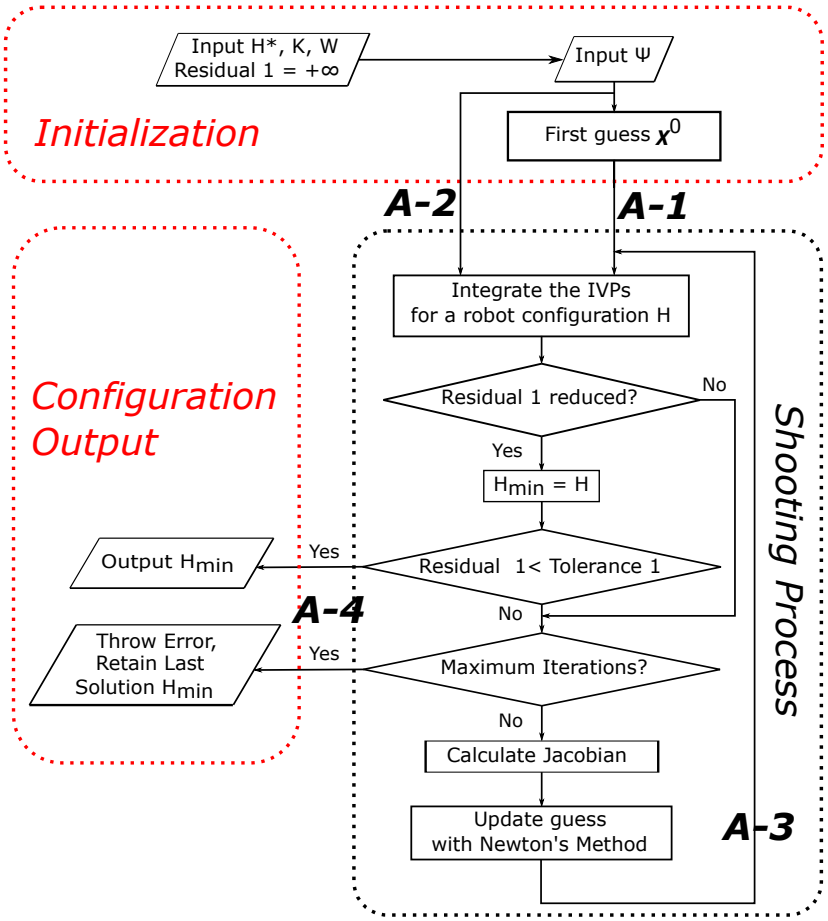

FIGURE III.6 – Shooting method to solve the BVP for the robot configuration H corresponding to a given value of tendon location parameter Ψ.

It iteratively guesses $\boldsymbol{\chi}$ to have the entire set of initial values H(0) at the base, integrates the initial value problem (IVP) (III.54) by using accurate explicit numerical integration schemes, and evaluates the set of boundary conditions at the distal end (III.58). The guess is updated by using Newton's method [Kelley 03]:

$$\boldsymbol{\chi}^{\eta+1} = \boldsymbol{\chi}^{\eta} - J_{\eta}^{-1}\boldsymbol{F}^{\eta} \tag{III.62}$$

where η is the iteration index, $\boldsymbol{F}$ is the system of error functions at the distal end (derived by converting the equations (III.58) to the form $\boldsymbol{F}(\boldsymbol{u}(\mathrm{l}), \boldsymbol{v}(\mathrm{l})) = 0$), $J = \partial\boldsymbol{F}/\partial\boldsymbol{\chi}$ is Jacobian matrix of this system that will be numerically calculated via finite differences as illustrated in Algorithm 1. The value of $\boldsymbol{\chi}$ will be updated by equation (III.62) until the residual value is satisfied within a specified tolerance. Alternatively, if the tolerance within the maximum iterations is not satisfied, the program will retain the last successful solution corresponding to the minimum residual value obtained to guarantee that the algorithm terminates within a finite time. As shown in Fig. III.6, the algorithm returns to a configuration H of the tube that minimizes the residual value and subjects to the given tendon parameter Ψ. The distal errors $\boldsymbol{F}$ contains three force components $\boldsymbol{F}_n = [F_1, F_2, F_3]^T$

and three torque components $\boldsymbol{F}_m = [F_4, F_5, F_6]^T$, we then choose **Residual 1** $= \frac{D_i}{2}\|\boldsymbol{F}_n\| + \|\boldsymbol{F}_m\|$ to make sure that $\boldsymbol{F}$ tends toward 0. In our implementation, the residual must be less than 1e-12 Newtons-meters (**Tolerance 1**) to satisfy the termination criteria.

Quasi-solve *Problem B*

Assuming that we somehow have a tube kinematics H. Generally, H is not the global solution of the main problem. Indeed, the tendon location parameter Ψ corresponding to H can be quickly obtained by employing the proposed method for the ESP problem. Nevertheless, because of the tendon load on the tube, the combination (Ψ & H) is not fixed. Indeed, if we use H(0) and integrate the equations (III.54) by taking into account Ψ, we will find a new configuration H_{new} of the tube. Again, if we resolve the ESP problem using H_{new}, we will obtain a new tendon location parameter Ψ_{new}. In general, Ψ_{new} will be different from Ψ. If we continue this process, it will recur an infinite number of times.

$$\mathrm{H}(0)\ \&\ \Psi \xrightarrow[\text{solved}]{\text{IVP}} \mathrm{H}_{new} \xrightarrow[\text{solved}]{\text{ESP}} \Psi_{new} \xrightarrow[\text{solved}]{\text{IVP}} \mathrm{H}^1_{new} \xrightarrow[\cdots]{} \tag{III.63}$$

Thus, instead of solving the ESP problem for just a given tube kinematics H (using the proposed algorithm), we will try to find the solution of *Problem B* corresponding to a given value of H(0) as the fixed "point" $\bar{\Psi}$ of the process (III.63), that is: $\bar{\Psi}_{new} = \bar{\Psi}$, thus $\bar{\mathrm{H}}^1_{new} = \bar{\mathrm{H}}_{new}$. Nevertheless, finding the exact value of $\bar{\Psi}$ is almost impossible. Hence, Ψ is said to be the quasi-solution of *Problem B* that corresponds to a given value of H(0), if after the process (III.63), the residual errors $(\Psi_{new} - \Psi)$ and $(\mathrm{H}^1_{new} - \mathrm{H}_{new})$ are satisfied within specified tolerances (see Fig. III.7). In other words, the combination (Ψ & H_{new}) is a nearly fixed state corresponding to the given H(0).

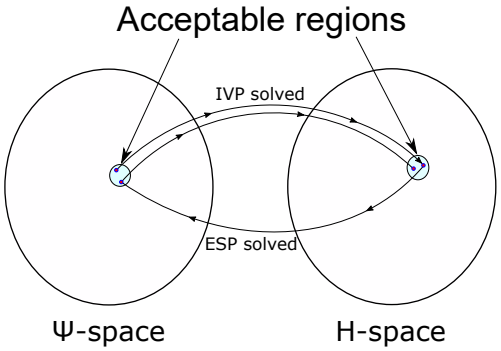

FIGURE III.7 – The quasi-solution of Ψ results in the residual errors satisfied within the corresponding acceptable regions.

Theoretically, if Ψ and H are considered as discrete quantities, we can find the quasi-solution of *Problem B* by numerically solving the nonlinear optimization for the residual errors between Ψ and Ψ_{new} and between H_{new} and H^1_{new} at each

discret point with Newton's [Kelley 03] and Levenberg-Marquardt's algorithms [Levenberg 44]. These algorithms return to the set of discretized values of Ψ and H along the tube length. However, to describe precisely the tendon, a large number of sampling points are still required. It then results in a heavy calculation burden due to the inverse Jacobian matrix within these mentioned methods.

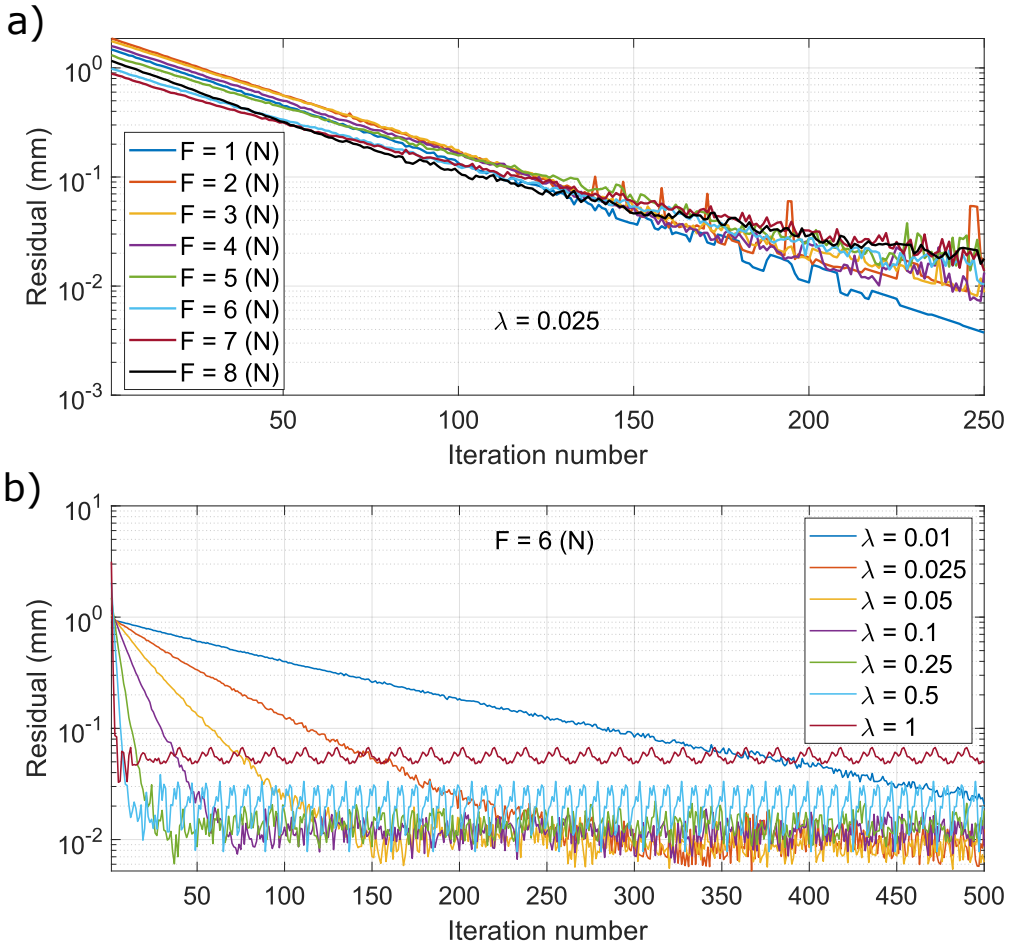

FIGURE III.8 – The elastic (3D-printing) tube with the centerline in 3D space as described later in this section is chosen for this test. We fix $\boldsymbol{v}(0) = [0\ 0\ 1]^T$, $\boldsymbol{u}(0) = [0\ 0\ 0]^T$ for the entire H(0). a) fix $\lambda = 0.025$, the residual always decreases with any force from 1 to 8 (N), which demonstrates the correctness of the iterative guess. b) fix $F = 6(N)$, for any λ between 0 and 1, each residual error consist of 2 parts: 1) it reduces when the guessing value is away from the quasi-solution, then 2) there exists a resistance radius around the exact solution where the residual reduction cannot occur any more. Higher values of λ allow obtaining faster residual reductions but correspond to greater resistance radii.

In this work, we propose a different approach to solve this problem. We first define the residual error of the problem as the sum of the root-mean-square deviations (after process III.63) of the tendon location and of the tube centerline in order to ensure that both deviations tend to zero. As presented in [Nguyen 22], the

tendon path consists of geodesic-curved segments (T_c) on the inner surface of the tube where the Gaussian curvature is negative and straight segments (T_s) joining them. When the tendon is stressed, it makes the centerline of the tube bent toward the direction where the tendon is, thus making the Gaussian curvature of the inner surface in the vicinity of (T_c) even more negative. As an observation result, the difference between Ψ and Ψ_{new} will reduce to its local minimum during process (III.63). That is, if we update Ψ by Ψ_{new} for the next iteration, we will obtain a reduction in the residual error. Nevertheless, after a certain number of iterations, the residual error does not reduce anymore. Instead, it fluctuates about this final value as shown in figure III.8. In an abstract manner, from the current point Ψ in Ψ-space, by following the way towards Ψ_{new}, we will get closer to the solution $\bar{\Psi}$ of the problem. Even so, when the current Ψ is closer to $\bar{\Psi}$, the "jumping step" from Ψ to Ψ_{new} becomes too large. Then, the guessing point Ψ passes by $\bar{\Psi}$ and moves around it within a certain radius of error instead of getting closer to it. For that reason, in the interval between (Ψ, Ψ_{new}), we expect to find a better solution than the current Ψ which can continue reducing the residual error. In our implementation, the tendon location parameter is updated by a virtual proportional gain λ ($0 < \lambda \leq 1$):

$$\Psi^{\eta+1} = \Psi^{\eta} + \lambda\,(\Psi_{new} - \Psi^{\eta}) \tag{III.64}$$

where η is the iteration index and Ψ_{new} is the result if we apply process (III.63) for Ψ^{η}. The variable gain λ is adjusted accordingly to obtain the residual reduction. We start λ from 1 for a rapid residual reduction as shown in figure III.8. If neither step reduces the residual norm, λ is successively decreased by a small value until a reduction in the residual occurs. This value is chosen of 0.05 in our implementation. Alternatively, the program will throw an error and output Ψ^{η} as the last successful solution.

As illustrated in Fig. III.9, the algorithm will terminate if 1) **Residual 2** is smaller than **Tolerance 2**, 2) the maximum iterations are reached, and 3) the residual does not reduce with all tests for $\Psi^{\eta+1}$ between Ψ^{η} and Ψ_{new} (for every attempted value of λ). In the algorithm, **Tolerance 2** is 100 times smaller than the inner diameter of the tube (**Tolerance 2** $= \frac{D_i}{100}$).

Global solution of the coupled problem

In order to obtain the global solution of the coupled problem between the tube shape and the tendon location, we need to combine the shooting process block (*Block A*) that solves *Problem A* (see Fig. III.6) and the tendon quasi-solve block (*Block B*) in the algorithm for solving *Problem B* (see Fig. III.9) in a common algorithm where the output of one will be connected to the input of the other and vice versa. As the tendon position changes incrementally with a small displacement inside the tube through process (III.63) and as the requirement of **Tolerance 2** is not as demanding as **Tolerance 1**, we can always find the quasi-solution of Problem B satisfied within the tolerance, while it is not easy for Problem A. For that reason, to improve the robustness of the shooting process, we integrate into

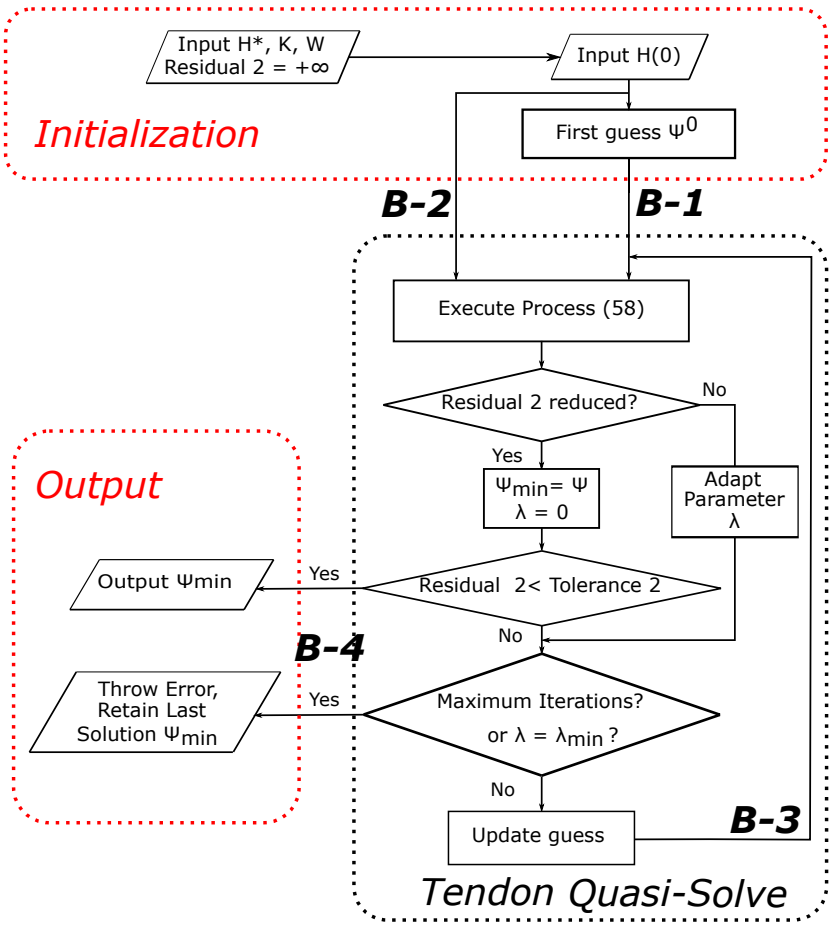

FIGURE III.9 – Algorithm to determine the tendon location parameter Ψ corresponding to a given value of H(0).

Block B a new task to aid the guessing value $\boldsymbol{\chi}$ received from *Block A* closer to the solution. By fulfilling this task, *Block B* will find the quasi-solution for the tendon location corresponding to the adjusted value of $\boldsymbol{\chi}$ and thus, the value of H(0) ($\boldsymbol{\chi} \subset$ H(0)). Then, the adjusted value of H(0) and its corresponding quasi-solution Ψ will be sent to *Block A* via the connections from port ***B-4*** to port ***A-1*** and to port ***A-2***, respectively.

For more details, figure III.10 illustrates the algorithm to find the global solution of the coupled problem. At the initialization step, the first guesses H(0) and Ψ^0 need to be chosen close enough to the solution. In our implementation, we determine Ψ^0 by solving the ESP problem in case of ignoring all loads on the tube. By employing the obtained tendon path, we solve the boundary conditions at distal end (III.58) for $\boldsymbol{v}(l)$ (called $\boldsymbol{v}_b$) and $\boldsymbol{u}(l)$ (called $\boldsymbol{u}_b$). If we only consider the tendon load on the tube ($\boldsymbol{f}_g = 0$ and $\boldsymbol{l}_g = 0$), the equation (III.54c) will depend on just $\boldsymbol{v}$ and $\boldsymbol{u}$. Thus, we can numerically integrate inversely from the tip to the base in order to obtain H(0) for the initial guess.

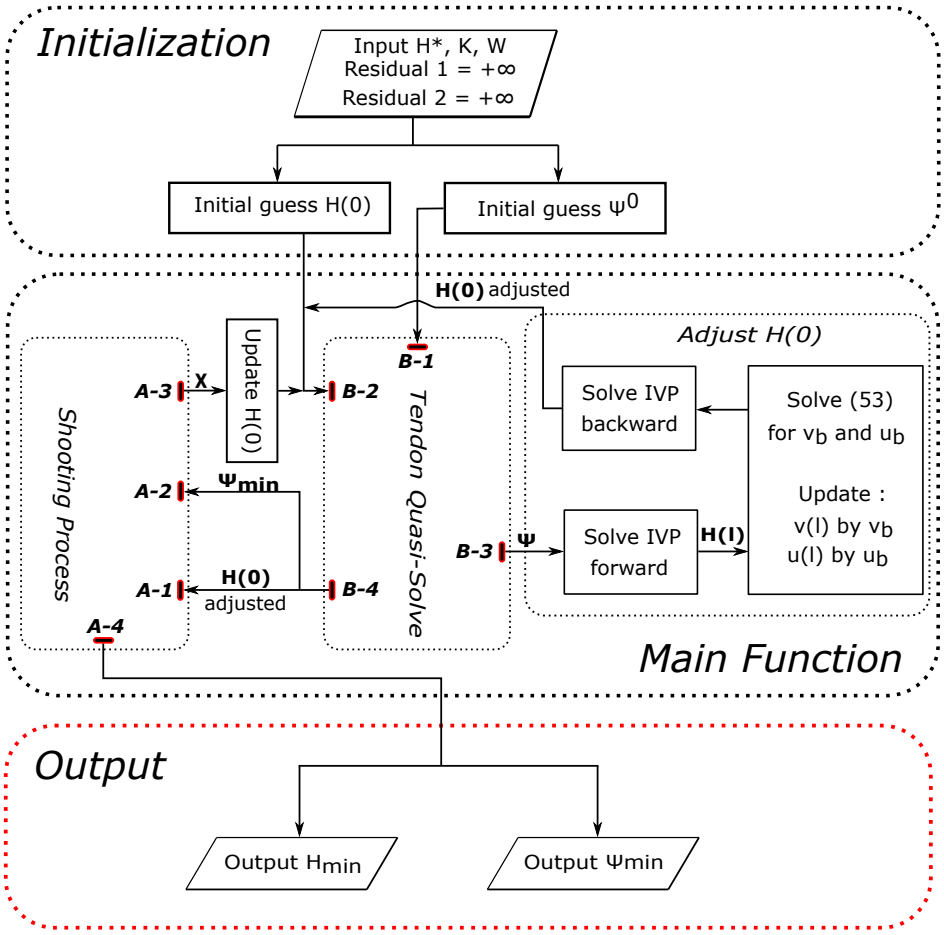

FIGURE III.10 – Global algorithm. The ports A-1,2,3,4 and B-1,2,3,4 are as shown in figure III.6 and figure III.9, respectively. A-1 : input/update $\boldsymbol{\chi}$, A-2 : input/update Ψ_{min}, A-3 : transfer new guess $\boldsymbol{\chi}$ to solve *Problem B*, B-1: input the initial guess Ψ^0, B-2 : input/update H(0), B-3 : update guess Ψ, B-4 : output Ψ_{min} and $\boldsymbol{\chi}$ (hence H(0)) adjusted.

After this step, the initial guesses will be transferred to *Block B* via port ***B-1*** and ***B-2***. In *Main Function* stage, if the stopping condition of *Block B* is not satisfied, it will update the value of Ψ and send it to the *Adjust H(0)* block instead of backing to port ***B-1*** as in figure III.9. After that, we will receive the adjusted value of H(0) by solving equation (III.54c) from the base to the tip, updating $\boldsymbol{v}(l)$ and $\boldsymbol{u}(l)$ by $\boldsymbol{v}_b$ and $\boldsymbol{u}_b$ respectively, then re-solving equation (III.54c) from the tip to the base, and finally updating the obtained H(0) by considering the boundary conditions at the base for $\boldsymbol{p}(0)$ and $R(0)$ (III.55). This loop recurs until the stopping condition of *Block B* is met. Then, the adjusted value of $\boldsymbol{\chi}$ and its corresponding quasi-solution Ψ_{min} are sent to *Block A* to execute the shooting process. During the shooting, if the stopping condition is not satisfied, *Block A* will update the

guess $\boldsymbol{\chi}$ and transfer to *Block B* via port ***A-3***. Otherwise, it will output the global solution H_{min} and Ψ_{min}.

Results

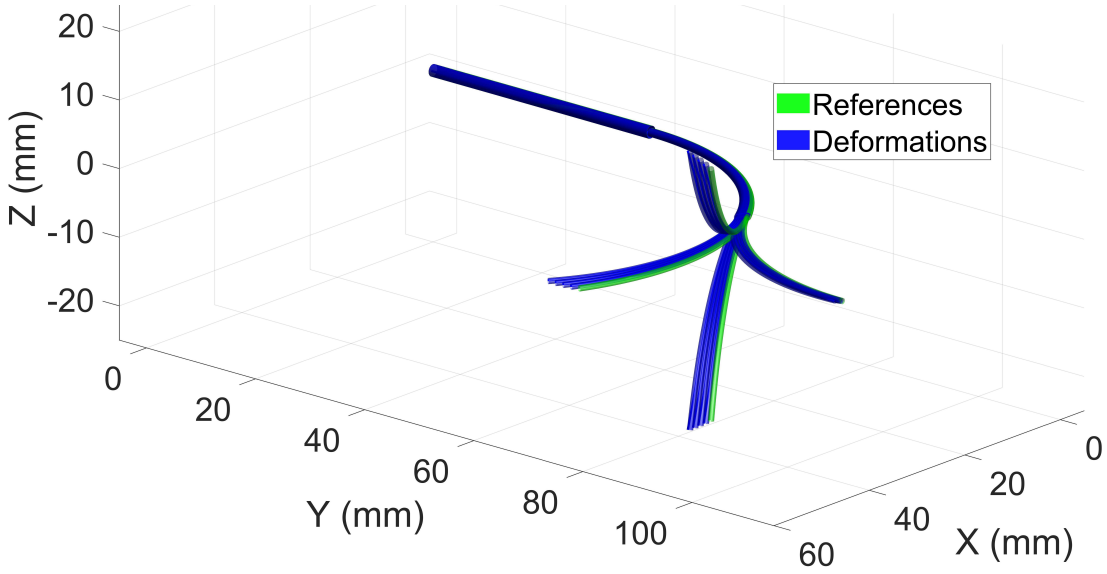

FIGURE III.11 – Deformation of a multi-stiffness tube under the free internal tendon load. The references correspond to the differences in bending angle between the two curved segments are $0°, 90°, 180°$, and $270°$. The tendon tension increase gradually from 0 to 12 N.

In figure III.11, we demonstrate a simple application of the proposed method to estimate the deformation of an elastic tube with multi-stiffness segments made up of three concentric tubes under the free internal tendon load. Nitinol tubes (Young Modulus $E = 60$ GPa) are chosen for this simulation. The outer/inner diameters of the tubes in order from outermost to innermost tubes are: (1.80/1.40), (1.20/1.02), (0.86/0.66) mm, respectively. The mass of the tubes can be neglected. We assume that the reference state of the CTR (no external load) includes three segments: 4 cm straight followed by two identical curved segments of 4 cm long and the bending radius of 4 cm. As a simulation result, the deformation has the highest value when the two curved segments bending in the same direction. With the tendon tension of 12 N, the tip error (between the deformed and reference state) is 4.4% of the total length (or 6.6% of the curved length) and the angular error is 11.3° (see figure III.12). In practice, we apply the model to estimate the deformation of the CTR under a given tendon tension before fabricating it. The tension is determined by testing on the bending of the wrist (normally, 1-2 N). Then, we expect to select the diameters of the tubes as well as their material to obtained a negligible deformation of the CTR caused by the tendon load.

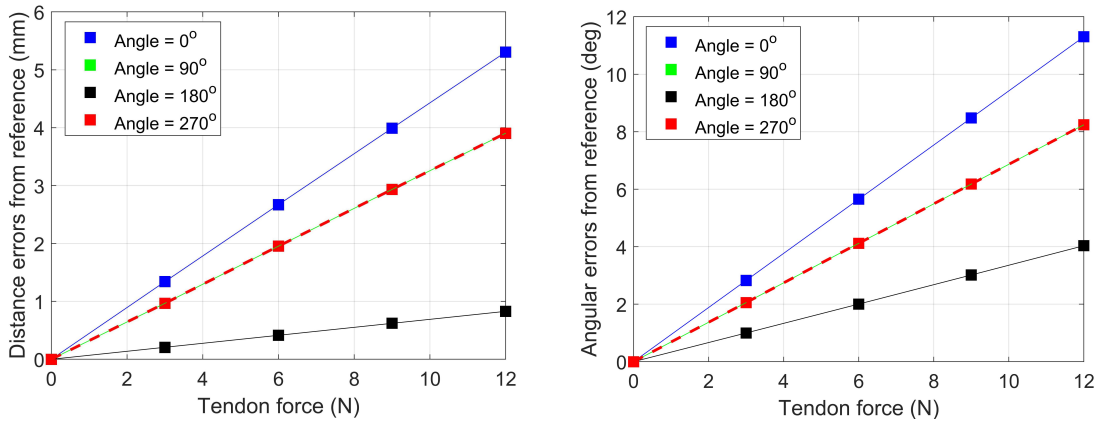

(a) (b)

FIGURE III.12 – Distance and angular tip errors between the deformed shapes and the reference of the CTR under the tendon load. Four referenced configurations of the CTR are created by choosing the difference in bending angle between the two curved segments being $0°, 90°, 180°$, and $270°$.

One can confirm that the deformation of the CTR under the free internal tendon load is small. Thus, we expect to use a softer material for the experimental validation of this model that allows a larger deformation of the centerline. Then, several experiments are conducted using two continuum robot prototypes fabricated by using 3D printing machine from Formlabs. The tubes are made of elastic resin and have the same uniform annular cross-section with outer and inner diameters of 10.6 mm and 5.6 mm respectively as shown in figure C.1. The Young's modulus of the tubes is 3.1 MPa identified through experiments and the Poisson's ratio ν is held constant at 0.5 to validate the incompressible material hypothesis [James 43]. The mass density of the tubes is 1.00 g/cm^3. The experimental validation are detailed in the Appendix. C.1.

In this section, we have derived the model of the CTR as well as described its deformation under the tendon load. To obtain the complete modeling of the hybrid CTR, the bending of the wrist need to be studied. This is the principal aim of the next section.

III.3 Notched Tube with Tendon-Actuated

The asymmetric notched tube design was early proposed by York and Swaney *et al.* [York 15, Swaney 17]. Compared to other designs for the needle-size wrist, this technique has two main advantages: (i) it makes the neutral bending plane of the tube shifted to the non-cutting side, increasing the radius of curvature; (ii) the design requires only a single tendon to actuate the bending wrist that simplifies the actuation unit. The authors have derived the models of the wrist

for both kinematics and statics approaches. However, as a tendon elongation is observed in practice and considering the small dimensions of our robot (1-2 mm in diameter), the model prediction error of the kinematic model caused by the tendon elongation is not negligible. Thus, it is preferable to rely on the static model for our proposed robot. The model proposed in [York 15, Swaney 17] is based on the assumption that all the notches deform with the same curvature during operation which can lead to the shape error between model predictions and experimental results. Indeed, the the bending angle of each notch are generally different in practice [Pacheco 21]. This phenomenon can be theoretically explained by the friction between the tendon and the wrist that varies the tension of the tendon. In separate work, [Eastwood 16] proposed a kineto-static model that uses Castigliano's Second Theorem subject to external forces to determine the wrist deformation. However, the tendon friction was not considered in their work.

To improve the precision of the wrist deflection model, recently, some static models have been derived in the literature by considering different curvature for each notche and applying the capstan equation to describe the friction between the tendon and the wrist [Legrand 21, Pacheco 21]. Even so, the deflection of the wrist is very sensitive to the depth of cut which mainly depends on the manufacturing process [Swaney 17]. A calibration for this quantity could be required for each fabricated wrist to ensure the adaptation of the model.

We apply in this study the simple static model proposed in [York 15, Swaney 17] with the calibration process to simplify the control problem. The model is then extended by considering the elastic deformation of the optical fiber. Then, experiments are conducted to validate the model.

III.3.1 Static model of the wrist with optical fiber

Bending wrist mechanism without optical fiber

The mechanism of the asymmetric notch joints (wrist) was originally described in [York 15] with both kinematics and statics models. In this section, the static one that maps the forced applied on the tendon at the robot base, F_{tendon}, to the resulting bending angle, θ_{total}, is briefly reviewed here for completeness, and then extended by taking into account the presence of the optical fiber (OF) inside the wrist.

By using Castigliano's first theorem and considering the frictional loss of the tendon tension due to $2n$ corners (two corners per cutout), the governing equation is given by (III.65)

$$F_{tendon} = \frac{1}{\eta^{2n} L} \frac{\partial U(\kappa)}{\partial \theta_{total}}, \tag{III.65}$$

where L is the moment arm length, $U(\kappa)$ denotes the total strain energy stored in the wrist which can be found by considering the bending portions as sets of one-dimensional stretched and compressed axial fiber elements and assuming the piecewise linear stress–strain curve behavior of Nitinol as detailed in [York 15].

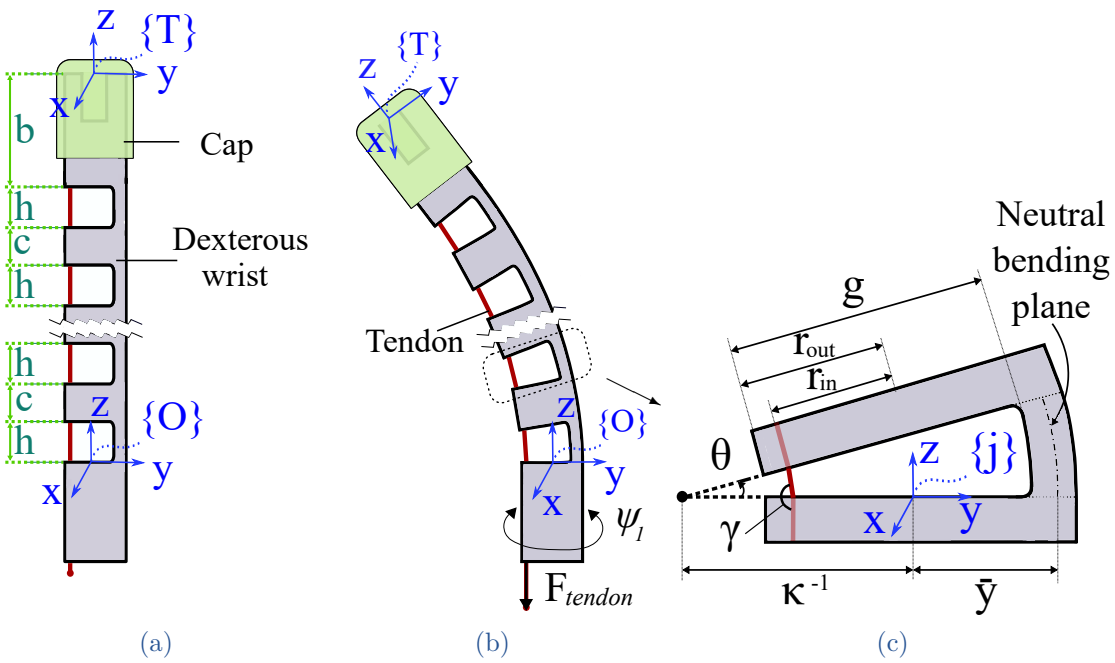

(a) (b) (c)

FIGURE III.13 – Geometric representation of the wrist with its parameters and frames used for the model, with (a) the initial state of the wrist integrated at the tip of the innermost tube, (b) the wrist bending under the actuation force, and (c) a cutout of the bent wrist.

The tension loss due to friction at a corner η can be expressed in terms of the static friction coefficient μ_s between the tendon and the wrist, and the deflection angle of the tendon $\gamma = \pi - \frac{\theta}{2}$ (see Fig. III.13c) using the static balance equation for a single corner, gives:

$$\eta = \frac{sin(\gamma/2) - \mu_s cos(\gamma/2)}{sin(\gamma/2) + \mu_s cos(\gamma/2)} \tag{III.66}$$

The relationship between the total bending angle θ_{total} and the bending curvature of one notch κ is shown in the following expression.

$$\theta_{total} = n\theta = \frac{nh\kappa}{1 + \bar{y}\kappa} \tag{III.67}$$

in which the number of cutouts n, the cut height h and the neutral bending plane location $\bar{y}$ are constant [York 15] (see figure III.13).

Optical fiber integration

As the stiffness of the embedded optical fiber (OF) cannot be neglected, the modeling of the wrist needs to be modified. Then, the strain energy of this fiber U_f should be added in the total strain energy U in (III.65). In the following, U_f will

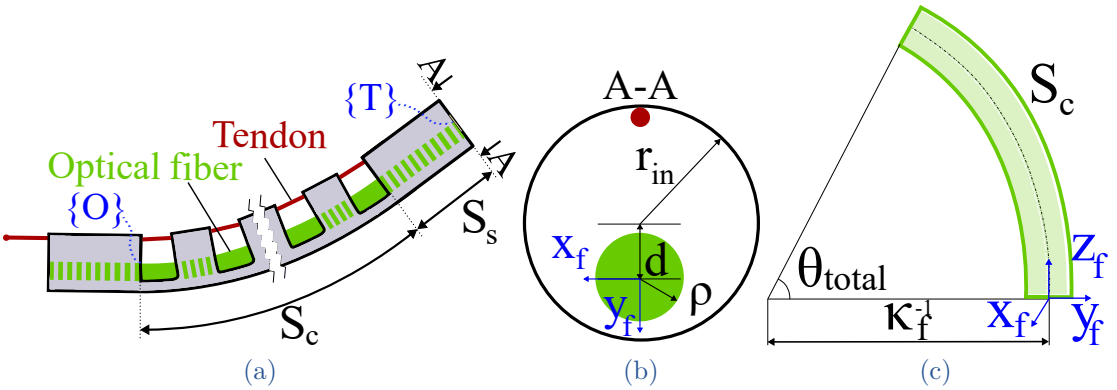

(a) (b) (c)

FIGURE III.14 – (a) Bending wrist with the integrated OF, (b) cross-section of the wrist, and (c) curved portion of the OF.

be expressed as a function of θ_{total}. For the purpose of similarity, the OF section contained in the wrist is assumed to be separated into two portions: straight (S_s) and curved (S_c) ones as shown in Fig. III.14a. The strain energy to be determined is stored in the curved portion S_c. Based on the constant curvature assumption, the strain along the length of the OF ϵ_f varies in a cross section of the bending portion according to:

$$\epsilon_f = \kappa_f(y - d) = \kappa_f y_f \tag{III.68}$$

where κ_f is the curvature of the OF and d is the distance between the centerlines of the optical fiber and of the tube (defined by the endcap fabrication). The y-axis of the body coordinate frame lying at the centerline of the OF $y_f = y - d$ is employed now to simplify the expression (as shown in Fig. III.14c). Considering a linear elastic deformation, the stress of the fiber can be found as

$$\sigma_f(\epsilon_f) = E_f \epsilon_f, \tag{III.69}$$

where E_f is the Young's modulus of the OF. By considering the curved portion of the OF as a set of one-dimensional stretched and compressed axial fiber elements, the strain energy density is given by:

$$W_f(\epsilon_f) = \int_0^{\epsilon_f} \sigma_f(e)de = \frac{1}{2} E_f \epsilon_f^2 \tag{III.70}$$

An axial fiber element locating at y_f has a length given by:

$$l_f = (\kappa_f^{-1} + y_f)\theta_{total} \tag{III.71}$$

The strain energy stored in the portion S_c is given by:

$$U_f = \int_{-\rho}^{+\rho} \left(2W_f l_f \sqrt{\rho^2 - y_f^2}\right) dy_f = \frac{\pi E_f \kappa_f \rho^4 \theta_{total}}{8} \tag{III.72}$$

where ρ is the radius of the OF. To obtain the relationship between κ_f and κ, the length of the curved portion S_c is approximated by (III.73).

$$S_c = \frac{\theta_{total}}{\kappa_f} \approx \frac{nh(1+\kappa d)}{1+\kappa\bar{y}} + (n-1)c \tag{III.73}$$

By using (III.67), (III.72), and (III.73), the strain energy U_f can be found as a function of θ_{total} according to:

$$U_f = \frac{\pi E_f \rho^4 \theta_{total}^2}{8\left[nh + (n-1)c - \theta_{total}(\bar{y} - d)\right]} \tag{III.74}$$

Now, we recalculate the total strain energy $U(\kappa)$ in equation (III.65) by adding U_f to it. The mapping between F_{tendon} and θ_{total} can be obtained by numerically solving (III.65). The knowledge of θ (using (III.67)) allows us to calculate the homogeneous transformation between frames $\{j\}$ and $\{j+1\}$ (see Fig. III.13c).

$$g_j^{j+1} = \begin{bmatrix} 1 & 0 & 0 & 0 \\ 0 & \cos(\theta) & -\sin(\theta) & \frac{(\cos(\theta)-1)}{\kappa} \\ 0 & \sin(\theta) & \cos(\theta) & \frac{\sin(\theta)}{\kappa} \\ 0 & 0 & 0 & 1 \end{bmatrix} \tag{III.75}$$

here, we assume that the wrist is deformed in the plane Oyz as shown in figure III.13. The kinematics of the dexterous wrist is obtained by repeatedly applying Eq. (III.75) in conjunction with the transformation matrix of the uncut portions of the wrist:

$$g_O^T = \left(g_j^{j+1} g_{z,c}\right)^n g_{z,b-c} \tag{III.76}$$

where $g_{z,b-c}$ and $g_{z,c}$ are respectively the translations along the z-axis by the distances $(b-c)$ and c.

III.3.2 Model calibration & sensitivity analysis

Due to the importance of the machining method's tolerance, a calibration step is necessary before using the wrist mechanism. Several experiments are conducted in this subsection to validate the model of the wrist. The M-112 compact micro-translation stage from Physik Instrumente (Germany) with 0.05 µm resolution was used to move the tendon and a force sensor (Phidgets CZL635) with 25 mN resolution measured the force applied on the tendon. We used a digital camera (DNT DigiMicro 2.0) to capture the images of the bending wrist.

A experimental comparison with the static model is shown in Fig. III.15a. To illustrate the sensitivity of the model to the cut depth g and the static friction coefficient μ_s which mainly depend on the machining tolerances, we fabricated 3 different wrists with the same nominal design parameters as mentioned in Chapter IV. For each prototype, we determined these two parameters that provided the best agreement with the experimental results. The wrists were fabricated with the Charmilles 2050 TW machine for wire-cut electrical discharge machining, with a wire diameter of 0.1 mm (see Chapter IV).

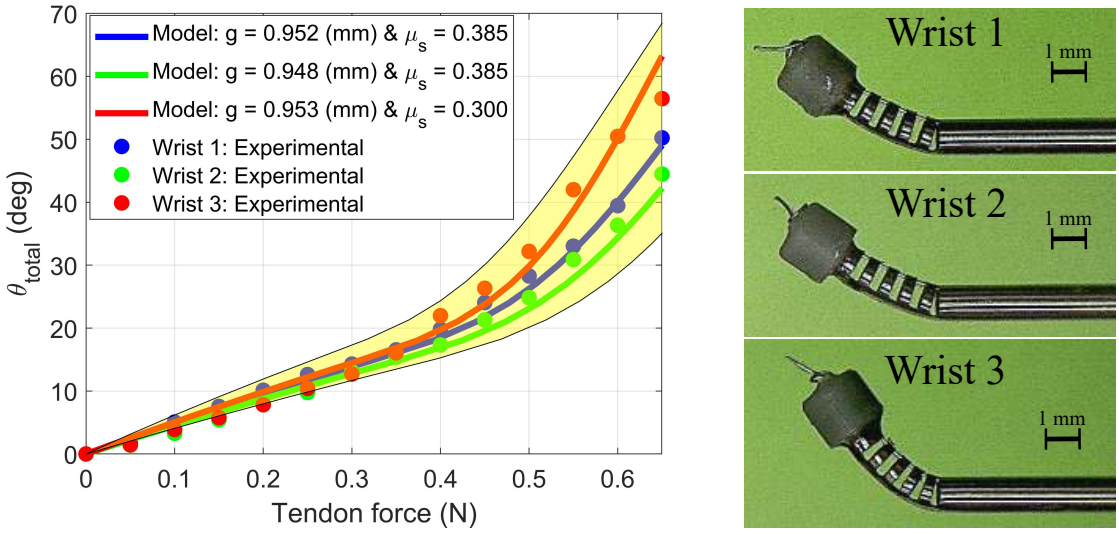

(a) (b)

FIGURE III.15 – (a) The static model prediction and experimental results with respect to the tendon force required to bend the wrists. We conducted three tests for each wrist by changing the speed of the translation stage to 5, 10, and 15 µm/s and calculated the average value of the experimental data. The yellow domain shows the sensitivity of the model (of wrist 1) with 1% variation of g and μ_s. As the static model is most sensitive to the cut depth, the red curve (wrist 3) with a big difference in μ_s still belongs to the yellow domain. (b) Wrist 1, 2 and 3 under the tendon force of 0.6 N.

As shown in Fig. III.15, a small variation in these parameters (within 1%) can lead to a non negligible difference in the bending of the wrists. One can conclude that the tolerance of the machining method is really important and a calibration step is mandatory before the use of the wrist. Now, we use wrist 2 for the following experiments. Fig. III.16a shows the validation tests of the tip spatial trajectory with $RMSE = 0.708$ mm. In the presence of the OF, the stiffness of the wrist increases. To fit the wrist model to the experimental results, we then estimate the Young's modulus of the OF ($E_f = 3.1$ GPa) considering the calibrated parameters g and μ_s. This estimated value is consistent with one reported in the literature (about 3 GPa) [Arrospide 17]. The static model is validated with $RMSE = 1.478°$ ($R^2 = 98.7\%$) and $RMSE = 1.330°$ ($R^2 = 96.8\%$) without and with embedded OF, respectively (Fig. III.16b).

The tendon force significantly increases to obtain the same bending angle in the presence of the OF that shows the importance of considering this fiber in the model. As shown in the experiment, the maximum curvature of the wrist is restricted by the allowable bending curvature of the OF that appears as the technical limitation of the device being used. Thus, a small bending radius must be an essential requirement of the OF for the future compact design to obtain a

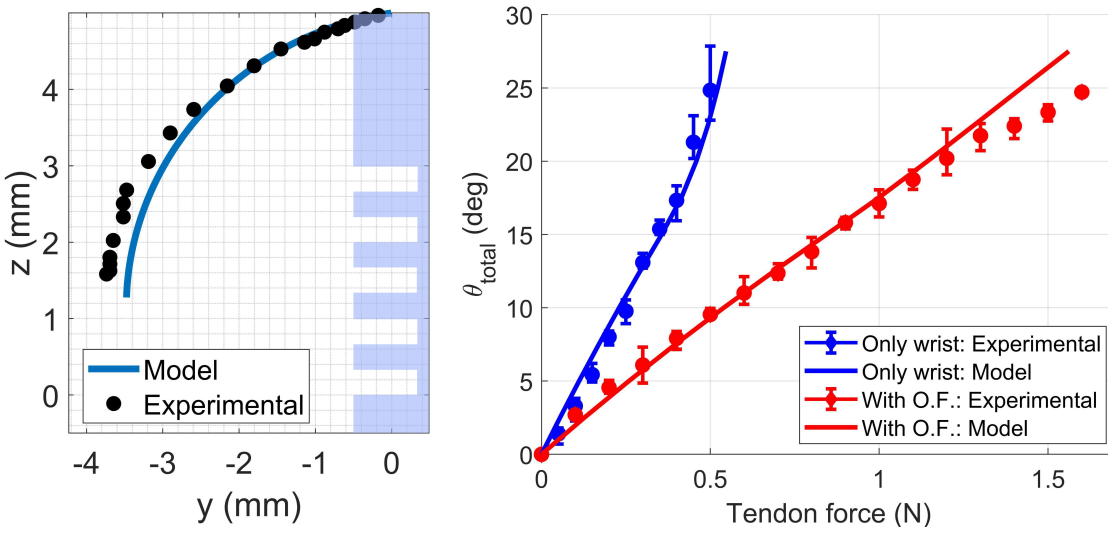

(a) (b)

FIGURE III.16 – (a) Model predicted and experimental tip spatial trajectories of the wrist (the maximum bending of 85^o without the OF). The error arises when the wrist bends with a high curvature. The main reason for this error is the non uniform bending during the test as demonstrated in Fig. III.15b caused by the different friction force at the corners (descending from proximal to distal cutouts). (b) Model validation in case of with and without the OF. We increase the bending angle of the wrist from zero to the maximum value. Parameters of the model: $\rho = 0.42\ mm$, $d = 0.12\ mm$, and $L = R_i$.

smaller bending radius [Uzan 21]. The maximal bending angle of the wrist in the presence of the OF is about 25° as shown in figure III.16. Experimental data are reported in Appendix C.2.

III.4 Graphical User Interface of the Hybrid CTR

As a result of the modeling, we provide the simulation of the proposed robot to visualize its behavior. In this work, we use Graphical User Interface (GUI) of MATLAB to investigate the relation of the proposed robot with respect to the design and actuation parameters which have been studied in this chapter. It allows us to select the length and curvature of each tube as well as the actuator parameters to modify the configuration of the robot. To improve the simulation speed, the deformation of the CTR under the tendon load is neglected in this program. The GUI will be useful for the positioning of the proposed robot such that it can be enter the entry hole to the tympanic cavity and perform collision test (see figure III.17). This will be discussed into detailed in Chapter III.

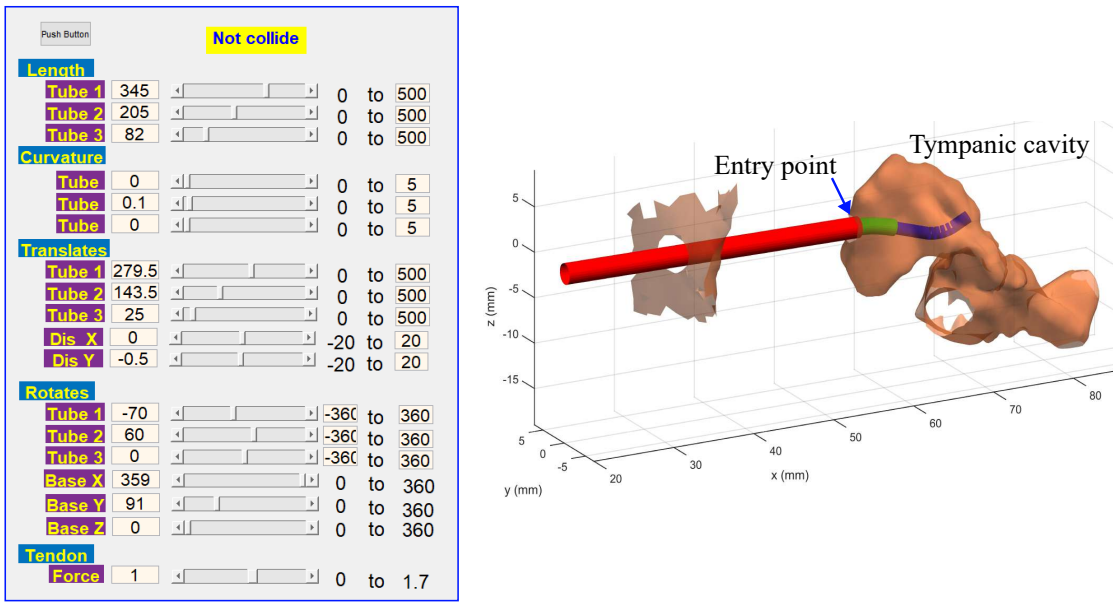

Figure III.17 – (LEFT) The slider and edit value selections of the proposed robot using GUI of MATLAB. (RIGHT) The proposed robot configuration that allows it to be inserted through the entry hole through the mastoid to the typanic cavity. The diameters of the robot is selected as given in Table IV.2

III.5 Conclusion

This chapter has presented the modeling of the proposed hybrid CTR by considering the kinematic model for the CTR and the static model for the wrist. Besides, the coupled actuation of the CTR and the wrist and the sensitivity of the wrist to the design parameters were also considered. Several experiments were conducted

to validate the model. We propose a graphical user interface for the selection and visualization of the robot configuration that will be useful to obtain the robot design parameters. The following chapter will present the robot synthesis based on the anatomy and the fabrication methods of its components.

Chapter IV

Robot Design Requirements and Fabrication

IV.1 Robot design requirements 92
IV.1.1 Anatomical reconstruction and analysis 92
IV.1.2 Robot synthesis based on the anatomy 95
IV.2 Robot fabrication 109
IV.2.1 Precurved tube shape setting 109
IV.2.2 Wrist 111
IV.2.3 End cap 113
IV.2.4 Tendon selection 117
IV.2.5 Benchtop prototype 118
IV.2.6 Laser ablation tool 119
IV.3 Conclusion 119

This chapter focuses on robot design requirements and fabrication. First, anatomical reconstruction of the ear has to be carried out, followed by a collision test between the ear model and the robot. This will help identify the largest possible coverage volume of the robot inside the tympanic cavity. The parameters corresponding to this volume will be selected for fabricating the hybrid CTR, whose components include a precurved tube, a wrist driven by a tendon, and an end cap. The resulting robot will then be manipulated by an actuation unit, which will also be described in this chapter.

IV.1 Robot design requirements

IV.1.1 Anatomical reconstruction and analysis

The middle ear is the middle portion of the ear that carries sounds from the auditory canal to the inner ear by transferring the acoustic energy from the air to the fluids within the cochlea. It contains the tympanic cavity that shields three tiny bones known as the ossicles: hammer, anvil, and stirrup responsible for the sound transmission to the cochlea. The tympanic cavity is the anatomical area of interest of this thesis figure IV.1. With its pocket-like shape located at the skull base, its lateral walls and roof are surrounded by bone structures [Luers 16].

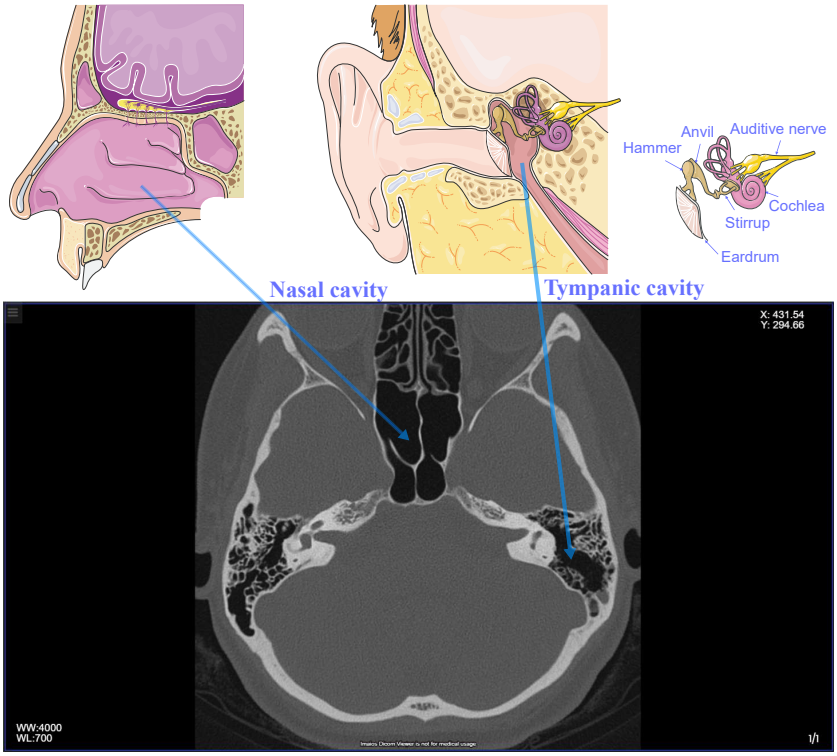

Figure IV.1 – A CT-scan DICOM image of the circular sector of the skull.

To define the anatomical constraints, CHRUB and INSERM have provided CT scans of different patients which will be converted to 3D STL (standard triangle language) file. The reconstruction process consists of three steps, namely image segmentation, 3D reconstruction and extraction of the anatomical constraint in form of a 3D meshed surface. The model has been reconstructed from the set of DICOM images as shown in figure IV.1 which allowed obtaining a 3D scanning of the circular sector of the skull including just the part of the ears. Then, the image segmentation and 3D reconstruction software Invesalius [1] [Amorim 15] was used to generate the anatomical volume as a cloud of disconnected and connected triangular meshes (see figure IV.2). Finally, Meshlab [2] was used for filtering and refining the triangular meshes to obtain the final STL surface of the anatomical constraint (see figure IV.3).

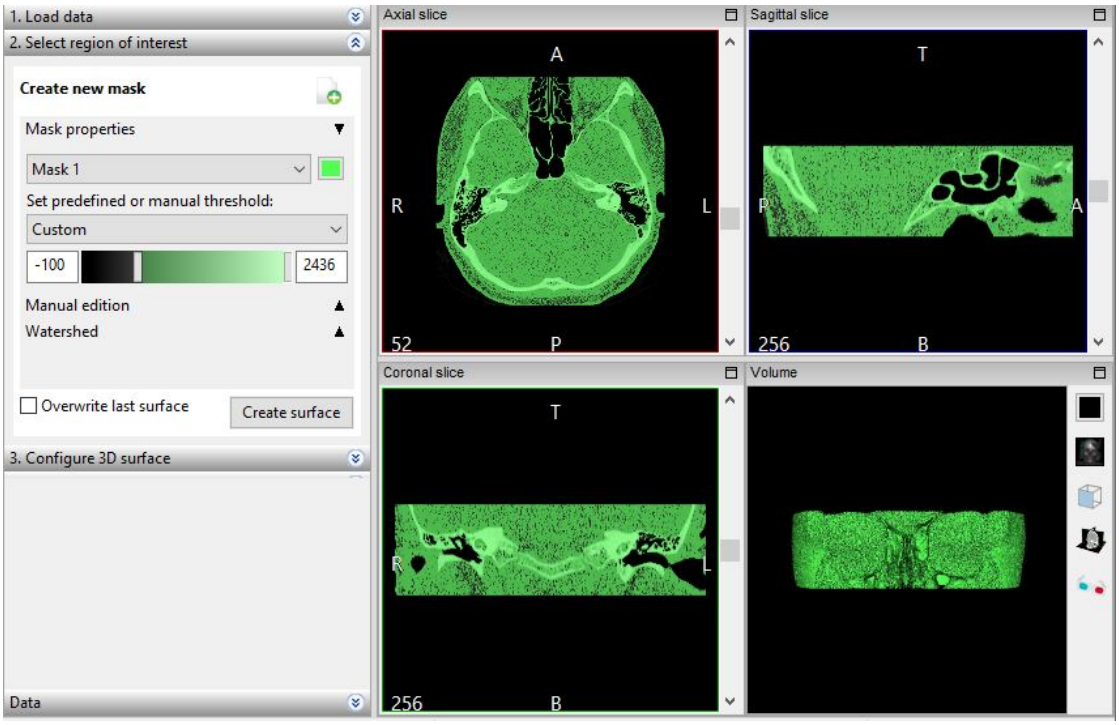

FIGURE IV.2 – Image segmentation and 3D reconstruction of the anatomy with Invesalius using DICOM images.

As open-sources and easy to utilize, these two softwares were often used for the 3D reconstruction of different anatomies [Boyle 09, Girerd 18]. After importing the set of images in Invesalius, the contrast threshold can be selected manually to adjust the obtained 3D reconstructed volume (see figure IV.2). As the bilateral symmetrical property of the human ear, the right ear was isolated and a process of re-meshing was applied using the Meshlab tools in order to eliminate any errors or super-positioning of vertexes or faces. To lower the computation time of collision

1. [Online] https://invesalius.github.io.
2. [Online] https://www.meshlab.net.

detection in this work, the mesh corresponding to the auditory canal and to the lateral wall of the tympanic cavity (the inner zones of the model considered for the collision test) were reduced in size. Then, the mesh was globally improved: zones with a high gradient of unnatural curvature were smothered out and tiny holes on the surface were closed (see figure IV.3). The ossicles were supposed to be dismantled beforehand, as the main challenge considered in this study was the middle ear coverage rather than path planning with obstacle avoidance to reach the desired site.

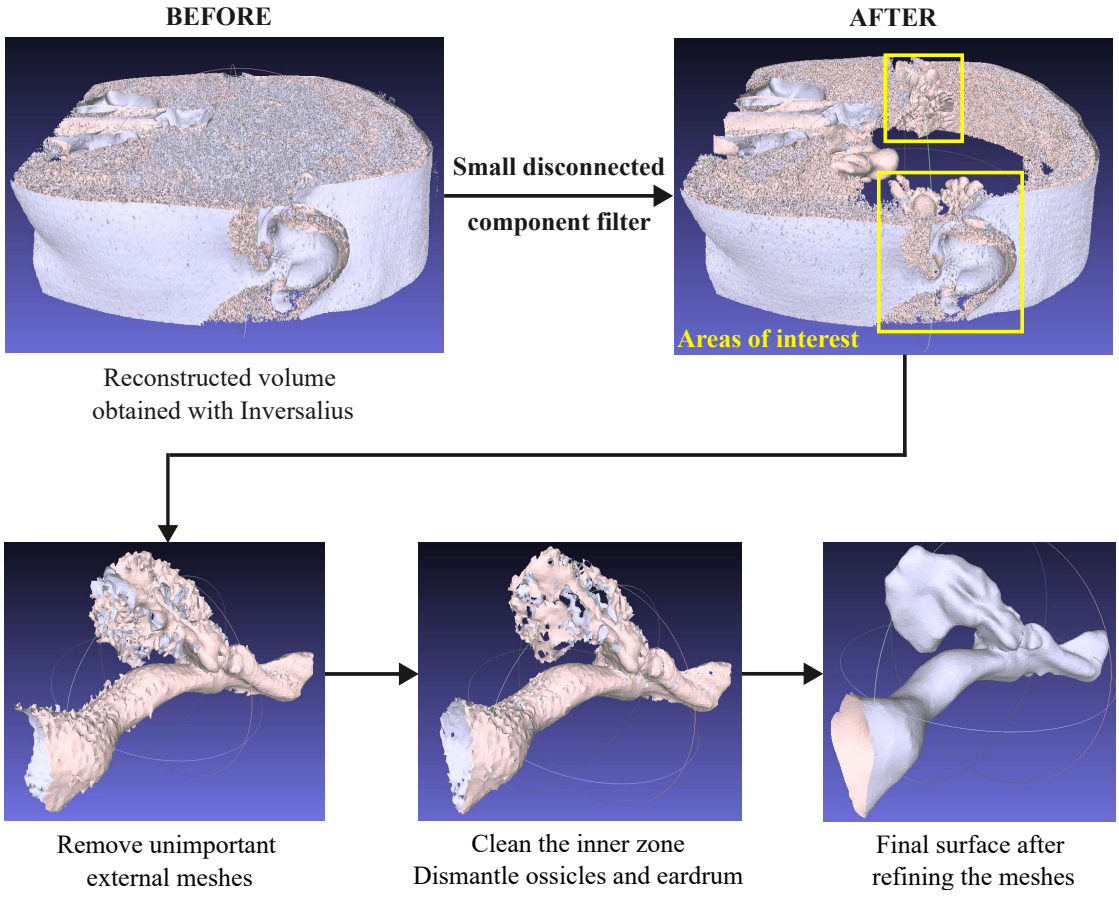

FIGURE IV.3 – Steps of the 3D model extraction using Meshlab. The mastoid is temporarily removed during this process to facilitate mesh selection.

Then, the access path via a 3 mm hole through the mastoid bone was created in this model. In order to perform the collision test between the proposed robot and the ear as detailed in the next subsection, *stlread* function of MATLAB software (the MathWorks Inc., Natick, USA) was used to read the STL model. An example of the right ear model was visible in figure IV.4. The measured inner volume of the tympanic cavity of the obtained 3D model was 950 mm^3, which was consistent with the typical values between 0.5 and 1 cm^3 in the literature [Stepp 05, Liem 04]. As shown in figure IV.4c-e, reaching the attic through the auditory canal was not a straightforward task that explained the need for the access path via a created

hold through the mastoid bone. As early mentioned, the following two accesses to the middle ear will be considered throughout this thesis: one through the auditory canal, and the other through a mastoid created hole.

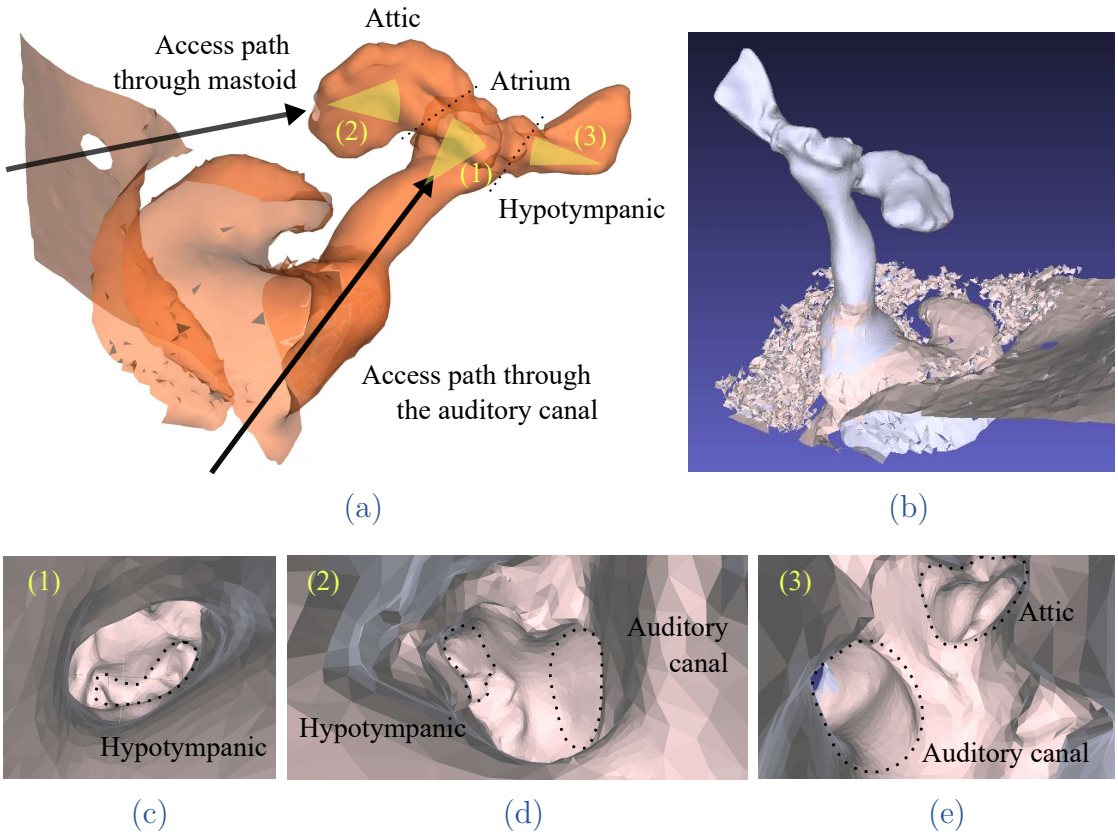

FIGURE IV.4 – (a) Visualization using MATLAB of the STL 3D right ear model with two accesses to the tympanic cavity. (b) Different view from the outside of the STL 3D model. (c) Inner zone of the model with the view from the auditory canal, (d) from the mastoid hole, and (e) from the hypotympanic.

IV.1.2 Robot synthesis based on the anatomy

The middle ear volumes in normal ears were reported to show a wide range, from 2 to 22 cm^3 with an average of $5.6 - 7.9$ cm^3 [Molvaer 78, Ahn 08]. This value was proven to have a significant disagreement between different methods of measurement [Carpenter 17] and could be changed in case of the lesioned ears [Ahn 08]. As part of the middle ear, tympanic cavity has a volume ranging from 0.5 to 1 cm^3 [Stepp 05, Ikui 00, Kürkçüoğlu 10] (see figure I.10). No statistically difference in tympanic cavity volume was found between of the both sexes and between both sites of the same individuals [Kürkçüoğlu 10]. Nevertheless, it has a significant variation according to the age groups and is approximately 1.5 times as large in adults as in infants [Ikui 00]. Due to the extreme inter-patient variability of the middle ear as well as of the tympanic cavity in particular, designing a unique

optimal robot for all subjects is a challenging objective. So in a first attempt, the contribution here is to propose a robot design synthesis based on a given tympanic cavity. The study on various tympanic cavities will be discussion on the perspective of this thesis. Here, the selection of the proposed robot design based on the chosen right ear model as shown in figure IV.4 will be presented. The scheme of the robot design synthesis is detailed in figure IV.5. Each of the design parameters will be considered within its range (depending on the manufacturing method and the anatomical constraint) to obtain a set of coverage volumes. The design that results in the greatest coverage volume will then be selected for fabrication.

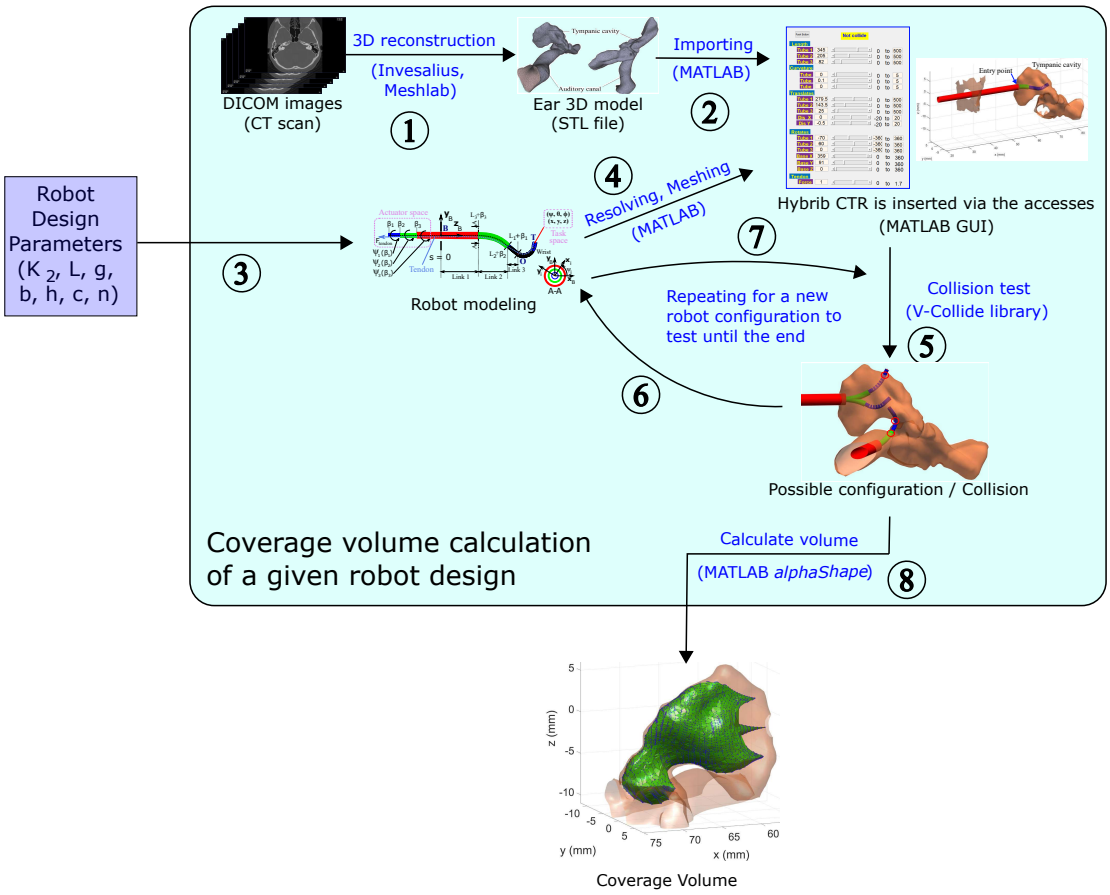

FIGURE IV.5 – Diagram of the robot synthesis based on the anatomical constraint. Each robot design will provide a particular coverage volume. By testing with various sets of design parameters, the design that corresponds to the largest coverage volume will be chosen for fabrication.

IV.1.2.a Collision test & coverage volume

Our objective is to design a robot that can completely cover the desired workspace inside the middle ear. For this, the volume to cover is compared to sets of sampled tip positions of the robot, corresponding to possible configurations. A configuration is called possible when it allows to reach a point inside the tympanic

cavity without any collision of the robot backbone and tip with the anatomy (figure IV.6). The V-Collide library [Hudson 97] is employed in this work to detect the collision between two volumes defined by triangular meshes. We also use the Parallel Computing Toolbox of Matlab [3] to enhance the computation speed. The first volume is the mesh of the robot created with Matlab whose centerline is obtained using the model developed in Chapter III, and the second one is the area of interest of the ear. To do this, we create different configurations by changing discretely the rotation and translation of the tubes ($\boldsymbol{q} = \{\psi_1, \ldots, \psi_n, \beta_1, \ldots, \beta_n\}$) as well as the bending angle of the wrist (θ_{total}) until the collisions occur. The discrete incremental values are 5 deg and 1 mm for the rotation and translation of the tubes, respectively and $\theta_{total_{max}}/5$ for the bending angle of the wrist. To improve the execution speed, the assumption of decoupling actuation between the CTR and the wrist is employed. This assumption holds for a CTR body that has a much higher stiffness than the wrist, which is the case in this work (detailed discussions will be given later in this chapter). The reachable volume is then computed as the envelop of all tip points reached by the robot. The final robot parameters are determined as the ones among discretized sets that provide the maximal volume covered inside the ear.

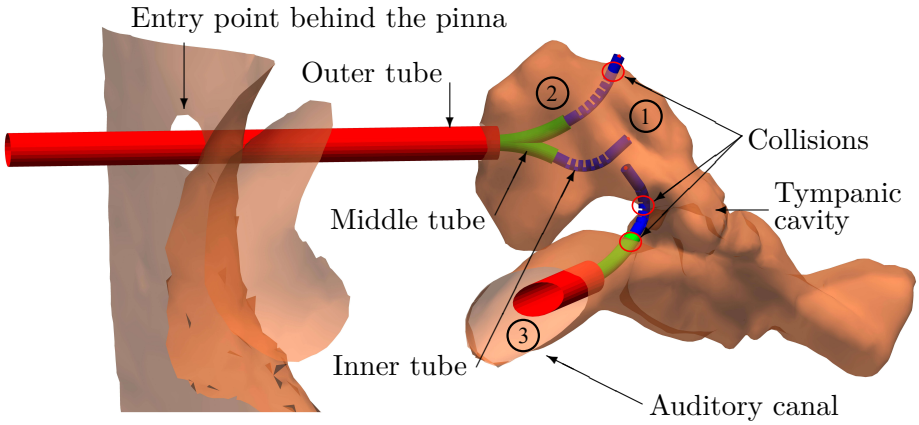

FIGURE IV.6 – Representation of robot configurations that reach the tympanic cavity through the two accesses. Configuration (1) is possible. Configuration (2) is not possible as the tip is outside the tympanic cavity. Configuration (3) is not possible because of collisions between the robot body and the ear model.

Concretely, the collision test consists of four tasks: reading the 3D model of the ear, computing the centerline of the robot for the considered actuation state, meshing the robot shape by taking into account the diameter along the bakcbone and checking for collisions between the robot and the ear model. In these four tasks, the first one is run only one time for all collision tests, thus its computation time can be ignored compared to the others which require to be repeated each time the robot shape is changed. Table IV.1 shows a comparison between the average computation times of the tasks corresponding to a given configuration of

3. https://fr.mathworks.com/products/parallel-computing.html

the robot. The robot consisting of 3 concentric tubes with their maximal active length (see Table IV.2) is considered for obtained 100 randomly configurations. The simulations are run on a machine with an Intel Core i5-8400 CPU @ 2.80 GHz processor containing six-core CPU and 16 GB RAM. It is easy to realize that the computation time of the test depends heavily on modelling and meshing the robot.

TABLE IV.1 – Computation time of the elemental tasks

Task	Mesh Ear	Compute Robot Model	Mesh Tubes	Test Collision
Time (s)	0.10	0.43	0.10	0.08

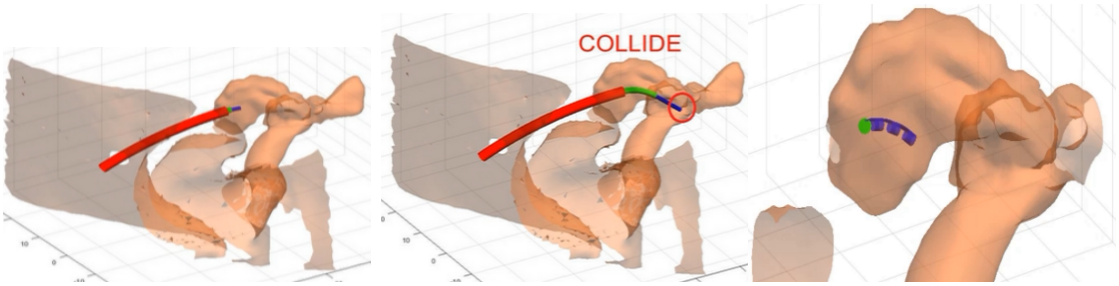

(a) (b) (c)

FIGURE IV.7 – The collision test of the hybrid CTR that is inserted via a $3-mm$ hole through mastoid: (a) step 1: inserting the robot through the entrance; (b) step 2: only the CTR is considered, the tubes are translated and rotated and the collision test is performed to obtain the set of possible configurations; (c) step 3: only the dexterous wrist is considered, the bending angle increases from 0° (for possible configurations found in step 2) to the maximum value to determine the set of tip positions of the robot corresponding to its possible configurations.

The coverage volume determination is performed in 3 steps as shown in figure IV.7. Firstly, the robot needs to be inserted through one of the entry paths of the tympanic cavity. Then, the bending angle θ of the wrist is fixed to 0° so that the robot works as a CTR. The tubes are translated and rotated, then the collision test is performed to obtain the possible configurations of the CTR. The third step consists in collision tests between the mesh surface of the wrist by increasing θ with a discretized value from the non-colliding configurations in the previous step and the middle ear. As the number of mesh variables (vertices and faces) of the wrist is much smaller than those of the whole robot, the computation time is significantly reduced. Finally, the point cloud of the tip positions corresponding to possible solutions is saved. Its volume is determined using the *alphashape* function in Matlab.

IV.1.2.b **Robot synthesis**

The robot synthesis consists of two steps: CTR design and wrist design. This procedure is appropriate for carrying out the collision test in the three phases previously indicated, which speeds up calculation. Furthermore,

CTR synthesis

In this work, a CTR made of 3 tubes will be considered. It is a common choice for this type of robot, in order to obtain a 6-DOF design. As the created hole through the mastoid and the auditory canal are both (nearly) straight, the outermost tube needs to be straight and substantially stiffer than the inner ones to constrain the robot to pass through these accesses. This requirement is considered satisfied if the proximal link has a stiffness 10 times higher than the adjacent one [Bergeles 15]. Next, the middle tube with a precurved shape is employed to navigate the robot inside the narrow space of the middle ear. Lastly, the innermost tube is chosen to be straight for the following reasons: 1) the combination of straight, curved and straight tubes ensures the absence of instabilities during the operation [Rucker 10b, Ha 16] which, if they occur, can be harmful to the patient; 2) only the wrist changes its pose when the innermost tube is rotated, which is a convenient way to partially decouple the motions of the tip compared to the rest of the robot body (see figure IV.8). Besides, in the absence of torsion due to interactions between overlapping curved tubes sections (only one precurved tube), the solution of the CTR kinematic model becomes independent of the transmission lengths, then the total length of each tube is no longer a design parameter, which also reduces the dimension of the problem of design synthesis. Thus, the total length of each tube can be properly chosen based on the robot specification as detailed in (Table IV.2) and the dimension of actuation unit. The curved segment length of the middle tube is chosen long enough (20 mm) to ensure the bending of the portion beyond the outermost tube of the middle one considering the anatomical constraint.

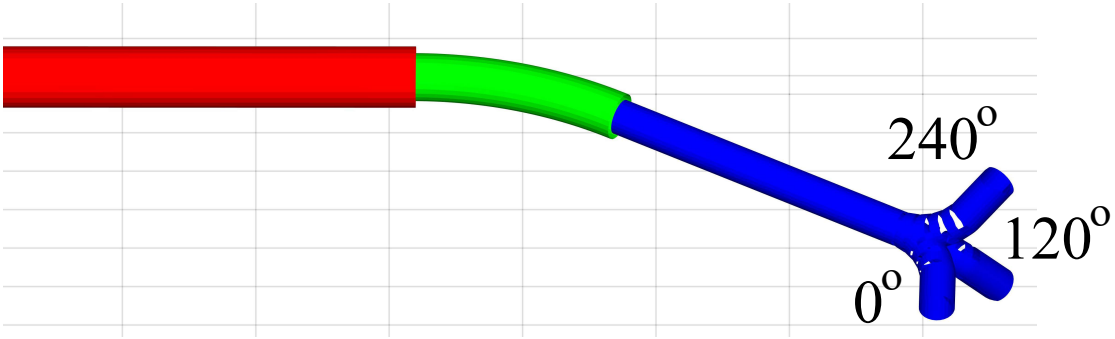

FIGURE IV.8 – Different configurations of the hybrid CTR with the innermost tube's rotation of 0°, 120°, and 240°.

Table IV.2 – Configuration of the concentric tube robot

Tube	Outermost		Middle		Innermost	
Diameter (mm)	Outer	Inner	Outer	Inner	Outer	Inner
	2.50	1.80	1.50	1.25	1.08	1.00
Active length (mm)	Straight		Straight	Curve	Straight	
	56		36-48	20	56-76	
Moving ability (deg-mm)	Rotary	Linear	Rotary	Linear	Rotary	Linear
	fixed at the base		full	12	full	20

The tube diameters are reported in Table IV.2 according to the diameters of the entry hole through the mastoid (3 mm in diameter), the tendon (0.1 mm in diameter) and the optical fiber (diameter of 0.42 mm). Note that the three tubes proposed in this table are based on the available tubes in our lab. Indeed, the ordering new tubes to our provider can take a long time, we prefer to first validate our approach and refine tube parameters if necessary. In addition, the specific optical fiber used for cholesteatoma detection is being studied by our project team, thus only laser optical fiber for cholesteatoma ablation is considered in this thesis. For future applications (e.g. integrating another optical fiber), the diameters of these tubes can be varied reasonably so that the assumption of a decoupling actuation still holds. The table also shows the requirements of the active length ($s > 0$, see figure III.1) and the movement ability of the tubes. Stainless steel (Young's modulus (E_3) = 200 GPa) is selected for the outer tube to reduce its deflection due to the curvature of the middle tube. The material selected for the middle and inner tubes is Nitinol ($E_1 = E_2 = 60\ GPa$) [4]. The design parameter of the CTR is only the precurvature of the middle tube, κ_2. The maximum value of this quantity is 0.1 mm^{-1}, given by Eq. (IV.1) [Webster 06].

$$\kappa_{2_{max}} = \frac{2\epsilon_{max}}{D_2\,(1+\epsilon_{max})}, \tag{IV.1}$$

where $D_2 = 1.5\ mm$ is the outer diameter of the middle tube and $\epsilon_{max} = 8\%$ is the estimated recoverable strain limit of Nitinol in the literature [Webster 06].

In the following, the wrist synthesis will be presented including the determination of the optimal cut depth (g) based on the static model of the wrist and the selection of the other design parameters corresponding to the maximal coverage volume.

4. The datasheet is available online on: https://www.euroflex.de/en/downloads.html.

Wrist synthesis - optimal cut depth

As mentioned, the deformation of the wrist is highly dependent on the depth of cut g. In the prior work, this value is usually chosen by the observation results in practice which corresponds to a maximum outer-fiber strain of approximately 10.4%, and does not guaranteed that all of the material of the wrist undergoes the recoverable strain [Swaney 17]. Moreover, manufacturing multiple wrists (to obtain the best value of g) requires a lot of cost and effort. Hence, a comprehensive analysis of g and its implications based on the model should be considered to select this design parameter for the fabrication.

We first consider the geometry of the asymmetric cutouts. Depending on the depth of cut, we have two different types of cutting part axial cross sections as illustrated in Fig. IV.9. We do not consider the case that $g < r_o$ as the constant cross-section assumption will not be valid anymore for the wrist when it bends. Obviously, the mapping between the actuator and configuration spaces largely depends on the location $\bar{y}$ of the neutral bending plane. This location is given in terms of the depth of cut g and the outer and inner radii of the tube (r_o and r_i).

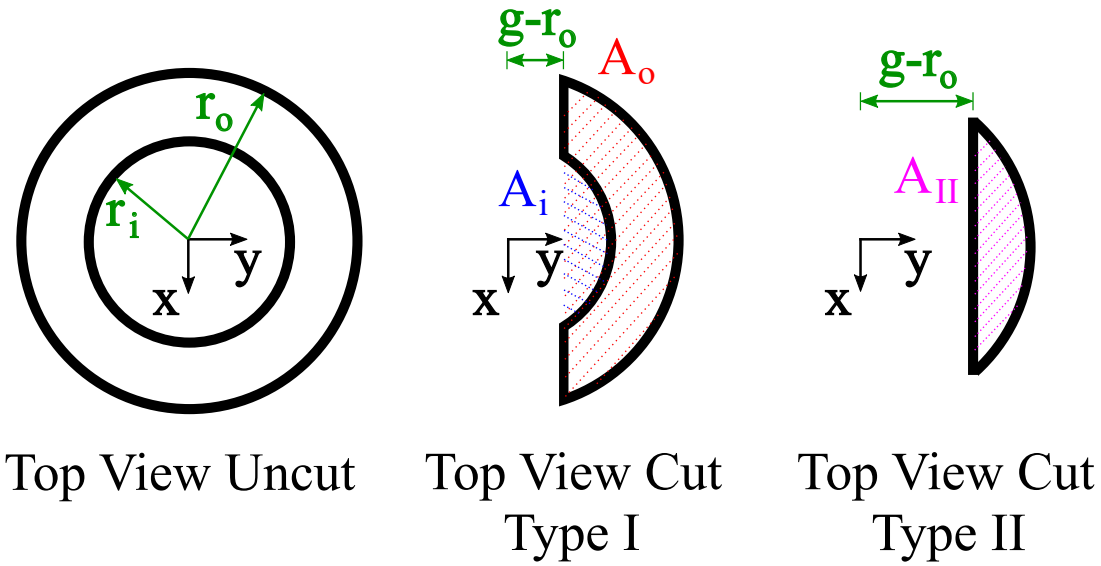

FIGURE IV.9 – Top view of different types of the notches

Type I: $r_o \leq g < r_o + r_i$

$$\bar{y} = \frac{\bar{y}_o A_o - \bar{y}_i A_i}{A_o - A_i} \tag{IV.2}$$

where A_o and A_i are the areas defined in Fig. IV.9 and $\bar{y}_o$ and $\bar{y}_i$ are their respective centroids. We have:

$$\begin{aligned} \bar{y}_o &= \frac{4r_o \sin^3\left(\frac{\phi_o}{2}\right)}{3\left(\phi_o - \sin\phi_o\right)} & \bar{y}_i &= \frac{4r_i \sin^3\left(\frac{\phi_i}{2}\right)}{3\left(\phi_i - \sin\phi_i\right)} \\ A_o &= \frac{r_o^2\left(\phi_o - \sin\phi_o\right)}{2} & A_i &= \frac{r_i^2\left(\phi_i - \sin\phi_i\right)}{2} \\ \phi_o &= 2\arccos\left(\frac{g - r_o}{r_o}\right) & \phi_i &= 2\arccos\left(\frac{g - r_o}{r_i}\right) \end{aligned} \tag{IV.3}$$

where $\phi_o = 2\arccos\left(\frac{g-r_o}{r_o}\right)$.

Type II: $g \geq r_o + r_i$

$$\bar{y} = \frac{4r_o \sin^3\left(\frac{\phi_o}{2}\right)}{3\left(\phi_o - \sin\phi_o\right)} \tag{IV.4}$$

After obtaining the location of the neutral bending plane, we consider that the strain of the bending section is linearly distributed about it. The strain of each fiber element of the wrist within the notch section is a function of its position on the y-axis and the bending curvature κ as follows:

$$\epsilon\left(y, \kappa\right) = \frac{\kappa\left(y - \bar{y}\right)}{1 + \bar{y}\kappa} \tag{IV.5}$$

where $\epsilon < 0$ represent the compression of the fiber element. It is easy to see that the maximal stretch of the wrist is obtained at the outermost fiber element ($y = r_o$) and at the maximum bending curvature ($\kappa = r_o^{-1}$) [York 15]. We have:

$$\epsilon_m = \frac{r_o - \bar{y}}{r_o + \bar{y}} = 1 - \frac{2}{1 + \frac{r_o}{\bar{y}}} \tag{IV.6}$$

We now analyze ϵ_m with respect to $\bar{y}$. The strain within the uncut region of the notched section is required not to exceed the allowable material strain at full bending. Then

$$\epsilon_m \leq \epsilon_{max} \tag{IV.7}$$

where ϵ_{max} is the largest allowable strain of the material. From equation (IV.6), ϵ will increase if $\bar{y}$ decreases and vice versa. In order to obtain equation (IV.7), $\bar{y}$ must be greater than a value $\bar{y}_{min}$. Replacing ϵ_m by ϵ_{max} and $\bar{y}$ by $\bar{y}_{min}$ in equation (IV.6), one can infer that

$$\bar{y}_{min} = \frac{r_o\left(1 - \epsilon_{max}\right)}{1 + \epsilon_{max}} \tag{IV.8}$$

Moreover, by using equations (IV.2) and (IV.4), we obtain that the function $\bar{y}(g)$ increases with g for both types of the notch. Thus, the depth of cut g must be greater than a value g_{min} in order to obtain the allowable strain for the outermost fiber element at maximum bending curvature. Thus, the uncut thickness of the notches (equals to $2r_o - g$) must be thinner in the y-axis to ensure the elastic

deformation. A thicker uncut part corresponding to ($g < g_{min}$) will result in a plastic deformation for the amount of the material at the very outside edge at the maximum bending. This is an interesting result and seems like a paradox. However, note that along these developments, the notched portions are assumed to has a constant cross-section. It is simple to hold this assumption in case of a thinner beam. When the uncut part of the notches is too thick, instead of having a plastic deformation as discussed, the wrist changes its cross-section shape that causes the fail of the assumption and the model is no longer valid (see figure IV.10).

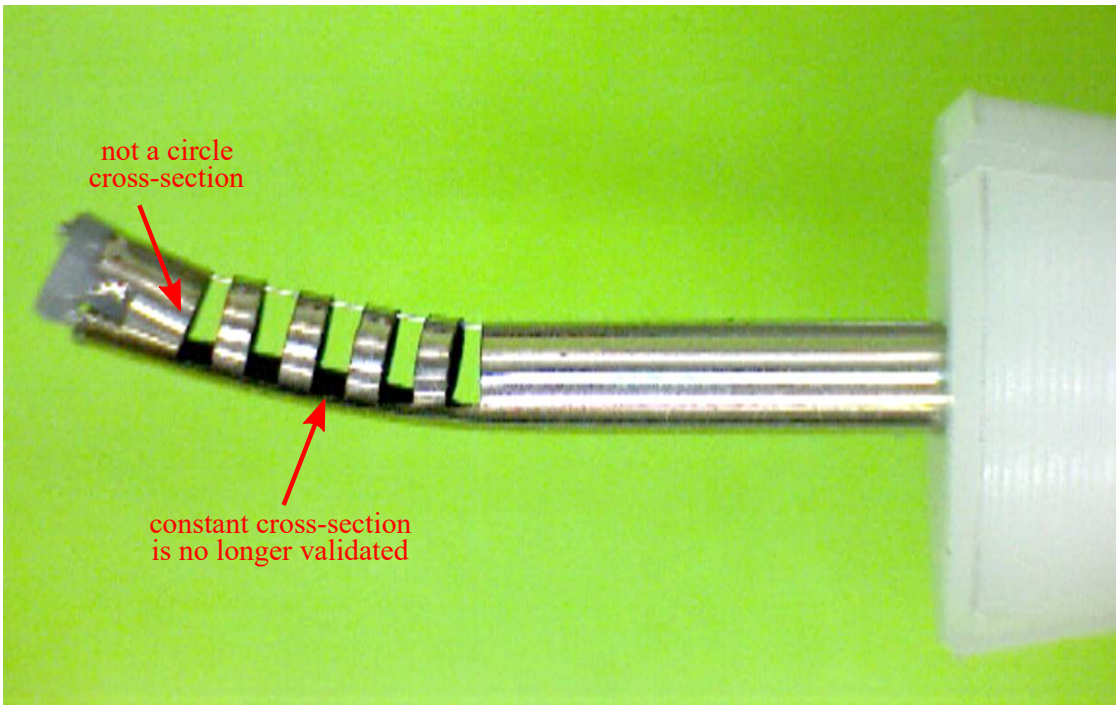

FIGURE IV.10 – Bending of the wrist with a cut depth smaller than g_{min}. The cross-sections of both cut parts and uncut parts change during the test. The notched tube fabricated by the wire-cut EDM has the outer and inner diameters of 2.68 mm and 2.50 mm, respectively. The calculated $g_{min} = 2.184$ mm while $g = 2.15$ mm.

In the following, we will try to solve for g_{min} as a function of r_o and r_i. For convenience, let $\lambda = r_i/r_o$ and $\nu = \frac{g-r_o}{r_o}$. The location of the neutral bending plane is given by

Type I:

$$\bar{y} = \frac{2r_o\left((1-\nu^2)^{3/2} - (\lambda^2-\nu^2)^{3/2}\right)}{3\left(\arccos(\nu) - \lambda^2\arccos\left(\frac{\nu}{\lambda}\right) - \nu\sqrt{1-\nu^2} + \nu\sqrt{\lambda^2-\nu^2}\right)} \tag{IV.9}$$

Type II:

$$\bar{y} = \frac{2r_o\left(1-\nu^2\right)^{\left(\frac{3}{2}\right)}}{3\left(\arccos(\nu) - \nu\sqrt{1-\nu^2}\right)} \tag{IV.10}$$

Substituting $\bar{y} = \bar{y}_{min}$ into the equations (IV.9) and (IV.10), we can determine g_{min} for both types of notches through the relation between ν and λ as shown in figure IV.11.

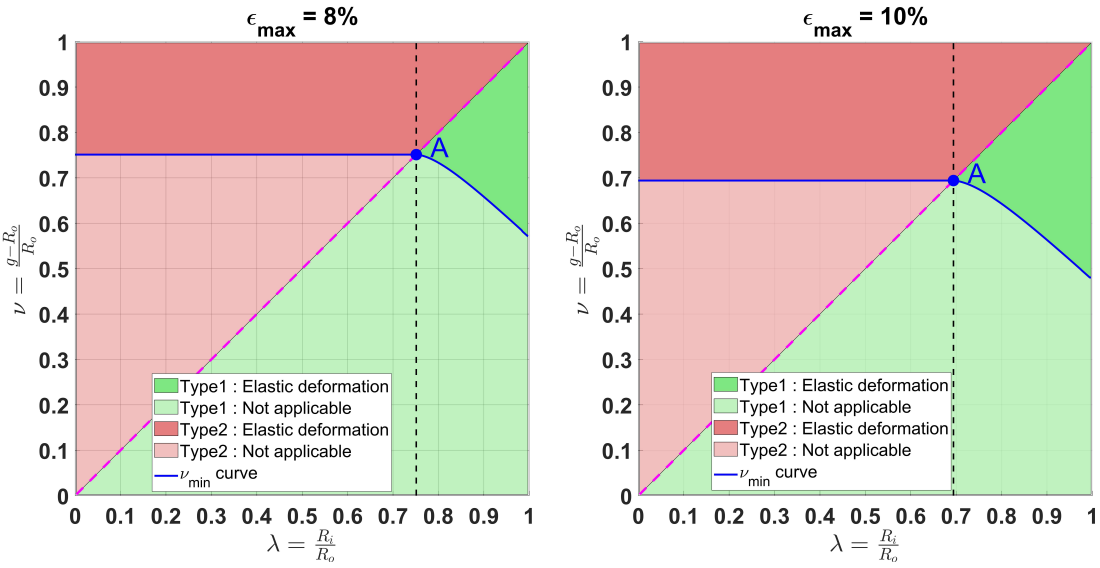

FIGURE IV.11 – Different domain of the wrist deflection based on g.

The blue curve represent the solutions ν_{min} of the equations (IV.9) and (IV.10). The region above this curve corresponds to the elastic deformation of the wrist and the one below this curve does not allows us to apply the static model as the cross-section of the notches could change during operation (see figure IV.10). For a higher value of ϵ_{max}, this curve "moves downward" and extends the elastic deformation domain of the wrist. For type II wrist, as $\bar{y}$ does not depend on λ (see equation (IV.10)), ν_{min} is a horizontal straight line. ν_{min} of type I wrist is a curve that decreases when λ increases. We have an intersection point A between the ν_{min} curve and the frontier between type I and type II wrists. The tube with $\lambda < \lambda_A$ does not allows the static model of type I wrist proposed in [York 15] for any value of g and type II cutouts must be considered.

As a conclusion, the value of g must be selected above the ν_{min} curve to ensure an elastic deformation of the wrist during operation. However, the value of g should not be close to $2r_o$ ($\nu \approx 1$). In other words, the uncut part of the notches $(2r_o - g)$ should not be too thin because the mechanical properties of the wrist can changes since the oxidation of the material surface during fabrication [Liu 18]. We observe through experiments that the safety thickness of the uncut part should be greater 0.13 - 0.16 mm. As the consequence, the optimal value for the depth of cut g for each ratio λ of the tube corresponds to a point X that just above the ν_{min} curve. In this thesis, the depth of cut g is selected of 0.93 mm. It has to be considered for a given r_o.

Wrist synthesis - other design parameters

After obtaining the value of cut depth, the bending stiffnesses of the tubes and of the wrist are given as follow:

TABLE IV.3 – Bending stiffnesses of the tubes and of the wrist

Outer tube	Middle tube	Inner tube	Wrist
0.2804 Nm^2	0.0077 Nm^2	0.0011 Nm^2	2.896×10^{-6} Nm^2

One can confirm that the bending stiffness of the wrist is less than 380 times that of the inner tube and 2600 times that of the middle tube. Thus, the deformation of the CTR can be neglected under the tendon load which is employed to bend (only) the wrist. Even taking into account the stiffness of the optical fiber that increases the tendon force about 3 times (see Section V.2.1), the decoupled actuation of the hybrid CTR is still valid. The length of the distal uncut portion b is chosen of 2 mm (including the height of the end cap of the wrist). The height of cut and other uncut portions (named as h and c respectively) are designed with the same dimensions. It is important to note that if the height of cut h is too large, the assumption of constant curvature will no longer hold, the risk of buckling-like failure will increase, and the friction loss will be greater [Swaney 17]. Otherwise, if h is too small, it will lead to a very sophisticated fabrication of the wrist and will limit its achievable curvatures. Thus, the value of h is considered between 0.25 and 0.50 mm. As the length of the upper part of the tympanic cavity is around 13 mm, the wrist length L (including the distal uncut portion) will be examined from 5 to 8 mm to find the best design which maximizes the coverage volume by inserting the robot through the entry hole in the mastoid. The number of cutouts n, which is now a variable depending on L, b, h, and c as given in (IV.11), will vary to obtain different values of h in the mentioned survey interval.

$$L = b + nh + (n-1)c \tag{IV.11}$$

The range of the design parameters of the wrist is summarized in Table IV.4.

TABLE IV.4 – Range of the design parameters of the wrist

g	b	L	h	c	n
0.93 mm	2 mm	$5-8$ mm	$0.25-0.5$ mm	equals h	using Eq. IV.11

Simulation results

This part presents the simulation results of the coverage volume within the tympanic cavity for different robot designs. In general, the design parameters of the wrist consist of L, h, c, g, b, and n. However, g and b have their specified values and c is fixed at the same value as h (see Table IV.4). The other parameters L, h, n are related to each other through (IV.11). Once we determine any two of these three variables, the other can be deduced automatically. Since n must be a natural number, it should be one of the two design parameters determined beforehand. In this study, we let L run from 5 to 8 mm, then calculate all possible values of n so that h ranges between 0.25 and 0.5 mm. Besides, the CTR has only

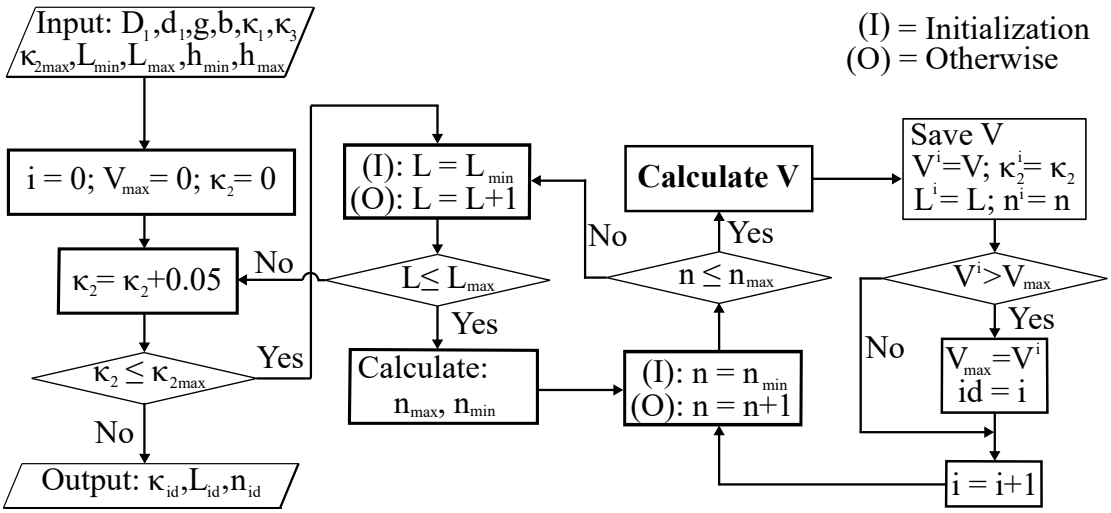

FIGURE IV.12 – Algorithm for determining the robot design parameters. κ_2, L, and n will be sequentially examined within their limits. The block "Calculation V" is the coverage volume calculation task.

one design parameter κ_2 that leads to the total iterative variables of the solving algorithm, which are κ_2, L, and n. The best values of these quantities will be selected corresponding to the maximum coverage volume.

The algorithm for determining the robot design parameters is illustrated in figure IV.12. The inputs of this algorithm include the inner and outer diameters of the innermost tube (d_1, D_1), the depth of cut (g), the height of distal uncut part (b), and the limited (minimum and maximum) values of the design parameters (except for n) as shown in Table IV.4. Note that the limited values of n will be calculated using the considered value of the wrist length L and the range of h. For each combination of the robot design parameters (κ_2, L, n), the function "Calculation V" will be run for obtaining the coverage volume (see Subsection IV.1.2.a). By comparing among the set of different coverage volumes, we can figure out the combination (κ_2, L, n) maximizing this volume which is also the output of the algorithm.

TABLE IV.5 – Middle ear coverage volume (mm^3) by different robot designs depending on L (mm), n, and κ_2 (mm^{-1}) using the mastoid entry path.

L-n	κ_2		L-n	κ_2		L-n	κ_2	
	0.10	0.05		0.10	0.05		0.10	0.05
5-4	432	387	5-5	**434**	386	5-6	433	385
6-5	419	368	6-6	418	367	6-7	417	366
6-8	417	366	7-6	414	337	7-7	412	337
7-8	412	336	7-9	410	336	7-10	410	336
8-7	371	281	8-8	371	280	8-9	372	280
8-10	373	281	8-11	373	278	8-12	374	277

The comparison of accessible spaces using different hybrid CTR designs is demonstrated in Table IV.5. As the attic is the most frequent site of residual cholesteatoma [Gaillardin 12] and as it is difficult to reach this part from the auditory canal, the transmastoid access to the attic is the most important one considered in this thesis. In general, the coverage volume is larger for the higher value of κ_2. The coverage volume of robot designs with the same values of κ_2 and n will decrease if L increase from 5 to 8 mm. The correlation between the coverage volume and the number of cuts n is only positive when $\kappa_2 = 0.1\ mm^{-1}$ and $L = 8\ mm$ and is negative in all other cases. Based on the simulation result, $\kappa_2 = 0.1\ mm^{-1}$, $L = 5\ mm$, and $n = 5$ are chosen to fabricate the hybrid concentric tube robot for the purpose of the biggest coverage volume. The coverage volume obtained is 434 mm^3 through the entry hole on the mastoid and 527 mm^3 through the auditory canal. The total coverage volume is 884 mm^3, which corresponds to 93.1% of the tympanic cavity volume (see Fig. IV.13d). In addition, Fig. IV.13 shows the comparison of accessible spaces using different robot designs through the created mastoid hole. The coverage volume using the hybrid CTR (434 mm^3 (see Fig. IV.13c)) is almost twice as large as that obtained by only employing the wrist (214 mm^3 (see Fig. IV.13a)) or only employing the CTR (220 mm^3 (see Fig. IV.13b)). One can confirm that hard-to-reach locations of the middle ear can be accessed by the hybrid CTR.

It is important to note that the found set of design parameters depends on the diameters of the tubes selected for fabrication. In this work, we have tried to shrink the innermost and the middle tubes with diameters of 0.86/0.66 mm and 1.20/1.02 mm, respectively. Thus, the obtained design parameters is changed, in specific $\kappa_2 = 0.1\ mm^{-1}$, $L = 6\ mm$, and $n = 6$. Both two versions of the hybrid CTR will be utilized in this thesis.

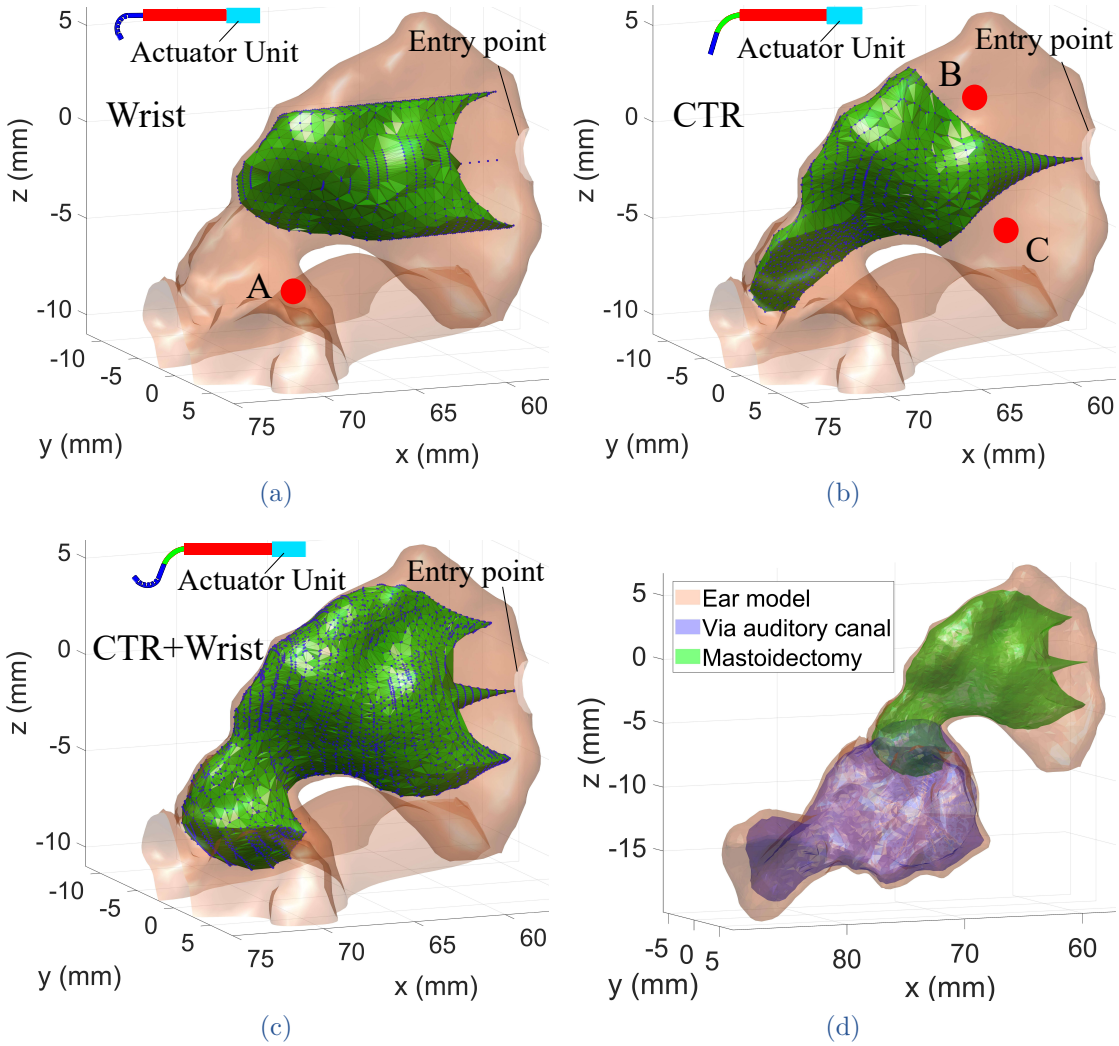

FIGURE IV.13 – Simulations of the tympanic cavity coverage volume by the robots that are inserted via a $3-mm$ hole through mastoid: (a) only 1-segment unidirectionally notched tube is considered, point A cannot be accessible by neither the robot that has only 1 wrist nor one that has 2 wrists in terms of C and S shapes as the inserting path requires bending in two different planes; (b) only the CTR is considered, the robot cannot reach point B and C due to the limitation of the precurvature of the tubes; (c) the CTR with the distal wrist significantly improves the coverage volume inside the tympanic cavity. (d) Total tympanic cavity coverage volume by the hybrid concentric tube robot inserted via the two accesses.

IV.2 Robot fabrication

This section will introduce the fabrication of the hybrid CTR including the precurved shape setting of the tubes, the machining of the notched wrist, and the printing of the end cap. Different methods will be considered for each part, then the obtained results will be discussed.

IV.2.1 Precurved tube shape setting

The tubes which constitute the CTR were acquired in a straight shape from Euroflex GmbH, Germany [5]. Nitinol alloy has been selected for the precurved middle tube thank to its shape memory and superelasticity property [Jani 14]. However, making curved devices out of this material from the straight initial shape is not a straightforward task due to the consideration of the proper shape-setting method (involved in the obtained accurate shape) and of the mechanical properties (e.g., retaining superelasticity). Besides, a quick, easy, and accurate shape-setting technique is highly desirable in research community for a custom fabrication of very low volume prototypes by Nitinol. In the literature, many heat treatments

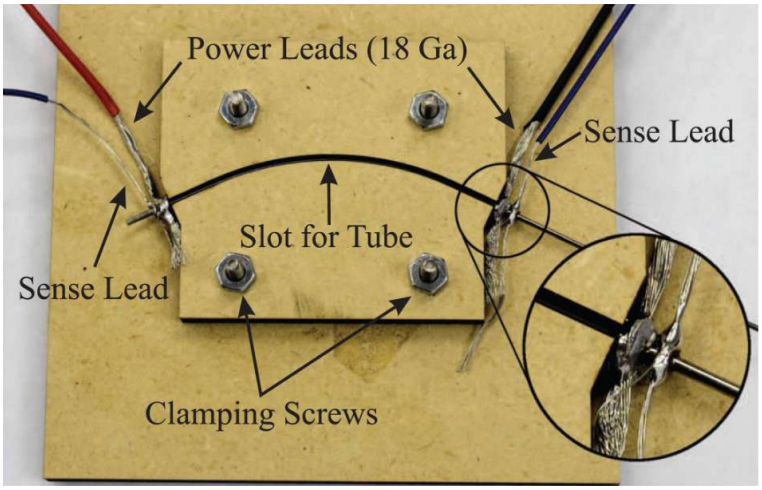

Figure IV.14 – Shape setting of Nitinol using Joule heating property [Gilbert 15].

with different samples, varying treatment times and temperatures were proposed to study the creation of Nitinol samples with desired curvature and mechanical properties [Morgan 04]. Heating methods can be generated using either a furnace [Kim 14] or an electrical resistance heating technique [Gilbert 15]. The later one (see figure IV.14) that uses Joule heating was proven as a fast shape setting method which reduced the overall cost and improved the accuracy of the obtained results with less springback. Even so, in [Gilbert 15] it required a complete system for closed loop, high temperature resistance heating of Nitinol tubes. Indeed, the fixtures were made of inexpensive medium density fiberboard (MDF), an Arduino

microcontroller board was employed to regulate the measured resistance of the heated part by switching between on-off states, and a MOSFET is used to control the flow of current based on the command from the microcontroller.

At FEMTO-ST institute, we employ a furnace for the tube shape setting. This approach is typically recommended by Nitinol manufacturers for low-volume laboratory prototyping applications on medical devices and robotics. The temperature range of 500-550°C was recommended in many studies [Kim 14, NDC, Inc. 22]. However, to obtain more accurate shape of high bending curvature with a minimal springback, the increase in temperature is required [Pelton 04]. In this work, the temperature of the air furnace is set to 600°C which has already been proposed by our colleague in [Kudryavtsev 18]. The air furnace model N 32/H from Nabertherm GmbH company (Germany) [6] with the adjustable temperature up to 1280°C was used for heating of the Nitinol tubes. The shape-setting of the middle tube was performed using a mold with grooves of the desired curvature. The tube specimen was placed in an air furnace at 600°C for 20 minutes, and then rapidly quenched in cold water for immediate cooling.

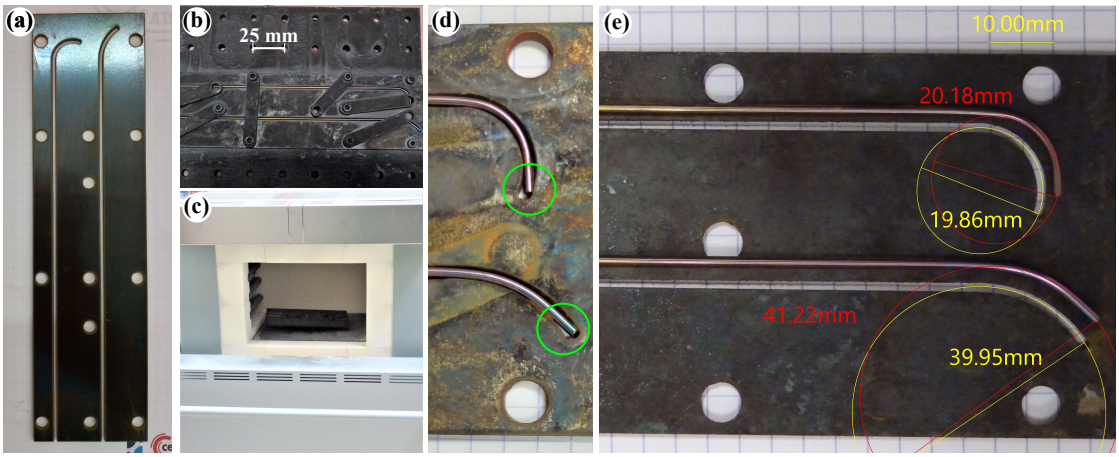

FIGURE IV.15 – Nitinol tubes shape-setting. (a) Creating the grooves of the desired curvatures (10 *mm* and 20 *mm* radius) on the template utilizing a ProtoMAX water jet cutter machine (from OMAX company, France). (b) Inserting the tube into the fixtures (template and support). (c) Putting the fixtures and the tubes in the air furnace at 600°C for 20 min. (d) The obtained result after quenching in cold water. (e) The final result after cleaning.

The curving process is shown in figure IV.15. Two curved tubes of different curvatures: 0.05 and 0.1 mm^{-1} are created. The obtained curved tubes are almost identical to the grooves (see figure IV.15e) with a very small springback (less than 3%). To obtain the curvature of the tubes as well as of their grooves, the calibration and measurement process of Toupview [7] is used for the 2D image captured by a digital camera (DNT DigiMicro 2.0). The main observed error is caused by the air

5. The EUROFLEX company website: https://www.euroflex.de/en.html.
6. Nabertherm GmbH company website [Online]: https://nabertherm.com/en.

gaps between the grooves and the tubes that allow these tubes to not be exactly constrained to the desired curvature (see figure IV.15d). It is important to select material for the fixtures with a coefficient of thermal expansion (CTE) close to that of Nitinol to reduce the air gaps during the heating. The CTE of Nitinol is about 11×10^{-6} K^{-1} [Uchil 99]. Thus, we employ steel to create the fixtures with CTE of 11-13 $\times 10^{-6}$ K^{-1} depending on its composition [Xie 08].

IV.2.2 Wrist

Fabricating the distal wrist of the proposed hybrid CTR requires notching the Nitinol innermost tube using a micromachining method. As shown in Table. IV.6, the notching techniques proposed in the prior works includes: CNC milling [York 15, Swaney 17, Eastwood 16], laser cutting [Eastwood 18, Chitalia 20b, Pacheco 21], and electrical discharge machining (EDM) [Kutzer 11, Gao 16a, Legrand 21].

TABLE IV.6 – Different fabrication techniques of the notched wrist in the literature. OD and ID stand for the outer and inner diameters of the notched tubes.

Reference	Fabrication method	OD - ID (mm)	(g) - (h) (mm)	Possible cut height (mm)
[Kutzer 11]	wire EDM	5.00 - 3.99	3.00 - 0.81	> 0.13
[York 15]	CNC mill	1.16 - 0.86	0.97 - 0.51	> 0.51
[Gao 16a]	wire EDM	6.00 - 4.00	-	-
[Eastwood 16]	CNC mill	1.80 - 1.40	1.32 - 1.14	> 0.51
[Swaney 17]	CNC mill	1.16 - 0.86	0.97 - 0.51	> 0.51
	wire EDM	0.46 - 0.28	0.33 - 0.15	-
[Eastwood 18]	laser cutting	1.25 - 1.05	-	> 0.05
[Chitalia 20b]	laser cutting	1.93 - 1.82	1.60 - 0.50	-
[Pacheco 21]	laser cutting	1.62 - 1.40	1.40 - 0.50	-
[Legrand 21]	wire EDM	2.30 - 1.80	2.14 - 1.14 [8]	-

IV.2.2.a CNC milling

Notching Nitinol tubes using CNC milling requires gluing the tube in a channel drilled in an aluminum block, then standard two-flute square end mills (0.02 *in* in diameter) are used to create the notches (see figure IV.16). This technique provides square corners of the cutout but the height of cut is limited by the diameter of the end mill which is difficult to be reduced in size for a durability guarantee. The

7. [Online]: http://www.toupview.com/product/showproduct.php?id=143&lang=en.
8. Selected among many different designs of the wrist presented in the research article.

smallest diameter of the end mill proposed in the literature is 0.02 in (≈ 0.5 mm) [Swaney 17]. To scale down the height of cut of the notches, a wire EDM or a laser cutting will be used.

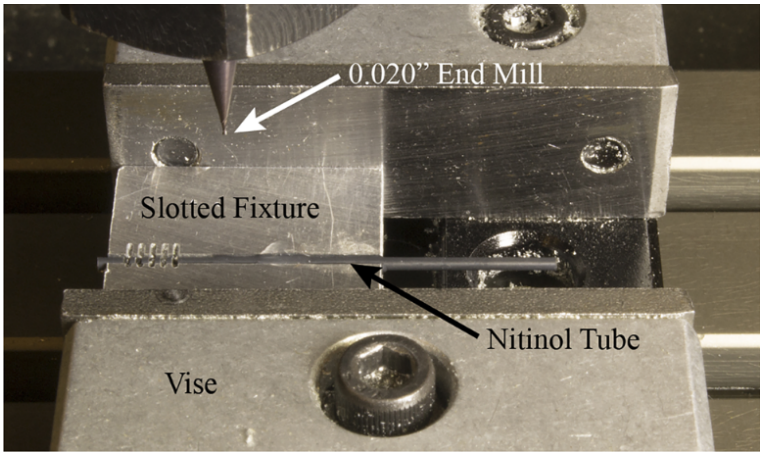

FIGURE IV.16 – Fabricate the wrist by using a CNC manufacturing process with 0.02 in end mill [Swaney 17].

IV.2.2.b **Laser cutting**

The laser cutting method based on the laser ablation of metal material with the smallest width that can be cut (i.e. 0.05 mm) has a better performance in comparison with the two other ones. Thus, it is a good candidate for fabricating notched wrists with dimension of $1 - 2$ mm in diameter (see Table IV.6). The company Preco Inc., USA has provided a small diameter laser tube cutting machine model RT1000 (duty cycle 12%, power 250 W, and pulse frequency 500 Hz) that incorporates the rotation of the tube during cutting process [Kim 20]. Even so, to perform a precise narrow cut as well as to avoid most of the unwanted effects of the heat affected zone during the laser ablation, ultra-short laser (e.g., femtosecond) need to be used [Garasz 16].

IV.2.2.c **EDM process**

Through the wire EDM process, the desired shape of Nitinol tube is obtained by using a series of rapidly recurring current discharges between two electrodes, separated by a dielectric liquid (e.g., water) and subject to an electric voltage. The obtained results with wire EDM are nearly identical to the CNC wrists except for the rounded corners. The radius of these rounded corners is dependent on the diameter of the EDM wire. The rounded corners allow reducing the strain concentrations during operation compared to the square corners. However, the heat of the wire EDM process may induce unexpected characteristics of the wrist that could result in the small decrease in the fatigue life of the wrist [Swaney 17].

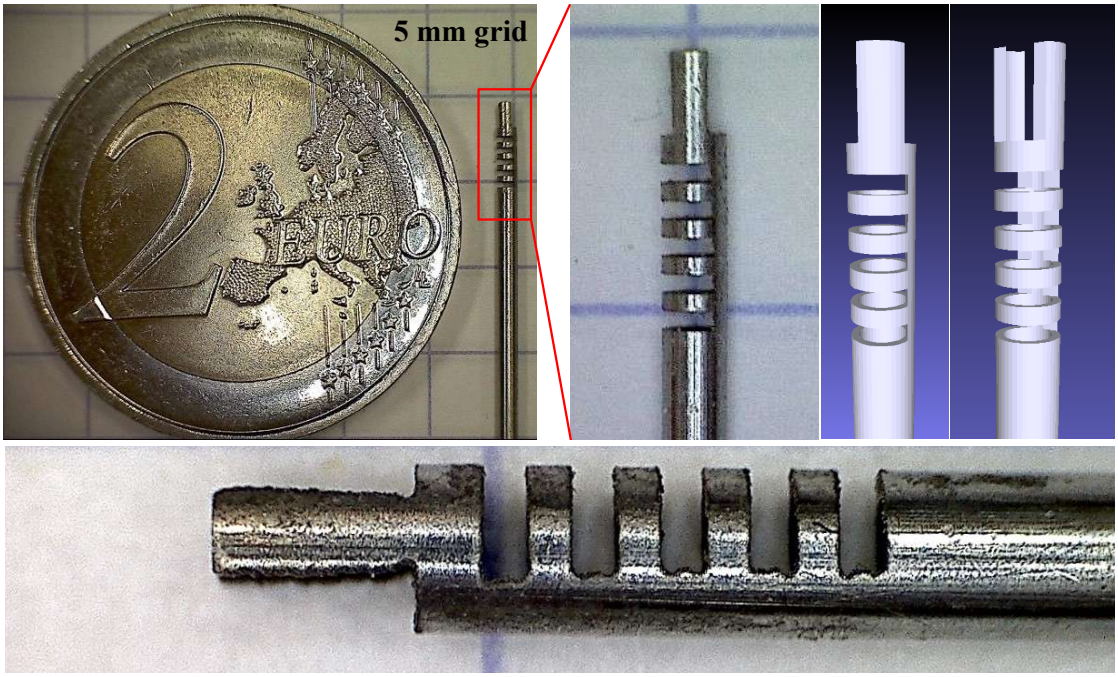

FIGURE IV.17 – The distal end of the inner tube is notched with EDM method. The parameters of the wrist is selected as the simulation result including: $g = 0.93\ mm$, $b = 2\ mm$, $L = 5\ mm$, $h = c = 0.33\ mm$, and $n = 5$ cutouts. Two additional notches (1.5 mm cut height and 0.2 mm cut depth) are created to fix the relative rotation of the end cap with respect to the wrist.

At FEMTO-ST Institute, the Charmilles 2050 TW machine for wire-cut EDM, with the diameter of the wire being 0.1 mm was employed to create the wrist. The cutting time was less than 2 minutes. The final notching result is shown in figure IV.17. Two notches were added at the distal section of the wrist to fix the relative rotation of the end cap. In addition to this design, these additional notches can be situated symmetrically on either side of the line connecting the centers of the two holes [Nguyen 21a]. The following section will present the specific end cap used of the proposed hybrid CTR.

IV.2.3 End cap

The cap of the wrist has a specific design to fix its relative rotation with respect to the wrist and constrain the tip location of the tendon and of the optical fiber. Two notches are added to the distal end of the tube (see figure IV.17) and there are parts of the end cap that match with these two distal notches to fix the relative rotation between the end cap and the innermost tube. The diameter of the end cap is approximated to that of the inner tube ($\approx 1\ mm$). Through it, there are two tiny holes to constrain the position of the laser optical fiber (0.42 mm in diameter) and the tendon (0.1 mm in diameter). As the specific design of the end cap requires the

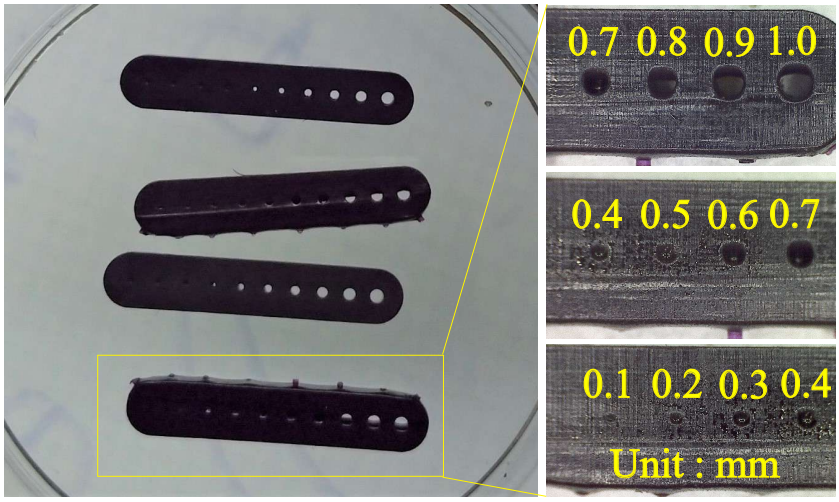

FIGURE IV.18 – Test of printing tiny holes with diameters from 0.1 to 1.0 mm with the machine from Formlabs. Some holes are not through as printing errors.

FIGURE IV.19 – Hybrid CTR is built according to the simulation results. The laser optical fiber protrudes about 1 *mm* from the outside of the end cap. The outer and inner diameters of the three tubes are: 2.50 and 1.80 *mm*, 1.50 and 1.25 *mm*, 1.08 and 1.00 *mm*,

fabrication at very small scale, 3D printing methods are considered for its creation instead of machining methods. The following will present a comparison result of different 3D printing methods often used in practice.

The low-cost 3D printing machine from Formlabs was first used. This technique is a simple and fast way to create the end cap based on the STL file of the sample. With the new technology Low Force Stereolithography (LFS), Formlabs has completely re-engineered its approach to resin-based Desktop 3D printing to considerably reduce the forces exerted on parts during the print process. This technique uses a flexible tank and linear illumination to deliver surface quality and print accuracy. Additionally, lower print forces allow for light-touch support structures that tear away with ease. A test was conducted to evaluate the performance

8. [Online] https://www.nanoscribe.com/fileadmin/Nanoscribe/Solutions/Materials/Folder-Printing-Materials.pdf.

of this 3D printing method to create the tiny holes. The holes with diameters varies from 0.1 to 1.0 mm were considered for 4 times of printing. As shown in figure IV.18, the tiny holes ($\sim$ 0.20 mm in diameter) for fixing the tendon were not through as given in the design. Indeed, only holes with a diameter greater than or equal to 0.8 mm were guaranteed to be through. The method failed to print holes smaller than 0.4 mm. For holes with a diameter from 0.4 to 0.7 mm, the obtained results were pretty random.

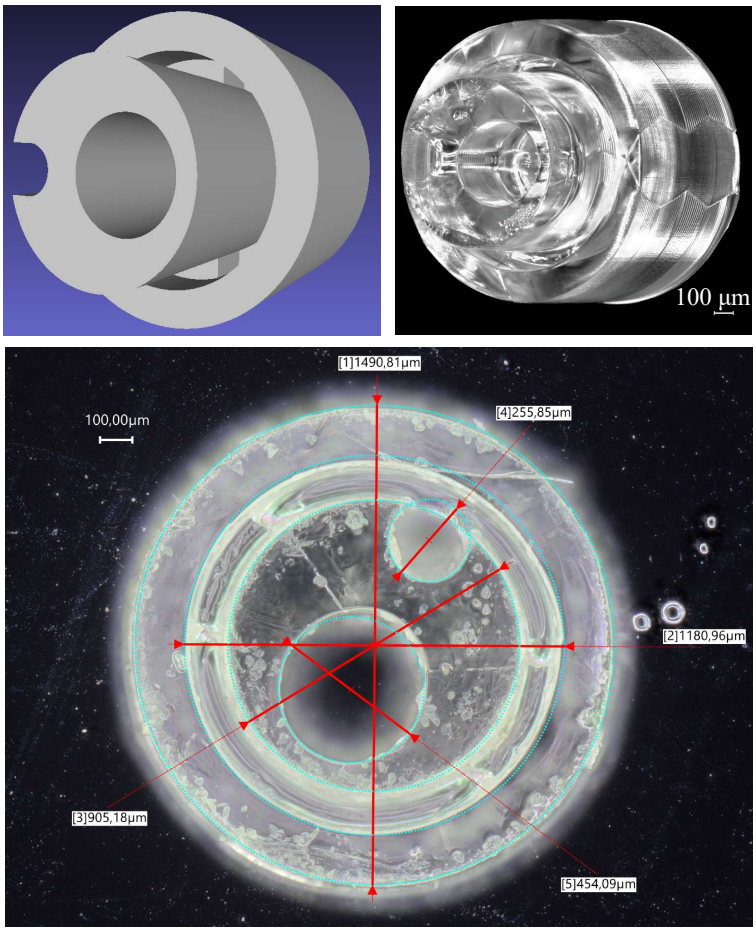

FIGURE IV.20 – End cap of the wrist fabricated using Nanoscribe 3D printing resin IP-Q material. Two tiny holes for the tendon and the optical fiber are 0.23 mm and 0.48 mm in diameter. The end cap has parts corresponding to two additional notches of the wrist for fixing the relative rotation between them. These parts locate symmetrically on either side of the line connecting the centers of the two holes.

Nanoscribe 3D printing uses a product line of negative-tone resins, called IP Photoresins, which are optimized for Two-Photon Polymerization (2PP). This technique can be applied to ample disciplines, some of which involve industrial mastering (e.g. refractive and diffractive microoptics), scientific microfabrication (e.g. life sciences, material engineering), and integrated photonics (e.g. on-fiber

and on-chip printing). It was proven as a better choice for wafer-scale fabrication of high precision (resolution 100 nm). Thus, the problem of printing the tiny hole was solved. Even so, as using resin IP-Q material with degradation temperature of 242°C [9], the printing method carried a risk of thermal distortion of the end cap during laser ablation. To avoid this unexpected phenomenon, the distal end of the optical fiber was required protruding from the outside of the end cap a short distance (about 1 mm) as shown in figure IV.19. A Nanoscribe 3D printed end cap was used in our work [Nguyen 21a]. It took 1 hour and 20 minutes to print this end cap. In order to evaluate the precision of the printing method, the microscope images of this end cap were used. The diameters of the tiny holes that constrain the optical fiber and the tendon were measured with an error about 26 μm for both holes (see figure IV.20).

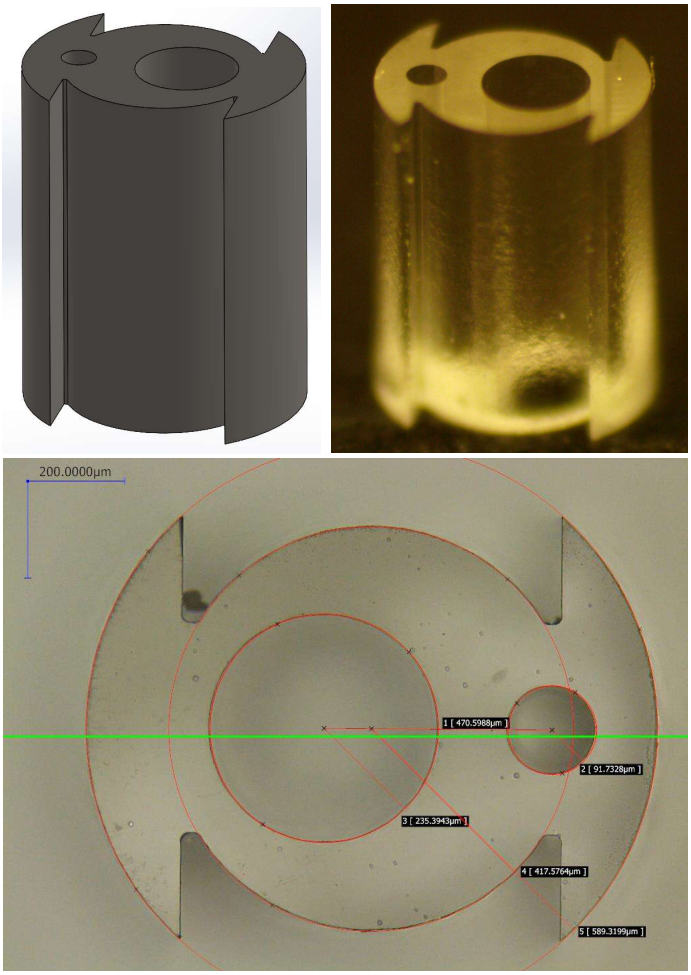

Figure IV.21 – Microscopic image of the end cap created with FEMTOprint. The outer radius of the end cap is 589 μm (nominal value: 600 μm). The radii of the two tiny holes are 91 μm (nominal value: 75 μm) and 235 μm (nominal value: 220 μm). The distance between the centers of these holes is 470 μm (nominal value: 470 μm).

FEMTOprint can be considered as a good candidate to fabricate the end cap. It is a 3D printing technology that uses a light source focused inside glass to locally modify the refractive index and density of the material. It enables the production of sub-micron glass structures that can be used in fields like microoptics, microfluidics, electronics, and micromolding. This technique is also high-performing with a resolution smaller than 1 μm. In addition, by using glass material that can only be molded at very high temperature (approximately 1400°C to 1600°C), it allows avoiding the thermal distortion of the end cap during operation. The glass is also a biocompatible material and is resistant to corrosion, abrasion, and scratches as well as chemical reaction. The obtained result is shown in figure IV.21 where the nominal diameters of the tiny holes are 150 μm and 440 μm for the tendon and the optical fiber, respectively. The measurements show that the dimensional printing error is about 30 μm.

IV.2.4 Tendon selection

As the wrist is at millimeter size, the selection of the tendon is important. It needs to be thin enough to be integrated inside the tube lumen but durable with a tension of about $1 - 2$ N. Consider these requirements, nylon wire with diameter of 0.15 mm seems to be a good choice for the tendon of the wrist (see Fig. IV.22a).

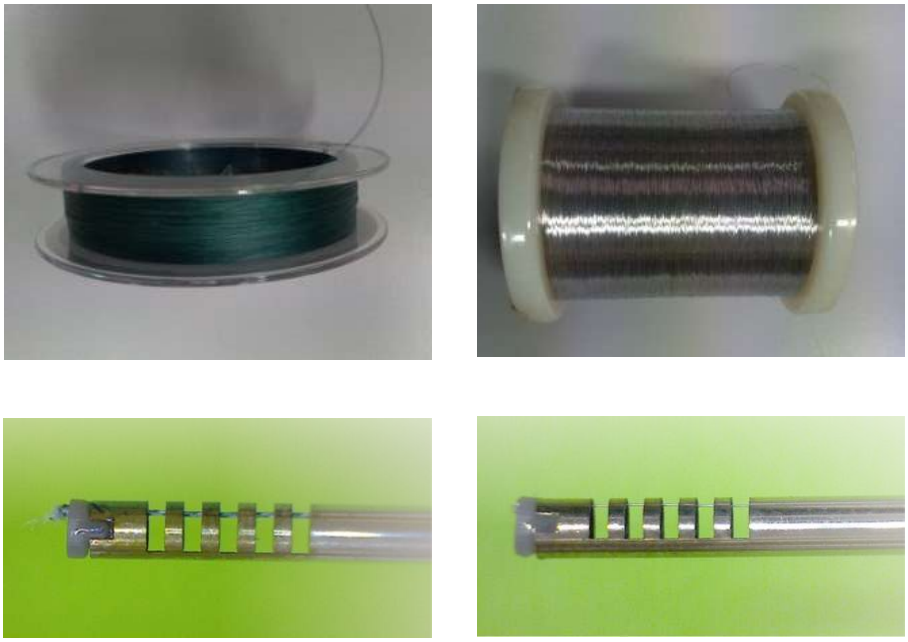

(a) (b)

FIGURE IV.22 – Consideration of different tendons used to bend the wrist: (a) nylon material with diameter of 0.15 mm and (b) steel wire with diameter of 0.1 mm. The wrists shown in this figure are only for the purpose of demonstration and does not have the same parameters as that of the proposed hybrid CTR.

Furthermore, such a tendon is almost an ideal string without the shearing force. However, as made up of many small twisted nylon fibers, the end of this wire is always spread out and makes it difficult to be gotten through the tiny hole of the end cap. In addition, fibers of the nylon wire can be broken by friction interaction with the corners of the cutouts. Thus, a thin steel wire is considered in this thesis (see Figure IV.22b). It allows obtaining a smaller hole on the end cap to attached itself at the distal end of the wrist and does not wear out due to the friction. To be considered as an ideal string, it needs to have a small diameter (0.1 mm).

IV.2.5 Benchtop prototype

After fabricating, the components are integrated with each other to form the hybrid CTR, which is controlled by an actuator unit. Experimental assessments of the hybrid CTR were performed on a benchtop prototype (see figure IV.23) which has already been used as our validation robot for the kinematic model proposed in [Pourafzal 21]. As a reminder, this benchtop prototype has a total length of 56 cm. It is equipped with an actuator unit with 3 linear and 3 rotary stages. The translations and rotations were generated using Beckhoff step motors with a positioning accuracy level lower than 1 μm and 0.02° for the translation and rotation, respectively. The linear-rotation stages and motor brackets were quickly fabricated by 3D printing. Each tube is fixed with a compliant gripper in order to avoid local deformation and excessive friction. A force sensor (ID CZL635) from Phidgets INC, Canada [10] was employed to measure the tendon force. This sensor has a 50 N measuring range and a 25 mN resolution.

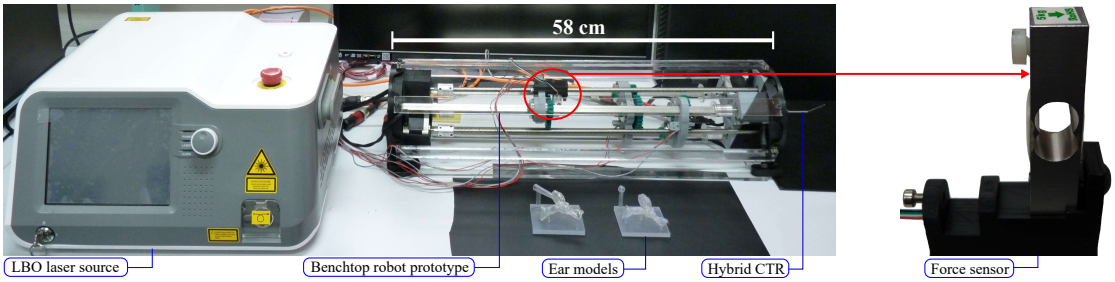

FIGURE IV.23 – Our experimental setup. The actuator unit consists of three part. Each part can perform a translation and a rotation. The outermost tube is fixed to the actuator unit's frame. Two linear-rotary stages are used to translate and rotate the middle and the innermost tubes. The last linear-rotary stage equipped with a force sensor is employed to drive the tendon and measure its tension force. Thus, 5 degrees of freedom is used in this letter.

10. https://www.phidgets.com/

IV.2.6 Laser ablation tool

An LBO fibered laser (Velas-8G) with the wavelength of 532 nm, and the adjustable power from 0.5 to 8 W (see figure IV.23) [11] was employed to vaporize cholesteatoma samples collected from Besançon Hospital [12]. The LBO laser has the same wavelength as the recommended KTP one (Potassium-Titanyl-Phosphate laser) for cholesteatma laser surgery [Le Nobel 16]. The emission mode including continuous, repetitive, or single shot with the pulse duration between 10 µs and 3 s. It is equipped with a pedal to activate the laser beam. The optical fiber has a core diameter of 400 µm and a numerical aperture of 0.22. It is important to note that the optical fiber used in this thesis is not an optimal one for the requirements of the middle ear surgery as it leads to a technical limitation of the bending radius of the wrist as discussed in Chapter III. Even so, it was used in this work to complete the experiments that illustrate the operation of the proposed hybrid CTR.

IV.3 Conclusion

This chapter began by analyzing the reconstructed anatomical model of the middle ear, afterward the robot synthesis based on the anatomy was presented. We first provided a comprehensive analysis of the cut depth of the wrist to obtain the optimal value of this quantity based on the radii of the innermost tube. Then, the other design parameters of the proposed hybrid CTR were chosen based on the workspace that can cover the maximal volume of the tympanic cavity, the decoupled actuation between the wrist and the CTR, as well as the tolerance of the fabrication methods. We showed that the proposed robot can cover 93.1% of the tympanic cavity volume and the coverage volume can be improved by employing the hybrid CTR two times as much as using simply a CTR or just a notched wrist. After obtaining the design parameters, the fabrication processes of the robot components were carried out. Different manufacturing methods were considered for the fabrication of each robot component. The shape setting of Nitinol tube using an air furnace to obtain the middle tube of the CTR was realized with a springback error less than 3%. The fabrication of the notched wrist was fulfilled using the wire-cut EDM method, with the cut height scaling to 0.33 mm. We design a specialized wrist end cap to attach the tendon, constrain the optical fiber, and fix its relative rotation to the wrist. Because the fabrication of this component needs a high level of accuracy, Nanoscribe 3D printing and FEMTOprint techniques have been utilized with printing errors of 26 μm and of 30 μm, respectively. Last but not least, the benchtop prototype was also described in this chapter. The following chapter will present several experimental tests of the robot on this benchtop prototype.

11. The Laser In Surgery company website [Online]: https://laserinsurgery.fr.
12. The samples used are human surgical wastes collected under ethical approval.

Chapter V
Experimental Tests

V.1 Prototype performance assessment 122
V.1.1 Robot repeatability 123
V.1.2 Motion path following 125
V.2 Demonstration 130
V.2.1 Deployment in confined space 131
V.2.2 Cholesteatoma ablation 132
V.3 Conclusion 135

In this chapter, the experiments conducted after robot fabrication will be described. They are categorized into two groups: (i) to assess the prototype performance, and (ii) to demonstrate how the robot works. The former aims at examining the robot repeatability and the ability of the robot to follow a predetermined motion path. The latter, on the other hand, shows the deployment of the robot in confined space and the cholesteatoma laser ablation. As the technical limitation on bending radius of the optical fiber that limits the bending angle of the wrist at 25°, we will only integrate this fiber into the hybrid CTR during the laser ablation test. In addition, as mentioned in Chapter IV, we use the design version with the innermost tube's diameters of 1.08/1.00 (version 1) for determining the robot repeatability (as it allows a clearer image with OCT volume scan) and for demonstrating the cholesteatoma ablation (as it eases the integration of the laser optical fiber). For the remaining experiments, we use the robot version with a smaller dimension (version 2). Table V.1 summarizes the use of these versions and the integration of the laser optical fiber in the following experiments.

Table V.1 – The use of robot design versions in the later tests

Robot repeatability	Version 1	without the OF
Path following assessment	Version 2	without the OF
Deployment in confined space	Version 2	without the OF
Cholesteatoma laser ablation	Version 1	with the OF

V.1 Prototype performance assessment

Experiments were conducted with the benchtop prototype to perform the robot repeatability assessment and the motion path tracking. The actuator unit including 6 Beckhoff step motors was controlled through an EtherCAT slave card which communicates with a computer using a realtime GNU/Linux operating system (Xenomai) (Dell Optiplex 7010 with an Intel Core^{TM} 3.4 GHz processor). This computer, which was known as the robot computer, can regulate the translation and rotation of the tubes by numbering the steps that were applied to the motors after a calibration procedure. The higher level control of the robot was done on another computer (a 2.80 GHz Intel 6-core i5-8400 CPU with a Windows 10 distribution) which sent the translation and rotation control values to the robot computer via a TCP/IP communication protocol. For monitoring and determining the pose of the robot tip, the high level control computer need to be communicated with an OCT scanning and an AURORA sensor respectively. The conceptual scheme of the robotic system used for testing the prototype performance was shown in figure V.1.

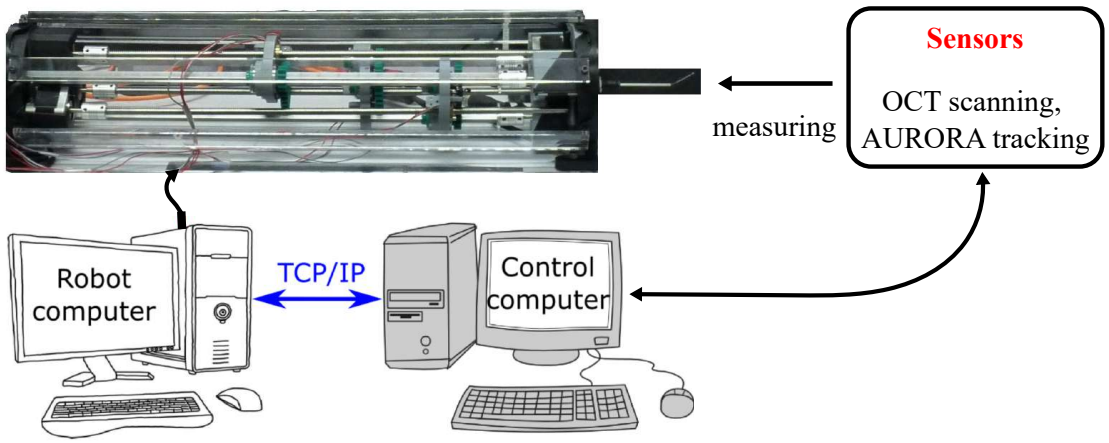

FIGURE V.1 – Conceptual scheme of the hybrid CTR used for the prototype performance assessment.

V.1.1 Robot repeatability

In order to perform sequentially the cholesteatoma detection and removal, the ability to return to the same position between these two phases is an indispensable requirement of the robot. In this section, we propose an efficient method to measure the repeatability of the hybrid CTR without adding any external sensor which can cause unexpected errors in the robot configuration at millimeter scale. This

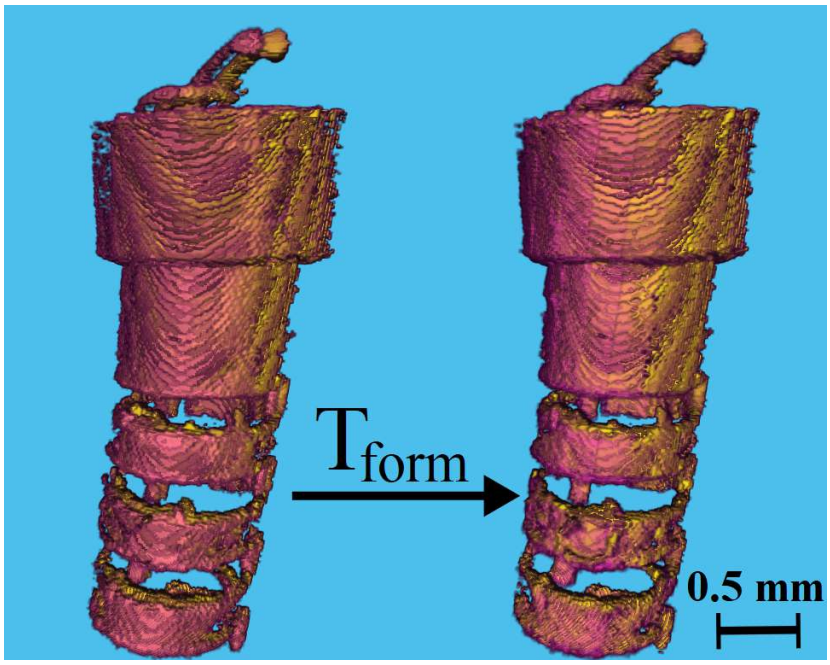

FIGURE V.2 – Left: two different OCT volume images (C-scan) of the same actuation set used for measuring the robot repeatability. Right: after applying the transformation matrix for one image to align it with the other one.

method is based on using OCT volume scanning image of the distal part of the robot and perform the point cloud registration as previously presented in [Wang 20]. A set of 40 volume images was obtained with a Telesto-II 1325nm spectral domain from ThorLabs by translating, rotating the tubes as well as bending the wrist, then returning to the same programmed configuration. The purpose of this method is to find the transformation matrix $T_{form} \in SE(3)$ to align the moving point cloud (volume image) with the reference point cloud. The first volume image was employed as the reference and the function *imregtform* of MATLAB was used to estimate the geometric transformation matrix as shown in figure V.2. This function uses one of two different algorithms: gradient descent optimization and one-plus-one evolutionary algorithm [Styner 00] to solve the image registration problem. The first one updates the transformation parameters such that the optimization moves in the direction of the extrema, following the gradient of the image similarity metric (to minimize the mean squared difference of corresponding pixels or to maximize the mutual information of the two images [Rahunathan 05]). For large errors (typically > 1 *mm* for distance error and > 5 *deg* for angular one), the function *imregtform* may not work efficiently. Thus, we need to enhance the alignment process by manually applying a raw transformation matrix $T_{raw} \in SE(3)$ to reduce the errors before running the function *imregtform*. Then, the transformation matrix to be found will be the product of T_{raw} and T_{form}.

The experimental results were shown in figure V.3 including a root mean square error (RMSE) of 0.7 mm for distance errors and 1.34° - 2.42° - 3.11° for the angular ones. These obtained results are acceptable for the requirements of the cholesteatoma ablation in a semi-automated mode. These values are explained by the use of a benchtop prototype not optimized to reach good repeatability. Indeed, the gears are not of good quality and the guides can be improved. These will be considered for the design of a compact and lightweight prototype.

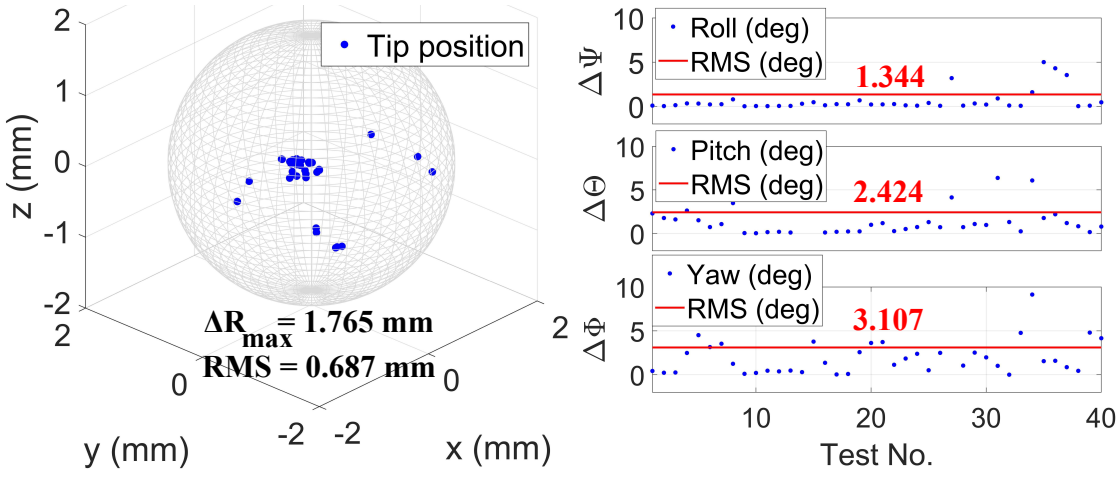

FIGURE V.3 – The measurement of repeatability value of the robot.

V.1.2 Motion path following

This section presents the ability of the hybrid CTR to follow a given path without any constraints on the motion. In the field of control theory, this type of issue can be split into two different problems including path following and trajectory tracking [Gasparetto 15]. The trajectory tracking issue is time-dependent, where the geometric path is time-parameterized. In contrast, the path following problem, is time-invariant, where the geometric curve is typically a function of the arc length without regard to time.

The effect of the time restriction on the path traced by the robot's tip are showed in figure V.4. While the trajectory tracking may not reach the target points to comply with the time limit, the path following remains the movement of the robot even though there will be a delay in reaching the next goal. As a result, the path following typically performs better than trajectory tracking in terms of geometric accuracy and convergence to the reference path.

From the surgeon's perspective, the precise duration of time needed to complete the planned curve is not significant. Indeed, the important factor is the ability of the surgical robot to follow exactly the reference path. Thus, the path following performance of the robot will be taken into consideration. For the purpose of simplicity, this section focus on the performance of the benchtop prototype to control

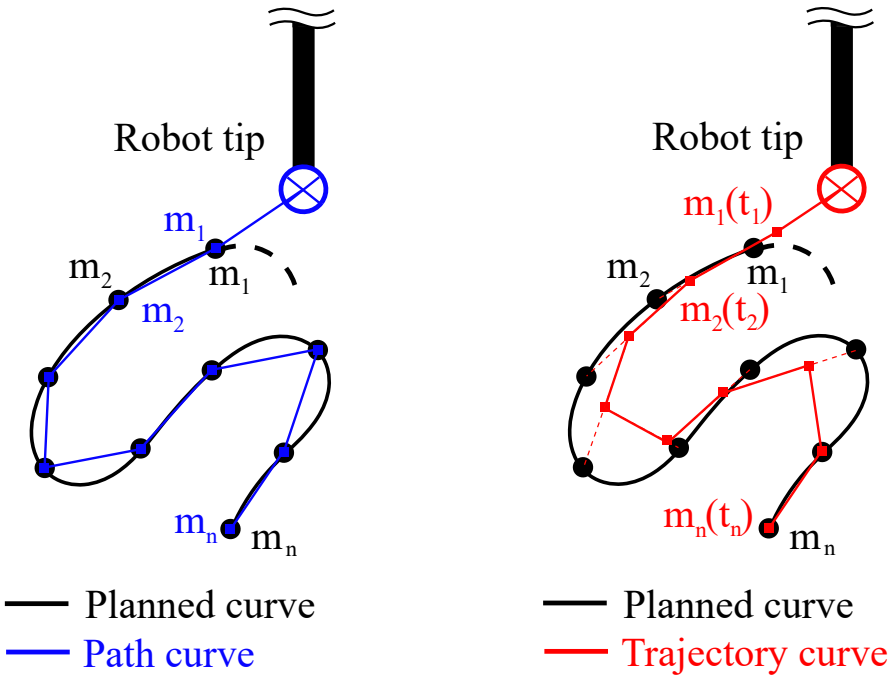

FIGURE V.4 – An illustration of time constraints affecting the paths traced by the robot tip. The movements are carried out by leading the tip directly toward the next target point. The blue line on the left is time-invariant (path following) and the red line on the right considers time constrains (trajectory tracking).

the CTR following a desired path based on its model instead of validating the bending of the wrist which was discussed in Chapter III.

Reference path

There are many algorithms to generate a planned curve in the literature depending on the intended use: to obtain the shortest path between the initial and the target points without collision with the obstacles [Gasparetto 15], to guarantee the smoothness of the path using the B-spline curve [Nguyen 21b], and to enable the surgeon to immediately create the desired curve on a touch screen [Renevier 16]. In this section, the proposed robot will be used to trace a square with edges of 46 mm, perpendicular to the main axis of the benchtop prototype, and 40 mm from the outermost tube's extremity. Starting from the center point of the top side, the next target point is determine by shifting the current point by 1 mm along the reference path (see figure V.5). As the translation and rotation speeds of the tubes are fixed at 2 mm/s and 5 rad/s, respectively, the tangent velocity of the robot's tip can change for different location on its curve. Therefore, the sampling time between two consecutive sets of control values sent by the high level control computer needs to be sufficient to guarantee the time-independent characteristic of the traced path. In this test, this time period is selected of 1 s.

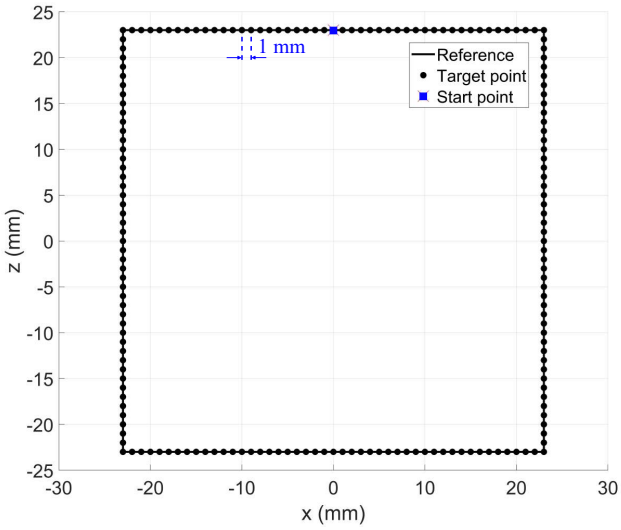

FIGURE V.5 – Reference path is a square of 46 mm.

Control scheme

As a first trial, an open-loop control based on the inverse Jacobian formulation of the CTR model is applied for the path following assessment. As the proposed robot has only one curved tube, it can be considered as piecewise constant curvature sections [Ha 16] that facilitates the inverse kinematic problem. Without loss of generality, assuming that the studied problem is as shown in figure V.6. We first calculate the curvature κ_{12} of the middle (green) section including the innermost

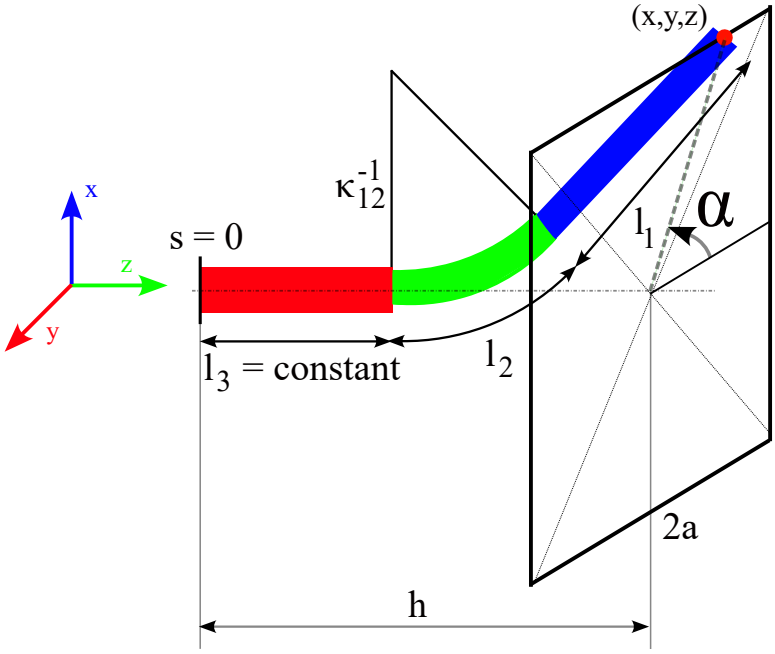

FIGURE V.6 – Illustration of the path following of the proposed robot which can be considered as piecewise constant curvature sections.

and the middle tubes by using equation B.17. This curvature is a constant value. As mentioned in figure IV.23, we fix the outer tube with the robot base. Hence, for each desired position (x^*, y^*, z^*), we numerically solve the inverse kinematic problem for the set (l_1, l_2, α) using Newton's method. The relation between the references (x^*, y^*, z^*) and the kinematic variables (l_1, l_2, α) is shown in equation V.1.

$$\begin{aligned} x^* &= sin(\alpha)\left[\kappa_{12}^{-1}(1 - cos(\kappa_{12} l_2)) + l_1 sin(\kappa_{12} l_2)\right] \\ y^* &= -cos(\alpha)\left[\kappa_{12}^{-1}(1 - cos(\kappa_{12} l_2)) + l_1 sin(\kappa_{12} l_2)\right] \\ z^* &= l_3 + \kappa_{12}^{-1} sin(\kappa_{12} l_2) + l_1 cos(\kappa_{12} l_2) \end{aligned} \tag{V.1}$$

These variables allow obtaining the control input $\boldsymbol{q}$ that will be sent to the robot computer (see figure V.7). In this test, $\boldsymbol{q}$ consists of 6 elements:

- q_1 : linear position of the middle tube
- q_2 : linear position of the inner tube
- q_3 : linear position of the tendon (used to control the bending of the wrist)
- q_4 : rotation angle of the middle tube
- q_5 : rotation angle of the inner tube
- q_6 : rotation angle of the tendon (used to control the twist of the tendon)

As the wrist is held in a straight position during this test, thus $\Delta q_3(k) = \Delta q_2(k)$ (where $\Delta q_i(k) = q_i(k) - q_i(k-1)$). In addition, to prevent twisting the tendon and friction between the middle and inner tubes, we set $\Delta q_4(k) = \Delta q_5(k) = \Delta q_6(k)$.

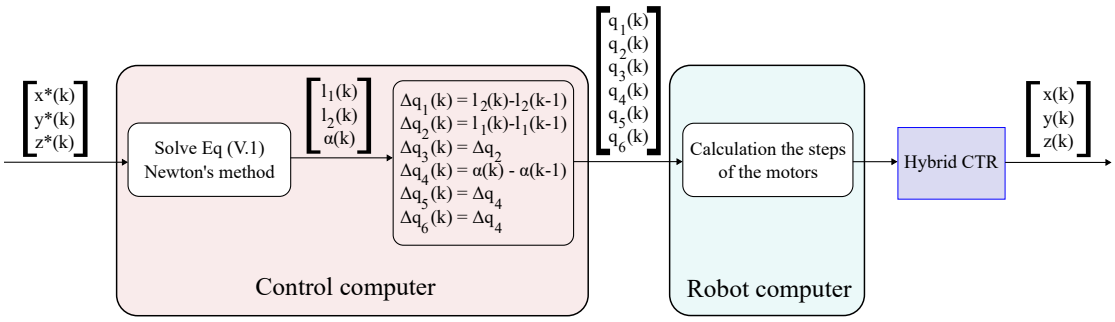

FIGURE V.7 – Open loop control scheme used for the path following assessment.

We have the following equations:

$$\begin{aligned} q_1(k) &= q_1(k-1) + l_2(k) - l_2(k-1) \\ q_2(k) &= q_2(k-1) + l_1(k) - l_1(k-1) \\ q_3(k) &= q_3(k-1) + l_1(k) - l_1(k-1) \\ q_4(k) &= q_4(k-1) + \alpha(k) - \alpha(k-1) \\ q_5(k) &= q_5(k-1) + \alpha(k) - \alpha(k-1) \\ q_6(k) &= q_6(k-1) + \alpha(k) - \alpha(k-1) \end{aligned} \tag{V.2}$$

The robot computer calculates the steps of each motor control the movements of the hybrid CTR.

Path following

Dissimilar to the repeatability assessment, in this experiment, the robot's tip travels in a workspace that is outside the OCT's range of measurement. Thus, the AURORA magnetic tracking [1] was used to measure its position. As the tracking sensor's distal end is rigid, it cannot be integrated into the lumen of the robot. Thus, a particular end cap of the hybrid CTR is needed to hold the sensor at the robot's extremity. The design of this specific end cap is shown in figure V.8. The cylinder shape of this cap, which measures 2.8 mm in diameter and 8 mm in length, makes it suitable for holding the sensor's end in both its primary and radial axes. Indeed, figure V.9 shows different designs of the end cap for fixing the magnetic sensor. Design 1 allows us to axially hold the sensor without impacting the tendon's end attachment. However, this concept does not allow determining the bending of the wrist with a 5 DoF AURORA sensor. Even so, it is not the case of the current test. Design 2 allows holding the sensor in the primary axis at the extremity of the end cap. However, such a long end cap can potentially close the tendon hole during printing, therefore it is necessary to make this hole larger than that of the end cap presented in Chapter IV. As a result, the tendon's attachment at the extremity may affect the sensor's holding. Because of this, we need to move the sensor's hole in order to separate it from the tendon. Additionally, as shown in design 3, we suggest using a dual sensor to adjust the measuring offset. In

FIGURE V.8 – Nanoscribe 3D printed end cap of the wrist dedicated to the integration of the AURORA magnetic sensor.

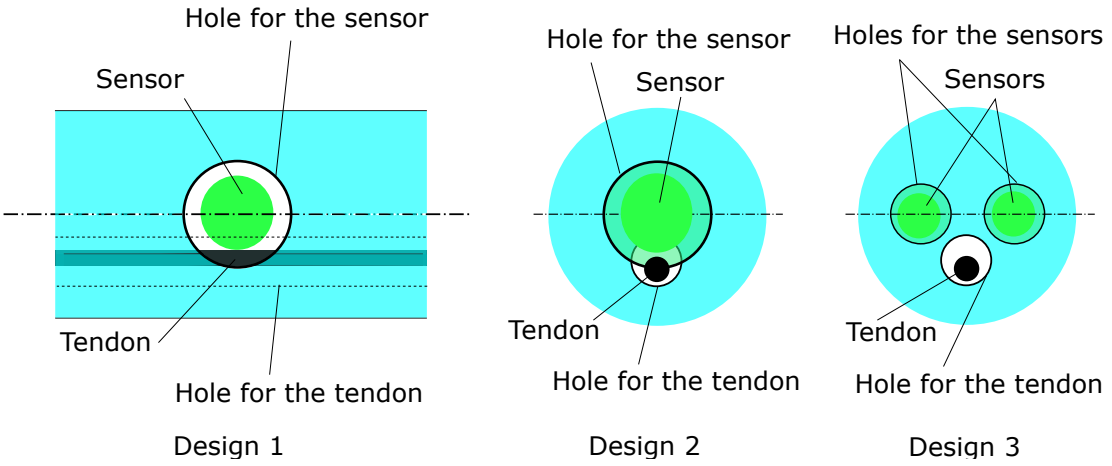

FIGURE V.9 – Conceptual scheme of holding the magnetic sensor with the robot's end cap. Design 1: using 1 mm hole to axially fix the sensor. Design 2: using 1 mm hole to fix the sensor in the principal axis. Design 3: Use two $0.5 - mm$ holes to hold two different sensors.

this work, we combine design 1 with design 3 to fabricate this end cap. Since the bending of the wrist is not taken into account in this test, design 1 is used to hold the sensor because it does more tightly and requires only one sensor to function.

The sensor registration is conducted in two steps. First, the benchtop prototype must be situated on the same plane as the AURORA magnetic generator so that its central axis is parallel to the Oxz plane of the AURORA sensor. Then, we translate the measurement point cloud so that the starting point coincides its corresponding point on the planned path. The sampling time for the tracking measurement is 0.2 ms. The experimental results are shown in figure V.10. The sensor's coordinate system was rotated 90° around Y-axis align with a normal view. The experimental path follows the reference with a mean error of 1.05 ± 0.79 mm and a maximum error of 3.61 mm. Compared to the edge of the square, these values are $2.28 \pm 1.72\%$ and 7.86% respectively.

1. [Online] https://www.ndigital.com/electromagnetic-tracking-technology/aurora/aurora-sensors

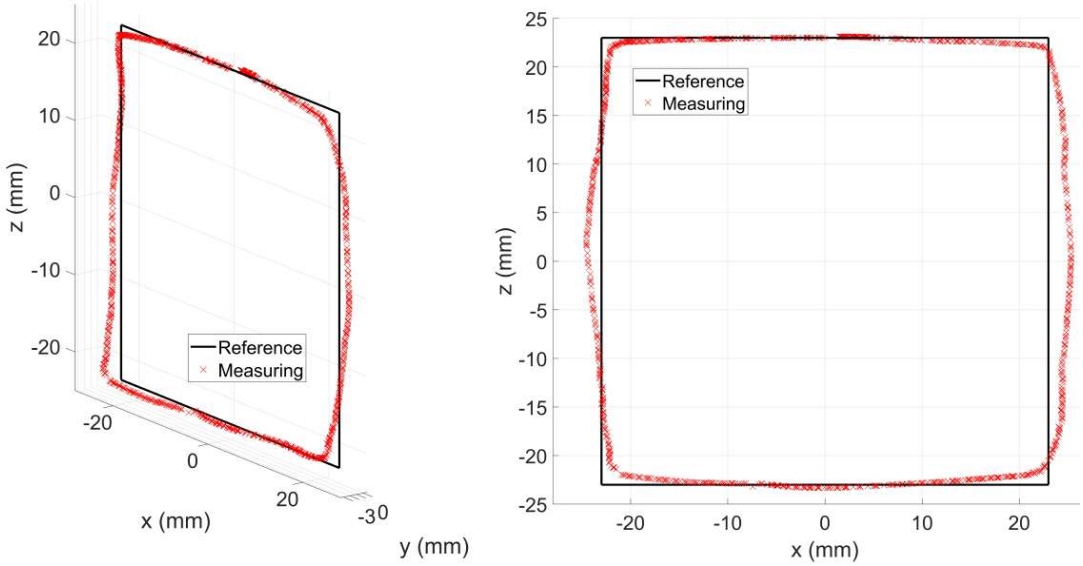

FIGURE V.10 – Reference and experimental paths performed by the hybrid CTR and measured by AURORA tracking sensor. Left: global view. Right: front view.

V.2 DEMONSTRATION

In this section, the deployment of the proposed hybrid CTR inside the confined space of the 3D printed middle ear phantom will be presented. Then, the ablation

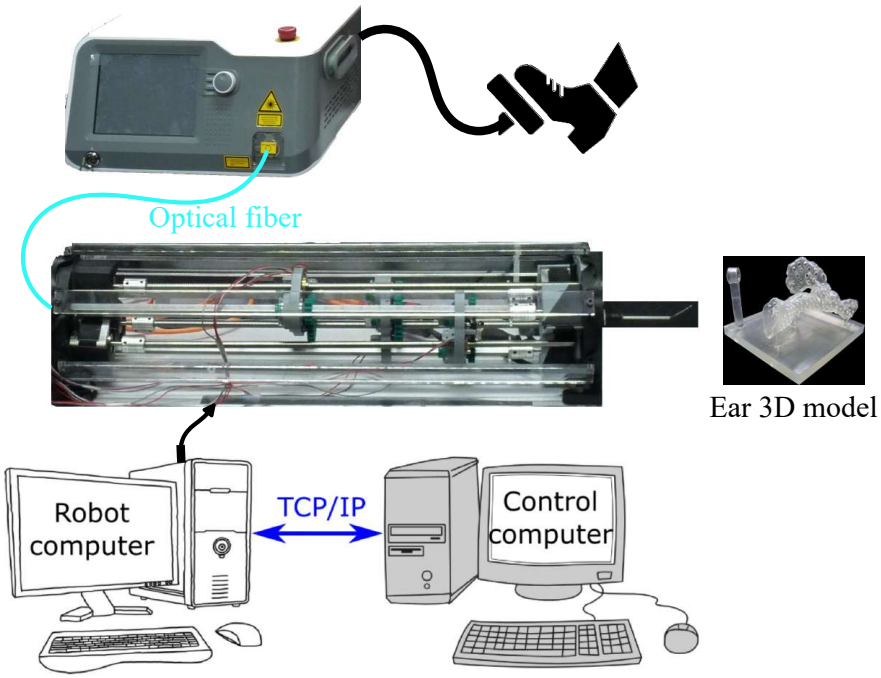

FIGURE V.11 – Conceptual scheme of the hybrid CTR for the deployment in confinded workspace and cholesteatoma laser ablation demonstrations.

of real cholesteatoma cells by the embedded optical fiber on the proposed robot will be demonstrated and the analysis of the ablated volume of the cells with respect to laser parameters will also be discussed. The system scheme used in this section is shown in figure V.11.

V.2.1 Deployment in confined space

The objective here is to demonstrate that the designed robot is able to reach areas where residual cholesteatoma are materialized. We created a 3D printed phantom of the ear model in which three red markers were placed as residual cholesteatoma. The ear model obtained using the 3D reconstruction method discussed in Chapter IV had a triangular mesh surface. Thus, Meshmixer, a free program

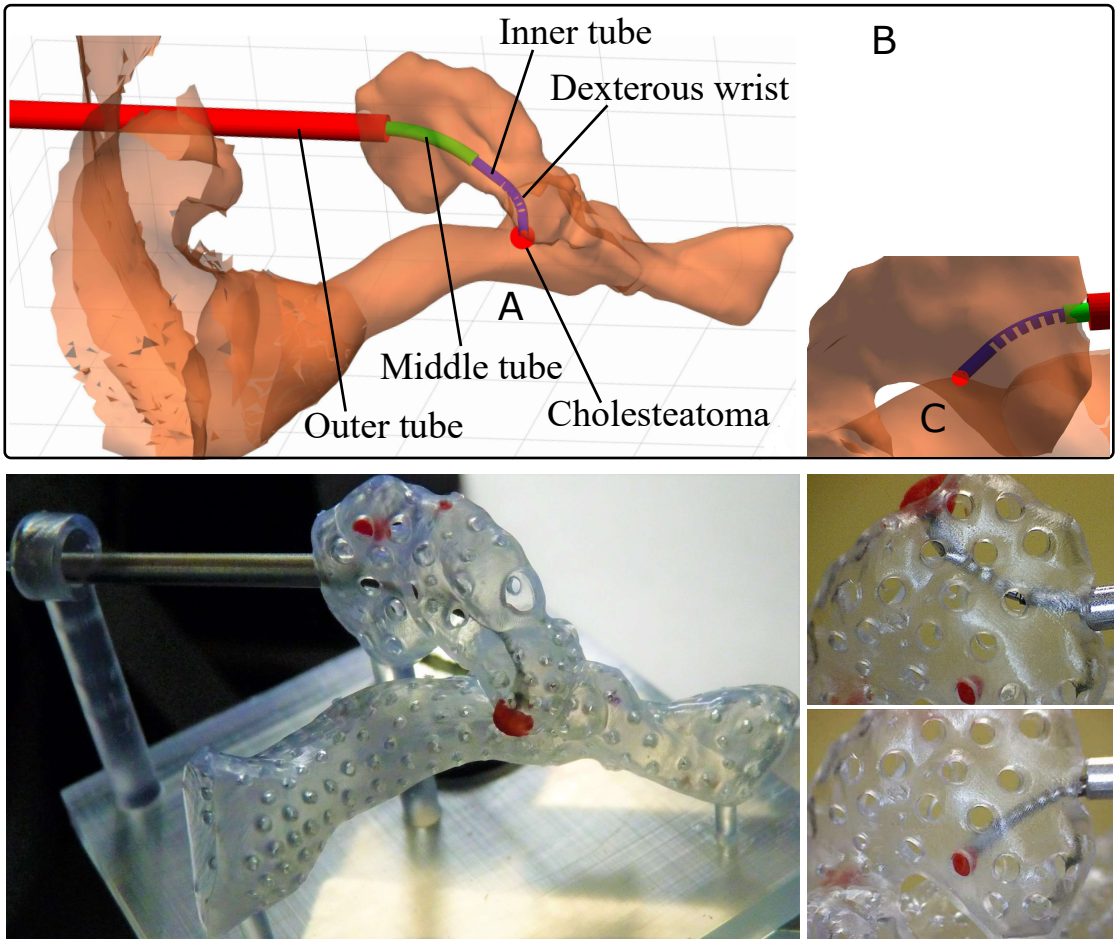

FIGURE V.12 – Deployment of the hybrid continuum robot in the middle ear phantom. Residual cholesteatoma are illustrated with red markers. The robot is inserted through a 3 mm diameter hole on the posterior wall of the tympanic cavity and approaches hard-to-reach positions in this confined workspace. Top: simulation results. Bottom: the surgical target is at the upper part of the eardrum, above the entry hole, and below the entry hole, respectively.

by Autodesk [2] was utilized to thicken the triangular mesh surface for 3D printing. The thickness of the 3D printed ear phantom was 0.6 mm to ensure that the robot was visible from the outside. In addition, we used SolidWorks [3] to make tiny holes all over the robot's surface to enhance visibility. These holes served as a convenient place to attach the red clay markers on the inner surface of the ear phantom. The residual cholesteatoma cells were placed at challenging positions inside the tympanic cavity using simply a CTR or a wrist as shown in figure IV.13.

Through teleoperated mode, the hybrid continuum robot was moved to reach the marked locations. It was inserted via the created 3-mm hole to the attic of the tympanic cavity. The experiments showed that three hard-to-reach points of the middle ear were accessed by the proposed robot (see figure V.12). It takes about 10 and 16 s to reach the target points in the attic (C and B, respectively) and 40 s for point A in the upper part of the membrane. In the following, actual cholesteatoma cells will be utilized for the laser ablation process.

V.2.2 Cholesteatoma ablation

To demonstrate the ability of the proposed robot to perform the surgical intervention, real cholesteatoma cells collected after surgical procedures from Besançon Hospital were used in this experiment. Through teleoperated mode, the proposed robot was moved to reach the target location and perform the ablation of the cholesteatoma by the LBO green laser (see figure V.13). We used laser pulses of 200 ms with a power of 8 W to ablate the cholesteatoma sample.

In addition, we can monitor the volume of the residual cholesteatoma cells by using the OCT 3D scan and image processing method [Boyer 22]. The volume images of the sample were obtained using a TELESTO-II OCT with an LSM03 probe. The voxel dimensions were 25 μm along the X and Y axes and 3.5 μm along the Z axis (optical axis). The main phases of the cholesteatoma segmentation were presented in figure V.14. First, the volume of matter including cholesteatoma and support were roughly separated from the background by applying a threshold (figure V.14b). Second, the support was removed from the obtained image by determining its surface (figure V.14c). As the support has a prismatic shape, it's surface can be approximated using linear interpolation between two arbitrary outlines obtained by applying the *edge* function in Matlab to two parallel cross-sections that only contained the support element, not the tissue (e.g., the $X-Z$ boundary plans of the image). Third, we employed *imfill* and *imopen* functions in Matlab to eliminate noises from the images including false negatives (holes in the middle of the matter) and false positives (matter in the background). The *imfill* function located and filled the holes characterized by background pixels that were inaccessible from the image's border pixels through the face connectivities (6-connected mode) while the opening morphological *imopen* operation using a 50 µm-radius ball as its structuring element allowed us to filter the false positives from the image. Finally,

3. [Online] https://www.autodesk.com/research/projects/meshmixer
3. [Online] https://www.solidworks.com/

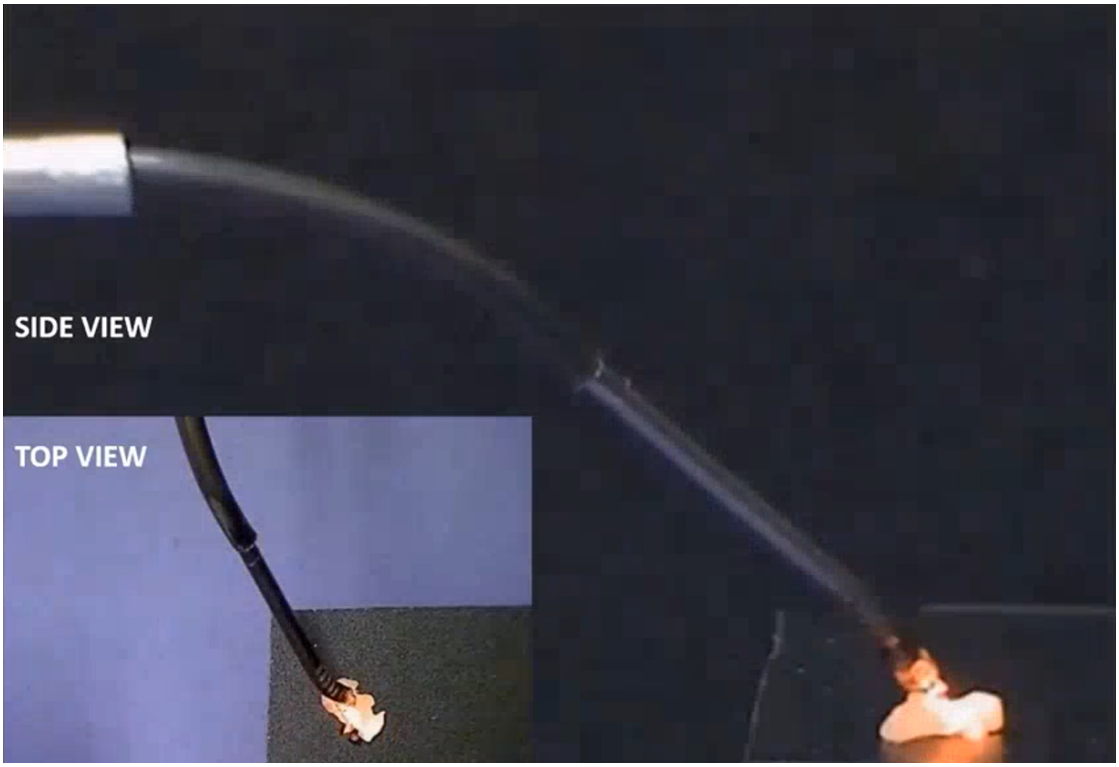

FIGURE V.13 – Cholesteatoma laser ablation using the LBO laser. Red light is used to determine the laser beam's incident position before performing the ablation.

the volume of cholesteatoma was extracted using the *bwselect3* function in Matlab as illustrated in figure V.14d. Its volume can be easily calculated by multiplying the total number of voxels to the volume of the individual voxel. With an Intel Core i5 processor running at 1.6 GHz, the segmentation computation takes around 5 seconds for a volume of 171 x 193 x 768 voxels. An example of result is shown in figure V.15 where the estimated volume is about 2.399 mm^3.

Then, we conducted the experiment with different laser powers (6 W and 8 W) with respect to variant time exposures to analyze the dependence of the ablated volume on these two quantities. As reported in [Boyer 22], the steady-state ablation rate increases when the laser power increases. Furthermore, for a given laser power, the ablated volume grows linearly with the exposure time (see figure V.16). The experimental results are in agreement with the computational model in the literature [Elkhalil 18].

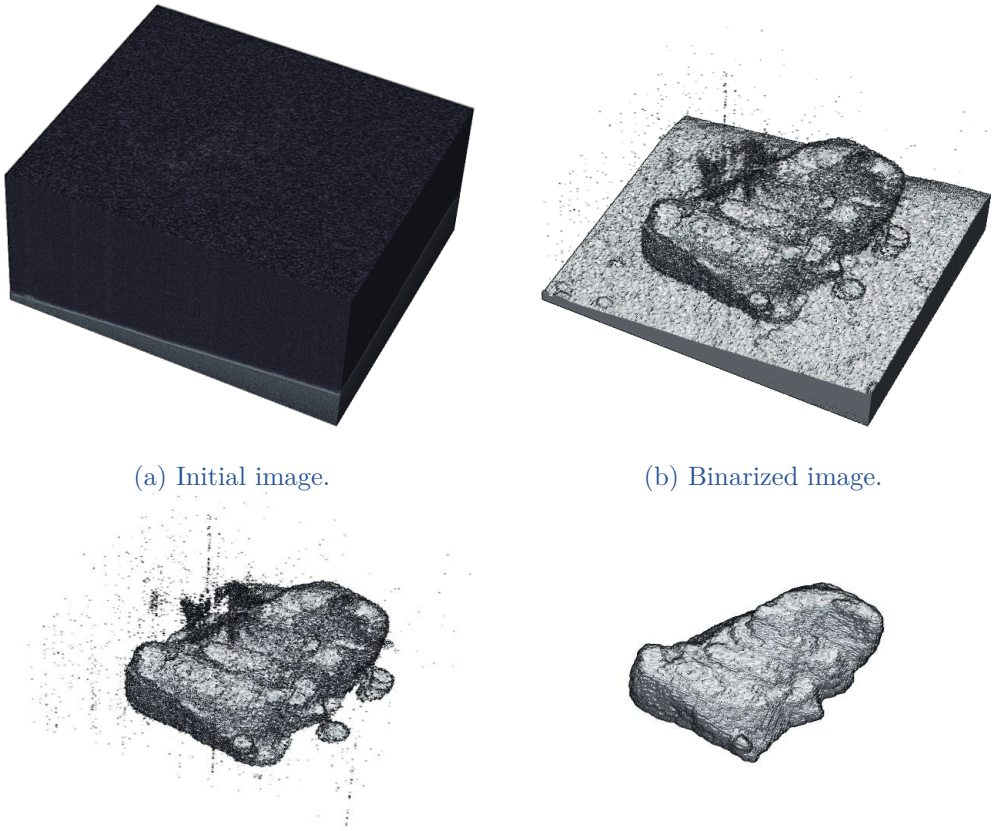

(a) Initial image.

(b) Binarized image.

(c) After support removal.

(d) Final image for volume estimation.

FIGURE V.14 – Steps of cholesteatoma OCT image processing [Boyer 22].

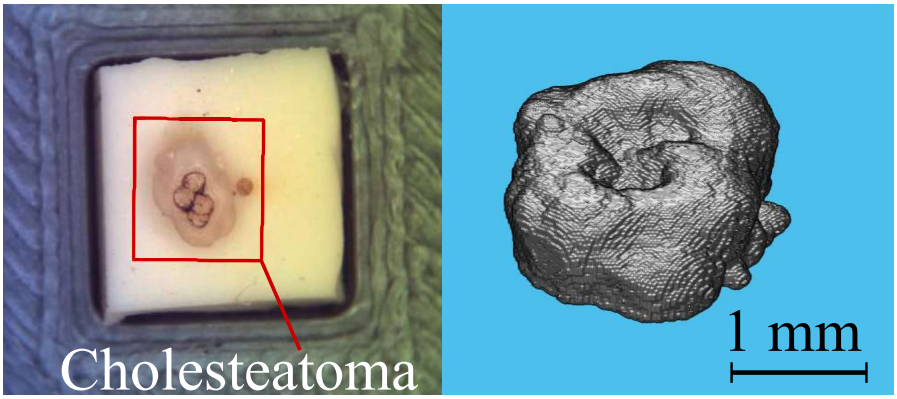

FIGURE V.15 – Left: cholesteatoma cells burned by using the LBO laser. Right: volume image of the residual cholesteatoma during the ablation.

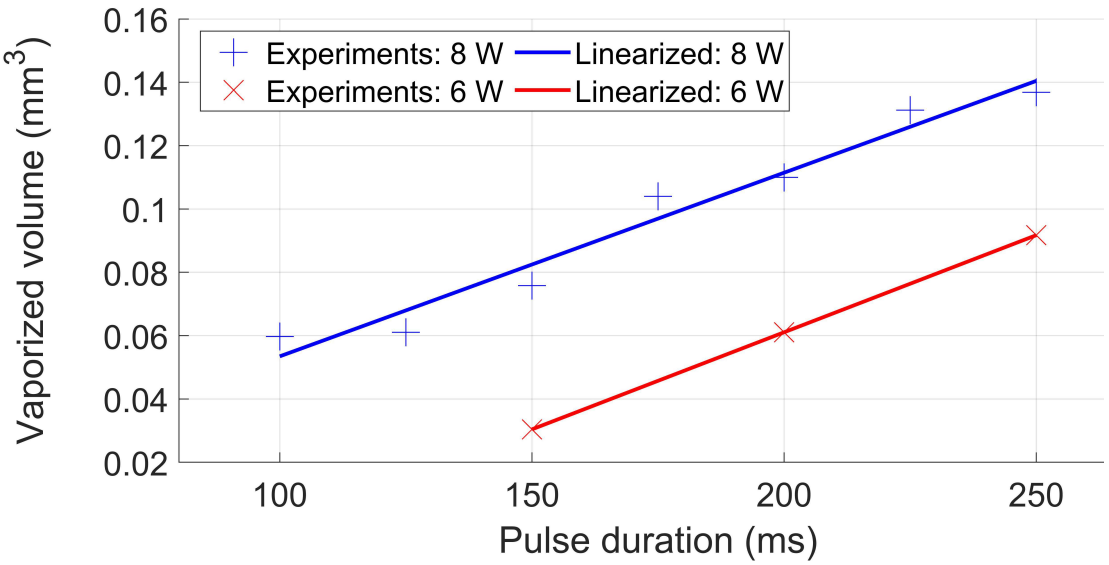

FIGURE V.16 – Vaporized volume as a function of exposure time.

V.3 CONCLUSION

This chapter starts by presenting a novel method to determine the repeatability of the proposed robot using OCT 3D scanning. As a result, the hybrid CTR has an acceptable repeatability (distance error of 0.7 mm and angular errors between 1 and 3 deg) for the requirements of the cholesteatoma ablation in a semi-automated mode. After that, its ability to follow a planned path will also be discussed. The obtained results show that the proposed robot can follow the reference with a mean error of 1.05 ± 0.79 mm and a maximum error of 3.61 mm. Then, some demonstrations were conducted to shown the deployment of the proposed robot inside a confined space of the middle ear phantom. It proved that the robot's tip can access challenging locations inside the tympanic cavity. Finally, the laser ablation of real cholesteatoma and the analysis of the ablated volume in function of the laser parameter have also been carried out.

Conclusions et perspectives

Conclusion

Cholesteatoma is one of the most frequent otological diseases with a great need for improving its treatment by modifying open surgery to minimally invasive one. Through a comprehensive review on the robotic systems that are related to the middle ear surgery and others dexterous surgical robots, there is no microrobotic system that completely satisfies the requirements of the exhaustive cholesteatoma surgery. The major difficulties are the miniature and dexterity of the surgical tool when operating in a confined space like the middle ear cavity.

As part of the μRoCS project, this PhD focuses on the design, modeling, fabrication, and demonstration of a microrobot dedicated to exhaustive cholesteama laser surgery. It starts by proposing a hybrid CTR with an embedded optical fiber for laser ablation using two accesses to the middle ear (through the ear canal and via a 3-mm created hole on the mastoid). The proposed robot employs a tendon-driven actuation by notching the innermost tube of a CTR to improve its distal dexterity. It allows obtaining an outer diameter smaller than 3 mm to ensure minimally invasive surgery and a lumen to integrate the optical fiber. In addition, the decoupled actuation between the distal end and the robot body allows sweeping the robot tip in the confined workspace while keeping the rest of the body in the constrained environment.

After that, the models of both the CTR and the tendon-driven wrist are presented. As a contribution, we propose a novel approach to determine the deformation of the CTR under free internal tendon load by simultaneously solving the boundary value and the shortest path problems. In addition, the wrist model is also improved and validated by taking the stiffness of the optical fiber into account. After obtaining the model of the hybrid CTR, the graphical user interface in Matlab was used to simulate the behavior of the proposed robot in 3D space.

Then, the robot design need to be chosen so that it neglects the instability of the CTR and has a rigid enough outermost tube to constraint the robot to be inserted through the entry paths. Furthermore, by using a set of CT scan DICOM images, a right ear 3D model is reconstructed using InVesalius, Meshlab, and Matlab. Based on this model, we proposed a generic method to select the best design parameters of the hybrid CTR to maximize the coverage volume. We also provide a comprehensive analysis of the cut depth of the wrist to obtain its optimal value. After acquiring the design parameters, the robot components were fabricated using different manufacturing methods. Among them, the end cap of

the wrist requires an innovative fabrication for attaching the tendon, constraining the laser optical fiber as well as fixing its relative rotation with respect to the wrist. Moreover, the dimension of this component is only about 1 mm.

After fabricating the robot components, several experiments are conducted with a prototype of the hybrid CTR and on the ear 3D printed phantom. We proposed a novel method to evaluate the robot repeatability using OCT 3D scanning. This technique enables measurement without the addition of any external sensor, which may result in unforeseen errors in the robot shape at the millimeter scale. In addition, the ability of the robot to follow a planned path, the deployment of the robot inside a ear phantom, and the real cholesteatoma laser ablation are also demonstrated. Last but not least, we also propose a new method to monitor the residual cholesteatoma during laser ablation and to analyze the ablated volume of the infected cells with respect to the laser paramaters.

Perspectives

To complete the μRoCS project, the optical fibers using for cholesteatoma detection need to be embedded in the lumen of the proposed robot. As mentioned in this manuscript, the maximum bending of the optical fiber is a technical limitation. The optical fibers used for the future version of the hybrid CTR needs to have a smaller dimension to obtain a higher curvature [Uzan 21]. Then, the hybrid CTR prototype needs to be reduced in size for integrating on an otolaryngology robot (e.g. RobOtol) to replace rigid surgical tools. For that, the tool-holding part of the otolaryngology robot should be modified in order to support the hybrid CTR. Such a compact design, lighter and fewer degrees of freedoms is developed within an internship work of our collaborator Quentin BOYER as shown in figure V.17. In this work, the hybrid CTR prototype is fixed on an UR3 robot [4] through 4 screws. The actuators utilize piezoelectric motors that allow improving the robot repeatability based on piezoelectric actuation. The robot only has a rigid straight outer tube and an precurved distal notched inner tube to ensure the compactness. More simulation results (as presented in Chapter IV) are required to obtain the best parameters of this design for an exhaustive cholesteatoma surgery. Finally, an in-vivo evaluation is required for the proposed robot to be used in practice.

So far, there are numerous approaches to follow-up our work. Consideration of the friction interaction and clearance among the tubes is necessary to improve the accuracy of the CTR model [Ha 18]. Besides, the non-constant curvature and the difference in friction between the tendon and the wrist at each notch's corner can be taken into account [Legrand 21]. However, there is a trade-off between the model accuracy and the computation time. The employment of the model in a real-time control scheme will become more challenging if the model is slowly solved. As a result, it is important to choose a model whose precision is sufficient to meet the middle ear surgery criteria without impairing the real-time control.

4. https://www.universal-robots.com/products/ur3-robot/

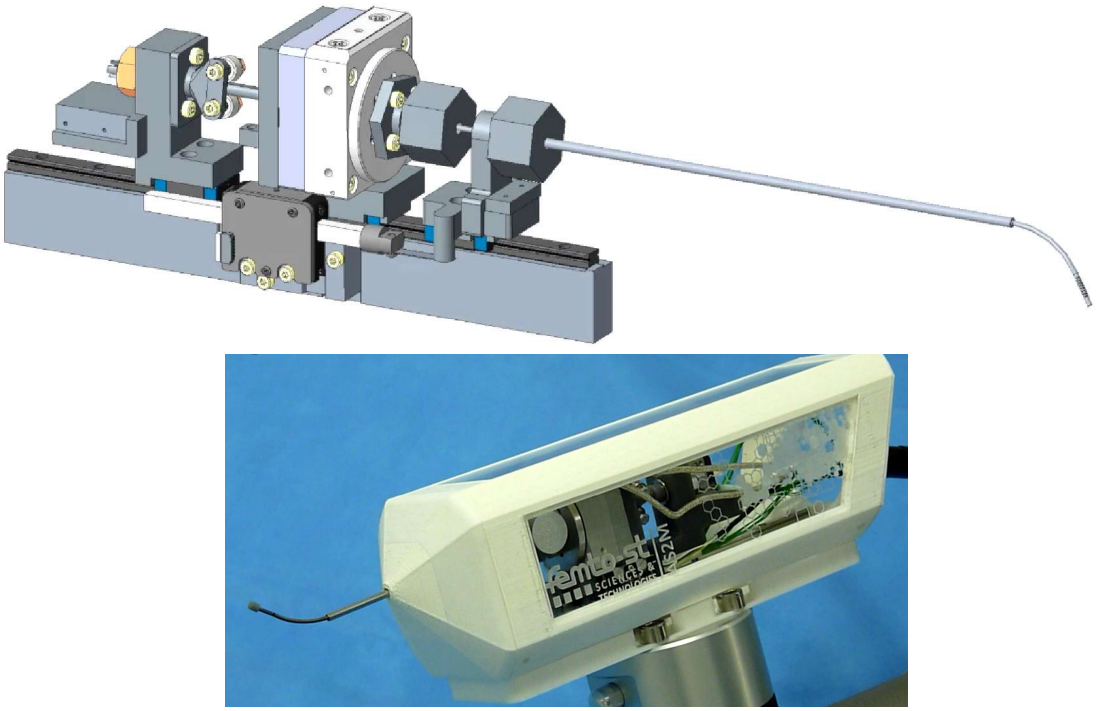

FIGURE V.17 – Compact and light weight prototype of the hybrid CTR for middle ear surgery.

In addition, close-loop control is required to improve the performance of the hybrid CTR to perform the path following mission. Various path following controllers have been described in the literature including nonlinear model predictive control for autonomous steering of CTRs [Khadem 20], automatic obstacle avoidance for CTRs during teleoperation [Torres 15], model-based control for follow-the-leader motion of continuum robots [Yan 22], or human-in-the-loop positioning for hand-held CTRs [Girerd 20]. For experiments conducted in free space, the feedback of the robot's pose can be obtained with a magnetic tracking sensor, eye-to-hand cameras or an OCT imaging system. However, the need for a minimally invasive surgery in a confined workspace like middle ear makes the mentioned techniques extremely challenging. Indeed, due to the bending of the wrist, the inflexible distal end of the AURORA magnetic sensor prevents it from being integrated into the robot lumen. A chip-on-tip camera [Gafford 21] can be integrated on the hybrid CTR (eye-in-hand mode) and/or on a separate endoscope device to obtain the pose of the robot's tip. Nevertheless, both solutions will cause the surgical procedure to be more invasive. Image scanning method using an eye-to-hand OCT system avoids the expansion of the entry hole to the surgical site. However, with a penetration depth of about 700 μm (depending on the type of tissue) [Aumann 19], this technique is not suitable for measuring inside the middle ear. In [Ryu 14], the authors present a promising real-time method for determining the 3D curvature of continuum robots using Fiber Bragg gratings (FBG)-based optical sensors. Nevertheless, adding more optical fibers necessitates expanding the robot's lumen

and significantly stiffens the wrist, which raises the applied tendon force. Thus, the compact robot presented in figure V.17 considers rotary encoders and linear position sensors to measure the rotation and translation of the tubes. In the literature, this method was used for the guidewire movement in vascular interventional surgery [Guo 18]. Even so, an additional force sensor will be required to determine the bending of the wrist due to tendon elongation. Besides, since the sensors are mounted at the base of the robot, air gaps and friction among the tubes may result in measurement errors. Therefore, a high accuracy model of the hybrid CTR will be required. In summary, additional researches are necessary to identify the best candidate to monitor the pose of the robot's tip inside the middle ear cavity.

To extend the application of the hybrid CTR for various anatomical constraints, future developments will be conducted relying on artificial intelligence (AI). More data of different patients will be collected. Then, a machine learning (e.g., k-mean algorithm [Likas 03]), will be utilized to classify the anatomical reconstructed models into different clusters. Each cluster will be characterized by similar anatomy structures (features). To obtain the best design parameters of the robot corresponding to each anatomy group (cluster), the proposed synthesis will be executed for its typical element (e.g. the "closest" reconstructed model to the cluster center).

Beside cholesteatoma surgery, the proposed robot can be applied for the laser stapedotomy and stapedectomy. These types of surgery is typically done for patients with otosclerosis and other diseases affecting the stapes bone. In otosclerosis, patients develop a fixation of the stapes (stirrup) bone over time that can result in a conductive hearing loss. To treat, the surgeon will create a tiny (0.8mm) opening in the base of the stapes (stapedotomy) or remove the pathologic fixed bone (stapedectomy) using a laser, and a stapes prosthesis will be placed to repaire the issue and restore the hearing [Cheng 18].

Finally, to facilitate the selection of the dimension of the tubes and extend the application of the proposed hybrid CTR, it is possible to consider different lab-made materials such as polymers [Morimoto 16] or flexible glass [Nwafor 22]. These approaches allow obtaining a custom dimension of each tube with a precurved shape using 3D-printing fabrication and thermal treatment method.

Appendix A
Notation and definitions

A.1 Nomenclature of the quantities used for the robot modeling 142

A.1 Nomenclature of the quantities used for the robot modeling

Symbol	Definition
	CTR
$*$	Variable in the reference configuration
$\cdot$	Derivative with respect to s
$\wedge$	Mapping from $\mathbb{R}^3$ to $\mathfrak{so}(3)$ and from $\mathbb{R}^6$ to $\mathfrak{se}(3)$
$\vee$	Inverse of the $\wedge$ operation. $\left(\hat{\boldsymbol{u}}^{\vee}\right) = \boldsymbol{u}$
N	Number of tubes in the CTR
i	Tube index, numbered in increasing diameter order
s	Curvilinear abscissa along the robot
β_i	Location of the base of tube i
ψ_i	Twisting angle of tube i
κ_i	Precurvature of tube i^{th}
K_i	Stiffness matrix for bending and torsion of tube i^{th}
K_{BT_i}	Bending and torsion stiffness matrix of tube i
K_{SE_i}	Shearing and extension stiffness matrix of tube i
L_i	Total length of tube i
$\boldsymbol{p}_i(s)$	3D position of tube i in the global frame
$R_i(s)$	Orientation of tube i in the global frame
$\boldsymbol{u}_i(s)$	Equilibrium curvature of tube i in local frame
$\boldsymbol{v}_i(s)$	Rate of change of position with respect to arclength in the local frame
D_i, d_i	Outer and Inner diameters of i^{th} tube
E_i	Young's modulus of i^{th} tube
I_i	Planar second moment of area of i^{th} tube
G_i	Shear modulus of i^{th} tube
J_i	Polar second moment of area of i^{th} tube
$\boldsymbol{n}_i(s)$	Internal force on i^{th} tube in the global frame
$\boldsymbol{m}_i(s)$	Internal moment on i^{th} tube in the global frame
$\boldsymbol{f}(s)$, $\boldsymbol{f}_s(s)$	Distributed force of the CTR and of the tendon in the global frame
$\boldsymbol{l}(s)$, $\boldsymbol{l}_s(s)$	Distributed moment of the CTR and of the tendon in the global frame
$\boldsymbol{p}_s(s)$	3D position of the tendon in the global frame
$\boldsymbol{r}_s(s)$	3D position of the tendon in the local frame
	Wrist
r_{in}, r_{out}	Inner and outer radii of the innermost tube

Continued on next page

Table A.1 – continued from previous page

ρ	Radius of the OF
l	Length of the wrist
n	Number of cutouts in the wrist
h	Height of cut
c	Distance between cuts
b	Length of the distal uncut section
g	Depth of cut
d	Location of the OF centerlines within a cross-section
θ	Bending angle within a cutout of the wrist
$\bar{y}$	Location of the neutral bending plane
ϵ_{max}	Maximum strain of the material
μ_s	Static friction coefficient between wrist and tendon
κ, κ_f	Bending curvatures of the wrist and the OF
E_f	Young's modulus of the OF
F_{tendon}	Force applied on the tendon
V	Tympanic cavity coverage volume

Appendix B
Basics of CTR kinematics

B.1 Torsional compliant kinematic model of the CTR 146

B.1 Torsional compliant kinematic model of the CTR

Elastic energy stored in the CTR

Considering an arbitrary portion from the arc length σ_1 to σ_2 of the CTR that containing n tubes of the same length (see figure B.1).

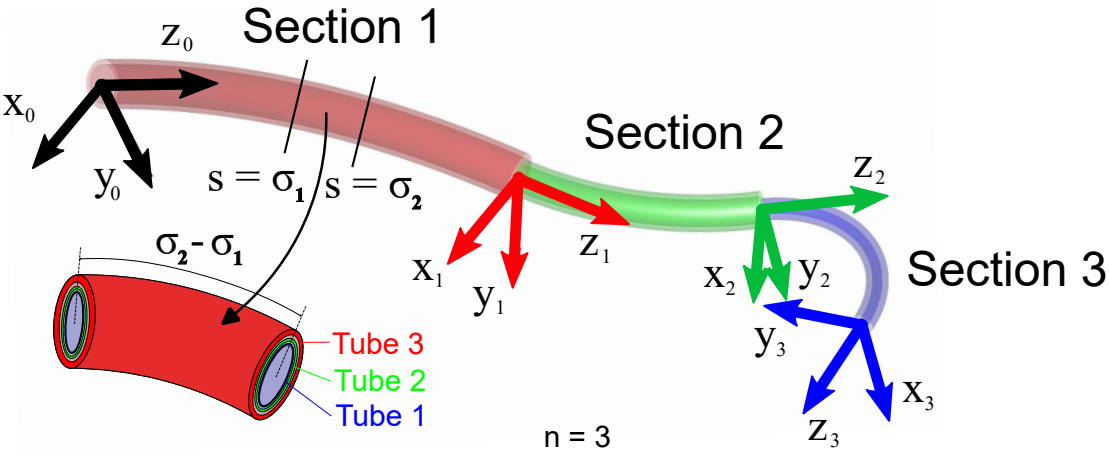

Figure B.1 – An example of a CTR portion of 3 tubes.

Let $\boldsymbol{u}_i^*(s)$ be the precurvature of the i^{th} tube and $\boldsymbol{u}_i(s)$ be the final curvature of it. The total elastic energy stored in this portion is given by

$$E_s = \frac{1}{2}\sum_{i=1}^{n}\int_{\sigma_1}^{\sigma_2}\left(\boldsymbol{u}_i(s)-\boldsymbol{u}_i^*(s)\right)^T K_i\left(\boldsymbol{u}_i(s)-\boldsymbol{u}_i^*(s)\right)ds \tag{B.1}$$

where K_i is the bending and torsion stiffness matrix as defined in the previous model. As each tube i has a different axial rotational angle $\theta_i(s)$ with respect to tube 1 (the innermost tube) we then obtain

$$R_i(s) = R_1(s)R_{\theta_i}(s) \tag{B.2}$$

where $R_{\theta_i}(s) = \begin{bmatrix}\cos(\theta_i(s)) & -\sin(\theta_i(s)) & 0\\ \sin(\theta_i(s)) & \cos(\theta_i(s)) & 0\\ 0 & 0 & 1\end{bmatrix}$. Using the definition of $\boldsymbol{u}_i(s)$ yields

$$\boldsymbol{u}_i(s) = R_{\theta_i}^T(s)\boldsymbol{u}_1(s) + \dot{\theta}_i(s)\boldsymbol{e}_3 \tag{B.3}$$

where $\boldsymbol{e}_3 = [0,0,1]^T$. Substituting (B.3) to (B.1), we can rewrite the stored energy E (detailed in [Rucker 11b]) as follows

$$E_s = \frac{1}{2}\int_{\sigma_1}^{\sigma_2}\left(\boldsymbol{u}_1(s)-\boldsymbol{\alpha}(s)\right)^T K\left(\boldsymbol{u}_1(s)-\boldsymbol{\alpha}(s)\right) + C ds \tag{B.4}$$

where

$$\boldsymbol{\alpha}(s) = K^{-1}\sum_{i=1}^{n} K_i \bar{\boldsymbol{u}}_i^*(s), \qquad K = \sum_{i=1}^{n} K_i, \tag{B.5}$$

$$\bar{\boldsymbol{u}}_i^*(s) = R_{\theta_i}(s)\boldsymbol{u}_i^*(s) - \dot{\theta}_i(s)\boldsymbol{e}_3, \quad C(s) = \sum_{i=1}^{n} \bar{\boldsymbol{u}}_i^{*^T}(s) K_i \bar{\boldsymbol{u}}_i^*(s) - \boldsymbol{\alpha}^T(s) K \boldsymbol{\alpha}(s) \tag{B.6}$$

Minimizing the elastic energy

We are now looking for the value of $\boldsymbol{u}_1(s)$ corresponding to the minimum value of E_s. Note that the expression of the elastic energy E_s expressed in (B.5) involves two quantities independent of the curvature $\boldsymbol{u}_1$, namely $\boldsymbol{\alpha}(s)$ and $C(s)$. It is easy to see that the energy E_s reaches its minimal value if

$$\boldsymbol{u}_1(s) = \boldsymbol{\alpha}(s) \tag{B.7}$$

For the purpose of convenience, we define the absolute rotational angle $\psi_i(s)$ of the i^{th} tube with respect to the common reference frame $F_0(s)$ (as defined in the previous model) along the length of the robot.

$$\psi_i(s) = \alpha_i + \int_{\beta_i}^{s} u_{iz} d\sigma \tag{B.8}$$

where α_i is the rotational angle of the i^{th} tube at its base ($s = \beta_i$) which is known as an actuator variable. We then obtain

$$R_i(s) = R_B(s) R_{\psi_i}(s) \tag{B.9}$$

where $R_B(s)$ is the rotation matrix of the Bishop frame coinciding with the fixed global frame at $s = 0$ and evolving along the centerline curve of the CTR. Its curvature vector can be determined using

$$\boldsymbol{u}_B(s) = \left(R_B^T(s)\dot{R}_B(s)\right)^{\vee} = \left[u_{Bx} u_{By} 0\right]^T \tag{B.10}$$

Then, we have the curvature vector of the i^{th} tube

$$\boldsymbol{u}_i(s) = R_{\psi_i}^T(s)\boldsymbol{u}_B(s) + \dot{\psi}_i(s)\boldsymbol{e}_3 \tag{B.11}$$

By rewriting equation (B.4) and solving for the minimum value of the resulting stored energy, we obtain

$$\boldsymbol{u}_B(s) = K^{-1}\sum_{i=1}^{n} K_i \left(R_{\psi_i}(s)\boldsymbol{u}_i^*(s) - \dot{\psi}_i(s)\boldsymbol{e}_3\right) \tag{B.12}$$

To determine the function $\psi_i(s)$, we apply the Euler-Lagrange equation n times for the expression (B.4) and subject to (B.11) and (B.12), this results in n second order differential equation

$$G_i J_i \ddot{\psi}_i(s) = \frac{E_i I_i}{EI} \sum_{j=1}^{n} E_j I_j \kappa_i \kappa_j sin(\psi_i - \psi_j) \tag{B.13}$$

Here, we assume that the precurvatures of the tubes have the form $\boldsymbol{u}_i^* = [\kappa_i, 0, 0]^T$ or $\boldsymbol{u}_i^* = [0, \kappa_i, 0]^T$. We can also rewrite the system of n equations as the set of $2n$ equations

$$\begin{aligned} \dot{\psi}_i &= u_{iz} \\ \dot{u}_{iz} &= \frac{E_i I_i}{EIG_i J_i} \sum_{j=1}^{n} E_j I_j \kappa_i \kappa_j sin(\psi_i - \psi_j) \end{aligned} \tag{B.14}$$

This set of equations form a multipoint BVP with as given in (B.15) and (B.16). The first boundary condition corresponds to the known angles by which the tubes are oriented at the point of arc length $s = 0$. Using (B.14) for the transmission lengths of each tube implies that u_{iz} is constant (as all the tubes are straight), thus ψ is linearly dependent on s. From (B.8), we infer

$$\psi_i(0) = \psi_i(\beta_i) - \beta_i u_{iz}(0) \tag{B.15}$$

Furthermore, as there is no external torque applied on the CTR, the torsion at the distal end of each tube must be zero, we have

$$u_{iz}(L_i + \beta_i) = 0 \tag{B.16}$$

After solving for the torsion of the tubes along their lengths, their curvature components along the x and y axes are computed using Eq. (B.17).

$$u_{ixy} = \frac{1}{EI} \sum_{j=1}^{n} R_{\psi_j - \psi_i} E_j I_j u_{ixy}^* \tag{B.17}$$

Appendix C
Experimental data

C.1 Tendon load on a soft tube 150
C.2 Bending of the wrist 153

C.1 Tendon load on a soft tube

Two special end caps with 8 small holes is utilized to select the location of the tendon at the ends of the tube. During the test conducted with the S-shaped tube, the tendon location is fixed at the base $[0\ D_i/2\ 0]^T$ (top point) and at the tip $[0\ -D_i/2\ 0]^T$ (bottom point). The applied force on the tendon varies from 0 to 12 N. As the deformation of the tube is planar, we used a digital camera and a calibration process to measure the robot shape. Then, the function '*bwmorph*' of Matlab will be employed to remove the interior pixels and leave the outline of the tube image as shown in figure C.2. To automatically detect the centerline of the tube, we utilize an algorithm to determine the median of the two boundary curves in the tube image.

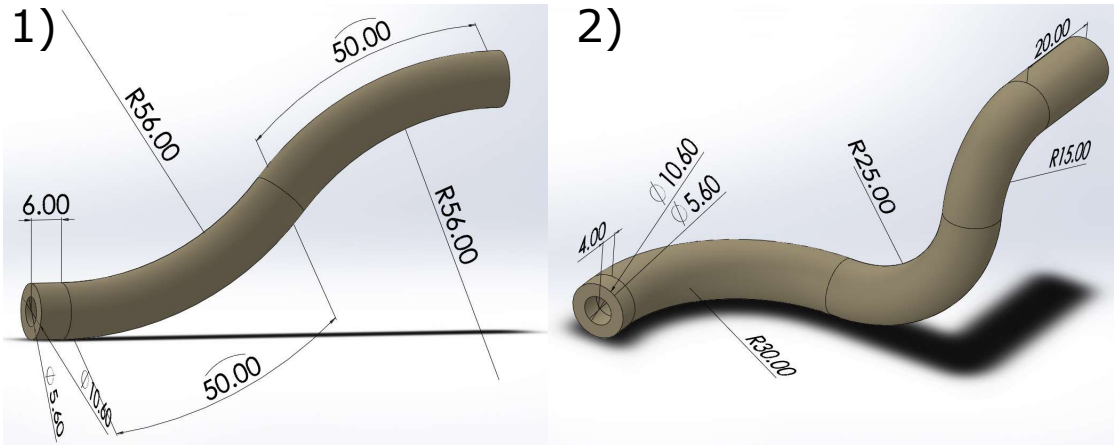

Figure C.1 – Dimension of the 3D-printing tubes. ① The centerline curve of the tube lies in a plane and comprises a 6 *mm* straight effective length and two precurved segments bending into two opposite directions with the length of 50 *mm* and the radius of 56 *mm*. ② The center-line curve of the tube is composed of 4 *mm* and 20 *mm* straight lengths at the proximal and distal end respectively and three curved segments belonging to three perpendicular planes and still ensuring the continuity of the tube. The arc measure of each curved segment is 90^o and their radii are 30 *mm*, 25 *mm*, and 15 *mm* in order from base to tip.

Table C.1 – Model RMS Errors (mm) for S-shaped Tube Experiments

S-shaped	mean (mm)	standard deviation (mm)	min (mm)	max (mm)
Test 1	0.37	0.06	0.27	0.54
Test 2	0.41	0.06	0.31	0.65
Test 3	0.42	0.05	0.32	0.59

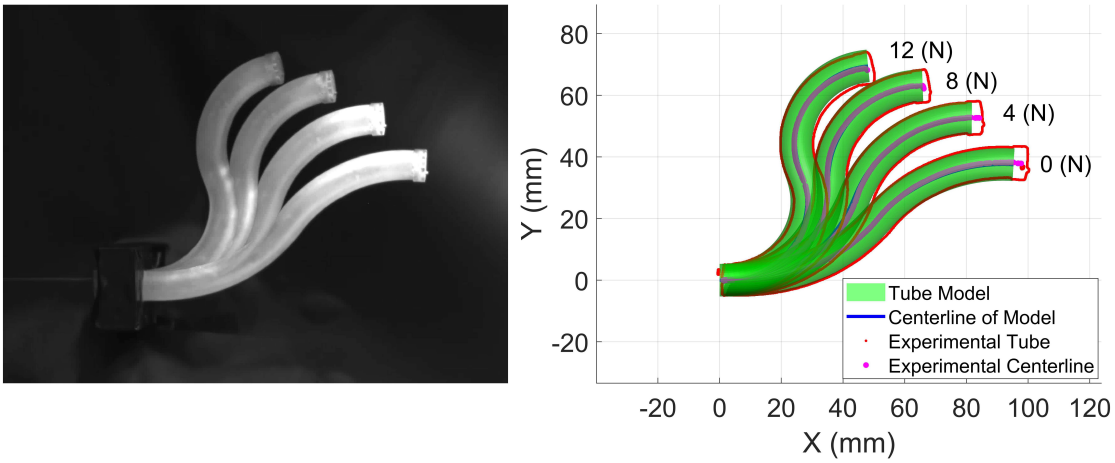

FIGURE C.2 – The experimental validations for the S-shaped tube with the tensions of 0, 4, 8, and 12 (N). To detect the experimental centerline in plane, we start by defining the two contours of the tube wall image and label them as two sets of points A and B. Then, for each point a_i of A, we find the corresponding point b_i in B that closest to it. Thus, the centerline is then the set of the midpoint m_i of the line segment $a_i b_i$.

The result of the first test is shown in figure C.2. The root mean square (RMS) positional errors between the computed centerline and the real one along the robot length was 0.37 mm as given in Table C.1 corresponding to 0.36% of the robot length. We repeated the test 3 times and obtained the mean errors vary within $[0.37, 0.42]$ (mm) corresponding to $[0.36\% - 0.41\%]$ of the robot length.

To validate our method on a more complex tube shape, we performed an experiment with the 3D precurved tube as shown in figure C.1 and applied different tension values between 0 and 6 N on the tendon. As the deformation of the tube is now in 3D space, we used 2 digital cameras to observe it as illustrated in figure C.3. In addition, we utilize the tip error instead of the root-mean-square error along the robot length to validate the model. The position and tangent vector to the centerline of the tube at the tip was measured by the Aurora magnetic tracking system (Northern Digital, Inc., Waterloo, ON, Canada).

TABLE C.2 – Model tip and angle errors for the 3D precurved tube.

	mean	standard deviation	min	max
Tip error (mm)	5.84	2.52	1.57	9.12
Angle error (deg)	2.35	0.67	1.54	3.75

In Table C.2, the mean tip error with the tension varying from 0 to 6 N is 5.84 mm, this corresponds to 4.45% of the robot length. The spatial orientation at the tip is quite well predicted by the model, with an angle error of only about

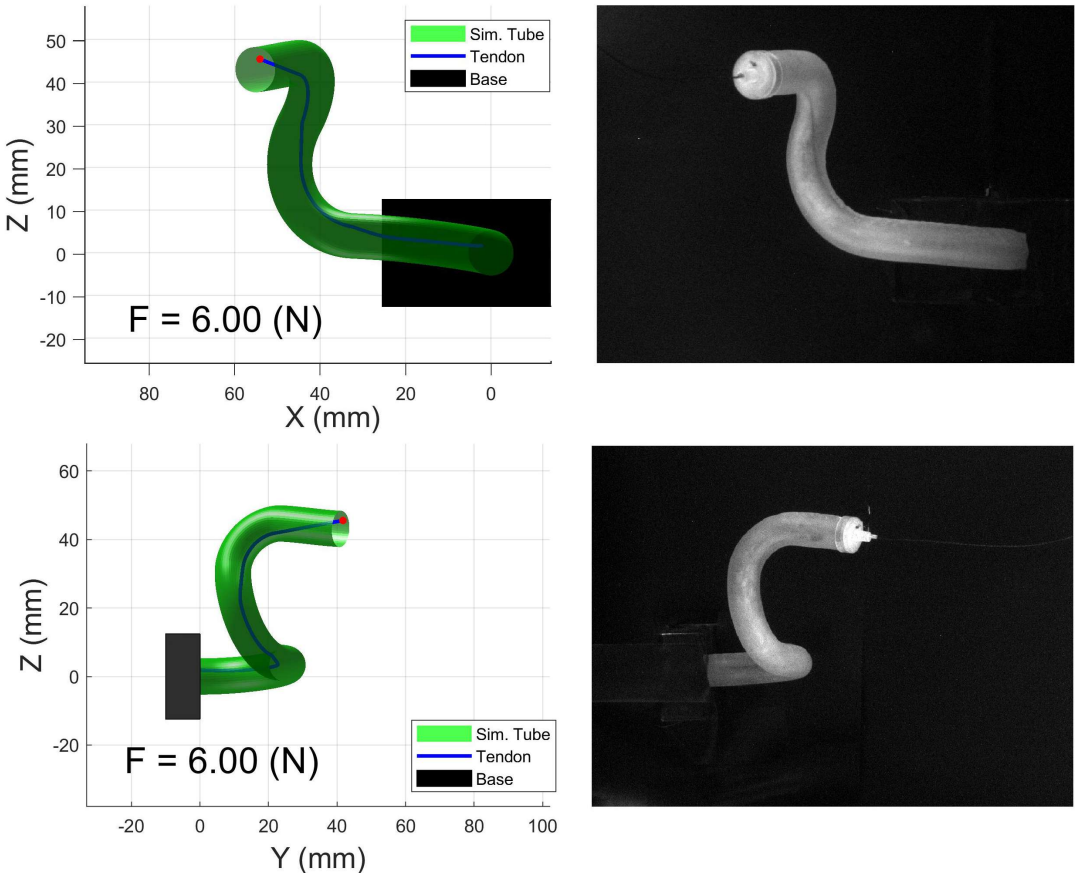

FIGURE C.3 – Side and front views of the simulation (left) and the experiment (right) with the 3D tube and the tension of $6N$. The tendon position is fixed at the top point for both the base and the tip.

3 degrees. We believe that the friction coefficient between the tendon and the lateral wall of the tube was the primary source of error, which resulted in the model and experimental tip points not aligning perfectly in figure C.3. Indeed, the frictionless assumption employed in the research allows considering that the tension is constant throughout the tendon length. Actually, the presence of friction will cause a decrease in tendon stress gradually towards the tip. Consequently, the tube is bent a bit more according to the model than it is in reality (figure C.3).

C.2 Bending of the wrist

Table C.3 – Tests of the wrist bending without and with the optical fiber.

Without the OF						
Force (mN)	v = 5 µm/s	v = 10 µm/s	v = 15 µm/s	Average (deg)	Model (deg)	Error (deg)
0	0.0	0.0	0.0	0.0	0.0	0.0
50	1.7	1.8	0.7	1.4	2.3	0.9
100	3.8	2.3	3.8	3.3	4.5	1.2
150	4.9	5.2	6.2	5.4	6.7	1.2
200	7.5	8.2	8.4	8.0	8.8	0.8
250	8.9	9.8	10.5	9.8	10.8	1.1
300	12.9	12.7	13.7	13.1	12.8	0.3
350	15.1	15.0	16.0	15.4	14.8	0.6
400	15.9	17.7	18.3	17.3	16.8	0.5
450	20.2	20.6	23.1	21.3	19.5	1.8
500	22.8	23.9	27.9	24.8	23.0	1.8

With the OF						
Force (mN)	v = 5 µm/s	v = 10 µm/s	v = 15 µm/s	Average (deg)	Model (deg)	Error (deg)
0	0.0	0.0	0.0	0.0	0.0	0.0
100	2.5	2.8	2.7	2.7	2.0	0.7
200	4.2	5.1	4.4	4.6	3.9	0.7
300	4.9	7.3	6.1	6.1	5.8	0.3
400	8.4	8.2	7.2	7.9	7.6	0.4
500	10.0	9.3	9.4	9.5	9.3	0.2
600	10.7	12.1	10.2	11.0	11.0	0.0
700	12.0	13.0	12.1	12.4	12.7	0.3
800	12.7	14.8	14.0	13.8	14.3	0.5
900	15.9	16.2	15.4	15.8	15.9	0.1
1000	18.1	16.2	17.1	17.1	17.5	0.4
1100	19.4	18.8	18.1	18.8	19.2	0.5
1200	22.2	19.3	19.1	20.2	21.0	0.8
1300	22.6	22.0	20.7	21.7	22.8	1.1
1400	22.9	22.8	21.5	22.4	24.6	2.2
1500	23.4	23.9	22.7	23.3	26.4	3.1
1600	24.7	24.6	24.8	24.7	28.2	3.5

Bibliography

[Abidi 18] H. Abidi, G. Gerboni, M. Brancadoro, J. Fras, A. Diodato, M. Cianchetti, H. Wurdemann, K. Althoefer & A. Menciassi. *Highly dexterous 2-module soft robot for intra-organ navigation in minimally invasive surgery.* The International Journal of Medical Robotics and Computer Assisted Surgery, vol. 14, no. 1, page e1875, 2018.

[Ahn 08] J.-Y. Ahn, H. J. Park, G.-H. Park, Y.-S. Jeong, H.-B. Kwak, Y.-J. Lee, J.-E. Shin & W.-J. Moon. *Tympanometry and CT measurement of middle ear volumes in patients with unilateral chronic otitis media.* Clinical and experimental otorhinolaryngology, vol. 1, no. 3, page 139, 2008.

[Alper 04] C. M. Alper. Advanced therapy of otitis media. PMPH-USA, 2004.

[Amorim 15] P. Amorim, T. Moraes, J. Silva & H. Pedrini. *InVesalius: an interactive rendering framework for health care support.* In International symposium on visual computing, pages 45–54. Springer, 2015.

[Ansó 14] J. Ansó, C. Stahl, N. Gerber, T. Williamson, K. Gavaghan, K. M. Rösler, M.-D. Caversaccio, S. Weber & B. Bell. *Feasibility of using EMG for early detection of the facial nerve during robotic direct cochlear access.* Otology & neurotology, vol. 35, no. 3, pages 545–554, 2014.

[Antman 05] S. Antman, J. Marsden & L. Sirovich. In Nonlinear Problems of Elasticity. New York: Springer, 2 edition, 2005.

[Aquino 11] J. E. A. P. d. Aquino, N. A. Cruz Filho & J. N. P. d. Aquino. *Epidemiology of middle ear and mastoid cholesteatomas: study of 1146 cases.* Brazilian journal of otorhinolaryngology, vol. 77, no. 3, pages 341–347, 2011.

[Arrospide 17] E. Arrospide, I. Bikandi, I. García, G. Durana, G. Aldabaldetreku & J. Zubia. *Mechanical properties of polymer-optical fibres.* In Polymer Optical Fibres, pages 201–216. Elsevier, 2017.

[Ataollahi 13] A. Ataollahi, R. Karim, A. S. Fallah, K. Rhode, R. Razavi, L. D. Seneviratne, T. Schaeffter & K. Althoefer. *Three-degree-of-freedom MR-compatible multisegment cardiac catheter steering mechanism.* IEEE Transactions on Biomedical Engineering, vol. 63, no. 11, pages 2425–2435, 2013.

[Aumann 19] S. Aumann, S. Donner, J. Fischer & F. Müller. *Optical coherence tomography (OCT): principle and technical realization.* High resolution imaging in microscopy and ophthalmology: new frontiers in biomedical optics, pages 59–85, 2019.

[Ayache 08] S. Ayache, B. Tramier & V. Strunski. *Otoendoscopy in cholesteatoma surgery of the middle ear: what benefits can be expected?* Otology & Neurotology, vol. 29, no. 8, pages 1085–1090, 2008.

[Badr-El-Dine 13] M. Badr-El-Dine, A. L. James, G. Panetti, D. Marchioni, L. Presutti & J. F. Nogueira. *Instrumentation and technologies in endoscopic ear surgery.* Otolaryngologic Clinics of North America, vol. 46, no. 2, pages 211–225, 2013.

[Baek 16] C. Baek, K. Yoon & D.-N. Kim. *Finite element modeling of concentric-tube continuum robots.* Structural Engineering and Mechanics, vol. 57, no. 5, pages 809–821, 2016.

[Baron 10] S. Baron, H. Eilers, B. Munske, J. Toennies, R. Balachandran, R. Labadie, T. Ortmaier & R. Webster III. *Percutaneous inner-ear access via an image-guided industrial robot system.* Proceedings of the Institution of Mechanical Engineers, Part H: Journal of Engineering in Medicine, vol. 224, no. 5, pages 633–649, 2010.

[Bell 12] B. Bell, C. Stieger, N. Gerber, A. Arnold, C. Nauer, V. Hamacher, M. Kompis, L. Nolte, M. Caversaccio & S. Weber. *A self-developed and constructed robot for minimally invasive cochlear implantation.* Acta oto-laryngologica, vol. 132, no. 4, pages 355–360, 2012.

[Bell 13] B. Bell, N. Gerber, T. Williamson, K. Gavaghan, W. Wimmer, M. Caversaccio & S. Weber. *In vitro accuracy evaluation of image-guided robot system for direct cochlear access.* Otology & neurotology, vol. 34, no. 7, pages 1284–1290, 2013.

[Ben-Israel 66] A. Ben-Israel. *A Newton-Raphson method for the solution of systems of equations.* Journal of Mathematical analysis and applications, vol. 15, no. 2, pages 243–252, 1966.

[Bergeles 15] C. Bergeles, A. H. Gosline, N. V. Vasilyev, P. J. Codd, J. Pedro & P. E. Dupont. *Concentric tube robot design and optimization based on task and anatomical constraints.* IEEE Transactions on Robotics, vol. 31, no. 1, pages 67–84, 2015.

[Berns 11] M. S. Berns, E. Tsai, J. Austin-Breneman, J. C. Schulmeister, E. Sung, C. K. Ozaki & C. J. Walsh. *Single Entry Tunneler (SET) for Hemodialysis Graft Procedures*. Transactions of the ASME-W-Journal of Medical Devices, vol. 5, no. 2, page 027524, 2011.

[Bertails 06] F. Bertails, B. Audoly, M.-P. Cani, B. Querleux, F. Leroy & J.-L. Lévêque. *Super-helices for predicting the dynamics of natural hair*. ACM Transactions on Graphics (TOG), vol. 25, no. 3, pages 1180–1187, 2006.

[Bhutta 11] M. F. Bhutta, I. G. Williamson & H. H. Sudhoff. *Cholesteatoma*. Bmj, vol. 342, 2011.

[Blanco 14] P. Blanco, F. González, J. Holguín & C. Guerra. *Surgical management of middle ear cholesteatoma and reconstruction at the same time*. Colombia Médica, vol. 45, no. 3, pages 127–131, 2014.

[Bordure 05] P. Bordure, A. Robier & O. Malard. Chirurgie otologique et otoneurologique. Elsevier Masson, 2005.

[Bordure 09] P. Bordure, S. Bailleul, O. Malard & R. Wagner. *Otite chronique cholestéatomateuse, aspects cliniques et thérapeutiques*. EMC-Oto-rhino-laryngologie, vol. 4, pages 1–16, 2009.

[Boyer 22] Q. Boyer, D. V. A. Nguyen, P. Rougeot, O. Gaiffe, B. Tamadazte, J. Szewczyk, L. Tavernier, Y. Nguyen & K. Rabenorosoa. *OCT as tool for laser ablation monitoring applied to cholesteatoma*. In Conference on New Technologies for Computer and Robot Assisted Surgery-CRAS, 2022.

[Boyle 09] G. B. R. Boyle, B. P. D. Koracin, P. R. Ä. Nefian, G. M. V. Pascucci, J. Z. J. Molineros & H. T. T. Malzbender. *Advances in visual computing*, 2009.

[Brancadoro 19] M. Brancadoro, M. Manti, F. Grani, S. Tognarelli, A. Menciassi & M. Cianchetti. *Toward a variable stiffness surgical manipulator based on fiber jamming transition*. Frontiers in Robotics and AI, vol. 6, page 12, 2019.

[Burdette 10] E. C. Burdette, D. C. Rucker, P. Prakash, C. J. Diederich, J. M. Croom, C. Clarke, P. Stolka, T. Juang, E. M. Boctor & R. J. Webster III. *The ACUSITT ultrasonic ablator: the first steerable needle with an integrated interventional tool*. In Medical Imaging 2010: Ultrasonic Imaging, Tomography, and Therapy, volume 7629, pages 283–292. SPIE, 2010.

[Burgner-Kahrs 15] J. Burgner-Kahrs, D. C. Rucker & H. Choset. *Continuum robots for medical applications: A survey*. IEEE Transactions on Robotics, vol. 31, no. 6, pages 1261–1280, 2015.

[Burgner 11] J. Burgner, P. J. Swaney, D. C. Rucker, H. B. Gilbert, S. T. Nill, P. T. Russell, K. D. Weaver & R. J. Webster. *A bimanual teleoperated system for endonasal skull base surgery.* In 2011 IEEE/RSJ international conference on intelligent robots and systems, pages 2517–2523. IEEE, 2011.

[Burgner 12] J. Burgner, P. J. Swaney, T. L. Bruns, M. S. Clark, D. C. Rucker, E. C. Burdette & R. J. Webster. *An autoclavable steerable cannula manual deployment device: Design and accuracy analysis.* Journal of medical devices, vol. 6, no. 4, 2012.

[Burgner 13] J. Burgner, D. C. Rucker, H. B. Gilbert, P. J. Swaney, P. T. Russell, K. D. Weaver & R. J. Webster. *A telerobotic system for transnasal surgery.* IEEE/ASME Transactions on Mechatronics, vol. 19, no. 3, pages 996–1006, 2013.

[Butler 12] E. J. Butler, R. Hammond-Oakley, S. Chawarski, A. H. Gosline, P. Codd, T. Anor, J. R. Madsen, P. E. Dupont & J. Lock. *Robotic neuro-emdoscope with concentric tube augmentation.* In 2012 IEEE/RSJ international conference on intelligent robots and systems, pages 2941–2946. IEEE, 2012.

[Butticè 16] S. Butticè, T. E. Sener, C. Netsch, E. Emiliani, R. Pappalardo & C. Magno. *LithoVue™: A new single-use digital flexible ureteroscope.* Central European Journal of Urology, vol. 69, no. 3, page 302, 2016.

[Camarillo 08] D. B. Camarillo, C. F. Milne, C. R. Carlson, M. R. Zinn & J. K. Salisbury. *Mechanics modeling of tendon-driven continuum manipulators.* IEEE transactions on robotics, vol. 24, no. 6, pages 1262–1273, 2008.

[Cao 08] D.-Q. Cao & R. W. Tucker. *Nonlinear dynamics of elastic rods using the Cosserat theory: Modelling and simulation.* International Journal of Solids and Structures, vol. 45, no. 2, pages 460–477, 2008.

[Carpenter 17] D. J. Carpenter, D. L. Tucci, D. M. Kaylie & D. O. Frank-Ito. *Disagreement in middle ear volume estimation between tympanometry and three-dimensional volume reconstruction in the context of tympanic membrane perforation.* Journal of otology, vol. 12, no. 2, pages 74–79, 2017.

[Carpi 09] F. Carpi & C. Pappone. *Stereotaxis Niobe® magnetic navigation system for endocardial catheter ablation and gastrointestinal capsule endoscopy.* Expert review of medical devices, vol. 6, no. 5, pages 487–498, 2009.

[Casati 13] R. Casati & F. Bertails-Descoubes. *Super space clothoids*. ACM Transactions on Graphics (TOG), vol. 32, no. 4, pages 1–12, 2013.

[Charreyron 18] S. L. Charreyron, E. Gabbi, Q. Boehler, M. Becker & B. J. Nelson. *A magnetically steered endolaser probe for automated panretinal photocoagulation*. IEEE Robotics and Automation Letters, vol. 4, no. 2, pages xvii–xxiii, 2018.

[Chautems 18] C. Chautems, S. Lyttle, Q. Boehler & B. J. Nelson. *Design and evaluation of a steerable magnetic sheath for cardiac ablations*. IEEE Robotics and Automation Letters, vol. 3, no. 3, pages 2123–2128, 2018.

[Cheng 18] H. C. Cheng, S. K. Agrawal & L. S. Parnes. *Stapedectomy versus stapedotomy*. Otolaryngologic Clinics of North America, vol. 51, no. 2, pages 375–392, 2018.

[Chikhaoui 14a] M. T. Chikhaoui, K. Rabenorosoa & N. Andreff. *Kinematic modeling of an EAP actuated continuum robot for active micro-endoscopy*. In Advances in Robot Kinematics, pages 457–465. Springer, 2014.

[Chikhaoui 14b] M. T. Chikhaoui, K. Rabenorosoa & N. Andreff. *Towards clinical application of continuum active micro-endoscope robot based on EAP actuation.* In SURGETICA 2014" Gestes médico-chirurgicaux assistés par ordinateur: problèmes scientifiques, outils et applications cliniques", pages 1–4, 2014.

[Chikhaoui 17] M. Chikhaoui, A. Cot, K. Rabenorosoa, P. Rougeot & N. Andreff. *Towards biocompatible conducting polymer actuated tubes for intracorporeal laser steering*. In The Hamlyn Symposium on Medical Robotics, page 79, 2017.

[Chitalia 20a] Y. Chitalia, S. Jeong, N. Deaton, J. J. Chern & J. P. Desai. *Design and kinematics analysis of a robotic pediatric neuroendoscope tool body*. IEEE/ASME Transactions on Mechatronics, vol. 25, no. 2, pages 985–995, 2020.

[Chitalia 20b] Y. Chitalia, S. Jeong, K. K. Yamamoto, J. J. Chern & J. P. Desai. *Modeling and control of a 2-DoF meso-scale continuum robotic tool for pediatric neurosurgery*. IEEE Transactions on Robotics, vol. 37, no. 2, pages 520–531, 2020.

[Clark 12] J. R. Clark, L. Leon, F. M. Warren & J. J. Abbott. *Magnetic guidance of cochlear implants: Proof-of-concept and initial feasibility study*. Journal of Medical Devices, vol. 6, no. 3, 2012.

[Cruveilhier 42] J. Cruveilhier. Anatomie pathologique du corps humain; ou, descriptions, avec figures lithographiées et coloriées, des diverses altérations morbides dont le corps humain est susceptible. Chez JB Baillière, 1842.

[Dahroug 18a] B. Dahroug. *Micro-Robotic Cholesteatoma Surgery: clinical requirements analysis and image-based control under constraints*. PhD thesis, Bourgogne Franche-Comté, 2018.

[Dahroug 18b] B. Dahroug, B. Tamadazte, S. Weber, L. Tavernier & N. Andreff. *Review on Otological Robotic Systems: Toward Microrobot-Assisted Cholesteatoma Surgery*. IEEE Reviews in Biomedical Engineering, vol. 11, pages 125–142, 2018.

[Dalvand 18] M. M. Dalvand, S. Nahavandi & R. D. Howe. *An Analytical Loading Model for n-Tendon Continuum Robots*. IEEE Transactions on Robotics, vol. 34, no. 5, pages 1215–1225, 2018.

[Danilchenko 11] A. Danilchenko, R. Balachandran, J. L. Toennies, S. Baron, B. Munske, J. M. Fitzpatrick, T. J. Withrow, R. J. Webster III & R. F. Labadie. *Robotic mastoidectomy*. Otology & neurotology: official publication of the American Otological Society, American Neurotology Society [and] European Academy of Otology and Neurotology, vol. 32, no. 1, page 11, 2011.

[Dario 00] P. Dario, M. C. Carrozza, M. Marcacci, S. D'Attanasio, B. Magnami, O. Tonet & G. Megali. *A novel mechatronic tool for computer-assisted arthroscopy*. IEEE transactions on information technology in biomedicine, vol. 4, no. 1, pages 15–29, 2000.

[Das-Purkayastha 12] P. K. Das-Purkayastha, C. J. Coulson, D. D. Pothier, P. Lai & J. A. Rutka. *Time trend analysis of mastoidectomy procedures performed in Ontario, 1987–2007*. Acta otolaryngologica, vol. 132, no. 1, pages 16–20, 2012.

[Davis 94] J. Davis & R. Hirschorn. *A model for the embedded tendon control of a slender three-dimensional flexible robot link*. Dynamics and Control, vol. 4, no. 2, pages 185–208, 1994.

[De Donno 13] A. De Donno, L. Zorn, P. Zanne, F. Nageotte & M. de Mathelin. *Introducing STRAS: A new flexible robotic system for minimally invasive surgery*. In 2013 IEEE International Conference on Robotics and Automation, pages 1213–1220. IEEE, 2013.

[De Foer 07] B. De Foer, J.-P. Vercruysse, A. Bernaerts, J. Maes, F. Deckers, J. Michiels, T. Somers, M. Pouillon, E. Offeciers & J. W. Casselman. *The value of single-shot turbo spin-echo*

diffusion-weighted MR imaging in the detection of middle ear cholesteatoma. Neuroradiology, vol. 49, no. 10, pages 841–848, 2007.

[De Foer 10] B. De Foer, J. Vercruysse, M. Spaepen, T. Somers, M. Pouillon, E. Offeciers & J. Casselman. *Diffusion-weighted magnetic resonance imaging of the temporal bone*. Neuroradiology, vol. 52, no. 9, pages 785–807, 2010.

[De Foer 14] B. De Foer, S. Nicolay, J.-P. Vercruysse, E. Offeciers, J. W. Casselman & M. Pouillon. *Imaging of cholesteatoma*. In Temporal Bone Imaging, pages 69–87. Springer, 2014.

[De Volder 10] M. De Volder & D. Reynaerts. *Pneumatic and hydraulic microactuators: a review*. Journal of Micromechanics and microengineering, vol. 20, no. 4, page 043001, 2010.

[Decroly 21] G. Decroly, P. Lambert & A. Delchambre. *A Soft Pneumatic Two-Degrees-of-Freedom Actuator for Endoscopy*. Frontiers in Robotics and AI, page 334, 2021.

[Dewaele 14] F. Dewaele, A. F. Kalmar, F. De Ryck, N. Lumen, L. Williams, E. Baert, H. Vereecke, J. P. Kalala Okito, C. Mabilde, B. Blanckaert*et al. A novel design for steerable instruments based on laser-cut nitinol*. Surgical innovation, vol. 21, no. 3, pages 303–311, 2014.

[Dijkstra 59] E. W. Dijkstra*et al. A note on two problems in connexion with graphs*. Numerische mathematik, vol. 1, no. 1, pages 269–271, 1959.

[Dillon 14] N. P. Dillon, R. Balachandran, A. M. dit Falisse, G. B. Wanna, R. F. Labadie, T. J. Withrow, J. M. Fitzpatrick & R. J. Webster III. *Preliminary testing of a compact bone-attached robot for otologic surgery*. In Medical Imaging 2014: Image-Guided Procedures, Robotic Interventions, and Modeling, volume 9036, pages 291–299. SPIE, 2014.

[Djalilian 10] H. R. Djalilian, M. Rubinstein, E. C. Wu, K. Naemi, S. Zardouz, K. Karimi & B. J. Wong. *Optical coherence tomography of cholesteatoma*. Otology & neurotology: official publication of the American Otological Society, American Neurotology Society [and] European Academy of Otology and Neurotology, vol. 31, no. 6, page 932, 2010.

[Djurhuus 10] B. D. Djurhuus, C. E. Faber, A. Skytthe*et al. Decreasing incidence rate for surgically treated middle ear cholesteatoma in Denmark 1977–2007*. Dan Med Bull, vol. 57, no. 10, page A4186, 2010.

[Djurhuus 15] B. D. Djurhuus, A. Skytthe, K. Christensen & C. E. Faber. *Cholesteatoma in Danish children–A national study of changes in the incidence rate over 34 years*. International journal of pediatric otorhinolaryngology, vol. 79, no. 2, pages 127–130, 2015.

[Doblan 21] A. Doblan, A. Yükkaldiran & B. Erden. *EFFECT OF POSTAURICULAR INCISION ON AURICLE PROTRUSION: ONE-YEAR EXPERIENCE*. In KBB-Forum: Elektronik Kulak Burun Boğaz ve Baş Boyun Cerrahisi Dergisi, volume 20, 2021.

[Du 15] Z. Du, W. Yang & W. Dong. *Kinematics modeling of a notched continuum manipulator*. Journal of Mechanisms and robotics, vol. 7, no. 4, page 041017, 2015.

[Dupont 09] P. E. Dupont, J. Lock, B. Itkowitz & E. Butler. *Design and control of concentric-tube robots*. IEEE Transactions on Robotics, vol. 26, no. 2, pages 209–225, 2009.

[Dupont 10] P. E. Dupont, J. Lock & B. Itkowitz. *Real-time position control of concentric tube robots*. In 2010 IEEE International Conference on Robotics and Automation, pages 562–568. IEEE, 2010.

[Dupont 12] P. Dupont, A. Gosline, N. Vasilyev, J. Lock, E. Butler, C. Folk, A. Cohen, R. Chen, G. Schmitz, H. Ren*et al. Concentric tube robots for minimally invasive surgery*. In hamlyn symposium on medical robotics, volume 7, page 8, 2012.

[Duverney 31] G. Duverney. *Traité de l'organe de l'ouïe. 1683*. Paris: Michallet, vol. 183, 1731.

[Eastwood 16] K. W. Eastwood, H. Azimian, B. Carrillo, T. Looi, H. E. Naguib & J. M. Drake. *Kinetostatic design of asymmetric notch joints for surgical robots*. In 2016 IEEE/RSJ International Conference on Intelligent Robots and Systems (IROS), pages 2381–2387. IEEE, 2016.

[Eastwood 18] K. W. Eastwood, P. Francis, H. Azimian, A. Swarup, T. Looi, J. M. Drake & H. E. Naguib. *Design of a contact-aided compliant notched-tube joint for surgical manipulation in confined workspaces*. Journal of Mechanisms and Robotics, vol. 10, no. 1, page 015001, 2018.

[Edelmann 17] J. Edelmann, A. J. Petruska & B. J. Nelson. *Magnetic control of continuum devices*. The International Journal of Robotics Research, vol. 36, no. 1, pages 68–85, 2017.

[El Naggar 20] A. El Naggar & M. A. Youssef. *Shape memory alloy heat activation: State of the art review*. AIMS Materials Science, vol. 7, no. 6, pages 836–858, 2020.

[Elkhalil 18] H. Elkhalil, A. Alshare, G. Shafirstein & J. Bischof. *A three-dimensional transient computational study of 532-nm laser thermal ablation in a geometrical model representing prostate tissue*. International Journal of Hyperthermia, vol. 35, no. 1, pages 568–577, 2018.

[Entsfellner 13] K. Entsfellner, R. Tauber, D. B. Roppenecker, J. D. Gumprecht, G. Strauss & T. C. Lueth. *Development of universal gripping adapters: Sterile coupling of medical devices and robots using robotic fingers*. In 2013 IEEE/ASME International Conference on Advanced Intelligent Mechatronics, pages 1464–1469. IEEE, 2013.

[Fagogenis 16] G. Fagogenis, C. Bergeles & P. E. Dupont. *Adaptive non-parametric kinematic modeling of concentric tube robots*. In 2016 IEEE/RSJ International Conference on Intelligent Robots and Systems (IROS), pages 4324–4329. IEEE, 2016.

[Fagogenis 19] G. Fagogenis, M. Mencattelli, Z. Machaidze, B. Rosa, K. Price, F. Wu, V. Weixler, M. Saeed, J. E. Mayer & P. E. Dupont. *Autonomous robotic intracardiac catheter navigation using haptic vision*. Science robotics, vol. 4, no. 29, page eaaw1977, 2019.

[Fang 13] C. Fang, A. Kumar & S. Mukherjee. *Finite element analysis of single-walled carbon nanotubes based on a rod model including in-plane cross-sectional deformation*. International Journal of Solids and Structures, vol. 50, no. 1, pages 49–56, 2013.

[Fichera 17] L. Fichera, N. P. Dillon, D. Zhang, I. S. Godage, M. A. Siebold, B. I. Hartley, J. H. Noble, P. T. Russell, R. F. Labadie & R. J. Webster. *Through the eustachian tube and beyond: A new miniature robotic endoscope to see into the middle ear*. IEEE robotics and automation letters, vol. 2, no. 3, pages 1488–1494, 2017.

[Fiedler 13] T. Fiedler, D. Boeger, J. Buentzel, D. Esser, K. Hoffmann, P. Jecker, A. Mueller, G. Radtke, D. Häfke, T. Bitter*et al.* *Middle ear surgery in Thuringia, Germany: a population-based regional study on epidemiology and outcome*. Otology & Neurotology, vol. 34, no. 5, pages 890–897, 2013.

[Filgueiras-Rama 13] D. Filgueiras-Rama, A. Estrada, J. Shachar, S. Castrejón, D. Doiny, M. Ortega, E. Gang & J. L. Merino. *Remote magnetic navigation for accurate, real-time catheter positioning and ablation in cardiac electrophysiology procedures*. JoVE (Journal of Visualized Experiments), no. 74, page e3658, 2013.

[Francis 18] P. Francis, K. Eastwood, V. Bodani, T. Looi & J. Drake. *Design, modelling and teleoperation of a 2 mm diameter compliant instrument for the da Vinci platform.* Annals of biomedical engineering, vol. 46, no. 10, pages 1437–1449, 2018.

[Gafford 21] J. Gafford, M. Freeman, L. Fichera, J. Noble, R. Labadie & R. J. Webster. *Eyes in ears: a miniature steerable digital endoscope for trans-nasal diagnosis of middle ear disease.* Annals of Biomedical Engineering, vol. 49, pages 219–232, 2021.

[Gaillardin 12] L. Gaillardin, E. Lescanne, S. Morinière, J.-P. Cottier & A. Robier. *Residual cholesteatoma: prevalence and location. Follow-up strategy in adults.* European annals of otorhinolaryngology, head and neck diseases, vol. 129, no. 3, pages 136–140, 2012.

[Gao 16a] A. Gao, J. P. Carey, R. J. Murphy, I. Iordachita, R. H. Taylor & M. Armand. *Progress toward robotic surgery of the lateral skull base: Integration of a dexterous continuum manipulator and flexible ring curette.* In 2016 IEEE International Conference on Robotics and Automation (ICRA), pages 4429–4435. IEEE, 2016.

[Gao 16b] A. Gao, R. J. Murphy, H. Liu, I. I. Iordachita & M. Armand. *Mechanical model of dexterous continuum manipulators with compliant joints and tendon/external force interactions.* IEEE/ASME Transactions on Mechatronics, vol. 22, no. 1, pages 465–475, 2016.

[Gao 19] Y. Gao, K. Takagi, T. Kato, N. Shono & N. Hata. *Continuum robot with follow-the-leader motion for endoscopic third ventriculostomy and tumor biopsy.* IEEE Transactions on Biomedical Engineering, vol. 67, no. 2, pages 379–390, 2019.

[Garasz 16] K. Garasz, M. Tański, M. Kocik, E. Iordanova, G. Yankov, S. Karatodorov & M. Grozeva. *The Effect of Process Parameters in Femtosecond Laser Micromachining.* Bulgarian Journal of Physics, vol. 43, no. 2, 2016.

[Garbin 18] N. Garbin, L. Wang, J. H. Chandler, K. L. Obstein, N. Simaan & P. Valdastri. *Dual-continuum design approach for intuitive and low-cost upper gastrointestinal endoscopy.* IEEE Transactions on Biomedical Engineering, vol. 66, no. 7, pages 1963–1974, 2018.

[Gasparetto 15] A. Gasparetto, P. Boscariol, A. Lanzutti & R. Vidoni. *Path planning and trajectory planning algorithms: A general overview*. Motion and Operation Planning of Robotic Systems: Background and Practical Approaches, pages 3–27, 2015.

[Gerber 14] N. Gerber, B. Bell, K. Gavaghan, C. Weisstanner, M. Caversaccio & S. Weber. *Surgical planning tool for robotically assisted hearing aid implantation*. International journal of computer assisted radiology and surgery, vol. 9, no. 1, pages 11–20, 2014.

[Gilbert 15] H. B. Gilbert & R. J. Webster. *Rapid, reliable shape setting of superelastic nitinol for prototyping robots*. IEEE robotics and automation letters, vol. 1, no. 1, pages 98–105, 2015.

[Gilbert 16a] H. B. Gilbert, D. C. Rucker & R. J. Webster III. *Concentric tube robots: The state of the art and future directions*. Robotics Research, pages 253–269, 2016.

[Gilbert 16b] H. B. Gilbert. Concentric tube robots: Design, deployment, and stability. Vanderbilt University, 2016.

[Girerd 18] C. Girerd, T. Lihoreau, K. Rabenorosoa, B. Tamadazte, M. Benassarou, L. Tavernier, L. Pazart, E. Haffen, N. Andreff & P. Renaud. *In vivo inspection of the olfactory epithelium: Feasibility of robotized optical biopsy*. Annals of biomedical engineering, vol. 46, no. 11, pages 1951–1961, 2018.

[Girerd 20] C. Girerd & T. K. Morimoto. *Design and Control of a Hand-Held Concentric Tube Robot for Minimally Invasive Surgery*. IEEE Transactions on Robotics, vol. 37, no. 4, pages 1022–1038, 2020.

[Gorissen 18] B. Gorissen, M. De Volder & D. Reynaerts. *Chip-on-tip endoscope incorporating a soft robotic pneumatic bending microactuator*. Biomedical microdevices, vol. 20, no. 3, pages 1–7, 2018.

[Gosline 12a] A. H. Gosline, N. V. Vasilyev, E. J. Butler, C. Folk, A. Cohen, R. Chen, N. Lang, P. J. Del Nido & P. E. Dupont. *Percutaneous intracardiac beating-heart surgery using metal MEMS tissue approximation tools*. The International journal of robotics research, vol. 31, no. 9, pages 1081–1093, 2012.

[Gosline 12b] A. H. Gosline, N. V. Vasilyev, A. Veeramani, M. Wu, G. Schmitz, R. Chen, V. Arabagi, J. Pedro & P. E. Dupont. *Metal MEMS tools for beating-heart tissue removal*. In 2012 IEEE International Conference on Robotics and Automation, pages 1921–1926. IEEE, 2012.

[Grassmann 18] R. Grassmann, V. Modes & J. Burgner-Kahrs. *Learning the forward and inverse kinematics of a 6-DOF concentric tube continuum robot in SE (3).* In 2018 IEEE/RSJ International Conference on Intelligent Robots and Systems (IROS), pages 5125–5132. IEEE, 2018.

[Gravagne 02] I. A. Gravagne & I. D. Walker. *Manipulability, force, and compliance analysis for planar continuum manipulators.* IEEE Transactions on Robotics and Automation, vol. 18, no. 3, pages 263–273, 2002.

[Gu 14] G.-Y. Gu, L.-M. Zhu, C.-Y. Su, H. Ding & S. Fatikow. *Modeling and control of piezo-actuated nanopositioning stages: A survey.* IEEE Transactions on Automation Science and Engineering, vol. 13, no. 1, pages 313–332, 2014.

[Guay-Lord 16] R. Guay-Lord, X. Attendu, K. L. Lurie, L. Majeau, N. Godbout, A. K. Bowden, M. Strupler & C. Boudoux. *Combined optical coherence tomography and hyperspectral imaging using a double-clad fiber coupler.* Journal of biomedical optics, vol. 21, no. 11, page 116008, 2016.

[Guo 18] S. Guo, Y. Wang, N. Xiao, Y. Zhao, Y. Zeng & J. Wu. *A novel master-slave robotic system with close loop control for vascular interventional surgery.* In 2018 IEEE International Conference on Mechatronics and Automation (ICMA), pages 591–596. IEEE, 2018.

[Ha 16] J. Ha & P. E. Dupont. *Designing stable concentric tube robots using piecewise straight tubes.* IEEE robotics and automation letters, vol. 2, no. 1, pages 298–304, 2016.

[Ha 18] J. Ha, G. Fagogenis & P. E. Dupont. *Modeling tube clearance and bounding the effect of friction in concentric tube robot kinematics.* IEEE Transactions on Robotics, vol. 35, no. 2, pages 353–370, 2018.

[Hamilton 05] J. W. Hamilton. *Efficacy of the KTP laser in the treatment of middle ear cholesteatoma.* Otology & Neurotology, vol. 26, no. 2, pages 135–139, 2005.

[Hanna 14] B. M. Hanna, I. Kivekäs, Y.-H. Wu, L. J. Guo, H. Lin, J. Guidi & D. Poe. *Minimally invasive functional approach for cholesteatoma surgery.* The Laryngoscope, vol. 124, no. 10, pages 2386–2392, 2014.

[Hart 68] P. E. Hart, N. J. Nilsson & B. Raphael. *A formal basis for the heuristic determination of minimum cost paths.* IEEE transactions on Systems Science and Cybernetics, vol. 4, no. 2, pages 100–107, 1968.

[Hendrick 15a] R. J. Hendrick, H. B. Gilbert & R. J. Webster. *Designing snap-free concentric tube robots: A local bifurcation approach.* In 2015 IEEE International Conference on Robotics and Automation (ICRA), pages 2256–2263. IEEE, 2015.

[Hendrick 15b] R. J. Hendrick, C. R. Mitchell, S. D. Herrell & R. J. Webster III. *Hand-held transendoscopic robotic manipulators: A transurethral laser prostate surgery case study.* The International journal of robotics research, vol. 34, no. 13, pages 1559–1572, 2015.

[Hildmann 06] H. Hildmann & H. Sudhoff. Middle ear surgery. Springer Science & Business Media, 2006.

[Hudson 97] T. C. Hudson, M. C. Lin, J. Cohen, S. Gottschalk & D. Manocha. *V-COLLIDE: Accelerated collision detection for VRML.* In Proceedings of the second symposium on Virtual reality modeling language, pages 117–124, 1997.

[Huisman 03] M. A. Huisman, E. De Heer & J. J. Grote. *Cholesteatoma epithelium is characterized by increased expression of Ki-67, p53 and p21, with minimal apoptosis.* Acta oto-laryngologica, vol. 123, no. 3, pages 377–382, 2003.

[Hussong 08] A. Hussong, T. Rau, H. Eilers, S. Baron, B. Heimann, M. Leinung, T. Lenarz & O. Majdani. *Conception and design of an automated insertion tool for cochlear implants.* In 2008 30th Annual International Conference of the IEEE Engineering in Medicine and Biology Society, pages 5593–5596. IEEE, 2008.

[Ikui 00] A. Ikui, I. Sando, S.-I. Haginomori & M. Sudo. *Postnatal development of the tympanic cavity: a computer-aided reconstruction and measurement study.* Acta oto-laryngologica, vol. 120, no. 3, pages 375–379, 2000.

[Ikuta 06] K. Ikuta, H. Ichikawa, K. Suzuki & D. Yajima. *Multi-degree of freedom hydraulic pressure driven safety active catheter.* In Proceedings 2006 IEEE International Conference on Robotics and Automation, 2006. ICRA 2006., pages 4161–4166. IEEE, 2006.

[Im 20] G. J. Im, K. do Han, K. H. Park, C. H. Cho, H. Jang, J. H. Lee & S. H. Lee. *Rate of chronic otitis media operations and cholesteatoma surgeries in South Korea: a nationwide population-based study (2006–2018).* Scientific reports, vol. 10, no. 1, pages 1–10, 2020.

[James 43] H. M. James & E. Guth. *Theory of the elastic properties of rubber.* The Journal of Chemical Physics, vol. 11, no. 10, pages 455–481, 1943.

[Jani 14] J. M. Jani, M. Leary, A. Subic & M. A. Gibson. *A review of shape memory alloy research, applications and opportunities*. Materials & Design (1980-2015), vol. 56, pages 1078–1113, 2014.

[Jeong 20] S. Jeong, Y. Chitalia & J. P. Desai. *Design, modeling, and control of a coaxially aligned steerable (coast) guidewire robot*. IEEE Robotics and Automation Letters, vol. 5, no. 3, pages 4947–4954, 2020.

[Kanagaratnam 08] P. Kanagaratnam, M. Koa-Wing, D. T. Wallace, A. S. Goldenberg, N. S. Peters & D. W. Davies. *Experience of robotic catheter ablation in humans using a novel remotely steerable catheter sheath*. Journal of Interventional Cardiac Electrophysiology, vol. 21, no. 1, pages 19–26, 2008.

[Kato 15] T. Kato, I. Okumura, S.-E. Song, A. J. Golby & N. Hata. *Tendon-driven continuum robot for endoscopic surgery: Preclinical development and validation of a tension propagation model*. IEEE/ASME Transactions on Mechatronics, vol. 20, no. 5, pages 2252–2263, 2015.

[Kato 16] T. Kato, I. Okumura, H. Kose, K. Takagi & N. Hata. *Tendon-driven continuum robot for neuroendoscopy: validation of extended kinematic mapping for hysteresis operation*. International journal of computer assisted radiology and surgery, vol. 11, no. 4, pages 589–602, 2016.

[Keller 18] H. B. Keller. Numerical methods for two-point boundary-value problems. Courier Dover Publications, 2018.

[Kelley 03] C. T. Kelley. Solving nonlinear equations with newton's method, volume 1. Siam, 2003.

[Kelly 96] K. E. Kelly & D. C. Mohs. *The external auditory canal: anatomy and physiology*. Otolaryngologic Clinics of North America, vol. 29, no. 5, pages 725–739, 1996.

[Kemppainen 99] H. O. Kemppainen, H. J. Puhakka, P. J. Laippala, M. M. Sipilä, M. P. Manninen & P. H. Karma. *Epidemiology and aetiology of middle ear cholesteatoma*. Acta oto-laryngologica, vol. 119, no. 5, pages 568–572, 1999.

[Khadem 20] M. Khadem, J. O'Neill, Z. Mitros, L. Da Cruz & C. Bergeles. *Autonomous steering of concentric tube robots via nonlinear model predictive control*. IEEE Transactions on Robotics, vol. 36, no. 5, pages 1595–1602, 2020.

[Khan 16] M. M. Khan & S. R. Parab. *Novel concept of attaching endoscope holder to microscope for two handed endoscopic tympanoplasty*. Indian Journal of Otolaryngology and Head & Neck Surgery, vol. 68, no. 2, pages 230–240, 2016.

[Kim 14] J.-S. Kim, D.-Y. Lee, K. Kim, S. Kang & K.-J. Cho. *Toward a solution to the snapping problem in a concentric-tube continuum robot: Grooved tubes with anisotropy.* In 2014 IEEE International Conference on Robotics and Automation (ICRA), pages 5871–5876. IEEE, 2014.

[Kim 20] J. Kim, T. Looi, A. Newman & J. Drake. *Development of deployable bending wrist for minimally invasive laparoscopic endoscope.* In 2020 IEEE/RSJ International Conference on Intelligent Robots and Systems (IROS), pages 3048–3054. IEEE, 2020.

[Koltai 02] P. J. Koltai, M. Nelson, R. J. Castellon, E.-N. Garabedian, J.-M. Triglia, S. Roman & G. Roger. *The natural history of congenital cholesteatoma.* Archives of Otolaryngology–Head & Neck Surgery, vol. 128, no. 7, pages 804–809, 2002.

[Kudryavtsev 18] A. V. Kudryavtsev, M. T. Chikhaoui, A. Liadov, P. Rougeot, F. Spindler, K. Rabenorosoa, J. Burgner-Kahrs, B. Tamadazte & N. Andreff. *Eye-in-hand visual servoing of concentric tube robots.* IEEE Robotics and Automation Letters, vol. 3, no. 3, pages 2315–2321, 2018.

[Kuntz 20] A. Kuntz, A. Sethi, R. J. Webster & R. Alterovitz. *Learning the complete shape of concentric tube robots.* IEEE transactions on medical robotics and bionics, vol. 2, no. 2, pages 140–147, 2020.

[Kürkçüoğlu 10] A. Kürkçüoğlu, Ş. S. Kürkçüoğlu, H. M. İnançli, M. Enöz, C. Pelin & R. Zagyapan. *Measurement of tympanic cavity volume by the Cavalieri principle in Turkish population.* The Turkish Journal of Ear Nose and Throat, vol. 20, no. 3, pages 137–141, 2010.

[Kutzer 11] M. D. Kutzer, S. M. Segreti, C. Y. Brown, M. Armand, R. H. Taylor & S. C. Mears. *Design of a new cable-driven manipulator with a large open lumen: Preliminary applications in the minimally-invasive removal of osteolysis.* In 2011 IEEE International Conference on Robotics and Automation, pages 2913–2920. IEEE, 2011.

[Lademann 07] J. Lademann, N. Otberg, H. Richter, L. Meyer, H. Audring, A. Teichmann, S. Thomas, A. Knüttel & W. Sterry. *Application of optical non-invasive methods in skin physiology: a comparison of laser scanning microscopy and optical coherent tomography with histological analysis.* Skin Research and Technology, vol. 13, no. 2, pages 119–132, 2007.

[Lau 21] K. Lau, M. Stavrakas, M. Yardley & J. Ray. *Lasers in cholesteatoma surgery: a systematic review.* Ear, Nose & Throat Journal, vol. 100, no. 1_suppl, pages 94S–99S, 2021.

[LaValle 98] S. M. LaValle. *Rapidly-exploring random trees: A new tool for path planning*. 1998.

[Le Nobel 16] G. J. Le Nobel & A. L. James. *Recommendations for potassium-titanyl-phosphate laser in the treatment of cholesteatoma*. The Journal of International Advanced Otology, vol. 12, no. 3, page 332, 2016.

[Legrand 18] J. Legrand, M. Ourak, A. Javaux, C. Gruijthuijsen, M. A. Ahmad, B. Van Cleynenbreugel, T. Vercauteren, J. Deprest, S. Ourselin & E. Vander Poorten. *From a disposable ureteroscope to an active lightweight fetoscope—characterization and usability evaluation*. IEEE robotics and automation letters, vol. 3, no. 4, pages 4359–4366, 2018.

[Legrand 21] J. Legrand, M. Ourak, T. Vandebroek & E. Vander Poorten. *A large displacement model for superelastic material side-notched tube instruments*. International Journal of Mechanical Sciences, vol. 197, page 106329, 2021.

[Leinung 07] M. Leinung, S. Baron, H. Eilers, B. Heimann, S. Bartling, R. Heermann, T. Lenarz & O. Majdani. *Robotic-guided minimally-invasive cochleostomy: first results*. GMS CURAC, vol. 2, page 1, 2007.

[Lemmerling 08] M. Lemmerling, B. De Foer, V. VandeVyver, J.-P. Vercruysse & K. Verstraete. *Imaging of the opacified middle ear*. European journal of radiology, vol. 66, no. 3, pages 363–371, 2008.

[Levenberg 44] K. Levenberg. *A method for the solution of certain nonlinear problems in least squares*. Quarterly of applied mathematics, vol. 2, no. 2, pages 164–168, 1944.

[Levy 13] L. L. Levy, N. Jiang, E. Smouha, R. Richards-Kortum & A. G. Sikora. *Optical imaging with a high-resolution microendoscope to identify cholesteatoma of the middle ear*. The Laryngoscope, vol. 123, no. 4, pages 1016–1020, 2013.

[Li 11] F. Li & R. Klette. *Euclidean shortest paths*. In Euclidean Shortest Paths, pages 3–29. Springer, 2011.

[Li 16] Z. Li, M. Zin Oo, V. Nalam, V. Duc Thang, H. Ren, T. Kofidis & H. Yu. *Design of a novel flexible endoscope—cardioscope*. Journal of Mechanisms and Robotics, vol. 8, no. 5, page 051014, 2016.

[Li 21] S. Li & G. Hao. *Current Trends and Prospects in Compliant Continuum Robots: A Survey*. In Actuators, volume 10, page 145. Multidisciplinary Digital Publishing Institute, 2021.

[Li 22] J. Li, N. Jufas, M. Forer & N. Patel. *Incidence and trends of middle ear cholesteatoma surgery and mastoidectomy in Australia—A national hospital morbidity database analysis.* Laryngoscope Investigative Otolaryngology, vol. 7, no. 1, pages 210–218, 2022.

[Liem 04] T. Liem. *Chapter 17 - The organ of hearing and balance.* In T. Liem, editeur, Cranial Osteopathy (Second Edition), pages 605–633. Churchill Livingstone, Edinburgh, second edition edition, 2004.

[Likas 03] A. Likas, N. Vlassis & J. J. Verbeek. *The global k-means clustering algorithm.* Pattern recognition, vol. 36, no. 2, pages 451–461, 2003.

[Lim 11] H. Lim, J.-M. Han, J. Hong, B.-J. Yi, S. H. Lee, J. H. Jeong, N. Matsumoto, M. Oka, S. Komune & M. Hashizume. *Image-guided robotic mastoidectomy using human-robot collaboration control.* In 2011 IEEE International Conference on Mechatronics and Automation, pages 549–554. IEEE, 2011.

[Lin 15] F.-Y. Lin, C. Bergeles & G.-Z. Yang. *Biometry-based concentric tubes robot for vitreoretinal surgery.* In 2015 37th annual international conference of the IEEE engineering in medicine and biology society (EMBC), pages 5280–5284. IEEE, 2015.

[Liu 13] J. Liu, B. Hall, M. Frecker & E. W. Reutzel. *Compliant articulation structure using superelastic NiTiNOL.* Smart materials and structures, vol. 22, no. 9, page 094018, 2013.

[Liu 14] T. Liu & M. C. Çavuşoğlu. *Three dimensional modeling of an MRI actuated steerable catheter system.* In 2014 IEEE international conference on robotics and automation (ICRA), pages 4393–4398. IEEE, 2014.

[Liu 18] J. Liu, C. Li, X. Fang, J. Jordon & Y. Guo. *Effect of wire-EDM on fatigue of nitinol shape memory alloy.* Materials and Manufacturing Processes, vol. 33, no. 16, pages 1809–1814, 2018.

[Lock 11] J. Lock & P. E. Dupont. *Friction modeling in concentric tube robots.* In 2011 IEEE International Conference on Robotics and Automation, pages 1139–1146. IEEE, 2011.

[Luers 16] J. C. Luers & K.-B. Hüttenbrink. *Surgical anatomy and pathology of the middle ear.* Journal of anatomy, vol. 228, no. 2, pages 338–353, 2016.

[Lyons 10] L. A. Lyons, R. J. Webster & R. Alterovitz. *Planning active cannula configurations through tubular anatomy.* In 2010 IEEE international conference on robotics and automation, pages 2082–2087. IEEE, 2010.

[Maier 10] T. Maier, G. Strauss, M. Hofer, T. Kraus, A. Runge, R. Stenzel, J. Gumprecht, T. Berger, A. Dietz & T. C. Lueth. *A new micromanipulator system for middle ear surgery.* In 2010 IEEE International Conference on Robotics and Automation, pages 1568–1573. IEEE, 2010.

[Maier 11] T. Maier, G. Strauss, F. Bauer, A. Grasser, N. Hata & T. C. Lueth. *Distance measurement in middle ear surgery using a telemanipulator.* In International Conference on Medical Image Computing and Computer-Assisted Intervention, pages 41–48. Springer, 2011.

[Majdani 09] O. Majdani, T. S. Rau, S. Baron, H. Eilers, C. Baier, B. Heimann, T. Ortmaier, S. Bartling, T. Lenarz & M. Leinung. *A robot-guided minimally invasive approach for cochlear implant surgery: preliminary results of a temporal bone study.* International journal of computer assisted radiology and surgery, vol. 4, no. 5, pages 475–486, 2009.

[McJunkin 14] J. McJunkin & R. Chole. *Clinical utility of MRI for cholesteatoma recurrence.* Current Surgery Reports, vol. 2, no. 8, pages 1–7, 2014.

[Miroir 08] M. Miroir, J. Szewczyk, Y. Nguyen, S. Mazalaigue & O. Sterkers. *Design of a robotic system for minimally invasive surgery of the middle ear.* In 2008 2nd IEEE RAS & EMBS International Conference on Biomedical Robotics and Biomechatronics, pages 747–752. IEEE, 2008.

[Miroir 10] M. Miroir, Y. Nguyen, J. Szewczyk, S. Mazalaigue, E. Ferrary, O. Sterkers & A. B. Grayeli. *RobOtol: from design to evaluation of a robot for middle ear surgery.* In 2010 IEEE/RSJ International Conference on Intelligent Robots and Systems, pages 850–856. IEEE, 2010.

[Mitros 20] Z. Mitros, S. Sadati, C. Seneci, E. Bloch, K. Leibrandt, M. Khadem, L. Da Cruz & C. Bergeles. *Optic nerve sheath fenestration with a multi-arm continuum robot.* IEEE robotics and automation letters, vol. 5, no. 3, pages 4874–4881, 2020.

[Molvaer 78] O. Molvaer, F. Vallersnes & M. Kringlebotn. *The size of the middle ear and the mastoid air cell: System measured by an acoustic method.* Acta oto-laryngologica, vol. 85, no. 1-6, pages 24–32, 1978.

[Morfa 09] G. M. Morfa, J. T. Blázquez, Á. M. P. Cordero, H. P. López, J. R. L. Echevarría & L. G. González. *A comparison of beating heart and arrested heart techniques for mitral valve replacement surgery.* MEDICC review, vol. 11, no. 1, pages 36–41, 2009.

[Morgan 04] N. Morgan & M. Broadley. *Taking the art out of smart!-Forming processes and durability issues for the application of NiTi shape memory alloys in medical devices.* Proceedings for the Materials and Processes for Medical Devices Coference, Anaheim, CA, pages 247–252, 2004.

[Morimoto 16] T. K. Morimoto & A. M. Okamura. *Design of 3-D printed concentric tube robots.* IEEE Transactions on Robotics, vol. 32, no. 6, pages 1419–1430, 2016.

[Moses 15] M. S. Moses, R. J. Murphy, M. D. Kutzer & M. Armand. *Modeling cable and guide channel interaction in a high-strength cable-driven continuum manipulator.* IEEE/ASME Transactions on Mechatronics, vol. 20, no. 6, pages 2876–2889, 2015.

[Müller 38] J. Müller. *Über den feineren Bau und die Formen der krankhaften Geschwülste. 1838.* Zit. nach ERD HEIM, 1838.

[Murray 94] R. M. Murray, Z. Li, S. S. Sastry & S. S. Sastry. A mathematical introduction to robotic manipulation. CRC press, 1994.

[NDC, Inc. 22] NDC, Inc. *Nitinol Devices & Components, Inc - Nitinol facts.* [Online] http://confluentmedical.com/tech-center/nitinol-facts/. Date accessed May 30, 2022.

[Neumann 16] M. Neumann & J. Burgner-Kahrs. *Considerations for follow-the-leader motion of extensible tendon-driven continuum robots.* In 2016 IEEE international conference on robotics and automation (ICRA), pages 917–923. IEEE, 2016.

[Nevoux 10] J. Nevoux, M. Lenoir, G. Roger, F. Denoyelle, H. D. Le Pointe & E.-N. Garabédian. *Childhood cholesteatoma.* European annals of otorhinolaryngology, head and neck diseases, vol. 127, no. 4, pages 143–150, 2010.

[Nguyen 12] Y. Nguyen, M. Miroir, G. Kazmitcheff, E. Ferrary, O. Sterkers & A. B. Grayeli. *From conception to application of a tele-operated assistance robot for middle ear surgery.* Surgical innovation, vol. 19, no. 3, pages 241–251, 2012.

[Nguyen 15] T.-D. Nguyen & J. Burgner-Kahrs. *A tendon-driven continuum robot with extensible sections.* In 2015 IEEE/RSJ International Conference on Intelligent Robots and Systems (IROS), pages 2130–2135. IEEE, 2015.

[Nguyen 21a] D. V. A. Nguyen, C. Girerd, Q. Boyer, P. Rougeot, O. Lehmann, L. Tavernier, J. Szewczyk & K. Rabenorosoa. *A Hybrid Concentric Tube Robot for Cholesteatoma Laser Surgery*. IEEE Robotics and Automation Letters, vol. 7, no. 1, pages 462–469, 2021.

[Nguyen 21b] N. T. Nguyen, L. Schilling, M. S. Angern, H. Hamann, F. Ernst & G. Schildbach. *B-spline path planner for safe navigation of mobile robots*. In 2021 IEEE/RSJ International Conference on Intelligent Robots and Systems (IROS), pages 339–345. IEEE, 2021.

[Nguyen 22] D. V. A. Nguyen, J. Szewczyk & K. Rabenorosoa. *An Effective Algorithm for Finding Shortest Paths in Tubular Spaces*. Algorithms, vol. 15, no. 3, page 79, 2022.

[Nikolopoulos 09] T. Nikolopoulos & P. Gerbesiotis. *Surgical management of cholesteatoma: The two main options and the third way – atticotomy/limited mastoidectomy*. International Journal of Pediatric Otorhinolaryngology, vol. 73, no. 9, pages 1222–1227, 2009.

[Nwafor 22] C. J. Nwafor, G. J. Laurent, P. Rougeot & K. Rabenorosoa. *The Caturo: A Submillimeter Diameter Glass Concentric Tube Robot with High Curvature*. Advanced Intelligent Systems, page 2200308, 2022.

[Olarte 15] O. E. Olarte, J. Andilla, D. Artigas & P. Loza-Alvarez. *Decoupled illumination detection in light sheet microscopy for fast volumetric imaging*. Optica, vol. 2, no. 8, pages 702–705, 2015.

[Olszewska 04] E. Olszewska, M. Wagner, M. Bernal-Sprekelsen, J. Ebmeyer, S. Dazert, H. Hildmann & H. Sudhoff. *Etiopathogenesis of cholesteatoma*. European Archives of Oto-Rhino-Laryngology and Head & Neck, vol. 261, no. 1, pages 6–24, 2004.

[Ongaro 18] F. Ongaro, S. Pane, S. Scheggi & S. Misra. *Design of an electromagnetic setup for independent three-dimensional control of pairs of identical and nonidentical microrobots*. IEEE transactions on robotics, vol. 35, no. 1, pages 174–183, 2018.

[Pacheco 21] N. E. Pacheco, J. B. Gafford, M. A. Atalla, R. J. Webster & L. Fichera. *Beyond Constant Curvature: A New Mechanics Model for Unidirectional Notched-Tube Continuum Wrists*. J. Medical Robotics Res., vol. 6, no. 1&2, pages 2140004–1, 2021.

[Pahlevaninezhad 16] H. Pahlevaninezhad, A. M. Lee, G. Hohert, S. Lam, T. Shaipanich, E.-L. Beaudoin, C. MacAulay, C. Boudoux & P. Lane. *Endoscopic high-resolution autofluorescence imaging and OCT of pulmonary vascular networks*. Optics letters, vol. 41, no. 14, pages 3209–3212, 2016.

[Pai 02] D. K. Pai. *Strands: Interactive simulation of thin solids using cosserat models*. In Computer graphics forum, volume 21, pages 347–352. Wiley Online Library, 2002.

[Pandey 15] R. Pandey, S. K. Paidi, J. W. Kang, N. Spegazzini, R. R. Dasari, T. A. Valdez & I. Barman. *Discerning the differential molecular pathology of proliferative middle ear lesions using Raman spectroscopy*. Scientific reports, vol. 5, no. 1, pages 1–8, 2015.

[Pelton 04] A. R. Pelton, T. Duerig & D. Stöckel. *A guide to shape memory and superelasticity in Nitinol medical devices*. Minimally Invasive Therapy & Allied Technologies, vol. 13, no. 4, pages 218–221, 2004.

[Persaud 07] R. Persaud, D. Hajioff, A. Trinidade, S. Khemani, M. Bhattacharyya, N. Papadimitriou, A. Kalan & A. Bhattacharyya. *Evidence-based review of aetiopathogenic theories of congenital and acquired cholesteatoma*. The Journal of Laryngology & Otology, vol. 121, no. 11, pages 1013–1019, 2007.

[Peyron 19] Q. Peyron. *Concept de robot à tube concentrique magnétique: introduction et analyse: application aux interventions minimalement invasives*. PhD thesis, Université Bourgogne Franche-Comté, 2019.

[Peyron 22] Q. Peyron, Q. Boehler, P. Rougeot, P. Roux, B. J. Nelson, N. Andreff, K. Rabenorosoa & P. Renaud. *Magnetic concentric tube robots: introduction and analysis*. The International Journal of Robotics Research, page 02783649211071113, 2022.

[Player 18] B. Player. *Earache*. In Nelson Pediatric Symptom-Based Diagnosis, pages 61–74. Elsevier, 2018.

[Pourafzal 21] M. Pourafzal, H. A. Talebi & K. Rabenorosoa. *Piecewise constant strain kinematic model of externally loaded concentric tube robots*. Mechatronics, vol. 74, page 102502, 2021.

[Prasad 14] S. Prasad, C. La Melia, M. Medina, V. Vincenti, A. Bacciu, S. Bacciu & E. Pasanisi. *Long-term surgical and functional outcomes of the intact canal wall technique for middle ear cholesteatoma in the paediatric population*. Acta Otorhinolaryngologica Italica, vol. 34, no. 5, page 354, 2014.

[Rahunathan 05] S. Rahunathan, D. Stredney, P. Schmalbrock & B. D. Clymer. *Image registration using rigid registration and maximization of mutual information.* In 13th Annu. Med. Meets Virtual Reality Conf, 2005.

[Remacle 15] M. Remacle, V. MN Prasad, G. Lawson, L. Plisson, V. Bachy & S. Van der Vorst. *Transoral robotic surgery (TORS) with the Medrobotics Flex™ System: first surgical application on humans.* European Archives of Oto-Rhino-Laryngology, vol. 272, no. 6, pages 1451–1455, 2015.

[Renda 21] F. Renda, C. Messer, C. Rucker & F. Boyer. *A sliding-rod variable-strain model for concentric tube robots.* IEEE Robotics and Automation Letters, vol. 6, no. 2, pages 3451–3458, 2021.

[Renevier 16] R. Renevier, B. Tamadazte, K. Rabenorosoa, L. Tavernier & N. Andreff. *Endoscopic laser surgery: Design, modeling, and control.* IEEE/ASME Transactions on Mechatronics, vol. 22, no. 1, pages 99–106, 2016.

[Riga 11] C. V. Riga, C. D. Bicknell, M. S. Hamady & N. J. Cheshire. *Evaluation of robotic endovascular catheters for arch vessel cannulation.* Journal of vascular surgery, vol. 54, no. 3, pages 799–809, 2011.

[Rucker 09] D. C. Rucker & R. J. Webster. *Parsimonious evaluation of concentric-tube continuum robot equilibrium conformation.* IEEE Trans. Biomed. Eng., vol. 56, no. 9, pages 2308–2311, 2009.

[Rucker 10a] D. C. Rucker, B. A. Jones & R. J. Webster III. *A geometrically exact model for externally loaded concentric-tube continuum robots.* IEEE transactions on robotics, vol. 26, no. 5, pages 769–780, 2010.

[Rucker 10b] D. C. Rucker, R. J. Webster III, G. S. Chirikjian & N. J. Cowan. *Equilibrium conformations of concentric-tube continuum robots.* The International journal of robotics research, vol. 29, no. 10, pages 1263–1280, 2010.

[Rucker 11a] D. C. Rucker & R. J. Webster III. *Statics and dynamics of continuum robots with general tendon routing and external loading.* IEEE Transactions on Robotics, vol. 27, no. 6, pages 1033–1044, 2011.

[Rucker 11b] D. C. Rucker. The mechanics of continuum robots: model-based sensing and control. Vanderbilt University, 2011.

[Ryu 14] S. C. Ryu & P. E. Dupont. *FBG-based shape sensing tubes for continuum robots.* In 2014 IEEE International Conference on Robotics and Automation (ICRA), pages 3531–3537. IEEE, 2014.

[Sadati 20] S. Sadati, Z. Mitros, R. Henry, L. Cruz & C. Bergeles. *Reduced-order real-time dynamics of concentric tube robots: a polynomial shape (PS) parametrization*. King's College London, Tech. Rep, vol. 134, 2020.

[Sajjadi 13] H. Sajjadi. *Endoscopic middle ear and mastoid surgery for cholesteatoma*. Iranian journal of otorhinolaryngology, vol. 25, no. 71, page 63, 2013.

[Salami 09] A. Salami, M. Dellepiane, E. Proto & R. Mora. *Piezosurgery in otologic surgery: four years of experience*. Otolaryngology—Head and Neck Surgery, vol. 140, no. 3, pages 412–418, 2009.

[Sears 06] P. Sears & P. Dupont. *A steerable needle technology using curved concentric tubes*. In 2006 IEEE/RSJ international conference on intelligent robots and systems, pages 2850–2856. IEEE, 2006.

[Sears 07] P. Sears & P. E. Dupont. *Inverse kinematics of concentric tube steerable needles*. In Proceedings 2007 IEEE international conference on robotics and automation, pages 1887–1892. IEEE, 2007.

[Sénac 19] T. Sénac, A. Lelevé, R. Moreau, C. Novales, L. Nouaille, M. T. Pham & P. Vieyres. *A review of pneumatic actuators used for the design of medical simulators and medical tools*. Multimodal Technologies and Interaction, vol. 3, no. 3, page 47, 2019.

[Sharma 20] S. Sharma, A. Swarup & A. James. *Use of the KTP laser in totally endoscopic cholesteatoma surgery*. The Journal of Laryngology & Otology, vol. 134, no. 4, pages 362–365, 2020.

[Sheehy 77] J. L. Sheehy, D. E. Brackmann & M. D. Graham. *Cholesteatoma surgery: residual and recurrent disease: a review of 1,024 cases*. Annals of Otology, Rhinology & Laryngology, vol. 86, no. 4, pages 451–462, 1977.

[Shibata 15] S. Shibata, K. Murakami, Y. Umeno & S. Komune. *Epidemiological study of cholesteatoma in Fukuoka City*. The Journal of Laryngology & Otology, vol. 129, no. S2, pages S6–S11, 2015.

[Shoa 08] T. Shoa, J. D. Madden, N. Fekri, N. R. Munce & V. X. Yang. *Conducting polymer based active catheter for minimally invasive interventions inside arteries*. In 2008 30th Annual International Conference of the IEEE Engineering in Medicine and Biology Society, pages 2063–2066. IEEE, 2008.

[Simaan 09] N. Simaan, K. Xu, W. Wei, A. Kapoor, P. Kazanzides, R. Taylor & P. Flint. *Design and integration of a telerobotic system for minimally invasive surgery of the throat.* The International journal of robotics research, vol. 28, no. 9, pages 1134–1153, 2009.

[Smith 06] J. A. Smith & C. J. Danner. *Complications of chronic otitis media and cholesteatoma.* Otolaryngologic Clinics of North America, vol. 39, no. 6, pages 1237–1255, 2006.

[Sone 12] M. Sone, T. Yoshida, S. Naganawa, H. Otake, K. Kato, R. Sano, M. Teranishi & T. Nakashima. *Comparison of computed tomography and magnetic resonance imaging for evaluation of cholesteatoma with labyrinthine fistulae.* The Laryngoscope, vol. 122, no. 5, pages 1121–1125, 2012.

[Stepp 05] C. E. Stepp & S. E. Voss. *Acoustics of the human middle-ear air space.* The Journal of the Acoustical Society of America, vol. 118, no. 2, pages 861–871, 2005.

[Styner 00] M. Styner, C. Brechbuhler, G. Szckely & G. Gerig. *Parametric estimate of intensity inhomogeneities applied to MRI.* IEEE transactions on medical imaging, vol. 19, no. 3, pages 153–165, 2000.

[Swaney 12] P. J. Swaney, J. M. Croom, J. Burgner, H. B. Gilbert, D. C. Rucker, R. J. Webster III, K. D. Weaver & P. T. Russell III. *Design of a quadramanual robot for single-nostril skull base surgery.* In Dynamic Systems and Control Conference, volume 45318, pages 387–393. American Society of Mechanical Engineers, 2012.

[Swaney 17] P. J. Swaney, P. A. York, H. B. Gilbert, J. Burgner-Kahrs & R. J. Webster. *Design, fabrication, and testing of a needle-sized wrist for surgical instruments.* Journal of medical devices, vol. 11, no. 1, 2017.

[Swarup 21] A. Swarup, K. W. Eastwood, P. Francis, N. Chayaopas, L. A. Kahrs, C. G. Leonard, J. Drake & A. James. *Design, prototype development and pre-clinical validation of a novel instrument with a compliant steerable tip to facilitate endoscopic ear surgery.* Journal of medical engineering & technology, vol. 45, no. 1, pages 22–34, 2021.

[Torres 15] L. G. Torres, A. Kuntz, H. B. Gilbert, P. J. Swaney, R. J. Hendrick, R. J. Webster & R. Alterovitz. *A motion planning approach to automatic obstacle avoidance during concentric tube robot teleoperation.* In 2015 IEEE international conference on robotics and automation (ICRA), pages 2361–2367. IEEE, 2015.

[Uchil 99] J. Uchil, K. Mohanchandra, K. G. Kumara, K. Mahesh & T. Murali. *Thermal expansion in various phases of Nitinol using TMA*. Physica B: Condensed Matter, vol. 270, no. 3-4, pages 289–297, 1999.

[Ullrich 14] F. Ullrich, S. Schuerle, R. Pieters, A. Dishy, S. Michels & B. J. Nelson. *Automated capsulorhexis based on a hybrid magnetic-mechanical actuation system*. In 2014 IEEE International Conference on Robotics and Automation (ICRA), pages 4387–4392. IEEE, 2014.

[Uzan 21] A. Uzan, P. Chiron, F. Panthier, M. Haddad, L. Berthe, O. Traxer & S. Doizi. *Comparison of Holmium: YAG and Thulium Fiber Lasers on the Risk of Laser Fiber Fracture*. Journal of Clinical Medicine, vol. 10, no. 13, page 2960, 2021.

[Valdez 14] T. A. Valdez, R. Pandey, N. Spegazzini, K. Longo, C. Roehm, R. R. Dasari & I. Barman. *Multiwavelength fluorescence otoscope for video-rate chemical imaging of middle ear pathology*. Analytical chemistry, vol. 86, no. 20, pages 10454–10460, 2014.

[Van der Heijden 02] G. Van der Heijden, A. Champneys & J. Thompson. *Spatially complex localisation in twisted elastic rods constrained to a cylinder*. International journal of solids and structures, vol. 39, no. 7, pages 1863–1883, 2002.

[Vasilyev 12] N. V. Vasilyev, P. E. Dupont & P. J. Del Nido. *Robotics and imaging in congenital heart surgery*. Future cardiology, vol. 8, no. 2, pages 285–296, 2012.

[Vittoria 21] S. Vittoria, G. Lahlou, R. Torres, H. Daoudi, I. Mosnier, S. Mazalaigue, E. Ferrary, Y. Nguyen & O. Sterkers. *Robot-based assistance in middle ear surgery and cochlear implantation: first clinical report*. European Archives of Oto-Rhino-Laryngology, vol. 278, no. 1, pages 77–85, 2021.

[Walsh 11] C. J. Walsh, J. Franklin, A. H. Slocum & R. Gupta. *Design of a robotic tool for percutaneous instrument distal tip repositioning*. In 2011 Annual International Conference of the IEEE Engineering in Medicine and Biology Society, pages 2097–2100. IEEE, 2011.

[Wang 04] T. D. Wang & J. Van Dam. *Optical biopsy: a new frontier in endoscopic detection and diagnosis*. Clinical gastroenterology and hepatology, vol. 2, no. 9, pages 744–753, 2004.

[Wang 17] Z. Wang, M. Fratarcangeli, A. Ruimi & A. Srinivasa. *Real time simulation of inextensible surgical thread using a Kirchhoff rod model with force output for haptic feedback applications*. International Journal of Solids and Structures, vol. 113, pages 192–208, 2017.

[Wang 20] G. Wang, N. M. Le, X. Hu, Y. Cheng, S. L. Jacques, H. Subhash & R. K. Wang. *Semi-automated registration and segmentation for gingival tissue volume measurement on 3D OCT images*. Biomedical Optics Express, vol. 11, no. 8, pages 4536–4547, 2020.

[Webster III 08] R. J. Webster III. Design and mechanics of continuum robots for surgery. The Johns Hopkins University, 2008.

[Webster III 10] R. J. Webster III & B. A. Jones. *Design and kinematic modeling of constant curvature continuum robots: A review*. The International Journal of Robotics Research, vol. 29, no. 13, pages 1661–1683, 2010.

[Webster 06] R. J. Webster, A. M. Okamura & N. J. Cowan. *Toward active cannulas: Miniature snake-like surgical robots*. In 2006 IEEE/RSJ international conference on intelligent robots and systems, pages 2857–2863. IEEE, 2006.

[Webster 08] R. J. Webster, J. M. Romano & N. J. Cowan. *Mechanics of precurved-tube continuum robots*. IEEE Transactions on Robotics, vol. 25, no. 1, pages 67–78, 2008.

[Wei 07] W. Wei, R. Goldman, N. Simaan, H. Fine & S. Chang. *Design and theoretical evaluation of micro-surgical manipulators for orbital manipulation and intraocular dexterity*. In Proceedings 2007 IEEE international conference on robotics and automation, pages 3389–3395. IEEE, 2007.

[Wei 08] W. Wei, R. E. Goldman, H. F. Fine, S. Chang & N. Simaan. *Performance evaluation for multi-arm manipulation of hollow suspended organs*. IEEE transactions on robotics, vol. 25, no. 1, pages 147–157, 2008.

[Williamson 12] T. M. Williamson, B. J. Bell, N. Gerber, L. Salas, P. Zysset, M. Caversaccio & S. Weber. *Estimation of tool pose based on force–density correlation during robotic drilling*. IEEE Transactions on Biomedical Engineering, vol. 60, no. 4, pages 969–976, 2012.

[Wu 06] Y. Wu & J. Y. Qu. *Autofluorescence spectroscopy of epithelial tissues*. Journal of biomedical optics, vol. 11, no. 5, page 054023, 2006.

[Wu 15] L. Wu, B. L.-W. Tan & H. Ren. *Prototype development of a hand-held robotic light pipe for intraocular procedures*. In 2015 IEEE international conference on robotics and biomimetics (ROBIO), pages 368–373. IEEE, 2015.

[Wu 16] L. Wu, R. Crawford & J. Roberts. *Dexterity analysis of three 6-DOF continuum robots combining concentric tube mechanisms and cable-driven mechanisms*. IEEE Robotics and Automation Letters, vol. 2, no. 2, pages 514–521, 2016.

[Xie 08] H.-j. Xie, X.-c. Wu & Y.-a. Min. *Influence of chemical composition on phase transformation temperature and thermal expansion coefficient of hot work die steel*. Journal of Iron and Steel Research International, vol. 15, no. 6, pages 56–61, 2008.

[Xu 14] K. Xu, J. Zhao & M. Fu. *Development of the SJTU unfoldable robotic system (SURS) for single port laparoscopy*. IEEE/ASME Transactions on Mechatronics, vol. 20, no. 5, pages 2133–2145, 2014.

[Yan 22] J. Yan, J. Chen, J. Chen, W. Yan, Q. Ding, K. Yan, J. Du, C. P. Lam, G. K. C. Wong & S. S. Cheng. *A continuum robotic cannula with tip following capability and distal dexterity for intracerebral hemorrhage evacuation*. IEEE Transactions on Biomedical Engineering, vol. 69, no. 9, pages 2958–2969, 2022.

[Yasin 17] R. Yasin, B. P. O'Connell, H. Yu, J. B. Hunter, G. B. Wanna, A. Rivas & N. Simaan. *Steerable robot-assisted micromanipulation in the middle ear: preliminary feasibility evaluation*. Otology & Neurotology, vol. 38, no. 2, pages 290–295, 2017.

[Yekutieli 05] Y. Yekutieli, R. Sagiv-Zohar, R. Aharonov, Y. Engel, B. Hochner & T. Flash. *Dynamic model of the octopus arm. I. Biomechanics of the octopus reaching movement*. Journal of neurophysiology, vol. 94, no. 2, pages 1443–1458, 2005.

[Yoon 18] H.-S. Yoon, J. H. Jeong & B.-J. Yi. *Image-guided dual master–slave robotic system for maxillary sinus surgery*. IEEE Transactions on Robotics, vol. 34, no. 4, pages 1098–1111, 2018.

[York 15] P. A. York, P. J. Swaney, H. B. Gilbert & R. J. Webster. *A wrist for needle-sized surgical robots*. In 2015 IEEE International Conference on Robotics and Automation (ICRA), pages 1776–1781. IEEE, 2015.

[Yu 16] H. Yu, L. Wu, K. Wu & H. Ren. *Development of a multi-channel concentric tube robotic system with active vision for transnasal nasopharyngeal carcinoma procedures.* IEEE Robotics and Automation Letters, vol. 1, no. 2, pages 1172–1178, 2016.

[Zhang 21] D. Zhang, Y. Sun & T. C. Lueth. *Design of a novel tendon-driven manipulator structure based on monolithic compliant rolling-contact joint for minimally invasive surgery.* International Journal of Computer Assisted Radiology and Surgery, vol. 16, no. 9, pages 1615–1625, 2021.

List of Figures

I.1 Difference between infected and normal ears [Bhutta 11]. (a) Normal tympanic membrane. (b) Red arrow: cholesteatoma arising in the upper part of left tympanic membrane (eardrum). Blue arrow: erosion of surrounding bone. 7

I.2 (a) Congenital and (b) acquired cholesteatoma [Nevoux 10]. 7

I.3 A statistical study of 1,146 cholesteatoma surgeries in the period between 1962 and 1988 from all regions of Brazil, of which 960 were adults and 186 were children [Aquino 11]. 8

I.4 The number of cholesteatoma interventions in France, where H71: the number of patients whose had a first cholesteatoma surgery, H95.0: the number of patients whose had another intervention to remove the residual cholesteatoma. The statistics in 2021 is in progress. 10

I.5 The three parts of the human ear. [1] 11

I.6 (a) The HRCT image shows complete erosion of the lateral wall of the lateral semicircular canal (arrow) in a right temporal bone with cholesteatoma. (b) For comparison the corresponding image is shown on the left side, where the intact lateral semicircular canal wall (arrow) is nicely depicted [Lemmerling 08]. 12

I.7 Surgical setup in middle ear surgery using microscopy [Maier 10]. . 13

I.8 The middle ear surveillance videos captured of three temporal bone specimens using a miniature steerable digital endoscope. ① Tympanic Membrane, ② Malleus, ③ Incus, ④ Stapes, ⑤ Mesotympanum, ⑥ Epitympanum, ⑦ Sinus Tympani. With the exception of sinus tympani, the picture quality of specimen 1 (left) always outperforms that of specimen 2 (middle). The picture quality of specimen 3 (right) lies between that of specimens 1 and 2. [Gafford 21] 13

I.9 OCT images of (a) normal middle ear mucosa and (b) cholesteatoma with the keratin layer (bracket) [Djalilian 10]. 15

I.10 (a) Schematic of the human middle ear including tympanic cavity, aditus ad antrum, antrum of mastoid, and mastoid air cells [Stepp 05]. (b) Different regions of the tympanic cavity (epi-, meso-, and hypotympanic) [Dahroug 18a]. 16

I.11 Different approaches to middle ear [2]. 17

I.12 (a) The transcanal approach with a temporary displacement of the tympanic membrane. (b) The endaural approach: top and side view. (c) The mastoidectomy with canal wall up (top) and down (bottom) processes where the external ear canal is conserved or partitial removed, respectively [Hildmann 06]. 17
I.13 Conceptual scheme of μRoCS system. 19
I.14 Standard otologic instruments set used in all regular microscopic ear surgery [Badr-El-Dine 13]. 20
I.15 (a) µRoCS targeted concept illustrated with RobOtol with (b) two accesses to the middle ear with endoscopic flexible microrobots and (c) multimodal optical system for simultaneous cholesteatoma detection and removal. 21

II.1 (a) Anatomical representation of the ear, (b) two accesses used for the proposed surgical protocol, and (c) dimensions of the ear [Nguyen 21a]. 25
II.2 RobOtol. (a) Master-slave surgical robotic system, and (b) experimental setup to demonstrate access to the middle ear. [Miroir 10]. . 28
II.3 (a) Master-slave MMS surgical robotic system with forceps tool [Maier 10], and (b) experimental setup of master-slave MMTS surgical robotic system: (1) joystick console, (2) energy supply, (3) MMS, (4) active gripping adapter, (5) carrier robot, (6) patient phantom, (7) OR-table [Entsfellner 13]. 30
II.4 The hybrid parallel-serial robot. (A) Parallel robot, distal dexterity robot, and rotation stage. (B) The stem, cannula, and gripper. (C) Different configurations of the gripper when it is extended and rotated [Yasin 17]. 32
II.5 The handle design of the miniature steerable digital endoscope with 3-DOF actuation which include Δz (insertion/retraction), Φ (axial rotation), and θ (tip deflection)) [Gafford 21]. 33
II.6 Different components of ARTORG robotic system: (A) robot arm, (B) surgical driller, (C) head clamp, (D) optical tracking, (E) touch screen as the interface to the planning software [Bell 12]. 34
II.7 Different types of continuum robot in the literature according to their actuation method: tendon-driven [Camarillo 08], concentric tubes [Hendrick 15b], multibackbone [Xu 14], pneumatic [Gorissen 18], hydraulic [Ikuta 06], smart material [Shoa 08], magnetic field [Filgueiras-Rama 13]. 36
II.8 (a) Global view on the Quadromanual robot with the four arms used for different tools [Swaney 12], and (b) the hand-held concentric tube robot with deployed tubes, actuation unit, and handle using a user interface [Girerd 20]. 38
II.9 (Left) Drive system of the intracardiac surgical robot. (Right) Ex vivo testing with a porcine heart in which the robot enters the right atrium from the superior vena cava [Gosline 12a]. 39

II.10 (Left) Prototype robot system actuates two cannulas for transnasal skull base surgery. (Right) Experimental setup of the transnasal skull base surgery using the bimanual robot in a human cadaver head [Burgner 13]. 40
II.11 Multi-arm CTR system for deep orbital interventions [Mitros 20]. . 40
II.12 LithoVue (Boston Scientific, Natick, USA): (a) distal flexible tip, (b) proximal non-rigid part, (c) handle [Legrand 18]. 42
II.13 (a) A flexible endoscope designed for mini-mally invasive cardiac surgery - cardioscope [Li 16]. Its flexible section is composed of an elastic tube, a number of spacing discs, a constraint tube and four tendons. (b) A high-strength cable-driven dexterous manipulator [Moses 15]. Its backbone is fabricated by notching on a Nitinol tube. (c) Structure of the endoscope end-effector with spring backbone for maxillary sinus surgery. (1) Assembled state. (2) Disassembled state. (3) Cross-sectional view of a cylinder [Yoon 18]. (d) A novel tendon-driven manipulator structure based on monolithic compliant rolling-contact joint for minimally invasive surgery [Zhang 21]. 43
II.14 (a) Uni- and bi-directional notched tubes [Eastwood 18], and (b) multi-directional notched tube design with 120 notch spacing, three cables and cable guides [Francis 18]. 44
II.15 Design of a robotic tool with two notched-tube segments that is always within the cone of visibility of the endoscope [Chitalia 20a]. 46
II.16 The tendon-driven continuum robot with 3 extensible sections based on CTR [Nguyen 15]. The magnetic spacer disks distribute with equidistant spacing due to magnetic repulsion forces at any section length. 46
II.17 The 6-DOF hybrid continuum robots where t stands for translational DOF and r stands for rotational DOF [Wu 16]. 47
II.18 (a) Coaxial tubes and dimensions, (b) demonstration of COAST achieving different curvatures and arc lengths, and (c) actuation stage using individual linear motors to control the COAST guidewire [Jeong 20]. 47
II.19 The proposed hybrid CTR scheme. 51

III.1 Representation of the hybrid concentric tube robot composed of a CTR and a dexterous wrist integrated to the inner tube, with associated parameterization. 55
III.2 The wrist of the robot can be considered as an equivalent endcap of the CTR in the static model. The length of the endcap δ is approximately 0. 60
III.3 The main problem to be studied: the static model (coupled Cosserat rod and string model) for the deformation of the tube coupling with the shortest path problem inside the tubular space for the tendon location. 62

III.4 Discrete approach for the ESP problem. (Left): Inner space of the tube transformed into a series of meshed circular disks and (Right): the directed graph [Nguyen 22]. 71
III.5 Three partitions of the shortest path inside the tubular space. At $\boldsymbol{A}$ belonging to **P3**, the VP cannot see the ending cross-section S_{N+1}. The correct direction corresponds to the longest-length-of-sight. At $\boldsymbol{B}$ belonging to **P2**, it can see S_{N+1}, but not $\boldsymbol{\Omega}$. The correct direction is towards the visible point $\boldsymbol{Y}$ in S_{N+1} so that the angle θ between $\boldsymbol{BY}$ and $\boldsymbol{B\Omega}$ is the smallest one. At $\boldsymbol{C}$ in **P1**, the particle can see $\boldsymbol{\Omega}$. The correct direction is towards $\boldsymbol{\Omega}$ [Nguyen 22]. 72
III.6 Shooting method to solve the BVP for the robot configuration H corresponding to a given value of tendon location parameter Ψ. . . 74
III.7 The quasi-solution of Ψ results in the residual errors satisfied within the corresponding acceptable regions. 75
III.8 The elastic (3D-printing) tube with the centerline in 3D space as described later in this section is chosen for this test. We fix $\boldsymbol{v}(0) = [0\ 0\ 1]^T$, $\boldsymbol{u}(0) = [0\ 0\ 0]^T$ for the entire H(0). a) fix $\lambda = 0.025$, the residual always decreases with any force from 1 to 8 (N), which demonstrates the correctness of the iterative guess. b) fix $F = 6(N)$, for any λ between 0 and 1, each residual error consist of 2 parts: 1) it reduces when the guessing value is away from the quasi-solution, then 2) there exists a resistance radius around the exact solution where the residual reduction cannot occur any more. Higher values of λ allow obtaining faster residual reductions but correspond to greater resistance radii. 76
III.9 Algorithm to determine the tendon location parameter Ψ corresponding to a given value of H(0). 78
III.10 Global algorithm. The ports A-1,2,3,4 and B-1,2,3,4 are as shown in figure III.6 and figure III.9, respectively. A-1 : input/update $\boldsymbol{\chi}$, A-2 : input/update Ψ_{min}, A-3 : transfer new guess $\boldsymbol{\chi}$ to solve *Problem B*, B-1: input the initial guess Ψ^0, B-2 : input/update H(0), B-3 : update guess Ψ, B-4 : output Ψ_{min} and $\boldsymbol{\chi}$ (hence H(0)) adjusted. . . 79
III.11 Deformation of a multi-stiffness tube under the free internal tendon load. The references correspond to the differences in bending angle between the two curved segments are $0°, 90°, 180°$, and $270°$. The tendon tension increase gradually from 0 to 12 N. 80
III.12 Distance and angular tip errors between the deformed shapes and the reference of the CTR under the tendon load. Four referenced configurations of the CTR are created by choosing the difference in bending angle between the two curved segments being $0°, 90°, 180°$, and $270°$. 81
III.13 Geometric representation of the wrist with its parameters and frames used for the model, with (a) the initial state of the wrist integrated at the tip of the innermost tube, (b) the wrist bending under the actuation force, and (c) a cutout of the bent wrist. 83

III.14(a) Bending wrist with the integrated OF, (b) cross-section of the wrist, and (c) curved portion of the OF. 84
III.15(a) The static model prediction and experimental results with respect to the tendon force required to bend the wrists. We conducted three tests for each wrist by changing the speed of the translation stage to 5, 10, and 15 µm/s and calculated the average value of the experimental data. The yellow domain shows the sensitivity of the model (of wrist 1) with 1% variation of g and μ_s. As the static model is most sensitive to the cut depth, the red curve (wrist 3) with a big difference in μ_s still belongs to the yellow domain. (b) Wrist 1, 2 and 3 under the tendon force of 0.6 N. 86
III.16(a) Model predicted and experimental tip spatial trajectories of the wrist (the maximum bending of 85^o without the OF). The error arises when the wrist bends with a high curvature. The main reason for this error is the non uniform bending during the test as demonstrated in Fig. III.15b caused by the different friction force at the corners (descending from proximal to distal cutouts). (b) Model validation in case of with and without the OF. We increase the bending angle of the wrist from zero to the maximum value. Parameters of the model: $\rho = 0.42\ mm$, $d = 0.12\ mm$, and $L = R_i$. 87
III.17(LEFT) The slider and edit value selections of the proposed robot using GUI of MATLAB. (RIGHT) The proposed robot configuration that allows it to be inserted through the entry hole through the mastoid to the typanic cavity. The diameters of the robot is selected as given in Table IV.2 88

IV.1 A CT-scan DICOM image of the circular sector of the skull. 92
IV.2 Image segmentation and 3D reconstruction of the anatomy with Invesalius using DICOM images. 93
IV.3 Steps of the 3D model extraction using Meshlab. The mastoid is temporarily removed during this process to facilitate mesh selection. 94
IV.4 (a) Visualization using MATLAB of the STL 3D right ear model with two accesses to the tympanic cavity. (b) Different view from the outside of the STL 3D model. (c) Inner zone of the model with the view from the auditory canal, (d) from the mastoid hole, and (e) from the hypotympanic. 95
IV.5 Diagram of the robot synthesis based on the anatomical constraint. Each robot design will provide a particular coverage volume. By testing with various sets of design parameters, the design that corresponds to the largest coverage volume will be chosen for fabrication. 96
IV.6 Representation of robot configurations that reach the tympanic cavity through the two accesses. Configuration (1) is possible. Configuration (2) is not possible as the tip is outside the tympanic cavity. Configuration (3) is not possible because of collisions between the robot body and the ear model. 97

IV.7 The collision test of the hybrid CTR that is inserted via a $3-mm$ hole through mastoid: (a) step 1: inserting the robot through the entrance; (b) step 2: only the CTR is considered, the tubes are translated and rotated and the collision test is performed to obtain the set of possible configurations; (c) step 3: only the dexterous wrist is considered, the bending angle increases from 0° (for possible configurations found in step 2) to the maximum value to determine the set of tip positions of the robot corresponding to its possible configurations. 98

IV.8 Different configurations of the hybrid CTR with the innermost tube's rotation of 0°, 120°, and 240°. 99

IV.9 Top view of different types of the notches 101

IV.10 Bending of the wrist with a cut depth smaller than g_{min}. The cross-sections of both cut parts and uncut parts change during the test. The notched tube fabricated by the wire-cut EDM has the outer and inner diameters of 2.68 mm and 2.50 mm, respectively. The calculated $g_{min} = 2.184\ mm$ while $g = 2.15\ mm$. 103

IV.11 Different domain of the wrist deflection based on g. 104

IV.12 Algorithm for determining the robot design parameters. κ_2, L, and n will be sequentially examined within their limits. The block "Calculation V" is the coverage volume calculation task. 106

IV.13 Simulations of the tympanic cavity coverage volume by the robots that are inserted via a $3-mm$ hole through mastoid: (a) only 1-segment uni-directionally notched tube is considered, point A cannot be accessible by neither the robot that has only 1 wrist nor one that has 2 wrists in terms of C and S shapes as the inserting path requires bending in two different planes; (b) only the CTR is considered, the robot cannot reach point B and C due to the limitation of the precurvature of the tubes; (c) the CTR with the distal wrist significantly improves the coverage volume inside the tympanic cavity. (d) Total tympanic cavity coverage volume by the hybrid concentric tube robot inserted via the two accesses. 108

IV.14 Shape setting of Nitinol using Joule heating property [Gilbert 15]. . 109

IV.15 Nitinol tubes shape-setting. (a) Creating the grooves of the desired curvatures (10 mm and 20 mm radius) on the template utilizing a ProtoMAX water jet cutter machine (from OMAX company, France). (b) Inserting the tube into the fixtures (template and support). (c) Putting the fixtures and the tubes in the air furnace at 600°C for 20 min. (d) The obtained result after quenching in cold water. (e) The final result after cleaning. 110

IV.16 Fabricate the wrist by using a CNC manufacturing process with 0.02 in end mill [Swaney 17]. 112

IV.17 The distal end of the inner tube is notched with EDM method. The parameters of the wrist is selected as the simulation result including: $g = 0.93\ mm$, $b = 2\ mm$, $L = 5\ mm$, $h = c = 0.33\ mm$, and $n = 5$ cutouts. Two additional notches (1.5 mm cut height and 0.2 mm cut depth) are created to fix the relative rotation of the end cap with respect to the wrist. 113
IV.18 Test of printing tiny holes with diameters from 0.1 to 1.0 mm with the machine from Formlabs. Some holes are not through as printing errors. 114
IV.19 Hybrid CTR is built according to the simulation results. The laser optical fiber protrudes about 1 mm from the outside of the end cap. The outer and inner diameters of the three tubes are: 2.50 and 1.80 mm, 1.50 and 1.25 mm, 1.08 and 1.00 mm, ... 114
IV.20 End cap of the wrist fabricated using Nanoscribe 3D printing resin IP-Q material. Two tiny holes for the tendon and the optical fiber are 0.23 mm and 0.48 mm in diameter. The end cap has parts corresponding to two additional notches of the wrist for fixing the relative rotation between them. These parts locate symmetrically on either side of the line connecting the centers of the two holes. . . 115
IV.21 Microscopic image of the end cap created with FEMTOprint. The outer radius of the end cap is 589 μm (nominal value: 600 μm). The radii of the two tiny holes are 91 μm (nominal value: 75 μm) and 235 μm (nominal value: 220 μm). The distance between the centers of these holes is 470 μm (nominal value: 470 μm). 116
IV.22 Consideration of different tendons used to bend the wrist: (a) nylon material with diameter of 0.15 mm and (b) steel wire with diameter of 0.1 mm. The wrists shown in this figure are only for the purpose of demonstration and does not have the same parameters as that of the proposed hybrid CTR. 117
IV.23 Our experimental setup. The actuator unit consists of three part. Each part can perform a translation and a rotation. The outermost tube is fixed to the actuator unit's frame. Two linear-rotary stages are used to translate and rotate the middle and the innermost tubes. The last linear-rotary stage equipped with a force sensor is employed to drive the tendon and measure its tension force. Thus, 5 degrees of freedom is used in this letter. 118

V.1 Conceptual scheme of the hybrid CTR used for the prototype performance assessment. 123
V.2 Left: two different OCT volume images (C-scan) of the same actuation set used for measuring the robot repeatability. Right: after applying the transformation matrix for one image to align it with the other one. 123
V.3 The measurement of repeatability value of the robot. 124

V.4 An illustration of time constraints affecting the paths traced by the robot tip. The movements are carried out by leading the tip directly toward the next target point. The blue line on the left is time-invariant (path following) and the red line on the right considers time constrains (trajectory tracking). 125

V.5 Reference path is a square of 46 mm. 126

V.6 Illustration of the path following of the proposed robot which can be considered as piecewise constant curvature sections. 127

V.7 Open loop control scheme used for the path following assessment. . 128

V.8 Nanoscribe 3D printed end cap of the wrist dedicated to the integration of the AURORA magnetic sensor. 129

V.9 Conceptual scheme of holding the magnetic sensor with the robot's end cap. Design 1: using 1 mm hole to axially fix the sensor. Design 2: using 1 mm hole to fix the sensor in the principal axis. Design 3: Use two $0.5 - mm$ holes to hold two different sensors. 129

V.10 Reference and experimental paths performed by the hybrid CTR and measured by AURORA tracking sensor. Left: global view. Right: front view. 130

V.11 Conceptual scheme of the hybrid CTR for the deployment in confinded workspace and cholesteatoma laser ablation demonstrations. . . 130

V.12 Deployment of the hybrid continuum robot in the middle ear phantom. Residual cholesteatoma are illustrated with red markers. The robot is inserted through a 3 mm diameter hole on the posterior wall of the tympanic cavity and approaches hard-to-reach positions in this confined workspace. Top: simulation results. Bottom: the surgical target is at the upper part of the eardrum, above the entry hole, and below the entry hole, respectively. 131

V.13 Cholesteatoma laser ablation using the LBO laser. Red light is used to determine the laser beam's incident position before performing the ablation. 133

V.14 Steps of cholesteatoma OCT image processing [Boyer 22]. 134

V.15 Left: cholesteatoma cells burned by using the LBO laser. Right: volume image of the residual cholesteatoma during the ablation. . . 134

V.16 Vaporized volume as a function of exposure time. 135

V.17 Compact and light weight prototype of the hybrid CTR for middle ear surgery. 139

B.1 An example of a CTR portion of 3 tubes. 146

C.1 Dimension of the 3D-printing tubes. ① The centerline curve of the tube lies in a plane and comprises a 6 mm straight effective length and two precurved segments bending into two opposite directions with the length of 50 mm and the radius of 56 mm. ② The centerline curve of the tube is composed of 4 mm and 20 mm straight lengths at the proximal and distal end respectively and three curved segments belonging to three perpendicular planes and still ensuring the continuity of the tube. The arc measure of each curved segment is 90^o and their radii are 30 mm, 25 mm, and 15 mm in order from base to tip. 150
C.2 The experimental validations for the S-shaped tube with the tensions of 0, 4, 8, and 12 (N). To detect the experimental centerline in plane, we start by defining the two contours of the tube wall image and label them as two sets of points A and B. Then, for each point a_i of A, we find the corresponding point b_i in B that closest to it. Thus, the centerline is then the set of the midpoint m_i of the line segment $a_i b_i$. 151
C.3 Side and front views of the simulation (left) and the experiment (right) with the 3D tube and the tension of $6N$. The tendon position is fixed at the top point for both the base and the tip. 152

List of Tables

I.1 The incidence rate of cholesteatoma surgery throughout different countries. 9

II.1 Summary of the mastoidectomy robotic system [Lim 11]. 28
II.2 Summary of RobOtol robotic system [Miroir 10] 29
II.3 Summary of MMTS robotic system [Entsfellner 13] 30
II.4 Summary of the hybrid parallel-serial robot [Yasin 17] 31
II.5 Summary of the bendable endoscope [Gafford 21] 33
II.6 The multi-arm CTR system for deep orbital interventions [Mitros 20] 41
II.7 The multi-segment notched-tube tendon-driven robot [Chitalia 20a] . 45
II.8 The COAST guidewire robot [Jeong 20] 48

IV.1 Computation time of the elemental tasks 98
IV.2 Configuration of the concentric tube robot 100
IV.3 Bending stiffnesses of the tubes and of the wrist 105
IV.4 Range of the design parameters of the wrist 105
IV.5 Middle ear coverage volume (mm^3) by different robot designs depending on L (mm), n, and κ_2 (mm^{-1}) using the mastoid entry path. 107
IV.6 Different fabrication techniques of the notched wrist in the literature. OD and ID stand for the outer and inner diameters of the notched tubes. 111

V.1 The use of robot design versions in the later tests. 122

C.1 Model RMS Errors (mm) for S-shaped Tube Experiments 150
C.2 Model tip and angle errors for the 3D precurved tube. 151
C.3 Tests of the wrist bending without and with the optical fiber. 153

sPIM

Titre : Robot continuum hybride pour la chirurgie de l'oreille moyenne : conception, fabrication et démonstration

Mots clefs: Robot à tube concentrique (RTC), actionnement hybride, conception de robot, modélisation, chirurgie au laser de l'oreille moyenne, cholestéatome

Résumé : Le cholestéatome est une maladie envahissant l'oreille moyenne (OM), qui peut entraîner de graves complications et doit être traitée par une chirurgie. L'incidence élevée de cholestéatome résiduel (CR) induit un deuxième examen douloureux du patient. Ainsi, ce manuscrit présente un RTC hybride, qui couvre le volume de l'OM pour une ablation au laser exhaustive du CR en utilisant deux accès: à travers le conduit auditif et via un trou mastoïdien. Ce microrobot reprend la compacité d'un RTC tout en améliorant la dextérité à son extrémité distale à l'aide d'un poignet à découpe asymétrique, actionné par un tendon. Un modèle géométrico-statique est établi pour décrire la configuration du robot en présence de la fibre optique. Les contraintes anatomiques sont obtenues puis les paramètres de conception du robot sont sélectionnés sur la base des configurations possibles qui évitent la collision entre le robot et le modèle de l'oreille. Un prototype du robot est fabriqué par des méthodes d'usinage et de mise en forme ainsi que des techniques de microfabrication. Une commande en boucle ouverte est utilisée pour effectuer certaines tâches de positionnement sur ce prototype. Des protocoles expérimentaux sont proposés pour évaluer la répétabilité du robot, le déploiement du robot à l'intérieur de l'OM pour atteindre des emplacements spécifiques de CR sur le fantôme d'OM imprimé en 3D, et l'ablation au laser de véritables cellules de cholestéatome sont utilisées pour évaluer le volume enlevé selon les paramètres du laser.

Title : Hybrid continuum robot for middle ear surgery: design, fabrication and demonstration

Keywords : Concentric tube robot (CTR), hybrid actuation, modeling, robot design, middle ear laser surgery, cholesteatoma

Abstract : Cholesteatoma is a disease invading the middle ear (ME), which can lead to serious complications and only be treated through a surgery. The high incidence of residual cholesteatoma (RC) induces a painful second examination of the patient. Thus, this manuscript presents a hybrid CTR, which covers the ME volume for exhaustive laser ablation of RC by using two accesses: through the auditory canal and via a mastoid hole. This microrobot takes the compactness of a CTR while improving the dexterity at its distal end using a notched wrist, actuated by a tendon. A kineto-static model is derived to describe the robot configuration in the presence of the laser optical fiber. The anatomical constraints are obtained, then the robot design parameters are selected through the possible configurations that avoid collision between the microrobot and the ear model. A robot prototype is fabricated by using conventional machining and shape-setting methods together with microfabrication techniques. An open loop control is utilized to perform some positioning tasks on the robot prototype. The experimental protocols are proposed to assess the robot's repeatability, the deployment of the robot inside the ME to reach some specific location of RC on the 3D printed ME phantom, and laser ablation of real cholesteatoma cells are shown on the prototype to evaluate the removed volume according to the laser parameters.

UBFC UNIVERSITÉ BOURGOGNE FRANCHE-COMTÉ

Université Bourgogne Franche-Comté
32, avenue de l'Observatoire
25000 Besançon